UNIVERSITY OF SOUTHAMPTON

FACULTY OF ENGINEERING AND THE ENVIRONMENT

Engineering Sciences Unit

Reducing conservatism in life assessment approaches: Industrial steam turbine blade to disc interfaces and the shot peening process

by

Katherine Anne Soady

Thesis for the degree of Doctor of Engineering

May 2013

UNIVERSITY OF SOUTHAMPTON

ABSTRACT

FACULTY OF ENGINEERING AND THE ENVIRONMENT

ENGINEERING SCIENCES UNIT

Doctor of Engineering

REDUCING CONSERVATISM IN LIFE ASSESSMENT APPROACHES: INDUSTRIAL STEAM TURBINE BLADE TO DISC INTERFACES AND THE SHOT PEENING PROCESS

By Katherine Anne Soady

Damage tolerant life assessment and the resulting component repair and replacement scheduling is crucial to the continued operation of UK power plant. Typically a major outage on a conventional power station takes 8 -12 weeks; there is a drive to minimise the scope of remedial works undertaken allowing the length of the outage to be reduced. Recent trends in life assessment methods are towards approaches that can be used to justify deferring invasive inspections and reducing the scope of the maintenance works. This thesis reports the development of a life assessment protocol for industrial steam turbine blade to disc interfaces which explicitly accounts for the residual stresses and strain hardening resulting from shot peening with a view to improving life cycle efficiency and reducing operator cost.

A modelling approach has been developed which allows for the effect of shot peening to be explicitly accounted for in the damage tolerant life assessment process. The approach requires the input of experimentally determined residual stress, surface roughness and strain hardening profiles. Whilst the methods for determining residual stresses are well standardised, the optimum means of determining both the surface roughness characteristics (two and three dimensional) and the strain hardening profile (microhardness, X-ray diffraction and electron backscatter diffraction) were investigated as a first step towards standardising these measurements: It was found that a three dimensional analysis of the surface topography is most likely to capture the worst case defect. X-ray diffraction and electron backscatter diffraction measurements of cumulative plastic strain were shown to be most similar, with microhardness measurements appearing to overestimate the strain hardened region.

Furthermore, the retained benefit of the shot peening process in terms of total life even under very high strain range LCF conditions has been clarified in terms of the applied stress distribution, specific material cyclic characteristics and residual stress relaxation. Under high strain range three point bend fatigue loading, the residual stresses and strain hardening in notched samples of the tempered martensitic steel under investigation did not change significantly. This allows the shot peening process to be specified for notched components under high strain range cyclic bend load, such as low pressure turbine disc blade interfaces, with an improved understanding of the resulting benefits.

Contents

List of tables

List of figures

:

Declaration of authorship

I, Katherine Anne Soady, declare that the thesis entitled:

'Reducing conservatism in life assessment approaches: Industrial steam turbine blade to disc interfaces and the shot peening process'

and the work presented in it are both my own, and have been generated by me as the result of my own original research. I confirm that:

- This work was done wholly or mainly while in candidature for a research degree at this University;
- Where any part of this thesis has previously been submitted for a degree or any other qualification at this University or any other institution, this has been clearly stated;
- Where I have consulted the published work of others, this is always clearly attributed;
- Where I have quoted from the work of others, the source is always given. With the exception of such quotations, this thesis is entirely my own work;
- I have acknowledged all main sources of help;
- Where the thesis is based on work done by myself jointly with others, I have made clear exactly what was done by others and what I have contributed myself;
- Parts of this work have been published as:

1. K. A. Soady, *Review: Life assessment methodologies incorporating shot peening process effects; mechanistic consideration of residual stresses and strain hardening. Part 1: The effect of shot peening on fatigue resistance*. Materials Science and Technology, 2013. **29**(6): p. 637 – 651.
2. K. A. Soady, B. G. Mellor and P. A. S. Reed, *Review: Life assessment methodologies incorporating shot peening process effects; mechanistic consideration of residual stresses and strain hardening. Part 2: Approaches to fatigue lifing after shot peening*. Materials Science and Technology, 2013. **29**(6): p. 652 – 664.

3. K. A. Soady, B. G. Mellor, J. Shackleton, A. Morris and P. A. S. Reed, *The effect of shot peening on notched low cycle fatigue*. Materials Science and Engineering A, 2011. **528**(29-30): p. 8579 – 8588.

4. K. A. Soady, B. G. Mellor, G. D. West, G. Harrison, A. Morris and P. A. S. Reed, *Evaluating surface deformation and near surface strain hardening resulting from shot peening a tempered martensitic steel and application to low cycle fatigue.* In press, International Journal of Fatigue, 2013, **DOI:10.1016/j.ijfatigue.2013.03.019.**

5. B. He, K. A. Soady, B. G. Mellor, A. Morris, P. A. S. Reed, *The effects of shot peening on short crack growth rate and resulting low cycle fatigue behaviour in a low pressure turbine blade material*. Materials Science and Technology, 2013. **29**(7): p. 788 – 796.

Signed:

Date: 22 May 2013

Acknowledgements

There are a great many people I wish to thank, without whom this thesis would not have been possible. First and foremost I would like to thank my supervisors at the University of Southampton to whom I am greatly indebted, Professor Philippa Reed and Dr. Brian Mellor, for their continuous patience, support and guidance over the last four and a half years. They have both contributed a great deal to my development both as a researcher and as a person and for that I will be forever grateful. I would also like to thank Professor Andy Morris at E.ON New Build and Technology for his valuable technical input and for ensuring the work retained an industrial focus.

Thanks are also extended to both Judith Shackleton and Gary Harrison at the University of Manchester for their help with XRD measurements and to Dr. Geoff West at Loughborough University for his help with EBSD measurements. Without the assistance of the Structural Integrity Team at E.ON New Build and Technology (Dr. Colin Wignall, Dr. Iain Paterson, Mehran Zanjani, Sukhjit Pabla and Xiaoling Zhang), I would not have been able to complete some of the modelling work which is included in this thesis and I am grateful for their input. I must also thank Dr. Mithila Achintha and Binyan He, both at the University of Southampton for their collaborative input to the wider project.

I am also indebted to several other past and present students at the University of Southampton: Firstly, Dr. Stewart 'Rat-chet' Everitt, for teaching me virtually everything I know about how to work the Instron; I will never forget our ratchet marks and 'spesh' banter! You have, and will continue to be, an inspiration and a true friend. I would also like to thank Dr. Alan Burke-Veliz for getting me started with Abaqus Standard and Dan Bray for both our subsequent discussions on modelling techniques and for providing the three dimensional model of the shot peening process. I must also thank the project students and summer interns, some of whom are now postgraduate students in the Faculty of Engineering and the Environment themselves, who helped collect some of the data which have gone into writing this thesis: Senzhe Shu, Shaun Ross, Victoria Sisson, Hannah Morton, Jenny Crump and Ross Downer. Your efforts did not go unnoticed! I would also like to thank the administrative staff (Gwyneth Skiller and Sue Berger) for their frequent help and the technical staff (Dave Beckett, Rob Barnes and Erik Roszkowiak), without whose helpful advice experimental work would have been even more challenging.

The provision of financial support for this work by EPSRC, the University of Southampton and E.ON New Build and Technology Ltd is gratefully acknowledged. I would also like to thank the Royal Commission for the Exhibition of 1851 for the

provision of funding for the final two years of my EngD and for the forthcoming year as part of an Industrial Fellowship. This financial assistance has been accompanied by frequent opportunities to meet other researchers and esteemed scientists and engineers at the many events laid on by the Commission which Nigel Williams and the team work tirelessly to ensure run smoothly. I am very grateful for all the opportunities that this Industrial Fellowship has offered me.

On a personal note, to my friends and family who supported me in the good times and helped pull me through the bad times, I will always be thankful for your love which pushed me on and helped shape the person I am today. To my partner, Tom, I couldn't have done it without you: I'm lucky I have you to love and depend upon!

Nomenclature

a	Edge crack length in direction of sample width
a_{Hv}	Vickers indent contact semi-width
a_{Hz}	Hertzian contact radius
b	Rate at which the size of the yield surface changes as plastic strain accumulates in isotropic hardening
c	Surface (corner) crack length
c_n	Notch depth
d_0	Strain free interplanar spacing
$\mathrm{d}a/\mathrm{d}N$	Fatigue crack growth rate
$\mathrm{d}c/\mathrm{d}N$	Surface fatigue crack growth rate
$d_{\varphi\psi}$	Interplanar spacing in direction defined by φ and ψ
$\mathrm{f,g}(a/W)$	Compliance functions
f_i	Elemental weight fraction
h_p	Depth of strain hardening affected layer
k	Crack aspect ratio
l	Short crack length measured from end of notch
l'	Transition length from short to long crack behaviour in notch 1. ~extent of notch elastic zone
m	Paris Law exponent
$\mathrm{m}(a,x)$	Weight function for a given component and crack geometry
m_{shot}	Mass of shot peening media
Δn	Transition length from short to long crack behaviour in notch 2. ~extent of notch cyclic plastic zone
n_f	Cyclic strain hardening exponent
n_m	Strain hardening exponent
n_m''	Biaxial strain hardening exponent
r_p	Extent of plastic zone ahead of crack tip
r_ρ	Extent of plastic zone calculated using dislocation theory
Δs_n	Notch cyclic plastic zone in direction of maximum shear
s	Loading span
v_{shot}	Velocity of shot peening media
w_σ	Strain energy per unit volume due to local stress
$w_{\sigma_{nom}}$	Strain energy per unit volume due to nominal remote stress
z	Depth beneath the shot peened surface
z_0	Overall depth of compressive residual stress layer

z_m	Depth of maximum compressive residual stress
z_p	X-ray penetration depth
A	Ramberg-Osgood constant
A'	Cyclic Ramberg-Osgood constant
A''	Biaxial Ramberg Osgood constant
B	Sample thickness
C	Paris Law constant
C_k	Initial kinematic hardening moduli
C_{ph}	Contrast between two phases
C_{sp}	Coverage
D_d	Dent diameter
D_s	Damage variable: ratio of effective area of cavities to area of intersection of the plane with the representative volume element
$D_{x,Hv}$	Vickers hardness indentation width
$D_{z,Hv}$	Depth of indentation by Vickers hardness indenter
$D_{z,shot}$	Depth of indentation by shot peening media
E	Elastic modulus
H_1	Bilinear material model strain hardening rate
HRC	Rockwell hardness C
$H_{v,PHv}$	Vickers hardness under load P_{Hv}
ΔJ	Cyclic J integral
J_{2a}	2nd invariant of the deviatoric stress tensor
K	Stress intensity factor
ΔK	Stress intensity factor range
ΔK_{eff}	Effective stress intensity factor range
ΔK_{th}	Threshold stress intensity factor range
$K_{closure}$	Stress intensity factor range at which the crack closes
K_I	Mode I stress intensity factor
K_{Ic}	Plane strain fracture toughness
K_l	Long crack K solution
K_{max}	Stress intensity factor under maximum stress
K_{min}	Stress intensity factor under minimum stress
K^p	Primary component of K in R6
K_r	Fracture criterion in failure assessment diagram
K_{rs}	Stress intensity factor arising from residual stresses
K^s	Secondary component of K in R6
K_s	Short crack K solution

K_{sf}	Ratio of fatigue limit at a given roughness to the fatigue limit wher the roughness is negligible
K_t	Elastic stress concentration factor
K_ε	Strain concentration factor
K_σ	Stress concentration factor
L	Centre of transition on a Kitigawa-Takahashi diagram
L_r	Plastic collapse criterion in failure assessment diagram
N	Number of fatigue cycles
N_f	Number of fatigue cycles to failure
N_α	Number of backstresses in kinematic hardening
ΔP	Load range
P_0	Maximum Hertzian contact pressure
P_{Hv}	Vickers indent load
P_{max}	Maximum load
P_{mean}	Mean Hertzian contact pressure
Q_∞	Maximum change in size of yield surface in isotropic hardening
R_a	Arithmetical mean vertical deviation of the assessed roughness line profile from the mean line
R_{eff}	Effective R ratio
R_{ku}	Roughness profile kurtosis
R_p	Ratio of minimum to maximum load in fatigue cycle
R_{shot}	Radius of shot peening media
R_{sk}	Roughness profile skewness
R_t	Total roughness profile height
R_z	Maximum height of roughness profile
R_ε	Ratio of minimum to maximum strain in fatigue cycle
R_σ	Ratio of minimum to maximum stress in fatigue cycle
S	Shot diameter
S_1	X-ray elastic constant
$½S_2$	X-ray elastic constant
S_a	Arithmetical mean vertical deviation of the assessed roughness areal profile from the mean surface
S_m	Mean spacing of adjacent local peaks of roughness profile
S_z	Maximum height of the roughness scale limited surface
T	Temperature
T_m	Material melting temperature
V/V_0	Potential difference to datum potential difference ratio in direct current potential drop technique

W	Sample width
Z	Atomic number
Z_h	Overall height of the target
α	Plasticity correction factor: Ratio of elastic-plastic indent diameter to elastic indent diameter
α_d	Material damping in Explicit finite element modelling
β_d	Stiffness dependent damping in Explicit finite element modelling
γ_k	Rate of change in kinematic hardening moduli as plastic strain accumulates in kinematic hardening
δ_t	Crack tip opening displacement
$\Delta\delta_t$	Crack tip opening displacement range
δ_x	Extent of surface plasticity around Vickers hardness indent
δ_z	Depth of plasticity beneath Vickers hardness indent
$\Delta\varepsilon$	Strain range
$\Delta\varepsilon_{11}$	Strain range in the direction parallel to the tensile axis
$\Delta\varepsilon_{eq}$	Elastic-plastic von Mises equivalent strain range
$\Delta\varepsilon_p$	Plastic strain range
ε^0	Yield strain
ε_{11}	Strain in the direction parallel to the tensile axis
ε_{11}''	Biaxial strain in the direction parallel to the tensile axis
ε_a	Strain amplitude
ε_a^0	Cyclic yield strain amplitude
ε_{eq}	Elastic-plastic von Mises equivalent strain
ε_{eq}^e	Elastic von Mises equivalent strain
ε_p	Plastic strain
$\bar{\epsilon}^{pl}$	Equivalent plastic strain
ε_t	Total strain
$\varepsilon_{\varphi\psi}$	Strain in direction defined by φ and ψ
η	Total backscatter coefficient
η_i	Backscatter coefficient for element 'i'
2θ	X-ray diffraction peak position
λ	X-ray wavelength
μ_{cf}	Coefficient of friction
ξ_d	Modal damping parameter in Explicit finite element modelling
ρ_k	Allows for interactions between primary and secondary components of K in R6
ρ_{shot}	Density of shot peening media

$\Delta\sigma$	Stress range
$\Delta\sigma_{11}$	Stress range in the direction parallel to the tensile axis
$\Delta\sigma_e$	Endurance limit
$\Delta\sigma_{eq}$	Elastic-plastic von Mises equivalent stress range
$\Delta\sigma_{rs,eq}$	Uniform residual stress resulting in the same 'negative stress intensity factor range' as shot peening residual stress distribution
$\frac{\partial\sigma}{\partial Z}$	Stress gradient
$\sigma\big\vert_0$	Yield strength at zero plastic strain
σ^0	Yield strength
$\sigma_{0.2}$	0.2 % proof stress
σ_{11}	Stress in the direction parallel to the tensile axis
σ_{11}''	Biaxial stress in the direction parallel to the tensile axis
σ_a	Stress amplitude
$\sigma_{B,0}$	Endurance limit under zero to tension bending
$\sigma_{B,-1}$	Endurance limit under fully reversed bending
σ_{eq}	von Mises equivalent stress
σ_{eq}^e	Elastic von Mises equivalent stress
$\sigma_{H,m}$	Mean hydrostatic stress
$\sigma_{H,max}$	Maximum hydrostatic stress
σ_m	Mean stress
σ_{max}	Maximum stress
σ_{mcrs}	Maximum compressive residual stress
σ_{nom}	Nominal bending stress
σ_{nom}^e	Nominal elastic bending stress
$\sigma_{res11,22}^{multi}$	In-plane residual stresses after unloading from multiple shot peening impacts
$\sigma_{res11,22}^{sing}$	In-plane residual stresses after unloading from a single shot peening impact
σ_{rs}	Residual stress
σ_{srs}	Surface residual stress
σ_{uts}	Ultimate tensile strength
$\sigma_{VM,a}$	von Mises stress amplitude
$f(\boldsymbol{\sigma}-\boldsymbol{\alpha})$	Equivalent Mises stress with respect to the backstress ($\boldsymbol{\alpha}$)
$\tau_{c,-1}$	Endurance limit under fully reversed torsion
υ	Poisson's ratio

φ	X-ray diffraction angle between a fixed direction in the plane of the sample and the projection in that plane of the normal to the diffracting plane
ψ	X-ray diffraction angle between sample normal and diffracting plane normal
Φ_e	Plastic shear deformation resulting from crack tip plasticity calculated using linear elastic fracture mechanics
Φ_p	Plastic shear deformation resulting from notch plasticity
Φ_s	Plastic shear deformation at the uncracked notch root
Φ_t	Total plastic shear deformation at the tip of a sharp crack
Φ_{th}	Threshold plastic shear deformation

BCC	Body centred cubic
BCT	Body centred tetragonal
BEI	Backscattered electron imaging
CTE	Coefficient of thermal expansion
CTOD	Crack tip opening displacement
CZM	Cohesive zone model
DCPD	Direct current potential drop
EBSD	Electron backscatter diffraction
EDM	Electro-discharge machining
ENT	E.ON New Build and Technology
EPFM	Elastic plastic fracture mechanics
ESED	Elastic strain energy density
FCC	Face centred cubic
FE	Finite element
FEG-SEM	Field emission gun scanning electron microscope
FWHM	Full width at half maximum
GOS	Grain orientation spread
G-T	Greninger-Troiano relationship
HAZ	Heat affected zone
HCF	High cycle fatigue
HP	High pressure
IP	Intermediate pressure
KAM	Kernel average misorientation
K-S	Kurdjumov-Sachs relationship
LAM	Local average misorientation

LCF	Low cycle fatigue
LEFM	Linear elastic fracture mechanics
LOS	Local orientation spread
LP	Low pressure
MPI	Magnetic particle inspection
NDT	Non-destructive testing
ND	Neutron diffraction
NFFM	Notch fatigue failure map
N-W	Nishiyama-Wasserman relationship
PBB	Plain bend bar
PSB	Persistent slip band
SEI	Secondary electron imaging
SENB	Single Edge Notch Bend
SENT	Single Edge Notch Tension
SIF	Stress intensity factor
SPE	Solid particle erosion
SWT	Smith Watson and Topper
TEM	Transmission electron microscopy
XRD	X-ray diffraction

Chapter 1

Introduction

1.1 Background

Within conventional power stations, steam turbine components are safety critical parts which are subjected to low cycle fatigue (LCF) stresses of thermal and mechanical origin during start up and shut down. Non-destructive testing (NDT) is carried out during routine maintenance inspections (approximately every 12 years) to locate and size any defects, especially at the fir tree blade-disc interfaces which contain several severe stress concentrations. A range of refurbishment activities are then undertaken to ensure the performance and integrity of the turbine rotor during the next operational cycle. Typically, a major outage on a conventional power station takes 8 – 12 weeks. For a large 500 MW unit the cost in lost generation over this period is substantial (>£M); as a result there is a drive to minimise the scope of remedial works undertaken allowing the length of the outage to be reduced. Hence, there is a great need to develop life assessment methods that can be used to justify deferring invasive inspections and reducing the scope of the maintenance works [1].

A damage tolerant fatigue lifing approach is used to determine the maximum number of future start up and shut down operations and allow component repair and replacement scheduling. Many UK operational turbines are of 1960s vintage and have undergone ~3500 start up / shut downs already; these ageing assets must be repaired or replaced in the most cost effective manner whilst maintaining safety margins [1].

It is the development of these life assessment methods which defines the scope of this study which represents a contribution to the development of life assessment procedures accounting for the fatigue life of turbine components with a view to improving life cycle efficiency and reducing operator cost. The remainder of this section describes in more detail the industrial context of the work: The power generation cycle and the configuration of steam turbines within it are described and consideration is made of the operating conditions which drive material requirements, manufacturing processes and possible failure modes. It is these failure modes which define the maintenance procedures also described.

1.1.1 Steam turbines in the power generation cycle

Although there is a drive in power plant design towards supercritical steam cycles, subcritical steam cycle power stations remain the dominant technology applied in conventional power generation plants of 1960s vintage, such as Ratcliffe on Soar, UK [2]. Chemical energy stored in fossil fuels is converted into electrical energy for distribution on the National Grid. High temperature and pressure steam is generated in the boiler; it is superheated and expanded through the steam turbine, converting thermal energy to mechanical energy.

The configuration of a typical sub-critical steam turbine is identified in Figure 1- 1, the scale of the plant can be visualised from the inset photographs. Steam flows from the high pressure (HP) turbine through the intermediate pressure (IP) turbine to the low pressure (LP) turbines which are typically dual flow for thrust balancing and ultimately the condenser. There are two common designs in operation in the UK [4]. In reaction turbines, the enthalpy drops over both the stators and the rotors whereas in impulse turbines, the enthalpy drops over the stators only. The rotating blades of all the turbines are attached to a central rotor turning at 3000 rpm, typically via a fir tree interface; thus mechanical energy is converted to electrical energy in the generator.

Conventional plant have historically operated on a two shift basis [4]; that is they operate at base load during the day, shut down overnight and hot start in the morning. However, with the current shift towards renewable energy, which is typically more volatile in terms of power yield than conventional plant, conventional plant are expected to operate more flexibly and pick up the residual load. This results in more frequent and quicker start up and shut down cycles and faster load changing rates [6]; whilst modern and upgraded plant can be designed for this, the resulting changes to the design life of older plant must not be overlooked.

These operating conditions drive the material requirements for high and low pressure turbine units; these are summarised in Table 1- 1.

Industrial steam turbine blades are typically manufactured from 9-12 Cr ferritic heat resistant steels since they meet the requirements in Table 1- 1 and can best meet flexible operating requirements. This is a result of their relatively low coefficient of thermal expansion and high thermal conductivity in comparison with other candidate materials (such as austenitic stainless steel) resulting in lower thermal stresses during start up and shut down and thus lower susceptibility to fatigue [7]. A more detailed review of these materials can be found in Section 1.2.

Turbine blades are typically forged into shape with final machining at regions of critical geometry, such as the blade root where a mechanical fit is required [15]. Regions of

stress concentration, such as blade roots and snubber blocks are shot peened in an attempt to improve fatigue resistance. The typical shot peening process which is applied to blades by Metal Improvement Company is MI230R 13A 200 %; i.e. the blade is peened at intensity 13A to 200 % coverage using shot of 0.58 mm diameter and hardness 42 <*HRC* <52. This process will be referred to as T0 for the remainder of this thesis. Shot peening results in plastic deformation at the surface of the component which is characterised by a dimpled topography and near surface strain hardening, increasing the local yield strength of the material. Compressive residual stresses are also formed as a result of the misfit strain between the plastically deformed surface and the elastically deformed sub-surface layers [16].

1.1.2 Steam turbine maintenance practice

As previously described, steam turbine components are safety critical parts which are subjected to both high cycle and low cycle fatigue. NDT is carried out every 12 years to locate and size defects, especially at stress concentrating regions such as fir tree blade-disc interfaces where fatigue crack initiation and subsequent propagation may occur. Damage tolerant remnant life modelling is performed based on the worst case defects to underwrite service for the next period or to define a repair and replacement schedule.

An understanding of the worst case defects requires consideration of the tolerance of the NDT technique in use. Several NDT techniques may be applied to establish the structural integrity of turbine blades; they can be broadly classified into surface methods such as visual inspection, magnetic particle inspection (MPI) and eddy current testing and volumetric methods, which primarily involve ultrasonics. Whilst MPI may be attractive in terms of cost, it may not always be appropriate on turbine geometries due to access and illumination issues. On a well prepared surface of relatively simple geometry, cracks of surface length 0.5 mm can be identified [17]. However, no information on through thickness crack depth is provided; this is typically the more important parameter for damage tolerant lifing and must be inferred from assumptions about crack shape. Furthermore, the surface preparation is critical; roughness affects the visual identification of the crack and in shot peened components limits the crack dimensions that can be observed.

Both phased array ultrasonics and eddy current arrays can be used to overcome these issues and identify cracking in critical regions on blade-disc interfaces. Although both are reliant on calibration blocks, phased array ultrasonics can offer a through thickness crack detection threshold of 0.5 mm [18] and eddy current arrays have been demonstrated to offer a crack detection threshold of 0.2 mm [5]. With appropriate calibration, the eddy current method is able to detect shorter cracks in the region of

0.1 mm [17, 19]. Surfaces which have been shot peened would require the application of shot peened calibration blocks to remove any effect from the reduced conductivity resulting from shot peening.

Typically the most attractive option if a service limiting defect is found is repair; this is usually carried out using the blend-polish-peen method. The component is grit blasted to remove oxide and scale and the crack is identified by MPI. A handheld pneumatic drill is used to grind out the crack creating a shallow notch like geometry. Any sharp radii are smoothed out using a sand bit; a finer grit may be used to improve the surface finish or the repair site may be shot peened depending on the application. There is no standard repair geometry; rather the repair process relies on the experience of the specific operator.

1.1.3 Project scope and thesis structure

This study is a contribution to the development of life assessment methods for power plant components. Whilst it is anticipated that in the future, the life assessment methodology under development in the present work will be extended and find application in many power plant components, LP turbine blade disc interfaces have been selected as the component for initial method development. The effect of shot peening on ambient LCF and the means by which this effect can be incorporated in the remnant life calculation are investigated; this represents an improvement to the current method in which any benefits are considered as an additional safety factor. Shot peening is widely believed to be beneficial in terms of fatigue life; the inclusion of the process effects in lifing methods may enable the extension of remnant life estimates resulting in significant cost savings to power station operators. The following broad objectives were identified to achieve this goal:

i. Characterise the monotonic and cyclic stress-strain behaviour of a representative turbine blade material and identify appropriate constitutive relationships describing both types of behaviour.

ii. Characterise the surface roughness, near surface strain hardening and compressive residual stresses resulting from shot peening a representative turbine blade material.

iii. Investigate the effect of LCF on near surface strain hardening and compressive residual stresses.

iv. Identify how these effects can be considered in component remnant life assessments.

The remainder of this chapter contains a brief introduction to 9-12 Cr steels and fatigue as a failure mechanism, since these are fundamental precursors to the remainder of the thesis. Chapter 2 is a literature review split into two main sections, the first considering the effect of shot peening on fatigue resistance and the second considering approaches to fatigue lifing after shot peening. Since shot peening is such a well-known manufacturing process which has been extensively documented, this review allowed identification of critical gaps in understanding which it was essential to investigate as part of this work.

Chapters 3-5 represent the bulk of the experimental and modelling work conducted as part of this study. Chapter 3 details the material baseline microstructural and mechanical properties, including a study on the cyclic behaviour of 9-12 Cr steels and the significance of material constitutive model selection when analysing local stresses and strains in fatigue. The surface roughness, strain hardening and residual stresses resulting from shot peening are characterised in Chapter 4 and the interaction of these effects with applied LCF stresses and strains is considered in Chapter 5, the discussion of which brings together aspects of all three chapters.

The conclusions are given in Chapter 6 and future directions are presented in Chapter 7. These future directions are still driven by the original literature review and will form the key objectives driving the work which is to be undertaken during the third year of a Royal Commission for the Exhibition of 1851 Industrial Fellowship. As such, this chapter contains details of the industrial application of the work reported in Chapters 3-5 and of the initial modelling work which has already been carried out in order to include the shot peening and LCF interactions reported in this thesis in remnant life models.

1.2 9-12 Cr steels

Ferritic heat resistant steels were identified in Section 1.1.1 as the material of choice for manufacturing LP steam turbine blades; in low temperature applications, the most important alloying additions include Mo, W, V, Nb, C, and N [20]. Whilst alloy development is not the focus of this study, an understanding of the microstructure-strength relationship is essential both in characterising the effects of the shot peening process and the micro-mechanisms of fatigue; this section describes the tempered martensitic microstructure which is to be expected in this class of material. Since the present study is concerned only with ambient temperature behaviour, this review does not consider high temperature behaviour; it is sufficient to acknowledge that there has been significant effort worldwide in improving the creep strength of these steels [3, 7, 21].

1.2.1 Formation of tempered martensite

Pure iron undergoes a phase transformation from face centred cubic (FCC) austenite (γ) to body centred cubic (BCC) ferrite (α); this transformation can be reconstructive (if cooling is sufficiently slow to allow diffusion of atoms during growth) or displacive (if cooling is too rapid for diffusion an invariant-plane strain shape deformation with a large shear component occurs). The addition of carbon means phase transformations in steel are governed by the metastable iron-cementite (Fe-Fe_3C) phase diagram; the equilibrium microconstituents of which are ferrite, cementite and pearlite. The 9-12 Cr power plant steels of interest are low carbon steels typically ~0.10 - 0.15 wt. % C and as such are hypo-eutectoid in nature.

However, alloying additions are typically made to allow solid solution strengthening and modify the carbides formed, optimising the properties for a particular application. Furthermore, transformation conditions are rarely equilibrium in nature as cooling rates are too rapid for diffusion processes and the formation of equilibrium phases. Under these conditions, displacive reactions occur forming the metastable martensite (α') or bainite microstructures. The phase transformations for a particular steel under non-equilibrium cooling conditions can be predicted from isothermal transformation diagrams and continuous cooling transformation diagrams.

Thus the formation of martensite is characterised by a diffusionless shear transformation during which the carbon atoms remain in solid solution, resulting in a lattice supersaturated with carbon and a body centred tetragonal (BCT) structure. The transformation occurs via a Bain strain in which the austenite is compressed along one <100> direction and expanded along a perpendicular plane. To ensure a coherent interface between the close packed {111} plane in FCC and {110} plane in BCC, the Bain strain is modified slightly by rotating it and adding a small inhomogeneous shear [22], most commonly via dislocation movement by slip in low C martensite [23, 24] which is characterised by a lath microstructure [23]. The simplest crystallographic relationship is the Kurdjumov-Sachs (K-S) relationship where the close packed directions in the FCC and BCC crystals are set parallel: $\{111\}_\gamma \| \{011\}_{\alpha'}$ and $\langle 10\bar{1}\rangle_\gamma \| \langle 11\bar{1}\rangle_{\alpha'}$ [22]; this relationship is reportedly dominant in low C steels [23, 25]. Other relationships include the Nishiyama-Wasserman (N-W) relationship, $\{111\}_\gamma \| \{110\}_{\alpha'}$ and $\langle \bar{1}10\rangle_\gamma \| \langle 001\rangle_{\alpha'}$, and the Greninger-Troiano (G-T) relationship which is inbetween K-S and N-W.

The typical crystallography of lath martensite in low carbon steels is illustrated schematically in Figure 1- 2. A prior austenite grain is divided into packets (groups of blocks with the same habit plane), each of which consists of blocks (containing laths of the same variant). This multiscale structure has been confirmed in 9-12 Cr ferritic heat resistant steels by Kimura *et al.* [26]. The dominant orientation relationship in the 9-12

Cr steels has been shown to be the G-T relationship. This results in misorientations between blocks of at least 5° [27], typically 10° [25] with mean misorientation between laths and subgrains within blocks being lower, around 2-3° [28, 29].

The strong but brittle nature of martensite means that the mechanical properties must be modified by tempering before structural application; the martensitic lath structure transforms to a BCC ferritic subgrain structure and fine, dispersed precipitates are formed in the matrix. In the 9-12 Cr steels of interest, austenitisation occurs in the temperature range 1020 – 1100 °C for sufficient time to dissolve the carbide and nitride particles. Martensite is then formed during air cooling on section thicknesses up to ~100 mm or oil quenching for thicker sections such as turbine rotors. For large components, tempering is most commonly performed as a two-step operation with first tempering at 570 °C and second tempering in the range 650 – 720 °C [30].

As a result of this tempering process, the microstructure observed in 9-12 Cr ferritic heat resistant steels is fully tempered martensite with well-formed laths and subgrains with a high free dislocation density of the order 10^{14} m^{-2}; some dislocations rearrange to form sub-grain boundaries of width typically ~0.5 μm [7, 31, 32]. An optical micrograph revealing the structure is shown in Figure 1- 3. Both free dislocations and sub-grain boundaries contribute to dislocation hardening within the alloy [7]. At these tempering temperatures, substitutionally alloyed elements can diffuse, allowing precipitation of complex alloy carbides; the following sections introduce firstly the phases which are present in 9-12 Cr steels and secondly the alloying additions made to optimise the phase distribution and material performance.

1.2.2 Phases present in the microstructure

There has been quite extensive work on precipitation reactions in this material, both by thermodynamic calculation [30, 33-35] and by experimental transmission electron microscopy using both energy filtering and energy dispersive X-ray spectroscopy (EDX) techniques [33-38] or atom probe field ion microscopy [39]. These works identify the key stable precipitates that may be present (Figure 1- 4); these are primary MX (metal) (C, N) which was undissolved during austenitisation and $M_{23}C_6$, M_2X and secondary MX precipitated during tempering.

- $M_{23}C_6$ is a chromium rich phase which is also known to contain Mo, Fe and W [33, 39]. It is recognised as being an equilibrium carbide for these steels, and is found as large particles present at the grain and sub-grain boundaries. A small amount of precipitation strengthening is generated, however it is thought that a more significant effect is helping stabilise the martensitic lath boundaries [33].

- MX and M_2X are two carbonitrides that are typically found as fine dispersoids within the material grains and sub-grains after tempering, both of which confer a strong precipitation hardening effect. Typically, MX is (V, Nb)(C, N) and M_2X is $(Mo, W, Cr, V, Nb)_2(C, N)$ [7, 20, 35, 38]. Janovec *et al.* [35] predict that for a low Cr steel with Mo:V ratio ~ 6, the Mo:Cr ratio for M_2X is ~3 (wt.%/wt.%). Reducing the Mo:V ratio reduced the Mo:Cr ratio. Both MX and M_2X are reported to form on, or at least be associated with, dislocations found within the sub-grains [30, 34]. M_2X forms prior to MX, since it requires little diffusion of chromium and thus is a more rapid reaction. Its presence in the matrix lowers the driving force for the precipitation of MX, which precipitates relatively slowly [30]. This explains the dominance of M_2X when the material is tempered at < 700 °C and MX when tempering temperature exceeds this [20, 38]. Both these particles confer significant strength to the alloy through precipitation strengthening, obstructing dislocation motion.

1.2.3 Alloying Additions

- Chromium

Chromium is the element added in the highest quantity, as large additions provide hardenability and resistance to corrosion [23]. Chromium also increases the solubility (by as much as an order of magnitude) of the V rich MX phase compared to low alloy steels [20]. However, increasing the chromium content is undesirable as it may lead to embrittlement of the steel at elevated temperatures [40].

- Molybdenum, Tungsten

Molybdenum and tungsten both confer solid solution strengthening as a result of their greater atomic radii than iron and can stabilise the M_2X phase. A molybdenum equivalent (1x%Mo + 0.5x%W) of 1 % has been suggested as optimal in terms of creep strength since during creep exposure, both Mo and W enter the Laves phase or the M_6X phase, reducing the solid solution strengthening component and depleting M_2X and MX levels [20]. However, whilst a lower wt.% of Mo is required to achieve this optimum, the addition of W may be more beneficial as it has been reported to result in a stable Laves phase which can contribute to precipitate strengthening [41] and to retard the rate of recovery of the martensitic lath structure [32] slowing the lath width growth rate.

- Vanadium, Niobium

Vanadium is present in both the beneficial M_2X and MX phases. V and Nb have a stronger affinity for C and N than Mo and W which are left in the matrix and continue to contribute to the solid solution strengthening [38]. The addition of Nb allows

precipitation of primary Nb(C,N) which may remain undissolved during austenitisation and prevent austenite grain growth, improving the toughness [30]. These primary niobium carbonitrides can however serve as nucleation sites for secondary VN precipitates; forming 'V-wings'. The effectiveness of these complex precipitates at pinning dislocations compared to fine dispersions has been questioned [20]. Furthermore, high Nb levels can result in precipitation of Laves phase and the transformation of M_2X and MX to the less beneficial Z phase during creep [38].

- Carbon, Nitrogen

Carbon and nitrogen are both added as interstitial solid solution strengthening elements which also allow the precipitation of beneficial carbides, nitrides and carbonitrides.

1.3 Fatigue as a failure mechanism

Before the main literature review (Chapter 2) which focusses on the effect of shot peening on fatigue resistance, it is necessary to introduce the main processes involved in the fatigue damage process. Fatigue failure occurs as a result of the application of cyclic stresses; it is influenced by the material microstructure, component and crack geometry, loading conditions and environmental conditions. Operation at high temperature can lead to creep fatigue and thermo-mechanical fatigue processes, whilst operation in a chemically aggressive environment can result in corrosion fatigue. Contact conditions can result in fretting fatigue as a result of frictional sliding between surfaces.

The present work considers the development of life assessment approaches in shot peened components under the sole effect of externally applied mechanical stresses. The application of these approaches may require the additional consideration of corrosion fatigue (e.g. in the LP turbine) [10-12], creep and thermomechanical fatigue (e.g. in the HP turbine) [42, 43] and fretting fatigue (e.g. at blade-disc interfaces) [44, 45] although a detailed consideration of these additional effects is beyond the present scope.

Fatigue damage generally progresses through the following stages:

- Initial cyclic damage in the form of cyclic hardening or softening.
- Crack initiation
- Short and long crack propagation

Each of these progressions is discussed in more detail in Sections 1.3.1 to 1.3.3. It is generally considered that initiation life is dominant in high cycle fatigue (HCF) whereas crack propagation life is dominant in LCF applications. These descriptions are intended to provide a general background to fatigue and not a detailed literature review of each stage, unless otherwise cited, the majority of the discussion is based on Suresh [46].

1.3.1 The evolutionary nature of mechanical properties

Under cyclic loading, it is possible for a material to harden, soften, remain neutral, or experience a combination of these (for example, some materials may harden initially and then soften). Cyclic hardening and softening are best represented by consideration of a material's stress range response to constant amplitude strain control loading (fully constrained loading conditions) since in components there is a degree of structural constraint at fatigue critical sites.

Cyclic hardening results in an increase in stress range with number of cycles, most commonly to a plateau after which the stress range remains constant. Cyclic softening results in a decrease in stress range with number of cycles, many softening materials continue to show some softening after an initial more rapid softening period. These differences are illustrated in Figure 1- 5.

The stress-strain history of each individual loading cycle can be represented as a hysteresis loop. During a material's transient response the hysteresis loops are open; in this 'shakedown' period the dislocation substructure continually evolves. If a stable configuration is reached, the stress amplitude is constant and the hysteresis loop remains essentially the same for each subsequent cycle; hence the loop is now closed.

The micro-mechanisms controlling cyclic hardening and softening are very complex. The behaviour of a specific material is determined by the evolution of the dislocation substructure and the behaviour of any precipitates, which can either by sheared by the repeated cutting motion of dislocations and result in additional softening, or be formed by secondary precipitation assisted by moving dislocations, leading to a hardening effect [48].

As a broad indicator, annealed polycrystalline metals (low monotonic strain hardening exponent) cyclically harden due to dislocation multiplication; work hardened polycrystalline metals (high monotonic strain hardening exponent) cyclically soften as pre-strain induced dislocation networks rearrange [48, 49].

For intermediate values of monotonic strain hardening exponent, stable or mixed behaviour can occur. For example, an investigation into the cyclic response of ASTM A-516 Gr70 low alloy steel has demonstrated that up to 0.4 % strain amplitude the

material cyclically softens and beyond it, the material cyclically hardens [50]. A similar response was found in a low carbon steel, at high strain amplitudes rapid long term hardening was followed by slight long term hardening, for small strain amplitudes initial softening was followed by slight long term hardening [51].

The dominant cyclic behaviour in ferritic heat resistant steel is softening [48, 52-64]. Data illustrating the cyclic behaviour of 9-12 Cr steels at temperatures relevant to those in the LP turbine are shown in Figure 1- 6. Behaviour at these temperatures tends to follow one of two trends:

- Initial hardening over approximately the first 10 cycles followed by continual cyclic softening [54, 58, 61] or cyclic softening and a brief period of stability [63] as illustrated in Figure 1- 6a.
- Rapid cyclic softening at the start of life followed by slower continual cyclic softening [48, 59, 60] as illustrated in Figure 1- 6b.

Where present, the initial hardening is a result of dislocation-dislocation, dislocation-solute atom or dislocation-precipitate interactions [61, 63]. The cyclic softening is a result of rearrangement in the post-quench dislocation structure resulting in a reduction in dislocation density and the conversion of the original fine lath structure to a coarser cellular structure in which the dislocation density at cell walls is higher than that in the cell interior [52-54, 58-61, 63, 65]. Although not discernible from the data of Rai *et al.* [63] at varying strain range presented in Figure 1- 6a, Yaguchi and Takahashi [66] used strain controlled testing with step changes in strain range to show that cyclic softening progressed slower at low strain ranges than at high strain ranges in a 9Cr-1Mo (0.09C, 9.78Cr, 0.94Mo, 0.21V) steel.

Comparison of the ambient temperature data with that at the higher temperatures in the LP turbine shows that at these relatively low temperatures, apart from a change in the peak stress attained, the shape of the curve remains the same. This allows consideration of ambient behaviour when developing the life assessment method, with the proviso that upon application in the LP turbine, material data relevant to the operational temperature is used. Indeed it has been shown by several authors [52, 58, 59] that the cyclic material response retains this form until the temperature exceeds ~500 °C at which point the softening becomes more severe. At high temperatures dislocations are more mobile and creep processes also start to be of importance: precipitate coarsening and a reduction in solid solution strengthening due to precipitation of adverse phases can accelerate cyclic softening [52, 58, 61]. At high temperatures precipitates may also shear reducing their ability to prevent dislocation rearrangement and facilitating softening [52, 58].

1.3.2 Fatigue crack initiation

In defect free components, crack initiation from a smooth surface is typically associated with different amounts of net slip on different glide planes and the formation of persistent slip bands (PSBs). Intrusions and extrusions at a free surface are caused by irreversible slip; these micro-notches can act as stress concentration sites for additional slip and eventual fatigue crack nucleation. Furthermore, since the boundary between the PSB and the matrix is a plane of discontinuity in terms of dislocation density and distribution, they act as preferential sites for fatigue crack nucleation.

Several micro-mechanistic models exist for fatigue crack initiation, an excellent review is contained in the work of Chan [67].Tanaka and Mura [68] developed a microstructure based initiation model in which irreversible slip was included as a result of the accumulation of dislocation dipoles. The applied stress parameter in this model is the range of cyclic resolved shear stress, a function of the complete stress tensor [69].

In engineering components, however, the above mechanism is rarely the cause of fatigue crack initiation which is made much easier by the presence of inclusions or constituent particles and macroscopic stress concentrations, such as scratches and other manufacturing defects or processes such as shot peening, as well as component geometry.

Initiation behaviour in 9-12 Cr steels has not been widely reported, though it is known that initiation may occur at both surface and subsurface inclusions [15, 70]. Aluminium oxide stringers oriented in the extrusion direction were shown to facilitate initiation in perpendicular loading directions. Whilst not an issue in the long axis of the blade along which the inclusions are aligned, in the machined root surface inclusions could result in more rapid initiation [15]; if considering a stress life to initiation approach, a probabilistic analysis based on inclusion shape size and position [70] might be appropriate.

Micromechanical models also exist for initiation at inclusions such as the Tanaka and Mura [71] model where the inclusion fractures as a result of dislocation pile up. Chan [67] extended the model to consider the crack length at initiation; differentiation with respect to the fatigue cycle allowed an equation to be developed for the growth rate of small cracks and the application to crack initiation at regions subjected to stress gradients, such as notches was demonstrated.

There is some debate about when a fatigue crack is considered to have initiated. Materials scientists prefer to consider the nucleation of a flaw on PSBs as initiation; this

is followed by short crack propagation. However, engineers prefer to consider the initiation life as that taken to initiate and grow a crack a length detectable by the NDT techniques described in Section 1.1.2. Whilst it is yet to find widespread application, the model of Chan [67] might offer a means to bridge this gap.

1.3.3 Fatigue crack propagation

Linear elastic fracture mechanics (LEFM) is the most widely used method of quantifying fatigue crack growth because it allows quantification of crack tip stresses in terms of the external loading conditions and crack and specimen geometry which are combined to calculate the stress intensity factor range (ΔK, Equation 1-1). Throughout this work, the focus is on the tensile opening mode (Mode I) of failure; in this case the stress intensity factor range can be defined by Equation 1-2.

$$\Delta K = K_{max} - K_{min} \tag{1- 1}$$

$$\Delta K_I = \mathrm{f}\left(\frac{a}{W}\right)\Delta\sigma\sqrt{\pi a} \tag{1- 2}$$

Where K_{max} and K_{min} are the stress intensity factors under maximum load and minimum load, $\mathrm{f}\left(\frac{a}{W}\right)$ is a geometrical correction factor and is dependent on crack length, a and sample width, W and $\Delta\sigma$ is the applied stress.

LEFM is formulated under the assumption of zero crack tip plasticity. However, LEFM predicts a stress singularity at the sharp crack tip; in reality these are redistributed due to plasticity in the plastic zone, the size (r_p) of which is typically approximated using the Irwin [72] approach (Equation 1-3 in plane strain). The result is that in order to apply LEFM, there must be sufficient surrounding material behaving in an elastic manner to provide constraint; i.e. Equation 1-4 [73] must be satisfied.

$$r_p = \frac{1}{3\pi}\left(\frac{K_I}{\sigma^0}\right)^2 \tag{1- 3}$$

$$W - a, a, B > \ 2.5\left(\frac{K_{IC}}{\sigma^0}\right)^2 \tag{1- 4}$$

Where σ^0 and K_{Ic} are the yield strength and plane strain fracture toughness of the material respectively and B is the thickness of the sample.

There are thus situations in which LEFM cannot be applied. This is most typically a problem when characterising the behaviour of short cracks [74] which tend to propagate faster than long cracks at a given ΔK and with more scatter in the data than long cracks. In such cases, elastic plastic fracture mechanics (EPFM) may be more

appropriate. Two parameters may be invoked: the *J*-integral and the crack tip opening displacement (CTOD, δ_t). The *J*-integral is the strain energy release rate based on non-linear elasticity and is a path independent line integral along a contour around the crack tip which represents the rate of change of potential energy with respect to crack advance. The CTOD is the distance between two points on the upper and lower crack faces where two 45 ° lines are drawn from the crack tip and intercept. Under conditions of LEFM, both parameters can be related to *K* using Equations 1-5 and 1-6.

$$J = \frac{K^2}{E} \tag{1- 5}$$

$$\delta_t = \frac{K^2}{\sigma^0 E} \tag{1- 6}$$

Where *E* is the elastic modulus of the material.

Fatigue crack propagation is typically identified as either stage I or stage II which differ in terms of the micromechanisms by which the fatigue crack grows [75].

- Stage I crack growth is typically associated with low *ΔK* levels when the zone of near tip plasticity is smaller than the grain dimensions, and can be observed in both long cracks with low applied stresses in the near threshold regime and short fatigue cracks just after initiation. This type of crack growth is highly microstructurally dependent and occurs by shear decohesion along pre-existing slip bands. Dislocation motion along the slip plane experiencing the maximum shear stress results in cumulative weakening and eventual failure.

- Stage II crack growth is observed at higher *ΔK* levels where the plastic zone at the crack tip extends across many grains; this regime of crack growth is largely independent of microstructure. Simultaneous dislocation movement occurs on multiple slip systems and the crack grows under mode I conditions typically perpendicular to the maximum principal applied stress [76] and is sometimes termed maximum principal stress dominated crack propagation [77]. The fracture surface exhibits striations which are formed by repeated opening and blunting of the crack under load and resharpening of the crack on load reversal as described by the Laird-Smith model [78]. When the plastic zone ahead of the crack tip is large with respect to the characteristic microstructural dimension, crack tip blunting is accommodated by shear on two slip systems at ~45 ° to the crack plane. Since cyclic slip is irreversible, it is simultaneous or alternating slip on these systems which causes crack advance on blunting [79].

As ΔK increases and final failure approaches, bursts of monotonic failure modes such as cleavage, intergranular separation and fibrous failure also occur making final failure

more dependent on microstructure than Stage II crack growth is. The dependence of K_{Ic} on the specific stress state (plane stress vs. plane strain) means that the critical ΔK for final failure is higher under plane stress than plane strain conditions.

Requirement	HP/IP Blades	LP Blades	Justification
Static tensile strength	Y	Y	Centrifugal (high rotational velocity) and pressure loading.
Toughness	Y	Y	Avoid sudden failure in cracked components.
Creep rupture strength	Y	N	HP and IP operate at high enough temperatures. Avoid possible creep rupture and prevent blade encroachment on turbine casing [7].
Oxidation resistance	Y	N	Avoid material loss and possible raised local temperatures [8]; HP and IP turbines operate at sufficient temperature.
Local corrosion resistance	Y	Y	Avoid possible local corrosion.
Corrosion fatigue strength	N	Y	Steam begins to condense as it reaches the LP turbine. This results in deposition of impurities and localised regions of high salt concentration. If condenser leakage results in HCl formation, the pH of water droplets is lowered. This combination can result in corrosion pits forming [9] and acting as start points for corrosion fatigue [10-12].
Stress corrosion cracking resistance	N	Y	LP turbine blades are susceptible [9, 11] since they are under stress in a chemically aggressive environment.
LCF and HCF resistance	Y	Y	LCF stresses of thermal and mechanical origin during start up and shut down [13] are especially critical because of two shift [4] and flexible operation [6]. HCF may become a problem due to external initiation such as from foreign object damage or changes in vibrational characteristics [13].
Erosion resistance	Y	Y	Solid particles may be present in steam [4].
Weldability	Y	Y	Manufacturing requirement.
Type IV cracking resistance	Y	N	Failure can occur in a weld heat affected zone under creep conditions [14].

Table 1- 1: Material requirements for HP and LP steam turbine blades. After Kern *et al.* [3].

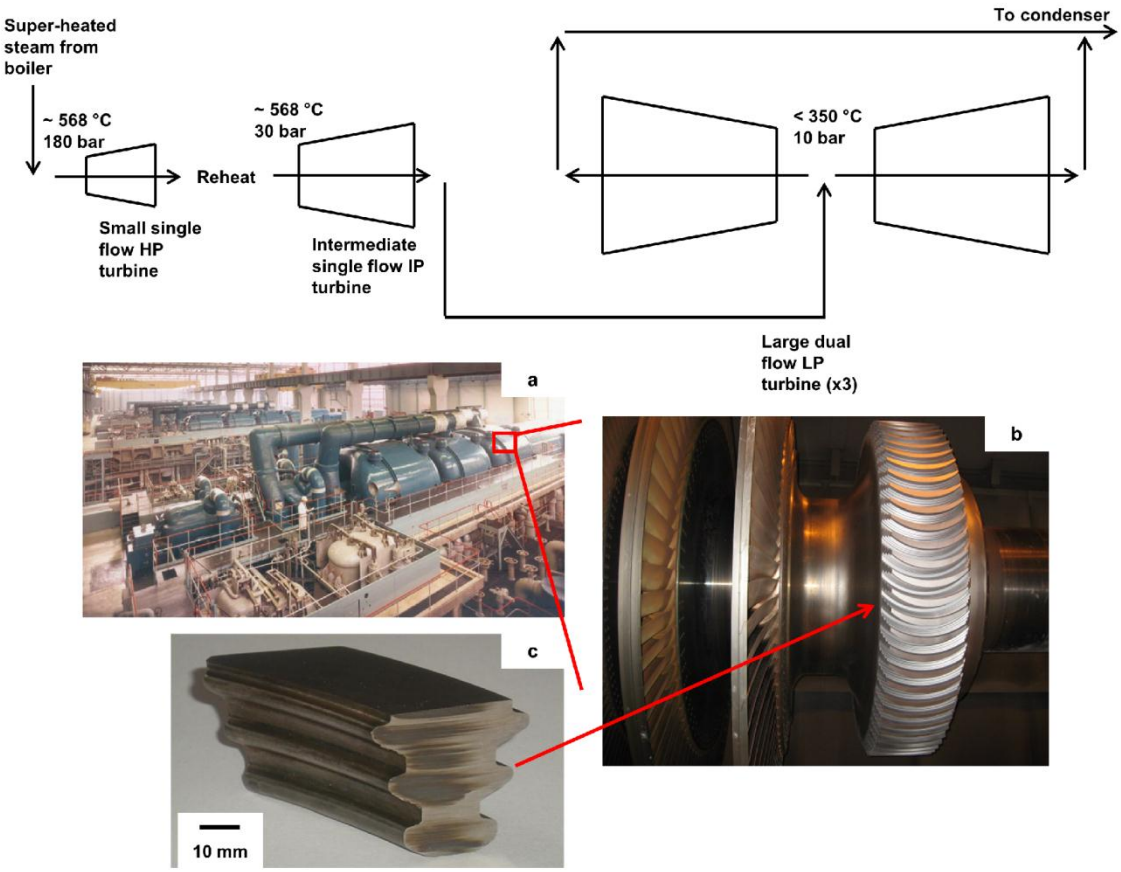

Figure 1- 1: Typical sub-critical plant steam turbine configuration (after Kern *et al.* [3]). The inset illustrates the scale of the plant: (a) a 500 MW turbine set (reproduced from Horseman [4]), (b) final stage LP curved entry fir tree interface slots (reproduced from Bloodworth [5]) and (c) stress concentrating regions on blade fir tree profiles.

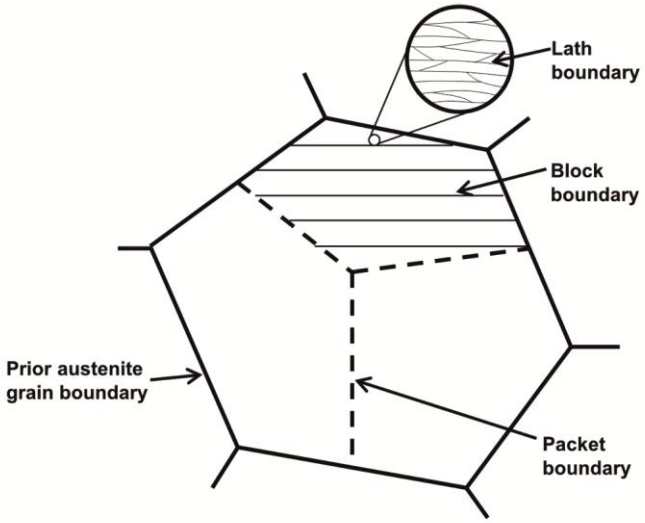

Figure 1- 2: Schematic representation of the structure of martensite. After Morito *et al.* [25] and Kimura *et al.* [26].

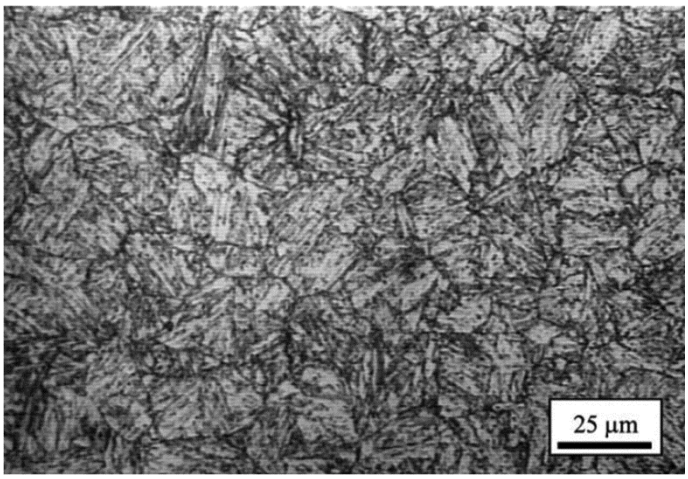

Figure 1- 3: Tempered martensitic microstructure of FV566 (0.1C, 11.0Cr, 1.35Mo, 0.15V). Reproduced from Perkins and Bache [10].

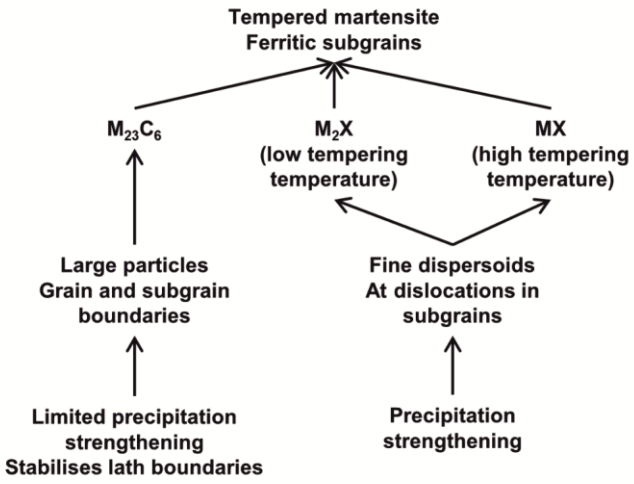

Figure 1- 4: The phases present in 9-12 %Cr steels after tempering.

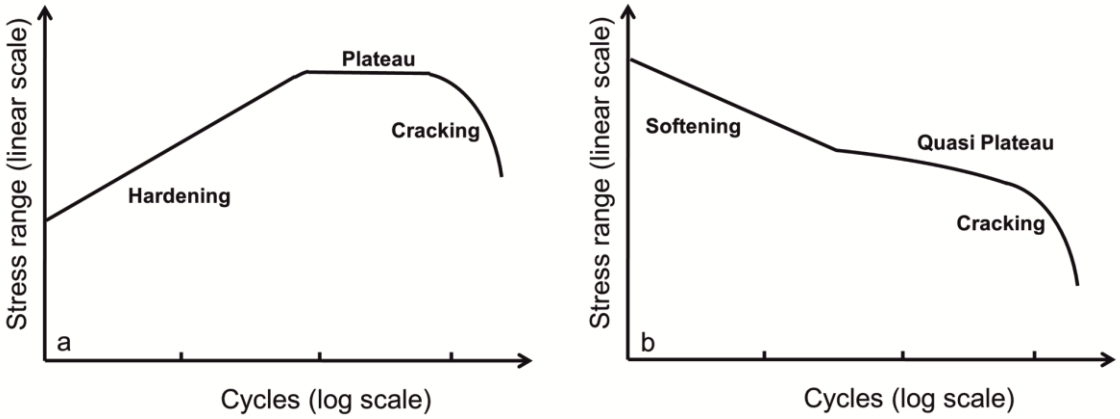

Figure 1- 5: Variation of stress with cycles under constant amplitude strain controlled loading for (a) a cyclically hardening material and (b) a cyclically softening material. After Hales *et al.* [47].

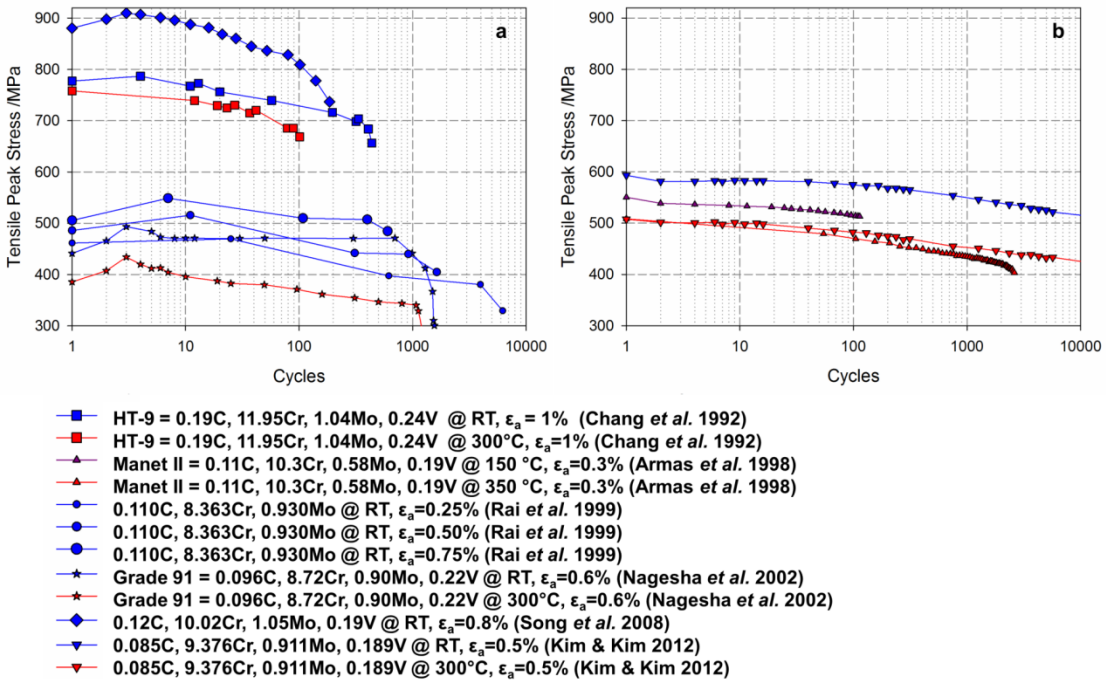

Figure 1- 6: Cyclic behaviour in 9-12 Cr steels at T < 350 ˚C illustrating (a) initial hardening followed by softening and (b) softening only. After Song *et al.* [54], Chang and Kai [58], Kim and Kim [59], Armas *et al.* [60], Nagesha *et al.* [61] and Rai *et al.* [63].

1.4 References

1. Soady, K.A., Mellor, B.G., Shackleton, J., Morris, A. and Reed, P.A.S., *The effect of shot peening on notched low cycle fatigue.* Materials Science and Engineering A, 2011. **528**(29-30): p. 8579 - 8588.

2. *Supercritical steam cycles for power generation applications*, 1999. UK Department for Trade and Industry.

3. Kern, T.-U., Staubli, M., Mayer, K.H., Escher, K. and Zeiler, G., *The European effort in development of new high temperature rotor materials up to 650 C - COST 522*, in *Proceedings of the 7th Liège Conference in Materials for Advanced Power Engineering*, Lecomte-Beckers, J., Carton, M. Schubert, F. and Ennis, P.J., Editors. 2002. Liège, Belgium: Forschungszentrum Jülich: p. 1049 - 1064.

4. Horseman, G., *Parsons 500 MW and 660 MW steam turbines operating experience and lessons learned*, in *Proceedings of the 8th International Charles Parsons Turbine Conference*. 2011. Portsmouth, UK: The Institute of Materials Minerals and Mining.

5. Bloodworth, T.J. and Keresztury, S.J., 2013. E.ON New Build and Technology Report ENT/12/TSI/1095/R.

6. Deckers, M., Thiemann, T. and Horseman, G., *Steam turbine design challenges addressing current and future power generation requirements*, in *Proceedings of the 8th International Charles Parsons Turbines Conference*. 2011. Portsmouth, UK: The Institute of Materials Minerals and Mining.

7. Maruyama, K., Sawada, K., and Koike, J., *Review: Strengthening mechanisms of creep resistant tempered martensitic steel.* ISIJ International, 2001. **41**(6): p. 641 - 653.

8. Fry, A., Osgerby, S. and Wright, M., *Oxidation of alloys in steam environments - A review*, 2002. National Physical Laboratory Report MATC(A)90.

9. Rawat, M.S., Jayaraman, T.R., Prasad, C.R.K. and Kalpana, Y., *Influence of shot peening on corrosion properties of steam turbine blading steel*, in *Proceedings of the the 7th International Conference on Shot* Peening. 1999. Warsaw, Poland: International Scientific Committee on Shot Peening: p. 184 - 191.

10. Perkins, K.M. and Bache, M.R. *Corrosion fatigue of a 12%Cr low pressure turbine blade steel in simulated service environments.* International Journal of Fatigue, 2005. **27**(10-12): p. 1499 - 1508.

11. James, M.N., Newby, M., Hattingh, D.G. and Steuwer, A., *Shot-peening of steam turbine blades: Residual stresses and their modification by fatigue cycling.* Procedia Engineering, 2010. **2**(1): p. 441 - 451.

12. Zhou, S. and Turnbull, A., *Influence of pitting on the fatigue life of a turbine blade steel.* Fatigue and Fracture of Engineering Materials and Structures, 1999. **22**(12): p. 1083 - 1093.

13. Carter, T.J., *Common failures in gas turbine blades.* Engineering Failure Analysis, 2005. **12**(2): p. 237 - 247.

14. Francis, J.A., Mazur, W. and Bhadeshia, H.K.D.H. *Review: Type IV cracking in ferritic power plant steels.* Materials Science and Technology, 2006. **22**(12): p. 1387 - 1395.

15. Perkins, K.M. and Bache, M.R., *The nfluence of inclusions on the fatigue performance of a low pressure turbine blade steel.* International Journal of Fatigue, 2005. **27**(6): p. 610 - 616.

16. Soady, K.A., Mellor, B.G., West, G.D., Harrison, G., Morris, A. and Reed, P.A.S., *Evaluating surface deformation and near surface strain hardening resulting from shot peening a tempered martensitic steel and application to low cycle fatigue.* International Journal of Fatigue, 2013. In press.

17. Brett, C., *Personal communication* to Soady, K.A. 2012.

18. Parvin, T. and Spurr, S.B., 2005. Power Technology report PT/05/BB7778/R.

19. Olympus Corporation, *Turbine dovetail inspection using eddy current arrays*. 2012. Available from: http://www.olympus-ims.com/en/applications/turbine-dovetail-inspection-eddy-current-array/; Accessed 13/11/2012.

20. Kuboň, Z., Foldyna, V. and Vodárek, V., *Optimized chemical composition of 9-12% Cr steels with respect to maximum creep resistance*, in *6th Liège Conference in Materials for Advanced Power Engineering*, Lecomte-Beckers, J., Schubert, F. and Ennis, P.J., Editors. 1998. Liège, Belgium: Forschungszentrum Jülich: p. 311 - 320.

21. Masuyama, F., *Review: History of power plants and progress in heat resistant steels.* ISIJ International, 2001. **41**(6): p. 612 - 625.

22. Morris Jr, J.W., Lee, C.S. and Guo, Z., *The nature and consequences of coherent transformations in steel.* ISIJ International, 2003. **43**(3): p. 410 - 419.

23. Bhadeshia, H.K.D.H. and Honeycombe, R.W.K., *Steels: Microstructure and Properties*. 3rd edn.; 2006, Oxford, UK: Butterworth-Heinemann.

24. Krauss, G., *Martensite in steel: Strength and structure.* Materials Science and Engineering A, 1999. **273 - 275**: p. 40 - 57.

25. Morito, S., Tanaka, H., Konishi, R., Furuhara, T. and Maki, T., *The morphology and crystallography of lath martensite in Fe-C alloys.* Acta Materialia, 2003. **51**(6): p. 1789 - 1799.

26. Kimura, M., Yamaguchi, K., Hayakawa, M., Kobayashi, K. and Kanazawa, K., *Microstructures of creep fatigued 9-12% Cr ferritic heat-resisting steels.* International Journal of Fatigue, 2006. **28**(3): p. 300 - 308.

27. Barcelo, F., Béchade, J.-L. and Fournier, B., *Orientation relationship in various 9%Cr ferritic/martensitic steels - EBSD comparison between Nishiyama-Wassermann, Kurdjumov-Sachs and Greninger-Troiano.* Phase Transitions, 2010. **83**(8): p. 601 - 614.

28. Sandvik, B.P.J. and Wayman, C.M., *Characteristics of lath martensite: Part 1, Crystallographic and substructural features.* Metallurgical Transactions A, 1983. **14**(4): p. 809 - 822.

29. Barcelo, F., de Carlan, Y., Béchade, J.-L. and Fournier, B, *Orientation relationship in Eurofer martensitic steels.* Phase Transitions, 2009. **82**(11): p. 808 - 820.

30. Hald, J. and Straub, S., *Microstructural stability of 9-12%CrMo(W)VNbN-steels*, in *Proceedings of the 6th Liège Conference in Materials for Advanced Power Engineering*, Lecomte-Beckers, J., Schubert, F. and Ennis, P.J., Editors. 1998. Liège, Belgium: Forschungszentrum Jülich: p. 155 - 169.

31. Qin, Y., Götz, G., and Blum, W., *Subgrain structure during annealing and creep of the cast martensitic Cr-steel G-X12CrMoWVNbN 10-1-1.* Materials Science and Engineering A, 2003. **341**: p. 211 - 215.

32. Sawada, K., Takeda, M., Maruyama, K., Ishii, R. and Yamada, M., *Dislocation substructure degradation during creep of martensitic heat-resisting steels with and without W.* in *Proceedings of the 6th Liège Conference in Materials for Advanced Power Engineering*, Lecomte-Beckers, J., Schubert, F. and Ennis, P.J., Editors. 1998. Liège, Belgium: Forschungszentrum Jülich: p. 575 - 583.

33. Schaffernak, B., Hofer, P. and Cerjak, H., *Description of the precipitation behaviour of advanced 9-12% Cr steels for power plant applications*, in *Proceedings of the 6th Liège Conference in Materials for Advanced Power Engineering*, Lecomte-Beckers, J., Schubert, F. and Ennis, P.J., Editors. 1998. Liège, Belgium: Forschungszentrum Jülich: p. 519 - 527.

34. Kadoya, Y., Dyson, B.F. and McLean, M., *Microstructural stability during creep of Mo - and/or W - bearing 12Cr steels*, in *Proceedings of the 6th Liège Conference in Materials for Advanced Power Engineering*, Lecomte-Beckers, J., Schubert, F. and Ennis, P.J., Editors. 1998. Liège, Belgium: Forschungszentrum Jülich: p. 593 - 602.

35. Janovec, J., Svoboda, M., Kroupa, A. and Výrostková, *Thermal induced evolution of secondary phases in Cr-Mo-V low alloy steels.* Journal of Materials Science, 2006. **41**(11): p. 3425 - 3433.

36. Hofer, P., Cerjak, H. and Warbichler, P., *Quantitative evaluation of precipitates in the martensitic cast steel G-X12CrMoWVNbN10-1.1*, in *Proceedings of the 6th Liège Conference in Materials for Advanced Power Engineering*, Lecomte-Beckers, J., Schubert, F. and Ennis, P.J., Editors. 1998. Liège, Belgium: Forschungszentrum Jülich: p. 549 - 557.

37. Gustafson, Å. and Hättestrand, M. *Coarsening of precipitates in an advanced creep resistant 9% chromium steel - quantitative microscopy and simulations.* Materials Science and Engineering A, 2002. **333**(1-2): p. 279 - 286.

38. Strang, A. and Vodarek, V., *Microstructural degradation of martensitic 12%Cr power plant steels during prolonged high temperature creep exposure*, in *Proceedings of the 6th Liège Conference in Materials for Advanced Power Engineering*, Lecomte-Beckers, J., Schubert, F. and Ennis, P.J., Editors. 1998. Liège, Belgium: Forschungszentrum Jülich: p. 603 - 614.

39. Hättestrand, M., Schwind, M. and Andrén, H.-O., *Microanalysis of two creep resistant 9-12% chromium steels.* Materials Science and Engineering A, 1998. **250**(1): p. 27 - 36.

40. Nichol, T.J., Datta, A. and Aggen, G., *Embrittlement of ferritic stainless steels.* Metallurgical Transactions A, 1980. **11**(4): p. 573 - 585.

41. Hald, J., *Microstructure and long-term creep properties of 9-12% Cr steels.* International Journal of Pressure Vessels and Piping, 2008. **85**(1-2): p. 30-37.

42. JianPing, J., Guang, M., Yi,S. and SongBo, X., *An effective continuum damage mechanics model for creep-fatigue life assessment of a steam turbine rotor.* International Journal of Pressure Vessels and Piping, 2003. **80**(6): p. 389 - 396.

43. Endo, T., *Progress in life assessment and design methodology for fossil power plant components.* International Journal of Pressure Vessels and Piping, 1994. **57**(1): p. 7 - 20.

44. Rajasekaran, R. and Nowell, D., *Fretting fatigue in dovetail blade roots: Experiment and analysis.* Tribology International, 2006. **39**(10): p. 1277 - 1285.

45. Barella, S., Boniardi, M., Cincera, S., Pellin, P., Degive, X. and Gijbels, S., *Failure analysis of a third stage gas turbine blade.* Engineering Failure Analysis, 2011. **18**(1): p. 386 - 393.

46. Suresh, S., *Fatigue of materials*. 2nd edn.; 2004, Cambridge, UK: Cambridge University Press.

47. Hales, R., Holdsworth, S.R., O'Donnell, M.P., Perrin, I.J. and Skelton, R.P., *A code of practice for the determination of cyclic stress-strain data.* Materials at High Temperatures, 2002. **19**(4): p. 164-185.

48. Lukáš, P. and Kunz, L., *Cyclic plasticity and substructure of metals.* Materials Science and Engineering A, 2002. **322**(1-2): p. 217 - 227.

49. Landgraf, R.W., Morrow, J.D., and Endo, T., *Determination of the cyclic stress-strain curve.* Journal of Materials, 1969. **4**(1): p. 176 - 188.

50. Lefebvre, D. and Ellyin, F. *Cyclic response and inelastic strain energy in low cycle fatigue.* International Journal of Fatigue, 1984. **6**(1): p. 9 - 15.

51. Polák, J., Klesnil, M. and P. Lukáš, *On the cyclic stress-strain curve evaluation in low cycle fatigue.* Materials Science and Engineering, 1977. **28**(1): p. 109 - 117.

52. Chang, H.J., Tsai, C.H. and Kai, J.J., *Effects of temperature on the cyclic deformation behaviour and microstructural changes of a 12Cr-1MoVW martensitic stainless steel.* International Journal of Pressure Vessels and Piping, 1994. **59**(1-3): p. 31 - 40.

53. Kanazawa, K., Yamaguchi, K., and Kobayashi, K., *The temperature depencence of low cycle fatigue behaviour of martensitic stainless steels.* Materials Science and Engineering A, 1979. **40**(1): p. 89 - 96.

54. Song, X.L., Yang, G.X., Zhou, S.L., Fan, H., Yang, S.S., Zhu, J.W. and Liu, Y.N., *Cyclic deformation behaviour and microstructural changes of 12Cr-WMoV martensitic stainless steel at elevated temperature.* Materials Science and Engineering A, 2008. **483 - 484**: p. 211 - 213.

55. Earthman, J.C., Eggeler, G., and Ilschner, B., *Deformation and damage processes in a 12%Cr-Mo-V steel under high temperature low cycle fatigue conditions in air and vacuum.* Materials Science and Engineering A, 1989. **110**: p. 103 - 114.

56. Vogt, J.-B., DeCallaix, G. and Foct, J., *Cyclic mechanical behaviour and microstructure of a 12Cr-Mo-V martensitic stainless steel.* Fatigue and Fracture of Engineering Materials and Structures, 1988. **11**(6): p. 435 - 446.

57. Dubey, J.S., Chilukuru, H., Chakravartty, J.K., Schwienheer, M., Scholz, A. and Blum, W., *Effects of cyclic deformation on subgrain evolution and creep in 9-12% Cr-steels.* Materials Science and Engineering A, 2005. **406**(1-2): p. 152 - 159.

58. Chang, H.J. and Kai, J.J. *Effects of temperature on the low cycle fatigue and microstructures of HT-9 ferritic steel.* Journal of Nuclear Materials, 1992. **191 - 194**(Part B): p. 836 - 840.

59. Kim, D.W. and Kim, S.S., *Contribution of microstructure and slip system to cyclic softening of 9wt.%Cr steel.* International Journal of Fatigue, 2012. **36**(1): p. 24 - 29.

60. Armas, A.F., Avalos, M., Alvarez-Armas, I., Peterson, C. and Schmitt, R., *Dynamic strain ageing evidences during low cycle fatigue deformation in ferritic-martensitic stainless steels.* Journal of Nuclear Materials, 1998. **258 – 263**(Part 2): p. 1204 - 1208.

61. Nagesha, A., Valsan, M., Kannan, R., Bhanu Sankara Rao, K. and Mannan, S.L., *Influence of temperature on the low cycle fatigue behaviour of a modified 9Cr-1Mo ferritic steel.* International Journal of Fatigue, 2002. **24**(12): p. 1285 - 1293.

62. Shankar, V., Valsan, M., Bhanu Sankara Rao, K., Kannan, R., Mannan, S.L. and Pathak, S.D., *Low cycle fatigue behaviour and microstructural evolution of modified 9Cr-1Mo ferritic steel.* Materials Science and Engineering A, 2006. **437**: p. 413 - 422.

63. Rai, S., Choudhary, B.K., Jayakumar, T., Bhanu Sankara Rao, K. and Raj, B., *Characterisation of low cycle fatigue damage in 9Cr-1Mo ferritic steel using X-*

ray diffraction technique. International Journal of Pressure Vessels and Piping, 1999. **76**(5): p. 275 - 281.

64. Swindeman, R.W., *Cyclic stress-strain-time response of a 9Cr-1Mo-V-Nb pressure vessel steel at high temperature*, in *STP 942, Low Cycle Fatigue,* Solomon, H.D., Halford, G.R., Kaisand, L.R. and Leis, B.N., Editors. 1988. West Conshohocken, PA, USA: ASTM: p. 107 – 122.

65. Sauzay, M., Brillet, H., Monnet, I., Mottot, M., Barcelo, F., Fournier, B. and Pineau, A., *Cyclically induced softening due to low cycle boundary annihilation in a martensitic steel.* Materials Science and Engineering A, 2005. **400 - 401**: p. 241 - 244.

66. Yaguchi, M. and Takahashi, Y. *Ratchetting of viscoplastic material with cyclic softening, part 1: Experiments on modified 9Cr-1Mo steel.* International Journal of Plasticity, 2005. **21**(1): p. 43 - 65.

67. Chan, K.S., *A microstructure-based fatigue-crack-initiation model.* Metallurgical and Materials Transactions A, 2003. **34**(1): p. 43 - 58.

68. Tanaka, K. and Mura, T. *A dislocation model for fatigue crack initiation.* Journal of Applied Mechanics, 1981. **48**(1): p. 97 - 103.

69. Telesman, J. and Ghosn, L.J., *The unusual near-threshold FCG behaviour of a single crystal superalloy and the resolved shear stress as the crack driving force.* Engineering Fracture Mechanics, 1989. **34**(5-6): p. 1183 - 1196.

70. Congleton, J. and Chen, W., *The fatigue life of a 13% Cr turbine blade steel.* International Journal of Fatigue, 1990. **12**(2): p. 91 - 98.

71. Tanaka, K. and Mura, T., *A theory of fatigue crack initiation at inclusions.* Metallurgical Transactions A, 1982. **13**(1): p. 117 - 123.

72. Irwin, G.R. *Plastic zone near a crack and fracture toughness*, in *Proceedings of the 7th Sagamore Ordnance Materials Conference*. 1960. New York: Syracuse University: p. 63 -78.

73. British Standard, *BS EN ISO 12737:2010: Metallic materials - Determination of plane strain fracture toughness*, 2010.

74. Suresh, S. and Ritchie, R.O., *Propagation of short fatigue cracks.* International Metals Reviews, 1984. **29**(6): p. 445 - 476.

75. Forsyth, P.J.E.. *A two stage process of fatigue crack growth*, in *Proceedings of the Crack Propagation Symposium*. 1962. Cranfield, UK: College of Aeronautics: p. 76 – 94.

76. Pook, L., *Metal fatigue. What is it, why it matters.* 2007, Dordrecht, The Netherlands: Springer.

77. Miller, K.J. and McDowell, D.L., *Overview*, in *STP 1359, Mixed-Mode Crack Behaviour,* Miller, K.J. and McDowell, D.L., Editors. 1999. West Conshohocken, PA, USA: ASTM: p. vii – ix.

78. Laird, C. and Smith, G.C., *Crack propagation in high stress fatigue.* Philosophical Magazine, 1962. **7**(77): p. 847 - 857.

79. Ritchie, R.O., *Mechanisms of fatigue-crack propagation in ductile and brittle solids.* International Journal of Fracture, 1999. **100**: p. 55 - 83.

Chapter 2

Literature review

As mentioned in Chapter 1, shot peening is a process applied to components in order to improve their fatigue resistance. In recent years there has been an increasing interest in including the effects of the shot peening process in life assessment models since this would allow a reduction in conservatism compared to those in current application. Indeed, the development of these approaches forms the basis of the project scope which can be separated into two main themes:

- Characterising the shot peening process and the effect on ambient low cycle fatigue (LCF).
- Incorporating the shot peening effect in life assessment methods.

This chapter seeks to review firstly the effects of the shot peening process (surface roughening, strain hardening and compressive residual stresses) and how the magnitude of these effects can be determined both experimentally and numerically. The reasons for the beneficial effect of shot peening on fatigue resistance are reviewed; this includes consideration of how different operating conditions can affect the magnitude of the benefit.

The second part of the review considers how these effects can be incorporated into life assessment modelling approaches with discussion of the relative merits of each approach. At the end of this section, a component life assessment process which accounts for the effect of the shot peening process is proposed.

This proposal forms the basis for refining the broad project objectives initially outlined in Chapter 1. This third part of the chapter uses the preceding review to identify the key gaps in the current understanding which are to be addressed in the remainder of this thesis.

This chapter is presented in the form of a two part review paper, each part standing alone and following one of the two main themes outlined above. As such, each part has an independent introduction and summary section with the summary from the first part strongly linked to the introduction to the second part. This chapter has been published in Materials Science and Technology largely in its present form except for some minor alterations:

K. A. Soady, *Review: Life assessment methodologies incorporating shot peening process effects; mechanistic consideration of residual stresses and strain hardening. Part 1: The effect of shot peening on fatigue resistance*. Materials Science and Technology, 2013. **29**(6): p. 637 – 651.

K. A. Soady, B. G. Mellor and P. A. S. Reed, *Review: Life assessment methodologies incorporating shot peening process effects; mechanistic consideration of residual stresses and strain hardening. Part 2: Approaches to fatigue lifing after shot peening*. Materials Science and Technology, 2013. **29**(6): p. 652 – 664.

2.1. The effect of shot peening on fatigue resistance

2.1.1. Introduction

Fatigue is a well-known failure mechanism which results from the application of cyclic loads to a component [1]. Hence the fatigue life of a component is related not only to the interaction between material characteristics and operational history but also to any deformation processes (which may or may not be cyclic) which may have occurred during manufacturing, including surface treatments designed to improve fatigue resistance. Furthermore, where the manufacturing process results in significant residual stresses, these must be considered when analysing the magnitude of the mean stress about which the operational cyclic stresses are applied.

The traditional Goodman, Gerber and Morrow stress life approaches all indicate that a tensile mean stress is detrimental to fatigue life [1]. Hence in components where cyclic loading may be expected, especially under bend loads where detrimental tensile stresses can peak near the surface, the introduction of a compressive residual stress during manufacturing is generally considered beneficial.

Shot peening is a cold work process applied to a wide range of components, many of complex geometry, across many industries, in order to improve their fatigue resistance. Examples illustrating this wide ranging application are detailed in Table 2-1; typically the components are peened in the stress concentration regions most susceptible to fatigue.

The component is bombarded with small spherical shot of a hard material at a relatively high velocity, in the region 40-70 ms^{-1}. The shot peening process is controlled by monitoring two parameters, namely intensity and coverage. Intensity is a measure of the plastic dissipation of the impinging shots [3] and is thus a function of shot size, hardness and velocity. This is controlled during industrial processes using one of three Almen strips of different thicknesses, namely ‘N’, ‘A’ and ‘C’. These are restrained strips of SAE1070 spring steel peened on one side only; when the strip is released, the induced compressive residual stresses cause strip deflection; a value of 10A indicates a 0.010” deflection of an ‘A’ strip [2]. Coverage is a measure of the area covered by peening indentations. If coverage is specified as greater than 100 %, this means that the processing time to achieve 100 % has been increased by the corresponding factor [2]. Occasionally shot peening may be specified by detailing each individual variable. This inconsistency can make comparing processes between studies in the literature very difficult.

It is well recognised in the literature that shot peening has three important mechanical effects [4]:

- Plastic flow results in a roughened surface the typical topography of which is illustrated in Figure 2- 1. Surface roughness measurements (most generally defined using R_a, the arithmetical mean vertical deviation of the assessed roughness profile from the mean line) are easily measured using either optical or tactile instruments and can vary from $1.2 < R_a < 4.3$ μm, although typical industrial processes tend to result in $R_a \sim 3.5$ μm often with standard deviations of approximately 10 % [5-8].
- Intense local plastic deformation occurs at the surface resulting in the tangling of dislocations and associated strain hardening or strain softening (with accompanying changes in local material yield strength). The case of strain hardening is assumed for the remainder of this review and as such shot peening is considered to result in localised increases in yield strength. Plastic strains can reach values of up to 50 %; for Inconel 718 peened at intensity 6-8A and coverage 100 %, the surface plastic strain was 20 % and the profile extended 70 μm into the material [9]. Near surface microstructural refinement [10-13] and strain induced phase transformations may also occur [14]; a clear example of the former is shown in Figure 2- 2.
- The amount of strain decreases with depth until at a certain depth, only elastic deformation has occurred. After contact has ceased, the elastically stressed region tends to recover to the unloaded state, whereas the plastically deformed region sustains some permanent deformation; the continuity condition requires the development of a compressive residual stress field parallel to the free surface in the near surface region with a balancing tensile stress beneath in order to maintain equilibrium (Figure 2- 3). A typical profile is illustrated in Figure 2- 4 and can be characterised by the surface residual stress (σ_{srs}), the maximum compressive residual stress (σ_{mcrs}), the depth at which this peak occurs (z_m) and the overall depth of the compressive layer (z_0).

Whilst it is recognised that surface roughening has a detrimental effect on fatigue life and the strain hardening and residual stress effects are beneficial, James *et al.* [16] have identified that there is still controversy in the literature as to whether the major benefits of shot peening should be ascribed to the generation of the compressive residual stress or the local plastic deformation and strain hardening. Hence the outcome of the shot peening process, and the resulting component fatigue life, is the result of the complex interactions between these three effects (which are geometrical, microstructural and mechanical in nature) and fatigue crack initiation and propagation.

Initial residual stress and strain hardening distributions resulting from shot peening can be determined either experimentally or numerically; these are essential inputs to life assessment models accounting for the effects of the process. Both analytical and finite element methods have been developed for approximating the residual stress and strain hardening profiles; these methods have been thoroughly considered in a recent review [17]. Whilst not the focus of the present review, these methods will be briefly introduced since an understanding of the residual stress and strain hardening profiles and their development through life is essential when considering the effect of shot peening on fatigue life.

The effects of shot peening on high cycle fatigue (HCF)[1] are relatively well understood, however the effects on LCF are less clear, especially given the potential for residual stress and strain hardening relaxation after loading to stresses in excess of yield strength. Residual stress relaxation during fatigue has already been reviewed [18]; this section aims to review those aspects most pertinent to lifing shot peened components, including consideration of more recent contributions to the field.

2.1.2. Shot peening residual stress and strain hardening profiles

The use of peening intensity as the process control parameter means that whilst inferences can be made about the residual stress and strain hardening profile shape and magnitude, quantitative assessment based on intensity alone is not possible. As such the profiles must be determined by other means.

2.1.2.1. Establishing residual stress profiles

Experimental methods are generally destructive and time consuming and thus are not often applied in extensive parametric studies of the effects of varying process parameters or process optimisation. However, they can allow quantification of a specific process or validation of analytical and finite element approaches. Common methods including laboratory incremental layer removal X-ray diffraction (XRD) (typically applying the $\sin^2\psi$ method) and hole drilling have been demonstrated to be

[1] When the number of cycles to failure is greater than 10^5, the process is termed high cycle fatigue (HCF). Conversely, for less than 10^5 cycles to failure, the process is termed low cycle fatigue (LCF) and typically macroscopic plasticity is evident. Lower stresses result in higher lives (HCF) and higher stresses result in lower lives (LCF). Further discussion is made of the distinction between HCF and LCF in terms of lifing approaches in the second half of this review.

sufficient for compressive residual stress measurement in the near surface region [5, 11, 15, 19-31].

Measurements of the balancing tensile residual stress can, however, be much harder to obtain since they occur at greater depths and the uncertainties in laboratory XRD results are much greater, since, for example, stress redistributions have to be taken into account. Hence there is little data in the literature illustrating complete residual stress profiles through the sample; as a result of this it is common for many papers to simply report the compressive stress field measured using either laboratory XRD or mechanical hole drilling methods.

Synchrotron XRD offers significantly greater penetration capabilities than laboratory XRD and has been successfully used to determine the residual stress distribution through shot peened 5 mm diameter hourglass samples of 12 Cr steel (Figure 2- 5a) [25]. There is no apparent peak in tensile stress; instead the profile is relatively constant through the sample thickness. This data can be used to consider the self-balancing nature of residual stress fields: the compressive force must balance the tensile force. This is illustrated by the example calculation detailed below for Figure 2-5a.

The average compressive stress was calculated based on the upper and lower bounding curves for the 'left' side of the sample (the residual stress field on the 'right' side of the sample can be seen to be symmetrical) using a numerical integration approach for the area under the curve and dividing by the corresponding z_0; the average compressive stress was -467 MPa. The area under compression was 3.70 mm^2 (based on the average z_0). Applying a force balance requires that the balancing tensile stress is 108 MPa based on an area under tension of 15.93 mm^2. This corresponds to the upper tensile stress shown and imparts a degree of confidence to the data in Figure 2- 5a. Conversely, the inability of laboratory XRD results to accurately determine the tensile field can result in an apparent imbalance of forces, for example as indicated in the data in Figure 2- 4; in this case the residual tensile stresses should be treated with some scepticism. This force balance can be applied to all measured residual stress fields as a simple indicator of the accuracy of the data.

The constant tensile residual stress profile indicated in Figure 2- 5a has also been demonstrated using neutron diffraction (ND) by Menig *et al.* in AISI 4140 steel [32]. However, there is still some debate as to the distribution of the balancing tensile stress; ND measurements on shot peened Udimet 720 (intensity 18 – 20A and 200 % coverage) revealed a tensile peak with a magnitude approximately 1/3 of the magnitude of the peak compressive residual stress (Figure 2- 5b). ND also offers similar benefits in terms of penetration, though resolution can be lower than that of

laboratory XRD and both ND and synchrotron XRD systems are much harder to access than laboratory XRD facilities [19].

Notable laboratory XRD contributions include that of Wang *et al.* [28] and subsequently by Gao *et al.* [21] where empirical relations for σ_{srs}, σ_{mcrs}, z_0 and z_m (Equations 2-1 to 2-4; stress values are in MPa and depth values in μm) were based on 60 process conditions in steels.

$$\sigma_{mcrs} = 0.86\sigma^0 - 51 \quad (2\text{-}1)$$

$$\sigma_{srs} = R(114 + 0.563\sigma^0) \quad \text{where} \quad 0.997 < R < 1.13 \quad (2\text{-}2)$$

$$z_0 = (1.41D_d - 0.09S)\left[1 + 0.09\left(C_{sp} - 1\right)^{0.55}\right] \quad (2\text{-}3)$$

$$z_m = 0.28z_0 \quad (2\text{-}4)$$

Residual stress magnitude is clearly dependent on the yield stress of the target material (σ^0 in MPa). The depth of the profile is dependent on peening parameters including shot diameter (S in mm), coverage (C_{sp} x100 %) and the peening indent diameter on the target material (D_d in μm), which is a function of the target material and the peening process parameters.

The error in σ_{mcrs} was reported as high as 20 % and thus these methods should be used as a first estimate of residual stress profiles in similar materials only. Other notable contributions include Mahagaonkar *et al.* [34] who considered the effect of varying process parameters on surface microhardness in two different steels using a full factorial experiment showing that the interaction effects between process parameters varied for different targets (as a result of different deformation characteristics); and Zinn and Scholtes [29] who showed that for different combinations of shot velocity and size at the same intensity, different residual stress profiles resulted. Furthermore, Guagliano and Vergani [35] found that for the same Almen intensity, doubling shot diameter (and reducing velocity appropriately) resulted in larger surface and maximum compressive stresses. These results confirm the dependence on both process conditions and target material hardening characteristics and the requirement of analysing the surface roughness, strain hardening profiles and residual stress profile for each target material – shot peening process system.

This requirement has been met by the development of analytical approximations and numerical finite element (FE) based models. A recent review [17] makes detailed consideration of the various methods. A detailed review is therefore not considered necessary although the brief discussion below considers the most pertinent modelling issues.

Hertzian contact theory based analytical approximations are advantageous in that they allow rapid consideration of various peening systems; however there are apparent difficulties in taking plastic deformation and complex material constitutive relationships into account. The premise of the initial methodology developed by Li *et al*. [36] is that the theoretical elastic Hertzian Mises stress distribution beneath a single impact is calculated based on quasi-static Hertzian criteria [37] and converted to elastic strain using Hooke's Law. The elastic strain is converted to a plastic equivalent, before conversion back to stress using the material model. Unloading criteria in the material model then allow calculation of the residual stress after one impact in a direction parallel to the free surface and equilibrium criteria are used to calculate the residual stress after multiple impingements. Inter alia, it should be noted that the use of a multilinear isotropically hardening model [36] is unable to allow for the Bauschinger Effect[2].

It is in development of the plasticity correction and material modelling that recent approaches have focussed. The initial work [36] used plastic indent diameter measurements to determine a correction factor based on the theoretical elastic indent diameter. Shen and Atluri [38] developed a non-linear equation for the calculation of plastic indent size, but since this is used to calculate the same correction factor, all the associated issues arising from the oversimplification of plasticity remain. This plasticity correction factor was still present in the work of Franchim *et al*. [39] although small improvements were made in the correlation of residual stresses near the sample surface by using a Ramberg-Osgood type material model with unloading criteria which were still defined isotropically. Perhaps the most comprehensive analytical model is that developed by Fathallah *et al.* [40] and which has been adopted by Metal Improvement Company for use in their Peenstress® residual stress prediction software [41]. The overlay materials model [42] implemented still relies on the incremental change in a variable to allow for plasticity, but no longer requires a simple correction based on the ratio of plastic to elastic indent size. The accuracy with which residual stresses can be predicted by this method is clearly shown in Figure 2- 6.

[2] Plastic deformation in one direction (tension or compression) lowers the yield strength upon load reversal. This is a result of changes in dislocation distribution upon reversed loading. The precise mechanism depends on the hardening mechanisms of the material in question and resulting dislocation-dislocation or dislocation-precipitate interactions. This effect can be modelled by kinematic hardening: under load, the yield surface moves in stress space such that straining in one direction reduces the yield strength in the opposing direction.

The application of the FE method solves, for the most part, the problems associated with analytical methods, since plasticity can be accounted for by the application of complex constitutive models where necessary. Whilst FE modelling methods can be time consuming, especially when implementing explicit analyses to solve dynamic problems in 3D, when single shot are modelled, or several shot repeatedly impact the same point, axisymmetric simplifications can be applied to reduce the computational time [43]. Thus it is important to consider the impact modelling approach that is required (implicit using energy equivalence [43, 44] or explicit [3, 45-51]; single [3, 44, 47, 50] or multiple impingement [43, 45-49, 51]) and to ensure the correct element type [3, 46], contact algorithm [3, 44, 51] and friction coefficient [44, 45] are used in the contact region.

Recent developments in modelling the laser shock peening process [52] have gone some way to alleviating the explicit vs. implicit model debate. The use of a dynamic analysis to obtain plastic strain distributions means that elastic fluctuations which affect residual stresses are no longer an issue and less stabilisation time is required after the initial shockwave. By using a restart analysis (or specifying the plastic strains as an initial condition) in a static elastic model, the residual stresses in varying workpiece geometries can be obtained without having to repeatedly re-run the time consuming dynamic model.

Like analytical modelling, FE modelling allows studies on the effects of varying process parameters to be made; notable contributions are Hong *et al.* [50] and the Meguid series [3, 45, 48]. In the original two works of Meguid *et al.* [3] and Hong *et al.* [50], all calculated residual compressive stresses (all the residual stresses reported here are the principal stresses which occur parallel to the free surface as opposed to equivalent stresses) were of a magnitude greater than the yield stress in a substrate based on a simple bilinear material model; this is an unrealistic result when compared with all the available experimental data. However, as previously noted, application of the FE method allows significant effort to be put into selecting an appropriate constitutive model and this can have a significant effect on the residual stress profiles predicted. Later works allowing for strain rate sensitivity [45, 46, 48] have shown that this can change the magnitude of the peak compressive stress observed by around 10–30 %; furthermore, Frija *et al.* [44] have implemented an elastic plastic isotropic hardening target material model with Lemaitre and Chaboche type damage formulation [53]. Without damage, the peak normalised (against yield) compressive residual stress was around -1.4 whereas with damage it was reduced to -1.3. Rouhaud *et al.* [43] demonstrated the differences between modelling a material as isotropically or kinematically hardening, since the latter allows for the Bauschinger Effect on unloading.

Further work on the development of substrate material models was carried out by Klemenz *et al.* [51]. In this work the use of combined isotropic and kinematic hardening in a viscoplastic material model allowed consideration of cyclic behaviour in AISI 4140 (which is known to exhibit cyclic softening [54]) and also the effect of strain rate and temperature changes in the shot peening process. The application of a multiple impingement modelling scheme resulted in the close prediction of experimental data as shown in Figure 2- 7 with a peak normalised compressive residual stress of -0.6. Indeed errors associated with measuring residual stress profiles are quite clearly shown since Figure 2- 7 contains data from three separate experiments; in the compressive region of interest, the simulated curve lies within the bounds of the experimental curves. Whilst this appears to be the most comprehensive target material constitutive model to date, it is noted that no systematic study as to the relative effects of strain rate sensitivity, temperature effects, damage and combined hardening behaviour exists.

The FE method is beneficial from a life assessment perspective since it enables the determination of the full residual stress and plastic strain profile whereas analytical and experimental methods generally only reveal information on the dominant surface-parallel stress component and inferred plastic strain profile. However, the complexities in modelling strategy and material modelling already discussed make its routine application difficult.

2.1.2.2. Establishing residual strain profiles

Inferences on strain hardening profiles can be made from microhardness, XRD line broadening (indicated by full width at half maximum (FWHM) measurements) and electron backscattered diffraction (EBSD) misorientation data [5, 6, 9, 12, 15, 22-24, 29, 57-63].

In experimental techniques the strain hardening profile is commonly quoted as a value of microhardness, FWHM or misorientation with no correlation made to strain magnitude [6, 15, 23]. It has been suggested that change in microhardness can be used to scale change in yield stress; several relationships have been applied with varying degrees of success [5, 11, 57, 63-66]. A calibration technique relating FWHM to plastic strain in uniaxial tension/compression samples has gone some way to alleviating this problem for FWHM data [9, 61]. Other approaches for FWHM data are analytical and include the classical Scherrer [67] and Stokes and Wilson [68] equations for average grain size and mean microstrain respectively (demonstrated for shot peened samples by Liu *et al.* [12]) and the combined Williamson and Hall [69] approach, which allows separation of crystallite size and microstrain from peak widths (demonstrated for shot peened samples by Tan *et al.* [59]). Whilst calibration

approaches for true plastic strain have also been applied to EBSD grain average and local misorientation data [70-74], and EBSD grain orientation spread data has been applied in determining the overall depth of the strain hardened profile in shot peened samples [6], as yet there is no application showing yield strength variation in the near surface region of shot peened material.

It should be noted that whilst residual stress measurement techniques are well refined, there is still some debate as to the relationship between hardness, EBSD and FWHM profiles [6, 58, 62]. This is a result of variations in strain hardening profile depths reported in the literature, this is considered for one exemplar system in Table 2- 2. From the work of Child *et al.* [6], EBSD profiles appear to extend to around half the depth of the microhardness profile, however the work of Kim *et al.* [15] indicates that the FWHM is elevated to approximately the same depth as the increased microhardness profile. Before strain hardening profiles can be utilised in lifing approaches, it is essential that a more standardised measurement system is adopted by the scientific community.

2.1.3. Improvements in fatigue life resulting from shot peening

In Section 2.1.1, the shot peening process was outlined; this surface treatment process is used to improve the fatigue resistance of treated parts. In this section, the interaction of the residual stress and strain hardening profiles as a cause of this benefit is described. In the latter half of the section, service conditions to which components are exposed are introduced as another factor controlling the relative improvement of fatigue life in a given component.

2.1.3.1. The effect of shot peening induced roughness, residual stress and strain hardening on fatigue life

The benefits of the residual stresses and strain hardening resulting from shot peening usually dominate any detrimental effects on initiation life resulting from surface roughening. The effect of surface roughness on fatigue life is well documented; it has been written into ESDU codes [75] (as the ratio of fatigue limit at a given roughness to the fatigue limit when roughness is negligible, K_{sf}) and also been the subject of a review paper [76]. Whilst roughness parameters such as R_t (total profile height) and shape information such as R_{sk} (profile skewness measures the degree of departure from symmetry of the measured distribution) and R_{ku} (profile kurtosis measures the 'degree of peakedness' of the distribution) would be beneficial in assessment of stress concentrating effects [76], as noted in Section 2.1.1, surface roughness data are generally presented as values of R_a. As a result, when modelling the effects of surface

roughness, simplifying assumptions must be made about the profile. Furthermore, recently there has been a drive towards three dimensional topographical characterisation of surfaces with some authors reporting areal parameters such as S_a [6]; this complicates the characterisation of surface roughness yet further as the relationships between areal parameters and the corresponding linear parameters are not well understood [77].

Koster [78] states that in the range $2.5 < R_a < 5$ μm, fatigue performance correlates better with surface microstructure and residual stress than with roughness. It is important to note, however, that the nature of component operation may affect this statement as any stress relief (such as thermal, or mechanical induced by LCF) may negate this dominance [79]. Furthermore, in propagation dominated applications such as LCF, where initiation is relatively insignificant, roughness would not be expected to be a major contributing factor to fatigue life. Interactions between surface roughness, initiation characteristics and loading conditions must thus be considered in any lifing study of shot peened components since there may be situations in which the roughness effect is significant. These interactions are discussed further in Section 2.1.3.2.

Thorough consideration of the effect of residual stress on failure [80] and more specifically fatigue [81] has already been made in published works. The compressive residual stress is (in the simplest case) summed with the applied stress range and the resultant reduction (given that compressive stresses are denoted as negative values) in effective mean stress is considered. The plastic deformation increases the dislocation density in the near surface region hindering the dislocation movement which is associated with crack initiation; the increased yield stresses in the cold worked region result in lower plastic strain amplitudes under stress controlled cycling [14]. Hence shot peening can be beneficial in increasing both the initiation and propagation life.

De los Rios *et al.* [82] demonstrated both delayed initiation and retarded crack propagation rates (especially in the short crack region) after shot peening in A316 stainless steel. After >100 % coverage 12 N intensity shot peening, the number of cycles to initiation (measured by replication) was increased from 8000 to 500000 (under pure bending fatigue with stress range $\Delta\sigma$ = 480 MPa and stress ratio $R_\sigma \sim -0.8$). Under the same conditions, crack growth rate, da/dN, in the short crack region was also shown to be significantly reduced by shot peening, as evidenced by Figure 2- 8. This delayed crack propagation in short cracks has also been shown using replication techniques on peened (full coverage, 8A intensity) Al 7475-T7351 samples by Gao and Wu [83].

Reduced crack propagation rates in shot peened samples up to a depth corresponding to the maximum compressive residual stress were also reported by Mutoh *et al.* [84]; this work also reported a reduction in crack aspect ratio whereby the ratio of crack surface length to depth was increased in peened samples compared to unpeened samples. Guagliano and Vergani [35] were able to demonstrate the presence of non-propagating fatigue cracks which arrested at approximately the depth of the maximum compressive residual stress. These non-propagating cracks were attributed to the dependence of the crack opening stress intensity factor on residual stress.

It has been postulated by some researchers [85, 86] that delayed crack initiation is insignificant compared to delayed (micro) crack propagation and that this may be influenced by plastic strain as well as by compressive residual stresses. Indeed de los Rios *et al.* [82] considered this to be a factor in the very slow crack propagation in short cracks in peened samples shown in Figure 2- 8 since work hardening restricts crack tip plasticity.

One of the more comprehensive studies on the individual consideration of shot peening effects and their interaction on total fatigue life was performed on titanium alloy samples by combining electropolishing to reduce roughness effects and stress relief heat treatments by Wagner [87]. The annealing stress relief heat treatment applied was shown to reduce the maximum compressive residual stress from -800 MPa after shot peening to -100 MPa after stress relief, this reduction is sufficient to consider the change in fatigue life to be approximately equal to the magnitude of the benefit resulting from residual stresses. Initiation was quickened by roughness, but retarded by work hardening (as illustrated in Figure 2- 9a). Propagation was accelerated in the presence of strain hardening alone (Figure 2- 9b). This was explained by low residual ductility in the work hardened layer, although it should be noted that this is in contrast to the work of de los Rios *et al.* [82] in which strain hardening was thought to reduce the rate of crack propagation. Indeed, given the generally accepted Laird-Smith model for fatigue crack growth in ductile metals, the relationship to crack tip plasticity described by de los Rios *et al.* [82] would appear to have more physical significance but cannot explain the data presented in Figure 2- 9b. Either way, it is clear from Figure 2- 9b that the effect on propagation is dominated by compressive residual stresses which significantly retard crack growth. Whilst reference was made to the dependence of an individual material's response on cyclic stress-strain characteristics and residual stress stability, no specific consideration was made in the investigation of Wagner [87].

Relative effects were also considered by Eleiche *et al.* [88], who showed that shot peening increased the endurance limit of a high strength martensitic steel by 20 % and that subsequent stress relief heat treatment only reduced this effect by 3 % (Figure 2-

10) indicating a strong HCF life improvement contribution from near surface strain hardening.

The preceding discussion detailing the individual effects of the surface roughness, residual stress and strain hardening profiles is summarised in Table 2- 3.

Peening intensity plays a key role in the residual stress and work hardening distributions [3, 45, 46, 50, 51] and thus on improvements in fatigue life resulting from shot peening. The existence of an optimum peening intensity in titanium alloys was presented by Wagner [89] and in magnesium alloys by Song *et al.* [90], contradicting the work in austenitic stainless steels of de los Rios *et al.* [82] who suggest that increasing intensity tends to improve both initiation and propagation response (although it is plausible that an intensity sufficient to cause a degradation in fatigue improvement was not reached; whilst the different materials under investigation might influence residual stress magnitudes, the trend of the effect of intensity would not be expected to be different). The conclusion of Wagner [89] is supported by work on aluminium alloys [84] in which very high energy peening conditions reduced the initiation life as a result of intense surface folding causing stress concentrations. Indeed, the data presented by Guagliano and Vergani [35] tends to suggest it is not just the intensity which is a factor, but also the way in which the intensity is achieved, since this can affect residual stress distributions. A 12A process resulted in a 41 % improvement in fatigue limit compared to unpeened samples using 0.3 mm diameter shot and only a 25 % improvement when smaller shot at higher velocities were used.

It is concluded that the specific residual stress and strain hardening profiles resulting from a peening process are required for consideration of the resulting effects on fatigue life. The overall resulting fatigue life will be a function of the start of life condition and any modifications to this condition caused by the complex interaction of residual stresses, service conditions (such as temperature and cyclic stresses, both of which can result in residual stress relaxation) and cyclic hardening or softening characteristics of the material. It is thus necessary to consider how service conditions may influence the effect of shot peening on fatigue resistance.

2.1.3.2. Interaction between shot peening induced residual stresses and strain hardening profiles and service conditions

The potential for substantial improvement in HCF endurance limit by shot peening was identified using the increase in endurance limit in Figure 2- 10. This can be rationalised by considering the effects of shot peening described in Table 2- 3. At lower applied stresses below the yield strength of the material (which is increased in the near surface

region by strain hardening and may also be affected by cyclic hardening material characteristics), initiation is limited because there is limited plastic deformation (dislocation movement). However, it was mentioned previously that the effects on LCF, where gross plastic deformation may occur, are less clear. This effect is illustrated by the intersection of the projected shot peened and un-shot peened material curves at N_f ~ $2x10^4$ in Figure 2- 10; the intersection at N_f ~ 10^4 is confirmed in other works [23, 91]. Given the scatter which is present in such S-N data, it might be more appropriate to postulate that shot peening appears to give little benefit when the projected life is $<5x10^4$ cycles this is a result of service conditions allowing more dislocation movement facilitating initiation and higher crack growth driving forces. This section describes the effect that service conditions may have on residual stress and strain hardening profiles, the situations where shot peening is most beneficial and the reasons why the benefits of shot peening in the LCF regime are less well understood.

Firstly, it is important to note the potential application of the component when specifying shot peening processes. It is the applied stress gradient experienced by a component which determines how effective the shot peening process will be at improving fatigue life [92]. Typically, components loaded in bend would be expected to see the maximum applied tensile stresses near the surface, hence deriving a maximum benefit from the compressive residual stresses and strain hardening, with surface initiation only occurring under high applied tensile stresses as illustrated in Figure 2- 11a. However, if the compressive residual stress is sufficient, initiation can occur where high applied tensile stresses coincide with the balancing tensile residual stresses, i.e. sub-surface [30]. This situation is most likely to occur under axial load with no stress concentration, although it is not uncommon in samples under bend load where applied tensile stresses extend sufficiently far into the component as to coincide with tensile residual stresses. Sub-surface initiation is illustrated in Figure 2- 11b; by increasing the Almen intensity, the compressive residual profile increased sufficiently as to resist surface initiation and force sub-surface initiation. This situation is particularly severe in samples exhibiting a sub-surface tensile residual stress peak, such as that in the residual stress profile illustrated in Figure 2- 5b; it is also noted that sub-surface initiation can be facilitated by the presence of inclusions in the region of tensile residual stress [30]. It is for this reason that the majority of applications listed in Table 2- 1, including gears, connecting rods, crankshafts and turbine blade disc interfaces, are subjected to bending fatigue loads and have regions of high stress concentration.

The use of stress relief heat treatments to isolate the effect of work hardening was discussed previously; however, it is possible this could occur in service. One such example might be shot peened nickel based superalloys applied in the hot end of aero-

engines [15]. At the typical upper service temperature for Udimet 720 Li in aero-engine turbine disc applications of 700 °C, after 10 hours of exposure, the compressive residual stresses were relaxed to half their original value [15]. This can be explained by the recovery of dislocations reducing the misfit in plastic strain.

Furthermore, residual stresses can be relaxed by the application of high stresses (corresponding to LCF) in service. This might be of concern in components such as shot peened ferritic heat resistant steel in power plant blade disc interfaces. These components undergo 10 % overspeed tests, for example to check rotor balance after maintenance; under these conditions, localised yielding can occur [25]. The interaction of the two mechanisms in both isothermal high temperature and thermo-mechanical fatigue must also be considered since the effect can be synergistic [93].

This potential for residual stress relaxation is one of the key differences causing the different relative effect of shot peening on HCF and LCF. The relaxation of compressive residual stresses during fatigue cycling has already been reviewed [18] and as such, only the papers most relevant to the present discussion of the shot peening process are considered.

The compressive residual stresses after shot peening are a result of the plastic misfit between regions only deformed elastically by the shot and those which are deformed plastically (in tension) (Figure 2- 3). If during fatigue cycling the residual stresses combine with the applied stresses to cause local plastic yielding, for example in regions previously deformed only elastically, the plastic misfit can be reduced, modifying the residual stress profile. This results in a large step relaxation after the first cycle (quasi static relaxation caused by load reversal); continued cycling can cause further logarithmic relaxation in residual stress in materials which exhibit cyclic softening characteristics [55]. Whilst this relaxation can occur under tensile or compressive loading, lower applied stresses are required for compressive loading due to superposition with residual compressive stresses and as a result of the Bauschinger effect [55, 82].

Zhuang and Halford [94] reviewed some of the previously proposed models for residual stress relaxation. Early mean stress, σ_m, relaxation functions such as that of Morrow and Sinclair [95] (Equation 2-5), developed based on uniaxial stress ratio R_σ = -1 tests and fitting constant b_1 to material softening and applied strain range, can be used for surface residual stress relaxation in situations of fully reversed axial load such that the surface residual stress is directly related to the applied mean stress. However, this situation is unlikely to occur in engineering components where both mean stress and stress ratio vary according to location within component. Logarithmic functions (based on experimental observation) such as that of Kodama [96] (Equation 2-6) are

valid after the initial quasi static relaxation; however, it is typically this first relaxation which is most significant in components. A new model for the ratio of residual stress after *N* cycles, σ_{rsN}, to initial residual stress, σ_{rs0}, was developed [94] (Equation 2-7) which was able to account for both quasi static relaxation and logarithmic softening and which was dependent on stress amplitude σ_a, R_σ and number of cycles *N* as the controlling parameters.

$$\frac{\sigma_{mN}}{\sigma_{m1}} = \frac{\sigma^0 - \sigma_a}{\sigma_{m1}} - \left(\frac{\sigma_a}{\sigma^0}\right)^{b_1} \log N \quad (2\text{- }5)$$

$$\sigma_{rsN} = A_1 + m_1 \log N \quad (2\text{- }6)$$

$$\frac{\sigma_{rsN}}{|\sigma_{rs0}|} = A_2 \left(\frac{2{\sigma_a}^2}{(1-R_\sigma)(C_w\sigma^0)^2}\right)^{m_2} (N-1)^{B_1} - 1 \quad (2\text{- }7)$$

The inclusion of degree of cold work C_w, material yield strength σ^0 and *m* (dependent on material stress strain response) allows for the Bauschinger effect. Some fitting to experimental data (for example in constants $A_{1,2}$ and $m_{1,2}$ (both dependent on cyclic stress strain response) and B_1 (relaxation rate with number of cycles)) is required. Nonetheless the model was able to predict the initial stress relaxation well, although as the number of cycles increased, the results diverged slightly from the FE results with which they were compared. Given that the most significant residual stress relaxation is usually the quasi-static contribution, this model can be successfully applied, particularly in materials that show limited changes in their stress-strain response after cycling. The application of FE methods to predict residual stress relaxation described in this work [94] was a significant contribution in its own right given the manner in which material properties were allowed to vary near the surface to account for yield strength changes with cold work and the non-linear isotropic/kinematic hardening model which was applied to allow for the Bauschinger Effect in order to predict residual stress relaxation with cycling. These FE approaches are discussed further in Section 2.2.3.2. Without further validation against experimental data, however, the model should be applied to real components with caution.

More recent analytical models for residual stress relaxation have been developed by Liu and Yuan [97]. Mechanically induced variations in residual stress caused by shot peening were described by three sets of differential equations which were solved using mathematical representations of residual stress and plastic strain as an input. Whilst this method was shown to be acceptable for turbine rotor design, the assumption that the cyclic mechanical load was in elastic shakedown meant no plastic hysteresis in cyclic loading and thus only first cycle relaxation was considered. Benedetti *et al.* [98] also applied a simple analytical system which was able to predict the quasi-static stabilisation of shot peening residual stresses reasonably well at the surface when

compared with FE results. They used a bilinear kinematic hardening law for stabilised cyclic stress-strain behaviour and like Liu and Yuan [97] made the assumption that cyclic loading is elastic and only the first load cycle results in plastic deformation. The results for low intensity peening processes and results beneath the surface were less satisfactory, although for application in total lifing approaches where only surface stabilised stresses are required, the method could be applied quite effectively.

There are numerous experimental investigations (typically implementing the XRD residual stress measurement technique) which have demonstrated this mechanical relaxation effect in shot peened components. The stress relaxation in un-notched samples of shot peened Udimet 720Li loaded axially at strain ratio $R_\varepsilon = 0$ (corresponding to a negative load ratio) has been reported [15, 22]. Two strain ranges, $\Delta\varepsilon$, were applied, 0.6 % representing service loads and 1.2 % representing an overload. Temperature was varied from 350 ˚C to 725 ˚C; typical operating temperatures would be expected to be 600 to 700 ˚C.

There was a clear step change in residual stress after the first cycle; this is illustrated in Figure 2- 12, followed by logarithmic through life relaxation. In the 350 ˚C data presented in Figure 2- 12 there is some apparent recovery of residual stresses between 30 and 1000 cycles, however the higher the fatigue temperature, the greater the logarithmic relaxation with increasing fatigue cycles. It is clear from the data presented that there is more significant relaxation in the direction parallel to loading than that which is perpendicular; this effect has also been reported in Holzapfel *et al.* [55].

Perhaps a comparison more relevant to service is that after 10,000 cycles at $\Delta\varepsilon = 0.6$ % and constant 700 ˚C temperature, the peak in plane compressive residual stress had relaxed to 50 % of its initial value. In the event of a single overload cycle to $\Delta\varepsilon = 1.2$ % at the same temperature, the residual stress was relaxed to less than 50 % of its initial value. The effect of possible overload events in service on residual stress distributions must not be overlooked in remnant life calculations.

Residual stress relaxation has also been demonstrated in aluminium alloy samples of un-notched cross section under four point bend load ($\sigma_a / \sigma^0 = 0.5$) at $R_\sigma = 0.1$ by Benedetti *et al.* [24]. The largest relaxation to approximately 80 % of initial maximum compressive stress value was observed within the first 1000 cycles, although no data specific to the first cycle was reported. Benedetti *et al.* also extended their investigation [5] to LCF under fully reversed bend loading, $R_\sigma = -1$, and showed similar relaxation in surface residual stress to that which was reported in the initial case in a different aluminium alloy but tested at the same σ_a / σ^0 ratio [24].

Bergström and Ericsson [26] have considered stress relaxation parallel and perpendicular to load in notched (stress concentration factor, $K_t = 1.75$) samples axially

loaded under varying load conditions. When load ratio R_p = -1 both parallel and perpendicular residual stresses relaxed at all globally applied stresses (σ_a / σ^0 = 0.35, 0.37 and 0.46); relaxation was slightly greater in the parallel direction. When R_p = 0, the relaxation in the surface residual stress in the parallel direction was no longer present, although the perpendicular stresses did still relax (albeit to a slightly lesser degree than when R_p = -1, this is in agreement with the predictions of Equation 2-7). Unfortunately, there was no detailed consideration of the subsurface residual stress profiles or the local stress distributions resulting from the applied loads and so the mechanism by which this retention in residual stress occurs is unclear. Whilst it could be postulated that under R_p = 0 load the yield stress was never exceeded in the loading direction and it is possible that in the perpendicular direction Poisson's ratio effects summed with compressive residual stresses meant that yield was exceeded in compression, the lack of loading stress distribution data prevents confirmation of this mechanism. This work is, however, noteworthy as it provokes an interesting question: how do the residual stress distributions interact with the specific applied loading conditions and are there certain combinations in which the residual stresses do not relax, allowing the maintenance of shot peening benefit to high applied stress?

It should be noted that in the majority of the work cited by McClung [18], relaxation is considered in un-notched, axially loaded samples. Some of the experimental work discussed earlier has gone some way towards considering geometrically more complex samples [26] or other loading conditions [5, 24, 99] but as yet there has not been an experimental investigation into the interaction between the two with a discussion in the light of the applied stress directionality as influenced by the stress concentration feature. This type of interaction is typical of those found in service and an investigation into these effects is required.

Meguid *et al.* [93] extended the symmetry cell modelling of the shot peening process discussed previously in Section 2.1.2.1 to consider the effect of subsequent thermomechanical loading on a target component using FE modelling. Despite the perhaps inappropriate isotropically hardening strain rate sensitive material model, it was shown that mechanical relaxation effects could be well represented by comparison with experimental data [55]. This material model was selected as it was deemed most appropriate for the initial shot peening simulation; when a kinematic hardening model was applied, at R_σ = -1, the predicted residual stress relaxation was greater and progressive, as a result of allowance for the Bauschinger Effect. The most significant result of this paper was the demonstration of the strong interaction effect between mechanical and thermal loading, especially when they are in phase (such that the high tensile loads correspond to high temperature and thus low yield stress). It is for this

reason that the individual effects of mechanical strain and thermal strain cannot be summed in thermo-mechanical fatigue and synergistic effects must be considered.

The variation in XRD FWHM with fatigue cycling has also been reported. 1.2 % strain range fatigue at 350 ˚C (the lowest temperature investigated) in Udimet 720Li resulted in no significant variation in the peak widths (Figure 2- 13a) [15, 22]. Given the lack of grain size variation resulting from the shot peening process (determined using EBSD), it was concluded that there was no change in the cold work levels / dislocation distribution with fatigue cycling. It was found that at temperatures more representative of service conditions (reaching 700 ˚C), there was a progressive decrease in peak width and that as for residual stresses there was a strong interaction effect between fatigue cycling and thermal exposure (Figure 2- 13b). This tends to indicate a reduction in dislocation density through recovery processes (dislocation redistribution and annihilation) in the near surface region and thus a reduction in any benefits obtained as a result of the increased yield strength in this region.

Dalaei *et al.* [23, 31] have also reported on the development of surface FWHM in pearlitic steel with increasing numbers of fatigue cycles at varying total strain amplitudes. Axial fully reversed fatigue testing was carried out at room temperature on un-notched samples. At $\Delta\varepsilon$ = 1.2 %, the surface absolute FWHM decreased from 3.3˚ to 2.3˚ after the first 1000 cycles showing an approximately logarithmic trend. Given a strain free baseline value of 2˚ (the stabilised value measured at the core of the sample was assumed to be strain free), this corresponded to an almost total reduction in surface strain hardening. Smaller logarithmic reductions in FWHM and residual stress occurred in samples cycled at lower strain amplitudes. This logarithmic trend means that the largest change occurs over the first few cycles, but the reduction in FWHM continues throughout the life.

This reduction in FWHM is also reported by Bathias *et al.* [99] after LCF of aluminium samples under three point bend R_p = 0.1. Whilst there was a clear reduction in FWHM in an apparently linear manner, since only four data points were presented for each material studied and the total drop in peak width was relatively small it is hard to draw firm conclusions as to the nature of the relationship between FWHM and number of cycles from this work. Given the logarithmic trend reported by Dalaei *et al.* [23, 31] and the logarithmic through life residual stress relaxation discussed previously, a logarithmic trend should be expected. Indeed this logarithmic relationship is reflected in the exponential dependence of yield stress on equivalent plastic strain accumulation in the isotropic contribution in combined isotropic and kinematic hardening material models [53]. Hence reductions in FWHM are strongly related to the specific cyclic behaviour of the material in question, and as such it is hard to extrapolate results from one material system to another; if cyclic material properties are to be considered in a

FE model, they should be validated against experimental data for the specific alloy in question.

Thus it can be summarised that the degree of relaxation in residual stress and strain hardening is a complex relationship between component geometry and specific loading mechanism. This is a key consideration in analysis of components with complex geometries under complex loading conditions, many such components were detailed in Table 2- 1. Furthermore, the importance of substrate material properties and the interaction of strain hardening from the shot peening process and through life cyclic hardening or softening behaviour of the material must not be overlooked.

2.1.4. Summary

Shot peening is a cold work process which results in significant changes to the surface layers of a component. Modifications to surface roughness and the generation of strain hardening and residual stress profiles all have an effect on the fatigue life of a component and thus are important considerations in life assessments.

The first issue which must be addressed in a life assessment which includes shot peening effects is the determination of the surface roughness, strain hardening and residual stress profiles since they may all be required as inputs to the procedure. The surface roughness can be readily measured using optical or tactile instruments. Experimental techniques for defining residual stress profiles are also well developed, although the complete profile is rarely determined, making the application of this data in life assessment challenging. Whilst analytical and finite element models can be used to alleviate this problem, there are concomitant issues with the modelling approach, including the definition of the materials constitutive model and the physical approach which is taken, both of which can have significant effects on the residual stress profile which results from the model. Strain hardening data is less readily available and can be experimentally approximated using microhardness traverses, XRD FWHM profiles and EBSD local misorientation measurements. However, the lack of consistency in results between methods has raised questions as to which method is most appropriate. Clearly before this data can be reliably applied in a structural integrity analysis a validated method must be accepted by the scientific community.

The effect of the shot peening process on fatigue is well understood, particularly in the HCF regime. Surface roughness accelerates initiation, although this effect is insignificant compared with the deceleration in initiation caused by strain hardening. There is some debate as to the role of strain hardening in crack propagation, however compressive residual stresses retard crack propagation and are the dominant effect in this regime. Shot peening is generally considered to be less beneficial in the LCF

regime; this is a result of the high applied stresses which can cause the residual stresses generated in the component to relax and the dislocations in the strain hardened region to recover causing a drop in strain hardening. The important consideration is how the residual and applied stress fields interact, not only is this required in assessing any potential sub-surface initiation, but it is also needed to assess the way in which the residual stresses might relax. This relaxation is also affected by high temperatures which increase the rate of recovery of dislocations in the near surface region and reduce the yield stress of the material, also making mechanical relaxation more likely. Changes in the residual stress distribution are not only affected by service conditions, but also by the material's cyclic stress strain characteristics, an effect that must not be overlooked in materials which exhibit cyclic softening.

2.2. Approaches to fatigue lifing after shot peening

2.2.1. Introduction

The focus of the first part of the review in Section 2.1 was not only on describing the physical mechanisms for the differences in fatigue lives, but also in explaining why they can lead to complications when trying to account for the effects of the shot peening process in mechanistic life assessment. These difficulties can be summarised as follows:

- Applying simplifying assumptions to the surface roughness profile and identifying situations in which surface roughness has a significant effect on fatigue life when compared with the effect of residual stresses and strain hardening.
- Accurately determining residual stress and strain hardening profiles resulting from shot peening.
- Considering the interaction between start of life residual stresses and cold work profiles and applied stress distributions in service as influenced by material cyclic hardening and softening characteristics and service temperatures.

This second part of the review considers the approaches which have been applied in allowing for these considerations when lifing shot peened components. Interest in these approaches is currently increasing, since they allow reduced conservatism compared to the currently applied models (which consider shot peening to be an additional safety factor) whilst maintaining safety margins in structural integrity assessments.

This section begins with an introduction to the classical total life and damage tolerant approaches to fatigue lifing and broad consideration of how they can be applied in

lifing shot peened components. The second part describes the manner in which the dependent variables (such as stress range, $\Delta\sigma$, strain range, $\Delta\varepsilon$ and any fracture mechanics parameters, such as ΔK) required for a life assessment are calculated. The final part discusses the various ways in which shot peening is accounted for in life assessments and considers the way in which the concepts can be applied in practice.

2.2.2. Approaches to determine component life

Traditionally, life assessment methodologies can be distinguished as either total life or damage tolerant in nature. Phenomenological continuum total life approaches characterise damage evolution, crack nucleation and crack growth stages of fatigue life as one parameter, number of cycles to failure, N_f. Damage tolerant approaches on the other hand consider the cycles taken for the growth of an initial defect to a critical size as a function of a crack tip driving parameter, such as stress intensity factor (SIF) range, ΔK, from linear elastic fracture mechanics (LEFM), or the cyclic J-integral, ΔJ, from elastic plastic fracture mechanics (EPFM). The damage tolerant methods discussed in this review use LEFM and thus ΔK as the fracture mechanics variable; as such EPFM are not discussed further in the present review. A combination approach may also be used whereby life to initiation of a defined defect size is summed with the life calculated from a damage tolerant model for propagation of the defect to failure.

2.2.2.1. Total life approaches

Total life methods rely on a relationship between the applied stress range, $\Delta\sigma$, (for HCF, i.e. when $N_f > 1\text{x}10^5$) or the applied strain range, $\Delta\varepsilon$, (for LCF, i.e. when $N_f < 1\text{x}10^5$). If a typical HCF S-N curve is converted to a log-log plot, the Basquin relation (Equation 2-8) [100] can be applied to determine the number of cycles to failure at a given stress amplitude, $\sigma_a = \Delta\sigma/2$. Similarly for a LCF S-N curve converted to a log-log plot, the Coffin Manson relation (Equation 2-9) [101, 102] can be applied using plastic strain range $\Delta\varepsilon_p/2$ as the dependent variable. σ_f' and ε_f' are the fatigue strength and ductility coefficients respectively, b_2 and c_1 are the fatigue strength and ductility exponents respectively; all require fitting to experimental data.

$$\frac{\Delta\sigma}{2} = \sigma_f'\left(2N_f\right)^{b_2} \tag{2- 8}$$

$$\frac{\Delta\varepsilon_p}{2} = \varepsilon_f'\left(2N_f\right)^{c_1} \tag{2- 9}$$

Residual stresses can alter the mean stress about which the fatigue cycle takes place. The dependence of fatigue life on mean stress, σ_m, is well recognised, hence when applying these approaches it is essential to take mean stress effects into consideration. For the HCF stress life approach, this correction often takes the form of a Goodman

[103] or Gerber [104] correction (Equations 2-10 and 2-11 respectively) and is dependent on the ratio of mean stress to ultimate tensile strength, σ_{uts}. For the LCF strain life approach a common correction is that after Smith Watson and Topper (SWT) (Equation 2-12) [105] in which the effect of the maximum stress, σ_{max}, is considered. E is the elastic modulus of the material.

$$\frac{\Delta\sigma}{2} = \frac{\Delta\sigma}{2}\Big|_{\sigma_m=0}\left\{1 - \frac{\sigma_m}{\sigma_{UTS}}\right\} \quad (2\text{-}10)$$

$$\frac{\Delta\sigma}{2} = \frac{\Delta\sigma}{2}\Big|_{\sigma_m=0}\left\{1 - \left(\frac{\sigma_m}{\sigma_{UTS}}\right)^2\right\} \quad (2\text{-}11)$$

$$\sigma_{max}\frac{\Delta\varepsilon}{2} = \frac{{\sigma_f'}^2}{E}\left(2N_f\right)^{2b_2} + \sigma_f'\varepsilon_f'\left(2N_f\right)^{b_2+c_1} \quad (2\text{-}12)$$

In components of complex geometry under operational loading, it is unlikely that the stress and strain range will be constant across the component. Total life methods can include both 'hot spot' and critical distance approaches. The former relates the fatigue life to the stress or strain range at a critical point on the component, typically at the surface near a geometrical stress concentrating feature. The critical distance method is well introduced by Taylor [106] and is most commonly applied to regions of stress concentration. A length scale is introduced which can be used within continuum mechanics models; in fatigue this is commonly defined by Equation 2-13 [107]. Typically, the length L is at the centre of the transition on a Kitagawa-Takahashi diagram [108] between LEFM behaviour exhibited by long cracks and small crack behaviour; hence L is dependent on the threshold SIF range, ΔK_{th} and the fatigue endurance limit, $\Delta\sigma_e$. More physically, L is defined as the critical crack size at which the threshold SIF is equal to that of long cracks [107].

$$L = \frac{1}{\pi}\left(\frac{\Delta K_{th}}{\Delta\sigma_e}\right)^2 \quad (2\text{-}13)$$

Since the residual stress profile is biaxial in nature, in certain situations (depending on the operational loads), it may be more appropriate to apply total life multiaxial fatigue life criteria to shot peened components. The multiaxial fatigue lifing problem is certainly non-trivial and the approaches relevant to the present review are introduced only very briefly here; further information on multiaxial methods can be obtained from texts such as ESIS Publication 31 [109] or the recent overview by Fatemi and Shamsaei [110]. The Crossland Criterion (Equation 2-14) [111] and Sines criterion (Equation 2-15) [112] are both examples of stress based multiaxial approaches which may be applied to shot peened components. J_{2a} is the 2nd invariant of the deviatoric stress tensor and represents octahedral shear stress amplitude (related to von Mises stress amplitude, $\sigma_{VM,a}$); the maximum hydrostatic stress, $\sigma_{H,max}$ (in Crossland) or the mean hydrostatic stress, $\sigma_{H,m}$(in Sines) allow for consideration of mean stress effects.

$$\sqrt{J_{2a}} + \alpha_c \sigma_{H,max} \leq \beta_c \quad \text{where} \quad \alpha_c = \frac{3\tau_{c,-1}}{\sigma_{B,-1}} - \sqrt{3} \quad \text{and} \quad \beta_c = \tau_{c,-1} \tag{2- 14}$$

$$\sqrt{J_{2a}} + \alpha_c \sigma_{H,m} \leq \beta_c \quad \text{where} \quad \alpha_c = \frac{3\tau_{c,-1}}{\sigma_{B,0}} - \sqrt{3} \quad \text{and} \quad \beta_c = \tau_{c,-1} \tag{2- 15}$$

Where $\sigma_{B,-1}$ is the endurance limit under fully reversed bending, $\sigma_{B,0}$ is the endurance limit from a zero to tension bending test and $\tau_{c,-1}$ is the endurance limit measured from a fully reversed cyclic torsion test.

It should be noted that the aforementioned stress based multiaxial criteria are most commonly applied to HCF problems; strain based criteria are generally considered more appropriate for LCF. Some, such as the Smith-Watson-Topper stress-strain critical plane model [105] also allow consideration of mean stress effects.

2.2.2.2. Damage tolerant approaches

Whilst total life methods can allow comparative studies in simple test sample geometries, they cannot be applied to more complex geometries without extensive experimental studies for each component. Furthermore, they do not allow for consideration of components which contain a crack, or indeed consideration of a defect which is too small to be detected by non-destructive testing (NDT); both these cases make damage tolerant assessment more attractive to the assessment of remnant life of components in service.

Damage tolerant approaches consider the number of cycles taken for the growth of an initial defect to a critical size (i.e. propagation life) and overcome the geometry dependence issues associated with total life approaches. The approach characterises a material's crack growth behaviour, typically in terms of ΔK (Figure 2- 14). ΔK is a useful parameter because it shows similitude, that is, for two differently sized cracks under the same stress intensity, the crack tip plastic zones are equal in size with equal stress and strain distributions along the borders. Most commonly, damage tolerant approaches consider growth from an initial crack length (commonly taken from NDT, sometimes defined as L and sometimes taken from a strain life to initiation approach) to a critical crack length (typically defined by use of a failure assessment diagram, as described by R6 [113] and BS7910 [114], which combines plastic collapse and fast fracture criteria) in region B of Figure 2- 14 where crack growth is stable (Stage II) and can be described by the traditional Paris Law (Equation 2-16) [115, 116].

$$\frac{\mathrm{d}a}{\mathrm{d}N} = C(\Delta K)^m \tag{2- 16}$$

It is possible to extend Equation 2-16 to account for region A in Figure 2- 14 where the average crack increment per cycle is microstructurally dependent (Stage I) and less

than the lattice spacing of the material, tending towards the threshold stress intensity factor, ΔK_{th} (Equation 2-17) [117]. The constant q_1 is introduced which controls the curvature in the near threshold region of the da/dN vs. ΔK plot. Corrections can also be found which allow for region C; however these do not find much application since the amount of time a crack spends in unstable propagation is relatively small and safety criteria are applied such that the component should never reach this regime.

$$\frac{\mathrm{d}a}{\mathrm{d}N} = C(\Delta K)^m \left(1 - \frac{\Delta K_{th}}{\Delta K}\right)^{q_1} \quad (2\text{-}17)$$

The presence of a mean stress may be considered as an R ratio effect, i.e. the ratio of minimum stress (or strain) to the maximum value is changed. In damage tolerant approaches, this can be considered by replacing ΔK in Equation 2-16 with the effective SIF range, ΔK_{eff}. This effective range is a useful parameter as it allows consideration of any crack closure effects which may be in operation.

The crack closure phenomenon occurs when the crack faces touch under tensile far field applied loads; the crack cannot propagate whilst the faces are in contact. This closure occurs at $K_{closure}$. If $K_{closure} > K_{min}$, $\Delta K_{eff} = K_{max} - K_{closure}$, which is less than the apparent SIF range caused by the loading. LEFM assumes that crack growth rates are affected by conditions ahead of the crack tip only (intrinsic effects), however the process of closure implies that the nature of the crack faces behind the tip also influence propagation (extrinsic effects). There are several mechanisms of closure, including plasticity, oxide and roughness induced mechanisms. Closure is generally more significant at low ΔK and low R ratios due to the lower minimum crack opening displacement

It is noted that there is an alternative means of representing the transient crack growth effects resulting from crack closure, which, it is claimed, account for the effect of R ratio intrinsically without the need to consider the aforementioned extrinsic closure approach and ΔK_{eff}. This two parameter (ΔK and K_{max}) approach has been popularised by Vasudevan and co-workers (see for example [118]); K_{max} is influenced by the internal stresses (which are influenced by the local R ratio) present ahead of the crack tip. It should be emphasised that this two parameter approach has not found its way into industrial standards [119] which are based on ΔK_{eff} and as a result is not discussed further in the present review.

The majority of work which takes crack closure into account is based on finite element calculations of $\Delta K_{eff.}$ However, it is worth mentioning that there are analytical models available for small crack growth which account for closure, such as Newman's FASTRAN (based on a modified Dugdale model for plastic zone size with a modification

to allow plastically deformed material to remain in the crack wake) which allow for consideration of crack closure in simple geometries [120].

2.2.2.3. Approaches to fatigue lifing after shot peening

Sections 2.2.2.1 and 2.2.2.2 considered the basics of fatigue life assessment; in particular the dependent variables for each approach to fatigue life modelling were introduced. Clearly one of the keys to the accurate lifing of a component is the successful determination of these variables. When lifing a shot peened component, the surface roughness, compressive residual stresses and strain must also be accounted for. The remainder of this second part of the review considers the manner in which the standard fatigue lifing methodologies can be adapted to allow for the shot peening process, and how these approaches could find application in industrial practice.

An attempt is made here to group the various approaches which have been taken to lifing shot peened components into method a and method b:

a. Use a fatigue lifing protocol in the standard form as introduced in Sections 2.2.2.1 and 2.2.2.2, but modify the way in which the dependent variables such as stress range, $\Delta\sigma$, and strain range, $\Delta\varepsilon$, and any associated fracture mechanics parameters such as ΔK are calculated so that the effects of the shot peening process are accounted for. This is most typically achieved through modifications to the FE approach applied, but for simple geometries weight functions and superposition methods may be appropriate.

b. Modify the fatigue lifing protocols such that the residual stresses, strain hardening and surface roughness are explicitly accounted for in the lifing equation. This method requires no adjustment to the manner in which input variables such as $\Delta\sigma$, $\Delta\varepsilon$ and ΔK are calculated.

Within these two broad umbrella groups, there are numerous approaches which are tailored to focus on different aspects of the shot peening effect depending on the specific requirements of the analysis in question. Not only must the analyst select the type of fatigue lifing approach (total life or damage tolerant) but they must also decide which of roughness, residual stress and strain hardening effects must be included in the analysis. Clearly there is a trade-off here between accuracy and complexity. These required decisions reflect the interactions between start of life residual stresses and cold work profiles, service conditions (HCF/LCF mechanical loads and temperatures) and material properties which were introduced in detail in Section 2.1.3.2.

The remainder of this section is structured such that in Section 2.2.3 the different approaches to determining the dependent variables are introduced. The focus of this section is on how the shot peening process effects can be incorporated in these calculations (method a) and the results applied in remnant life analysis. In Section 2.2.4, modifications to the previously introduced fatigue life calculations which allow the use of standard dependent variable calculations are considered (method b). Section 2.2.5 goes on to compare and contrast the results of the two approaches and consider how the approaches could be applied in practice.

2.2.3. Approaches to determine parameters for application in fatigue life models

At this juncture, it is assumed that the reader is already familiar with the principals of stress analysis and as such the focus here is on how the effects of surface roughness, residual stress and strain hardening can be considered. There have been several approaches applied including simple superposition and analytical methods to take account of residual stresses when determining the applied $\Delta\sigma$ or ΔK (which may require the application of weight functions), through to complex FE models which can account for residual stress and strain hardening distributions and complex material constitutive behaviour.

2.2.3.1. Analytical methods

The simplest formulation by which residual stresses can be accounted for in determining the relevant $\Delta\sigma$ and ΔK is the application of the principal of superposition. These principles are well introduced by Webster and Ezeilo [81]. This approach is only suitable for application in HCF cases where the residual stresses present at the start of life are not affected by the operating environment (i.e. low temperature applications). When R ratio effects are important, such as when considering the effect of mean stress on total life, Equation 2-18 for effective R ratio can be applied. Local stresses and strains (using an appropriate constitutive model) or SIFs can be simply calculated from the principal of superposition. If the mean stress is also calculated, it can be used in conjunction with the Goodman or Gerber (Equations 2-10 and 2-11) corrections.

$$R_{eff} = \frac{K_{min}+K_{rs}}{K_{max}+K_{rs}} = \frac{\sigma_{max}+\sigma_{rs}}{\sigma_{max}+\sigma_{rs}} \quad (2\text{-}18)$$

In their early work, Benedetti *et al.* [5, 24] use the principal of superposition of surface residual stresses on applied stresses and the resulting effect on mean stress in combination with Sines criterion (Equation 2-15) in predicting the fatigue life of test samples of relatively simple geometry. Allowance for the effect of surface roughness

on applied stresses was made by way of an elastic stress concentration factor, K_t. This was based on the work of Li *et al*. [121] which is summarised in Figure 2- 15.

Whilst it was found that within certain regimes the life could be well predicted (provided initiation occurred at the sample surface), it was found that at long life times, the fatigue life was underpredicted. It was suggested that in such situations (where strain hardening may have a significant effect, for example on initiation), a modelling approach which explicitly accounts for the effects of strain hardening may be more appropriate.

As discussed in Section 2.2.2.2, it is ΔK_{eff} which is often considered most appropriate for use in damage tolerant crack growth laws. In this case it is Equation 2-19 which is applied. Residual stresses affect the closure SIF, $K_{closure.}$.

$$\Delta K_{eff} = K_{max} - K_{closure} \qquad (2\text{-}19)$$

Xiang and Liu [117] presented a model based on LEFM calculations (for short and long cracks in notches [122]) of ΔK in components for which the geometry correction factor, Y, was known. The method was extended to allow for plastic deformation in LCF by using a cyclic-reversed plastic zone concept where the equivalent crack length is equal to the crack length plus the plastic zone size calculated using dislocation theory, r_ρ (Equation 2-20).

$$\Delta K_I = \mathrm{f}\left(\frac{a}{W}\right)\Delta\sigma\sqrt{\pi\left(a + r_\rho\right)} \quad \text{where} \quad r_\rho = a\left(\sec\frac{\pi\sigma_{max}(1-R_\sigma)}{4\sigma_{UTS}} - 1\right) \qquad (2\text{-}20)$$

The stress used when calculating $\Delta\sigma$ (and hence ΔK) and R_σ through life was allowed to relax as the number of cycles increased in accordance with the residual stress relaxation law described in Equation 2-6, although this law was noted to lack the capability of predicting initial quasi-static relaxation and so is less reliable for LCF applications. One of the other drawbacks of this approach is the inability to consider the effect of strain hardening, although allowance for surface roughness stress concentration effects in the calculation of applied $\Delta\sigma$ for short cracks was made in accordance with Figure 2- 15.

The damage tolerant lifing approach described by Equation 2-17 was modified so that C was replaced by $gb_3{}^{R\sigma}$ in order to take account of the R_σ ratio effects caused by the mean stress effects resulting from shot peening. Whilst this may be considered to be a modification to a lifing approach in order to take account of the shot peening process, and as such might be considered to be method b, this is actually considered to be a more general modification to the fatigue lifing approach, to allow for R_σ ratio effects, with specific allowances for the shot peening residual stress and surface roughness

effects made in the calculation method for $\Delta\sigma$ and R_σ. Hence this method's inclusion in this section as a method a approach.

The two fitting parameters, g and b_3 can be obtained from experimental data at varying R_σ. This approach did not require an initiation life, but instead considered the initial flaw size to be equivalent to L (Equation 2-13). Whilst relatively good life predictions were made in the HCF regime, results in the LCF regime were not so closely matched, perhaps a result of the combination of a greater than predicted residual stress relaxation in the first cycle and the relatively simple treatment of plasticity in long crack solutions.

This approach was nonetheless a useful contribution as it demonstrated both a means of considering residual stress relaxation and the resulting effect on R_σ through life, and surface roughness effects on short crack ΔK. However, the lack of consideration of strain hardening effects should not be overlooked and the use of $gb_3{}^{R_\sigma}$ rather than ΔK_{eff} may be considered to be a relatively simple and more empirical treatment of mean stress and possible crack closure effects.

Whilst it is often the case that applied stress distributions can be calculated in relatively simple geometries under relatively simple load conditions using analytical approaches, there are significantly fewer cases for which K can be calculated analytically. In these cases, the first alternative approach which is usually considered is a weight function method [123]. These methods are typically applied when complex geometrical and stress distributions exist such that stress intensity handbook solutions have not been derived. The basic premise of the method is that the weight function, m(a,x) (which depends only on component and crack geometry and can be taken from handbooks such as that of Wu and Carlsson [124]) is multiplied by the stress distribution along the prospective crack $\sigma(x)$ and integrated along the crack length in accordance with Equation 2-21. Thus for a given cracked body, the SIF due to any load distribution can be determined from the same weight function rather than deriving a new direct SIF solution for each internal stress distribution. These methods are particularly attractive in that they allow the computation of SIFs in relatively complex engineering structures without the requirement of a complex FE analysis of a cracked component.

$$K = \int_0^a \sigma(x)\mathrm{m}(a,x)\mathrm{d}x \qquad (2\text{-}21)$$

Knott *et al*. [125] used the weight function method to determine the 'negative ΔK' induced by shot peening cast aluminium samples. The principle of the approach is illustrated in the schematic Figure 2- 16. The defect length used in the analysis corresponded with the experimentally measured upper and lower bounds of initiation

defect (shrinkage cavity) size. The uniform compressive residual stress which resulted in the same 'negative ΔK' (as calculated using weight functions) was then determined ($\Delta\sigma_{rs,eq}$). It was found that the equivalent uniform compressive stress was approximately equal to the increase in stress range required for failure at a given number of cycles in the HCF regime; the effect was particularly clear in the endurance limit values. This fatigue endurance increase could be used in total life component design quite successfully, provided the data on its magnitude is sufficiently statistically significant. Alternatively, under HCF where an estimation in the change of local fatigue strength, or endurance limit, is required, the approach described by Winderlich [126] can be applied. A crack is only initiated if the local stress under load exceeds the local fatigue strength which is a function of the fatigue strength in the ground state, the local hardness (correlated to changes in local material properties), normalized stress gradient and the residual stress profile. Whilst this approach was originally developed for laser hardening, it has also found application in shot peened components [127].

Weight function methods are useful in that they allow the separate calculation of applied and residual stress contributions to SIFs before superposition to determine the resultant SIF. Another example of the approach is described by Gao and Wu [83] for single edge notch tension (SENT) samples. Small crack growth data was obtained by a replica technique in peened and unpeened samples and the results compared, showing, as expected, significantly slower crack propagation in peened samples for a > 80 µm. The data was considered in terms of the da/dN vs. ΔK curve and compared with long crack data. Without considering the SIF resulting from residual stresses, the crack growth rate results for short cracks in shot peened samples lay uncharacteristically to the right of the LEFM baseline. By incorporating residual stress effects into the ΔK calculation, the data was moved to the left of the baseline, where short crack data would be expected to lie. For the simple geometry under consideration, it was possible to calculate the damage tolerant fatigue life (assuming an initial defect of 0.02 mm) using the FASTRAN approach with considerable accuracy (Figure 2- 17).

However, whilst these results seem attractive, the shortcomings of this approach must not be overlooked. The FASTRAN method was developed for only a couple of specific geometries and represents a simpler representation of stress strain and displacement fields than can be achieved using a FE approach (although FE methods are not without mesh related complexities) [120]. Furthermore, weight functions would be difficult to apply for complex stress fields in components of complex geometry and the approach is unable to account for the effect of varying materials properties in the near surface region resulting from strain hardening distributions or for the effects of surface roughness.

2.2.3.2. Finite element methods

FE modelling is commonly applied in structural integrity assessments in order to facilitate the determination of the stress and strain distributions within a component under given loading conditions. Thus it is desirable to be able to make consideration of the shot peening effects using this tool. This modelling approach has the benefit of being able to account for residual stresses through incorporating them into the model. This can be achieved in two ways:

- Residual stresses can be directly imported as initial conditions [35]. This requires a precise knowledge of the complete residual stress field. Since this is seldom the case, particularly for experimental data in thick components (Section 2.1.2.1), it is not uncommon to require an iterative procedure so that the residual stresses obtained after the equilibration step are those required at the start of component life and which are representative of both the compressive residual stresses and balancing tensile residual stresses in the component [128].

- A more commonly applied approach is that which makes use of the concept of eigenstrains, an approach which was developed and applied in the works of Korsunsky *et al.* [90, 129-131], and also applied in the works of Cláudio *et al.* [132-135] and Benedetti *et al.* [57, 136]. This approach is based upon the premise that it is the presence of near surface eigenstrains (mis-fit strains) which cause residual stresses. The 'inverse eigenstrain method' can be used to generate the required residual stress field (typically measured experimentally as described in Section 2.1.2.1) in a FE model:

  The plastic strain resulting from a given shot peening process can be estimated using one of the approaches outlined in Section 2.1.2.2. This is applied to a FE model of the sample in which the residual stress was determined by specifying plastic strain as a function of distance from the shot peened surface (most commonly achieved by using a temperature distribution and setting appropriate coefficients of thermal expansion). After performing an equilibration step, the model can be interrogated for the residual stress distribution near the shot peened surface; the process is iterated until the specified plastic strain profile results in the correct residual stress distribution.

  The advantage of this approach is that it is geometry independent [130, 137]; that is the residual stress can be measured on a simple geometry and the required eigenstrain profile developed based on this geometry. The eigenstrain profile can then be imported into components of any geometry and upon

performing an equilibration step before the start of an FE analysis, the residual stress profile specific to that geometry is obtained.

One of the key benefits of using a FE approach is the ability to take plasticity effects into consideration. However, as discussed in Section 2.1.2.1, in order to achieve this, it is essential that the correct material model is selected for the component. There are two approaches that can be applied, the applicability of which depend upon the material cyclic hardening/softening characteristics. The first (i.) uses a combined isotropic and kinematic hardening material model which allows stabilisation of the hysteresis loops through application of many loading cycles and then considers the local stresses and strains [90, 132]; this will be able to capture any initial quasi-static residual stress relaxation and subsequent logarithmic behaviour. The second material model (ii.) uses kinematic hardening only, based on the stabilised hysteresis loops, in this case, just one load cycle is required to analyse the stress and strain distributions [57, 136].

Another advantage of the FE approach is the ability to include strain hardening effects as a variation in material properties with distance from the shot peened surface. Benedetti *et al.* [57, 136] describe a methodology for including material property variations in FE models. Microhardness depth profiles of shot peened samples were converted to cyclic yield strength by comparison with the microhardness of the axial fatigue samples used to determine the cyclic stress-strain curve. This information was used to scale the cyclic stress strain curve at each depth so that the elastic regime extended to the calibrated yield stress and the hardening curve was appropriately shifted in order to compensate the offset due to residual deformation. The temperature distribution used to define residual stresses was used to achieve this by specifying the hardening coefficients as temperature dependent. In the work of Song *et al.* [90] (where a more complex combined hardening model was applied), the variation in material properties with distance from the component surface was accounted for by using a linear relationship between the backstress (kinematic hardening) and plastic strain.

i. Combined isotropic and kinematic hardening models

Although the work of Song *et al*. [90] does not make specific attempts to predict the life of shot peened samples, the correlation between changes in the eigenstrain profile in a FE model employing combined hardening and changes in the residual stress profile measured (in-situ synchrotron XRD) in an identically step loaded LCF test sample shown in Figure 2- 18 demonstrates the capability of the eigenstrain technique and combined material models in predicting through life changes to the plastic strain and residual stress profiles resulting from shot peening. At 0.33 % applied compressive

strain, the plastic strain peak originally determined by the inverse eigenstrain technique was flattened slightly (Figure 2- 18a); this corresponded with a reduction in compressive residual elastic strain (~ residual stress) at 0.3 % strain in the experimental data (Figure 2- 18b). Continuing to increase the applied strain resulted in further reductions in residual plastic strain.

Cláudio *et al*. [132] used finite element modelling with combined hardening to present a comparison of hot spot and critical distance line methods in predicting the LCF life of notched 'washer specimens'. The line method was applied, this requires the averaging of the stress, strain or fracture mechanics variable along a line away from the notch equal in length to 2*L* for use in conjunction with total life methods. Whilst in shot peened components, critical distance methods were shown to be better than hot spot methods, the predicted life was still less than half the experimental value. This unacceptably high conservatism is a result of the high residual stress gradients imposed near the component surface and is clearly illustrated in Figure 2- 19 using stress life methods (and Goodman mean stress correction). Whilst the strain life methods (and SWT mean stress correction) show similar results for un-peened components to stress life methods, once shot peening is applied and considered in the model, the predicted life falls a long way below the desired experimental life = numerical life line. The best results were obtained in unpeened samples using an equivalent strain energy line method; this method also gave the best results for the shot peened samples, although results were still conservative.

However, as discussed previously, damage tolerant methods are much more attractive than total life methods. ΔK_{eff} calculated by FE methods has been used to successfully predict non-propagating cracks in shot peened components at depths which have been shown to correspond to those observed experimentally [35, 133].

Cláudio *et al*. [134, 135] have modified their approach to use a combined strain life to initiation (based on Equation 2-12) model and crack propagation (short and long crack solutions [122] based on ΔK_{eff}) to failure model using the same modified FE approach as was described in their original work [132] for both undamaged [134] and scratch damaged [135] samples. The predicted life for undamaged samples [134] is much closer to the experimental life than was the case with the total life approach described previously; this is shown clearly by comparison of Figure 2- 20 with Figure 2- 19; the combined approach results sit much closer to the desired experimental life = numerical life line. However, some results are now non-conservative illustrating the requirement for appropriate safety factors in component life assessments.

However, as mentioned previously, the key to life prediction in shot peened components is in the means of calculating the dependent variables; despite the

seemingly good prediction of fatigue life, the FE model used throughout the series of Cláudio *et al.* [132-135] to calculate strain range and stress intensity factor data did not consider the effects of roughness or strain hardening on initiation (which in this specific case were deemed to cancel out). Thus whilst this method provided good results in this system, there is no guarantee that it could be easily transferred to another in which, for example, initiation is more dominant.

ii. Kinematic hardening models

In a material which shows little yield surface expansion/contraction, i.e. minimal cyclic hardening/softening (residual stress relaxation is dominated by quasi-static behaviour), using a kinematic only hardening model has been shown to represent residual stress relaxation well in reverse plane bend samples [57] and has the obvious advantage of being less computationally expensive. It is important to remember though that material model selection is a critical modelling decision: in a material with more significant cyclic behaviour, this method may lead to unrepresentative results after many cycles and the combined hardening approach may be required.

Benedetti *et al.* [136] used the Sines criterion (Equation 2-15) in conjunction with a critical distance line method for the prediction of the fatigue life of notched components. The initial and stabilised residual stress fields [57] were compared as the input to the fatigue model, these influence the hydrostatic stress. The formulation of the criterion which allows for reconstruction of S-N behaviour is shown in Equation 2-22 illustrating the dependencies of each parameter. The implementation of the critical line method is clear; it is to be noted that both α and β are dependent on the number of cycles to failure rather than the endurance limits in Equation 2-15 since they are fatigue strengths at a given number of cycles.

The FE method (incorporating residual stresses and strain hardening) was used to determine the applied bending stress amplitude, $\sigma_{i,a}$, and thus the mean applied stress $\sigma_{i,m}$. and stabilised surface residual stresses, $\sigma_{i,srs}$. Clearly an iterative approach was required to solve the equation for $N_{f..}$

$$\frac{1}{2L(2N_f)}\int_0^{2L(N_f)}\left[\sigma_{VM,a}(\sigma_{i,a}) + \alpha(N_f).\sigma_m(\sigma_{i,m},\sigma_{i,srs})\right]\mathrm{d}y = \beta(N_f) \qquad (2\text{-}22)$$

For HCF, the critical distance $L(N_f)$ was assumed to be equal to L given by Equation 2-13. An extrapolation to medium cycle fatigue life was achieved using a power law relationship between the critical distance and the number of cycles to failure; even the author noted that this is heavy simplification due to the significant effect of the cyclic plastic behaviour of the material.

The method [136] was applied with varying degrees of success. In most cases, the error in predicted fatigue endurance was less than 10 %, however, after more intense peening, the fatigue endurance was overpredicted by 20 %. A comparison of the typical predicted fatigue lives and experimental lives is shown in Figure 2- 21. In the sharpest notch of radius 0.5 mm, using the initial surface residual stress distribution as the input parameter overpredicts fatigue life; using the stabilised surface residual stress distribution resulted in better predictions. A similar, though less significant, effect can be seen in the larger radius notch in the LCF regime.

The effect of using an analytical approach to calculate surface stabilised residual stresses rather than a FE approach in conjunction with the Sines criterion method was also considered [98]. It was concluded that whilst the method resulted in slightly worse results, the oversimplification of the Sines criterion in terms of fatigue life prediction was more significant than the simplified value of surface residual stress used, which varied by approximately 25 %. When compared with the variation between initial and stabilised residual stresses (the effect of which can be seen in Figure 2- 21), this resulted in only a small change in the predicted S-N curve. So whilst the FE method must be considered the gold standard, analytical approaches can be applied with a reasonable degree of accuracy.

Whilst these results demonstrate that the finite element approach, in conjunction with the lifing models presented in Section 2.2.2, offers the capability of predicting the life of shot peened components with a considerable degree of accuracy, it is important not to overlook some of the shortcomings of the FE approach which may impact the accuracy of the results in certain situations. Some of these considerations may result in the FE approach discussed previously being unsuitable for a particular engineering system; in these cases it may be more appropriate to select one of the other approaches discussed in this paper.

In damage tolerant models, where ΔK is calculated using J-integral techniques, it is essential that the correct contact condition is applied to prevent one surface penetrating another. Crack face contact can be defined from a contact pressure analysis and can be used to define the $K_{closure}$, allowing effective analysis of ΔK_{eff} for use in crack propagation analyses. It is also essential in these analyses to consider carefully whether a full 3D approach [35] is required (in which case submodelling may be required to achieve sufficient mesh density in the vicinity of the crack) or whether a 2D plane strain approximation [133] is sufficient. One such 2D approximation is shown in Figure 2- 22 illustrating an example mesh required for the fracture mechanics analysis of a crack.

Lei *et al.* [128] consider some issues associated with using the FE fracture mechanics approach: in the presence of residual stresses, the standard *J*-integral definition may become path dependent. To overcome this, the total strain may be considered as the sum of mechanical strain and an initial strain which remains unchanged during mechanical loading. The combined approach was shown to result in path independence for samples mechanically loaded in either four point bending or remote tension except very near the crack tip where meshing errors associated with the stress singularity occur.

The most obvious drawback to an elastic-plastic FE approach is the time consuming nature of the analysis. Additionally, the models are unable to explicitly take the effect of surface roughness into consideration. This may not be considered to be a major problem unless there is very significant residual stress relaxation and significant softening near the surface predicted; if this situation is identified from the model, the stress concentrations caused by surface roughness identified in Figure 2- 15 might be an additional requirement in the analysis.

Other recent work has considered the application of cohesive zone models (CZMs) in the process zone ahead of the crack tip to consider damage evolution under cyclic load [138]. This model was used to consider initiation and crack growth characteristics in simple cracked shot peened samples. Whilst the results show promise, and CZMs have been well developed for monotonic load situations, the application of CZMs to fatigue cracking, let alone fatigue cracking in the presence of residual stresses, is still at an early stage and is not yet advanced enough for application in structural integrity assessments. Furthermore, a means of integrating the models with consideration of surface roughness and strain hardening effects must be developed.

2.2.4. Modification of fatigue life models to account for shot peening

There are a couple of instances in the literature where rather than modify the way in which the dependent variables are calculated (as described previously in Section 2.2.3), the fatigue life equations themselves (introduced in Section 2.2.2) are modified to account for the shot peening process.

The first is described by de los Rios *et al.* [63] and uses three resistances to the applied load: a closure stress at the crack (representing residual stress effects), the material resistance to plastic deformation in the plastic zone (calibrated microhardness profiles were used to represent work hardening effects) and barrier strength at the grain boundary (which can be important for short fatigue cracks at low load where non-propagation can occur). From this, crack tip opening displacement can be determined and used in a modified Paris Law type equation (in terms of crack tip opening

displacement rather than ΔK) as the governing law for crack growth. Whilst this method has shown reasonable correlation in the HCF regime and is able to account for both residual stress and strain hardening effects, it is yet to find widespread application.

Fathallah *et al.* [139] modified the Crossland (Equation 2-14) and the alternative Dang Van (which implements an equation of similar form [140]) multiaxial criteria to account for strain hardening profiles and surface damage by considering the modifications to β_c (as a function of that in unstrained material, β_c^0) rather than by considering the effect through application of finite element models (Equation 2-23) [139]. The strain hardening profiles are accounted for by the ratio of the FWHM at a given depth, *FWHM(z)* to that in unstrained material, $FWHM_0$ and the work hardening exponent, n_m. Surface damage at depth $z = 0$ is accounted for by the variable D_s originally proposed by Lemaitre and Chaboche [53] and which represents the ratio of effective area of cavities to area of intersection of the plane with the representative volume element. When applied to HCF, consideration of residual stress relaxation was not required and thus the simple superposition of the original profile with applied stresses and consideration of the effect on mean stress was sufficient.

$$\beta_c(0) = {\beta_c}^0 \left(\frac{FWHM(0)}{FWHM_0}\right)^{n_m} (1 - D_S) \text{ for } z = 0 \text{ and } \beta_c(z) = {\beta_c}^0 \left(\frac{FWHM(z)}{FWHM_0}\right)^{n_m} \text{ for } z > 0 \quad (2\text{-}23)$$

The approach was used to determine the critical points for fatigue initiation – these were shown to be in keeping with experimental observations. Interestingly, it was concluded in this work that the inclusion of the damage variable was critical to the correct prediction of fatigue behaviour in shot peened parts; this variable has not been implemented in any of the other works reported in this review. Since this work was applied to HCF and more specifically whether shot peening would improve fatigue endurance, there was no attempt to predict the life of components using the method.

2.2.5. Discussion and application

The relative lengths of Sections 2.2.3 and 2.2.4 provide an immediate indicator of the most popular method to date for accounting for the effects of the shot peening process. Since shot peening influences the material properties and component stress state rather than the material fatigue parameters, it seems most physically representative to account for the effect of shot peening in the way the dependent variables are calculated (method a) rather than by modifying the fatigue life law itself (method b).

Damage tolerant analysis dominates industrial component lifing practice. It is beneficial, where possible to avoid having to run a full FE fracture mechanics analysis

for a component as it would be necessary to either run multiple iterations of the model with different defect lengths, or to implement a crack propagation algorithm in FE, which in itself is non-trivial. As a result, industrial practice tends towards the use of FE analysis to assess the stress state caused by loading in an uncracked component and then relies on handbook solutions (either directly, or using weight function methods) for the calculation of *K* to be used in fatigue life estimates [113, 119]. To this end, the weight function approach [83] is an attractive option and should be used where possible to predict shot peened component life; such models should be validated against full fracture mechanics approaches before routine implementation. This validation should be carried out using a defect of varying length to determine *K* as a function of crack length using FE at a critical point in the component; these results can then be compared with those from the weight function method.

The flow diagram shown in Figure 2- 23 illustrates a simplification of the typical component life assessment process and highlights how the effects of shot peening could be incorporated in validated industrial fatigue lifing protocols for shot peened components. The manner by which previous operational data and the proposed duty cycle for the next operational period for the component in question is used in the outage is shown; it should be noted that proposed duty cycles may vary from those applied in practice after the component is put back into service due to variations in operational demand - in this case the life assessment should be reviewed before further operation. The specified service period will vary component to component for example, for low pressure steam turbine blade to disc interfaces the typical required service period before re-inspection for these components is 12 years. A full fracture mechanics approach may not be required for each implementation, but a validation should be carried out before application of the simplified approach in new materials and component geometries.

2.2.6. Summary

It is not only necessary to carefully select the lifing criterion which will be applied, but also to choose the most appropriate means of calculating the driving parameters. Total life analyses in terms of S-N data are useful in design considerations and in analysing test samples, but application to components of complex geometry is difficult. For LCF, where initiation is not significant, a damage tolerant approach alone may be sufficient, however, in HCF, where initiation plays a more dominant role in terms of contribution to initiation life, a strain life to initiation plus damage tolerant approach may be more appropriate. Furthermore, industrial protocol calls for a damage tolerant assessment, this is especially important in components containing a pre-existing defect either measured by NDT or assumed based on NDT limits of detection; however the means of

considering the residual stresses and strain hardening profiles are as yet not well accepted.

Whilst analytical methods for this consideration have been proposed, they are unable to cover all the governing parameters and as such the importance of each parameter to the specific problem must be assessed in order to determine their applicability, it is this decision which is the key to the success of a lifing approach. However, it is typical to apply FE analysis in the determination of either the stress distribution or the fracture mechanics variables in industrial life assessment procedures. In situations of significant quasi-static and logarithmic residual stress relaxation, a full FE analysis including cyclic softening effects over many cycles may be required.

The most advanced model would seek to consider material cyclic properties as well as the residual stress and strain hardening profiles and their redistribution and the effect on fracture mechanics parameters in cracked components. Whilst not yet used in routine industrial assessments, good progress has been made in the use of pseudo temperature fields and initial conditions to define residual stresses and strain hardening and to determine the attendant effect on crack propagation. It is anticipated that once refined, these models will find application in life assessment techniques in the near future as the inclusion of the shot peening process effects in a remnant life assessment would reduce the conservatism that is present in current approaches and would allow for extended component life and thus reduced operating costs without compromising on safety margins.

Despite an extensive literature search, the author is aware that there have been relatively few references cited in this second part of the review. This is considered a reflection of the limited work in this field; despite the popularity of the shot peening process and increasing interest in incorporating its effects in fatigue lifing protocols, there has been relatively little work considering the means of doing so; perhaps this is the best indicator of the complexities involved in lifing shot peened components and of the work still required before the approaches can be standardised in industrial practice.

2.3. Refinement of objectives

A broad statement of the project objectives was made in Chapter 1. At this juncture, it is appropriate to reconsider those objectives in the light of the literature review and refine them accordingly.

There is a clear link between cyclic material behaviour and residual stress relaxation. The application of an appropriate constitutive model in any finite element stress

analysis is essential, not least in one which is required to predict changes in residual stresses through life. Thus the first objective is to establish the cyclic behaviour of the representative 9-12 %Cr turbine blade steel, i.e. whether the material first hardens and then softens or softens immediately from the first cycle, and corresponding constitutive models. However, cyclic constitutive models are typically data intensive and models such as the combined isotropic and kinematic hardening model which simulate the development of softening with fatigue cycling are computationally demanding, hence their routine application in life assessments is undesirable. Thus a sensitivity study is required to determine whether the model selection has a significant impact on the stresses calculated in the present system. Material constitutive models are developed in Chapter 3 and their significance on the local stresses and strains in notched fatigue samples is evaluated in Chapter 5.

The characterisation of the surface roughness, near surface strain hardening and compressive residual stresses with sufficient reliability for inclusion in a life assessment process requires well defined experimental or modelling procedures which have been demonstrated to be both accurate and reproducible. Experimental methods for determining residual stress profiles are well established and laboratory XRD is applied in the present study to obtain the post-peen residual stress distribution. However, the methods for determining the effects of surface plastic deformation are less well defined and a comparison of the methods for establishing near surface strain hardening is presented in Chapter 4. Also in Chapter 4, the surface roughness resulting from shot peening is characterised by using both tactile and optical two dimensional measurements and optical three dimensional measurements. The cumulative plastic strain (and hence strain hardening) is measured using microhardness, XRD FWHM and EBSD approaches and a calibration procedure is implemented based on measurements on uniaxially deformed samples. To the best of the author's knowledge, there has not yet been a comparison of calibrated microhardness, laboratory XRD and EBSD methods for evaluating plastic strain distribution reported. Before these measurements can be accepted into industrial component lifing procedures for shot peened components, the methods must be systematically evaluated and standards adopted; the comparisons of the methods in Chapter 4 are a first step in this process.

The baseline fatigue crack growth data for the representative turbine blade steel in question needed for the fracture mechanics life assessment is presented in Chapter 5. Shot peening is currently often specified in terms of Almen intensity; this may not be appropriate given the possible dependence of fatigue life not on intensity but on the interactions between surface roughness, residual stress and strain hardening. By comparing the effect of changing shot peening parameters and component shape on

the efficacy of the shot peening process in terms of total life, and considering this information in conjunction with the surface roughness, residual stress, strain hardening and applied stress distribution, a case is made in Chapter 5 for the consideration of each parameter in the optimisation of the peening process and of surface roughness, residual stress and strain hardening as independent entities in life assessment rather than simply considering peening intensity.

Whilst there has been quite considerable work reporting the changes to shot peening residual stresses and plastic strains during fatigue, an investigation into the effect of more complex bend loading at shot peened stress concentrations is still required; this configuration is more representative of service conditions than the axial loading of a uniform section. As a result, the effect of plane bending LCF on the residual stresses and plastic strain in a notched component is investigated with consideration of the interactions between material cyclic behaviour and both residual and applied stress distributions and the resultant effect on total fatigue life; these results are also reported in Chapter 5.

Figure 2- 23 illustrates the information and analysis processes required to reach the final aim of a validated life assessment process accounting for the shot peening process and in itself goes some way towards achieving the fourth objective (Section 1.1.3). The fatigue lifing protocol under development in the present work is based on the assumption that fatigue initiation and propagation processes are the same after shot peening as in the unpeened condition if local stress and strain conditions are the same; i.e. including the surface roughness, residual stress and strain hardening profile in the calculation of component stress and strain distributions is sufficient to account for shot peening. The data resulting from the previous three objectives are required either as an input to the model (constitutive model, start of life residual stresses and plastic strains) or in order to validate the model (total life data for simple geometries and developments in residual stress and plastic strain distributions). The eigenstrain method for importing residual stresses to finite element models and pseudo-temperature fields for varying material properties are both under investigation as means of incorporating the effects of shot peening when determining the required stress and strain distributions for damage tolerant assessment. These current directions are presented along with other future directions in Chapter 7.

Industry	Component	Example Target Materials
Aviation	Landing gear High pressure compressor rotor – welded regions Turbine blade disk interfaces Sheet and plate components Wing peen forming	High strength steel Ti-4Al-6V Nickel based superalloys e.g. Udimet 720Li, Inconel 718 2xxx Al, 7xxx Al and Al-Li alloys
Power generation	Turbine blade-disc interfaces Post grind-out crack repair - Feedwater heaters, heat exchanger tubing	Ferritic heat resistant 9-12 Cr steel
Automotive	Gears – root sections of tooth profile Connecting rods – radii next to I beams Crankshaft – main bearing journals and crankpin radii	Carburized steel – forged, cast or powder metallurgy Steel or titanium alloys
Biomedical	Joint replacement implants	Stainless steel or titanium alloys

Table 2- 1: Example applications of shot peening in improving fatigue resistance. Adapted from Metal Improvement Company [2].

Almen Intensity	After Child *et al.* [6]		After Kim *et al.* [15]	
	Grain Misorientation Profile Depth /μm	Microhardness Profile Depth /μm	FWHM Line Broadening Profile Depth /μm	Microhardness Profile Depth /μm
4-6A	47	96	N/A	N/A
5-7A	54	110	N/A	N/A
6-8A	71	140	100	120
7-9A	106	206	N/A	N/A
8-10A	103	247	N/A	N/A

Table 2- 2: Variations in strain hardening affected depths determined using microhardness, grain misorientation and diffraction peak broadening in an exemplar 200 % coverage shot peening system of varying Almen intensity using shot of diameter 0.28 mm and hardness 45-52 HRC on a Udimet 720Li target.

	Initiation	Propagation
Roughness	Quicker	No effect
Strain Hardening	Slower	Both quicker and slower reported
Residual Stress	No effect	Slower - non propagation possible Dominates propagation effect

Table 2- 3: Summary of the individual effects of roughness, strain hardening and residual stress resulting from shot peening on the initiation and propagation of fatigue cracks. Adapted from Wagner [87].

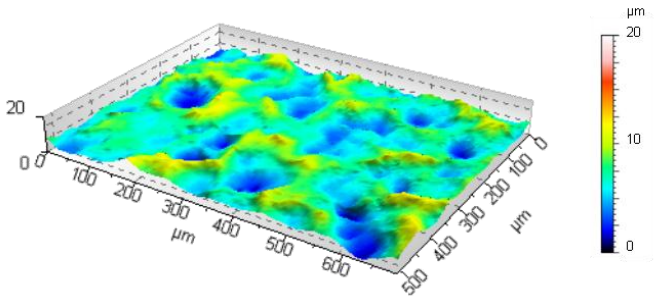

Figure 2- 1: 3D reconstruction by white light interferometry of 6-8A intensity and 200 % coverage peening applied to Ni based alloy Udimet 720Li illustrating the surface topography. Reproduced from Child *et al.* [6].

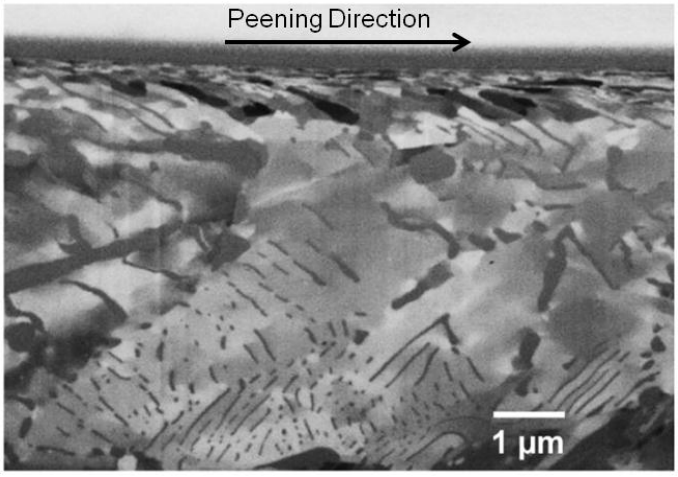

Figure 2- 2: Focussed ion beam image of the cross section of a pearlitic carbon steel sample shot peened (using S170 shot, i.e. diameter = 0.43 mm and hardness = 56 HRC) using a nozzle pressure of 2 bar at a distance from the sample of 80 mm with the nozzle inclined at 45° to the sample surface normal. Reproduced from Okolo *et al.* [10].

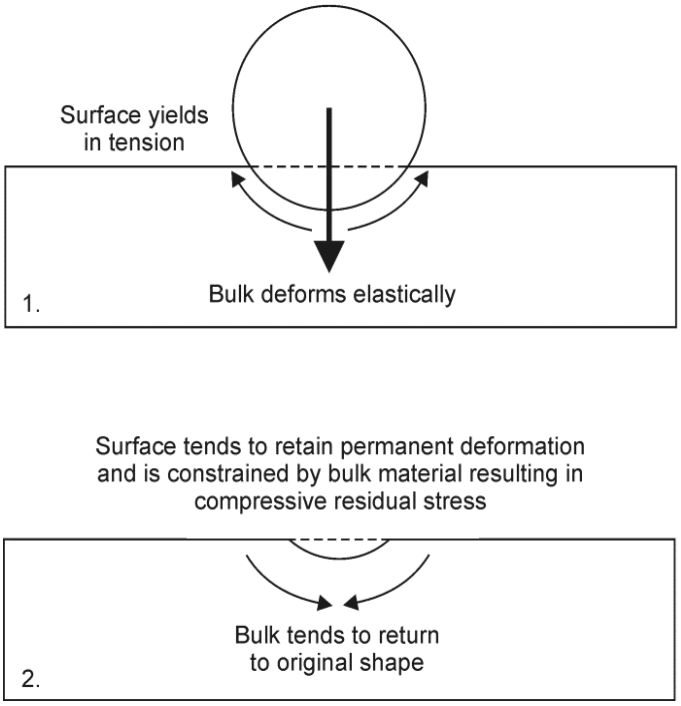

Figure 2- 3: Mechanism of formation of compressive residual stresses during shot peening.

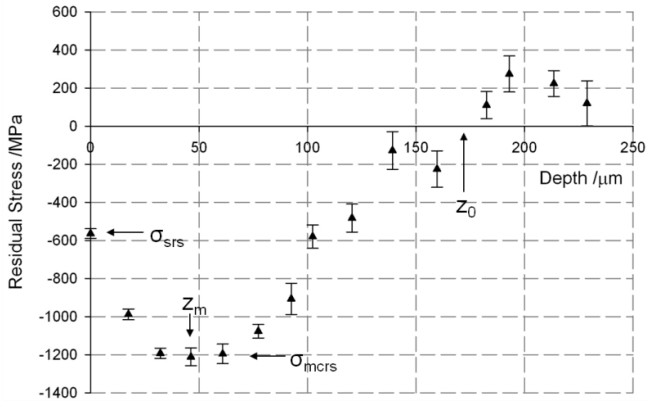

Figure 2- 4: Shot peening (6-8A intensity, 200 % coverage) induced residual stresses in Udimet 720Li measured using a layer removal X-ray diffraction ($\sin^2\psi$) methodology. After Kim *et al.* [15].

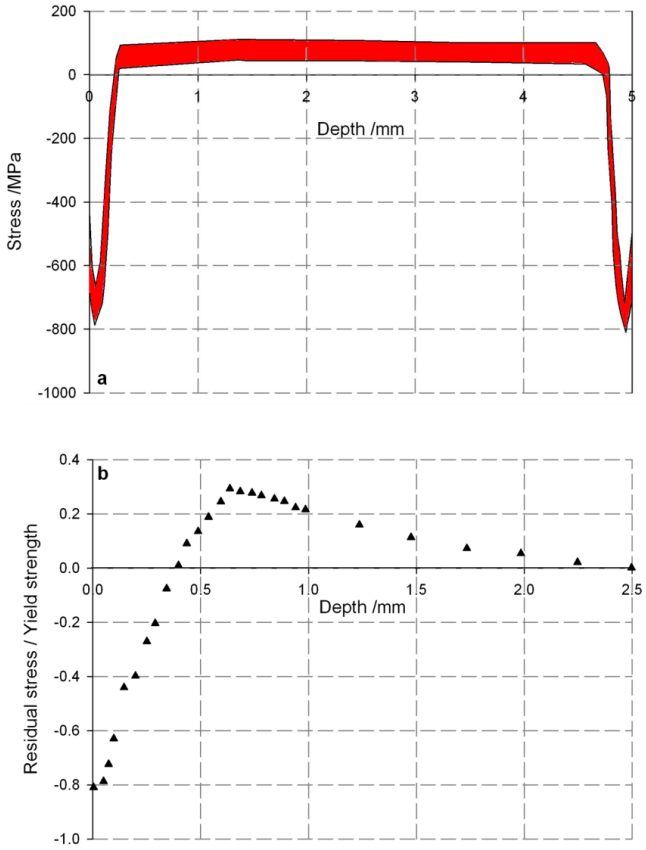

Figure 2- 5: (a) Synchrotron XRD measured through sample residual stresses in a 12 Cr steel peened using intensity 8A – 12A. The scatter shown is that in 8 samples peened at varying coverage from 75 % to 200 %, although there was no clear variation in profile resulting from this variation in coverage. (b) ND measured residual stresses in Udimet 720 peened using intensity 18A – 20A and coverage 200 %. After James *et al.* [25] and Ezeilo *et al.* [33] respectively.

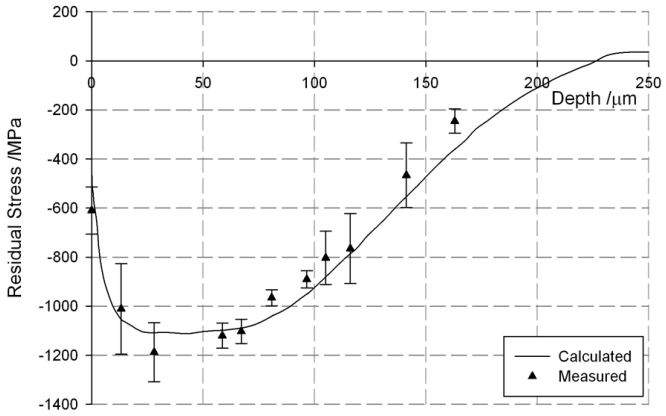

Figure 2- 6: Comparison between calculated and measured (XRD) residual stresses in Udimet 720 peened at an intensity of 8A and 100 % coverage. After Fathallah *et al.* [40].

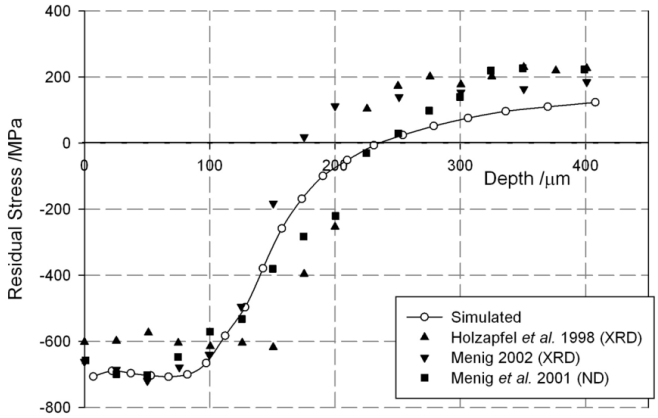

Figure 2- 7: Simulated residual stress profile resulting from a 100 % coverage process using 0.56 mm diameter shot of hardness 56 HRC impacting an AISI 4140 steel target at velocity 35 ms^{-1}. Results are compared with experimental data reproduced from three separate sources and representing both laboratory XRD [55, 56] and ND [32] results. After Klemenz *et al.* [51].

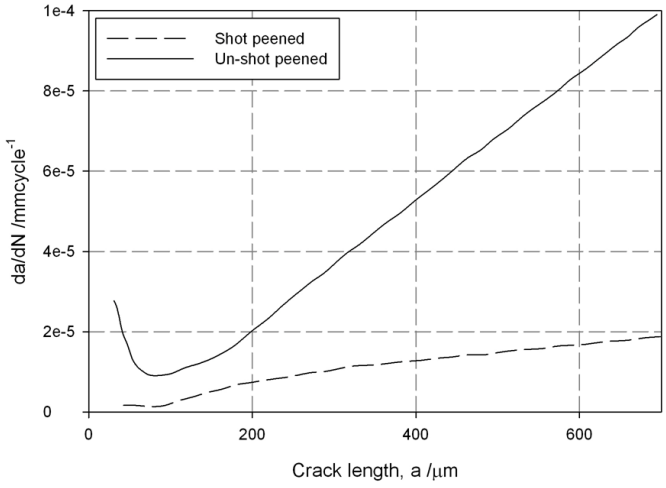

Figure 2- 8: Comparison of short crack propagation rates in peened (>100 % coverage, 12N intensity) and unpeened A316 stainless steel. After de los Rios *et al.* [82].

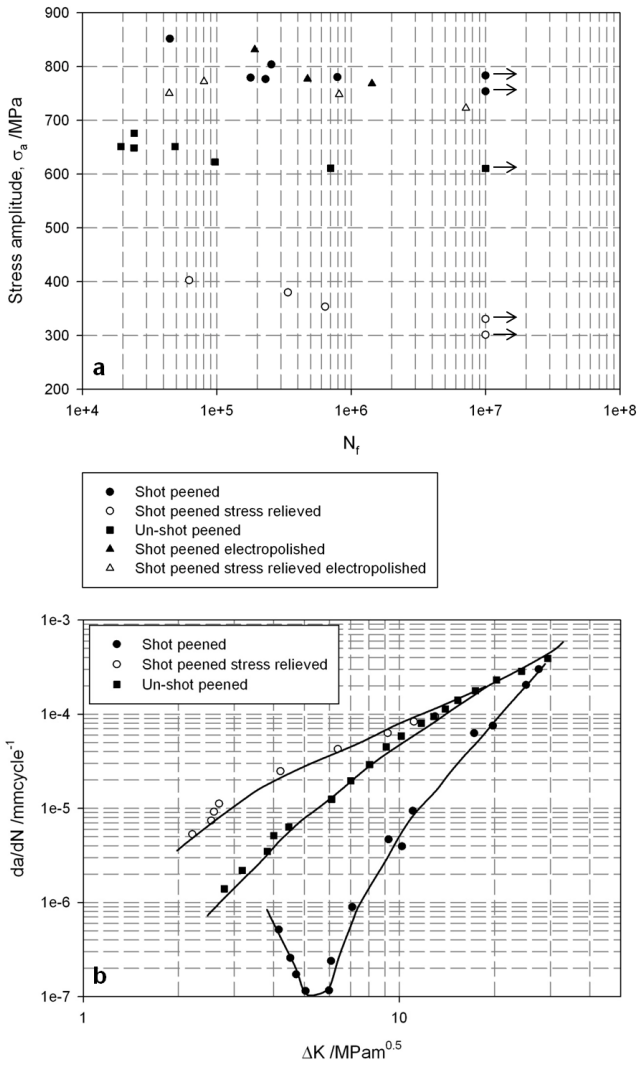

Figure 2- 9: Fully reversed room temperature fatigue performance of shot peened (100 % coverage using 0.6 mm diameter shot at intensity 12A) Ti-6Al-4V (fully lamellar microstructure) illustrating (a) total life behaviour and (b) near surface crack propagation behaviour at σ_a = 775 MPa examined by optical microscopy techniques. After Wagner [87].

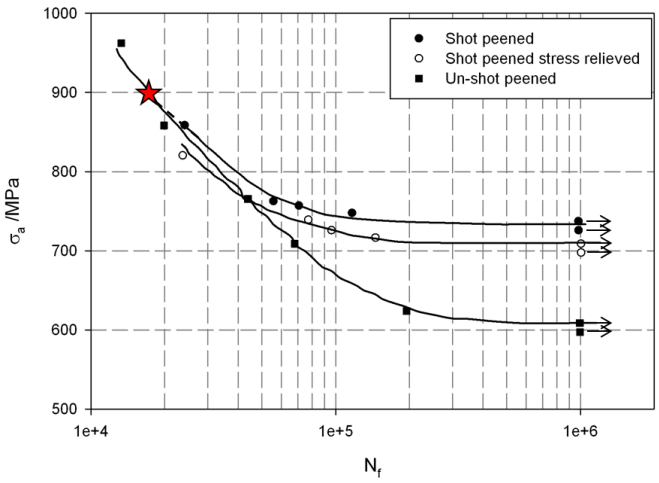

Figure 2- 10: Nominal stress-life (S-N) fatigue curves for smooth samples of a high strength martensitic steel (370 HB) tested under rotating bend illustrating the relative contributions of residual stresses and strain hardening to fatigue behaviour. After Eleiche *et al.* [88].

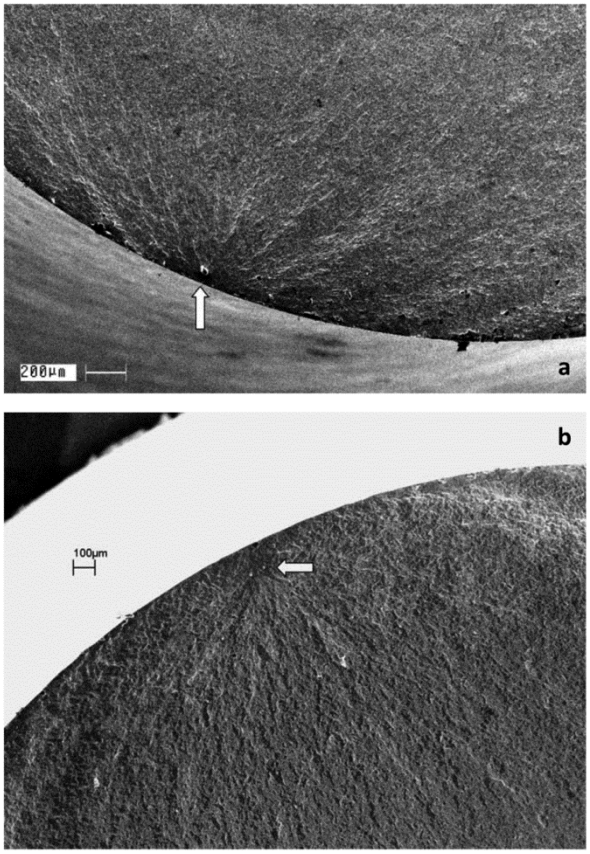

Figure 2- 11: Initiation in shot peened AISI 4340 subjected to rotating bend fatigue showing (a) surface initiation (coverage 200 %, intensity ~3A, σ_a = 931 MPa, N_f = 2.1x10^5 cycles and (b) sub-surface initiation at 105 µm from the surface (coverage 200 %, intensity ~ 8A, σ_a = 931 MPa, N_f = 5.5x10^5 cycles). Reproduced from Torres and Voorwald [30].

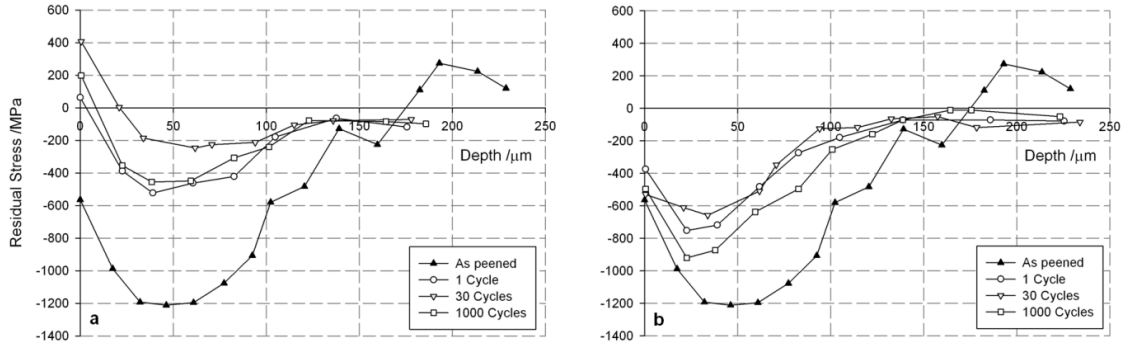

Figure 2- 12: Relaxation of the residual stress (illustrated in Figure 2- 4) in Udimet 720Li measured as a function of depth (incremental layer removal) after 1.2 % strain range controlled fatigue at 350 ˚C in axially loaded un-notched samples at $R_\varepsilon = 0$ (illustrating significance of loading direction) in (a) the loading direction and (b) the transverse direction. After Kim *et al.* [15].

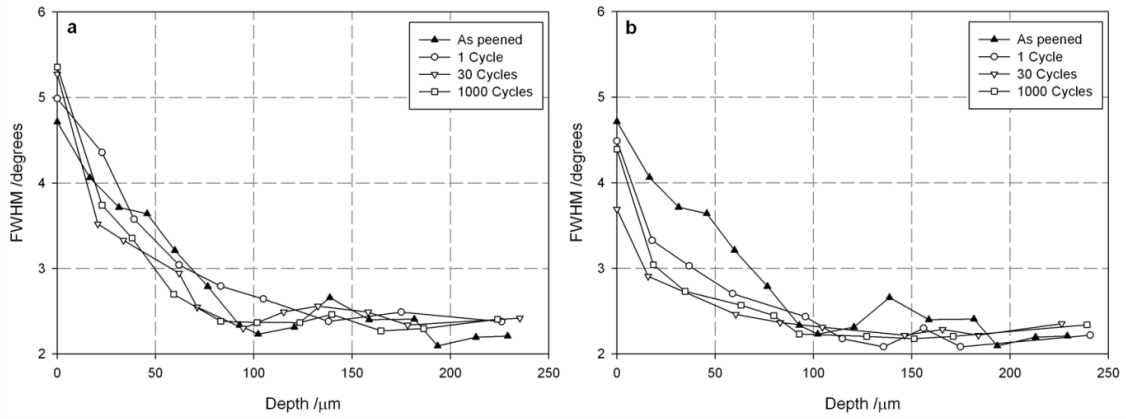

Figure 2- 13: XRD FWHM profiles in Udimet 720Li measured as a function of depth (incremental layer removal) after 1.2 % strain range controlled fatigue in axially loaded un-notched samples at $R_\varepsilon = 0$ at (a) 350 ˚C and (b) 700 ˚C. After Kim *et al.* [15].

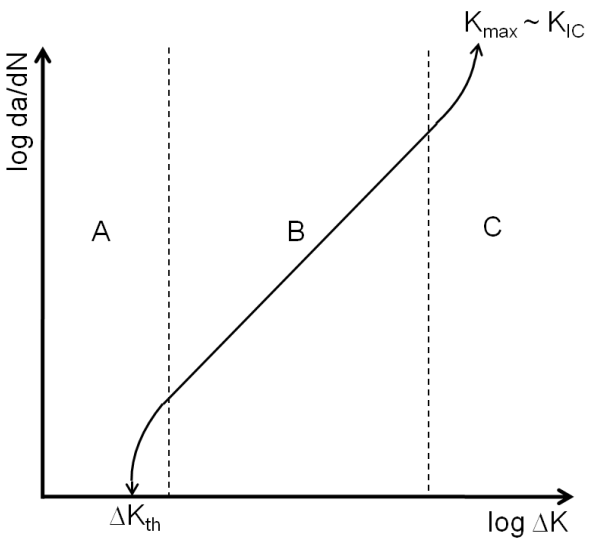

Figure 2- 14: A typical d*a*/d*N* vs. *ΔK* curve.

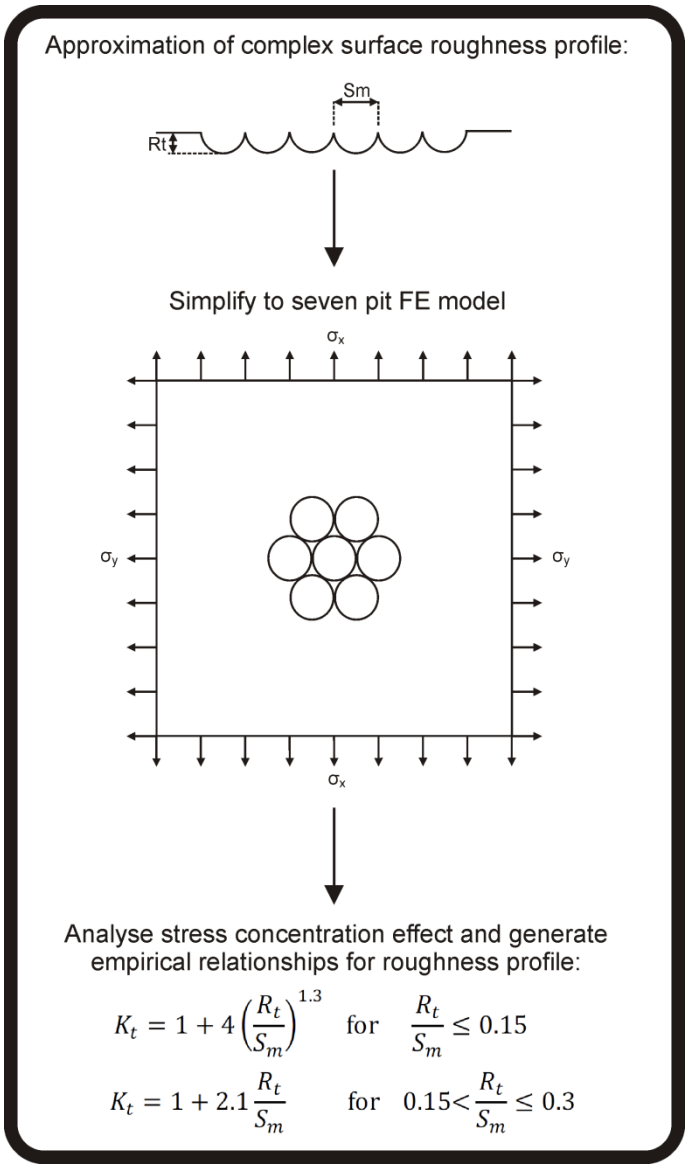

Figure 2- 15: Schematic illustrating a simplified approach to estimating the stress concentration resulting from shot peening induced surface roughness. The means of applying this model must be developed for complex geometries where there is already a stress concentrating factor upon which the roughness induced concentration would superimpose. After Li *et al.* [121].

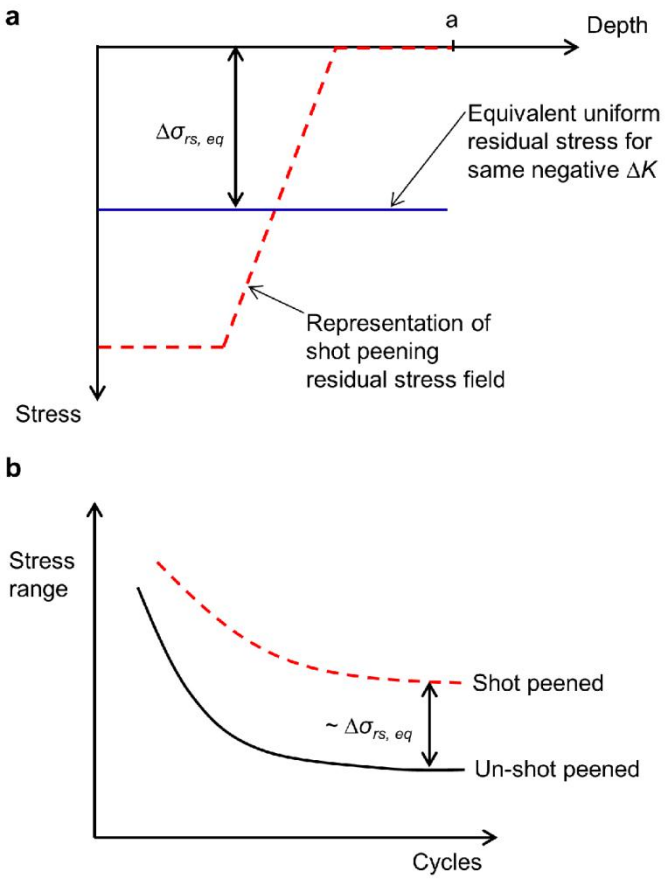

Figure 2- 16: Schematic illustration of the improvement in endurance life as calculated using the 'negative *ΔK*' approach described by Knott *et al.* [125] illustrating (a) the equivalent uniform residual stress and (b) the increase in endurance limit.

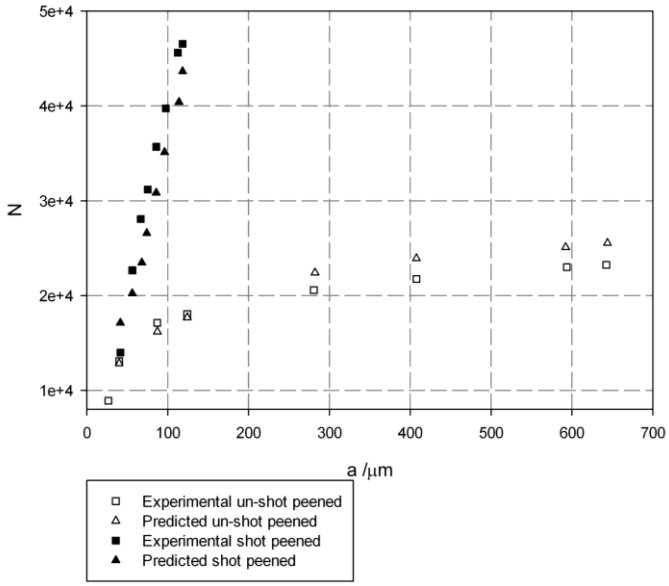

Figure 2- 17: Comparison of the predicted crack growth rate (FASTRAN) with experimental data (replica technique) for SENT samples of 7475-T7351. After Gao and Wu [83].

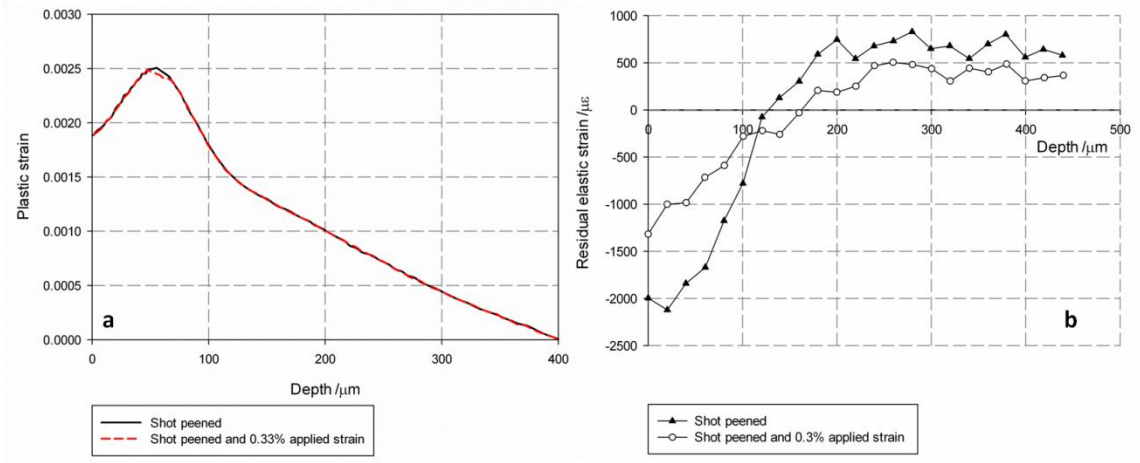

Figure 2- 18: (a) The evolution of eigenstrain (plastic strain) under compression as determined by FE modelling and (b) the evolution of residual elastic strains (~residual stresses) measured by synchrotron XRD under in-situ loading. After Song *et al.* [90].

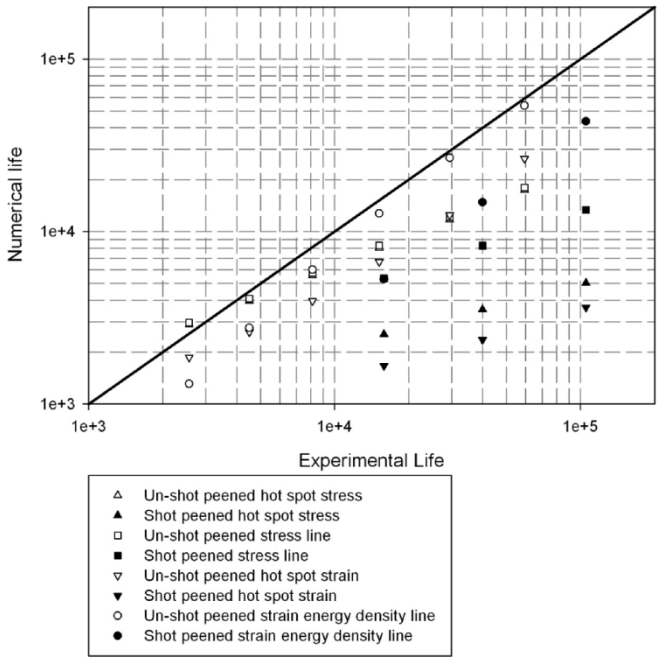

Figure 2- 19: Comparison of stress and strain based total life criteria in the analysis of the fatigue life of axially loaded shot peened and un-shot peened 'washer specimens' (manufactured from powder metallurgy Ni based superalloy RR1000 and considered representative of aero engine compressor discs) with K_t = 1.32. The graph shows the numerically predicted life vs. the experimentally determined one; the ideal solution is the straight line experimental life = numerical life shown. After Cláudio *et al.* [132].

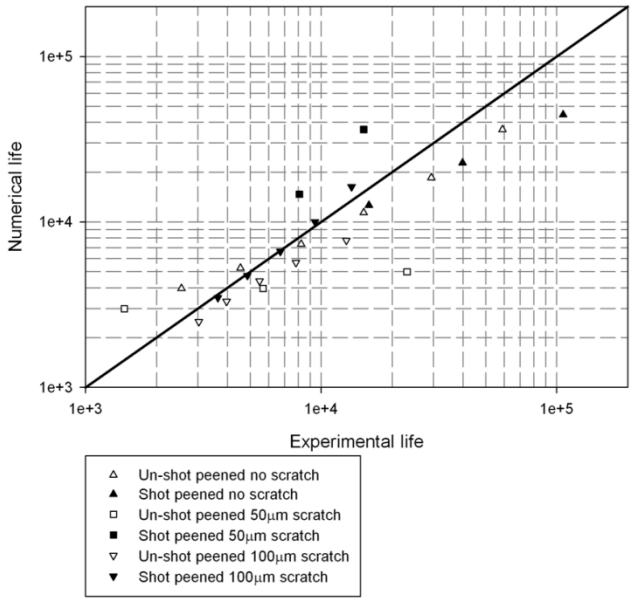

Figure 2- 20: Comparison of the numerically predicted fatigue life using a combined strain life to initiation and damage tolerant approach and the experimentally measured life using the 'washer specimens' (described in the caption to Figure 2- 19) with (50 and 100 μm) and without scratch damage at the stress concentrating region. After Cláudio *et al.* [135].

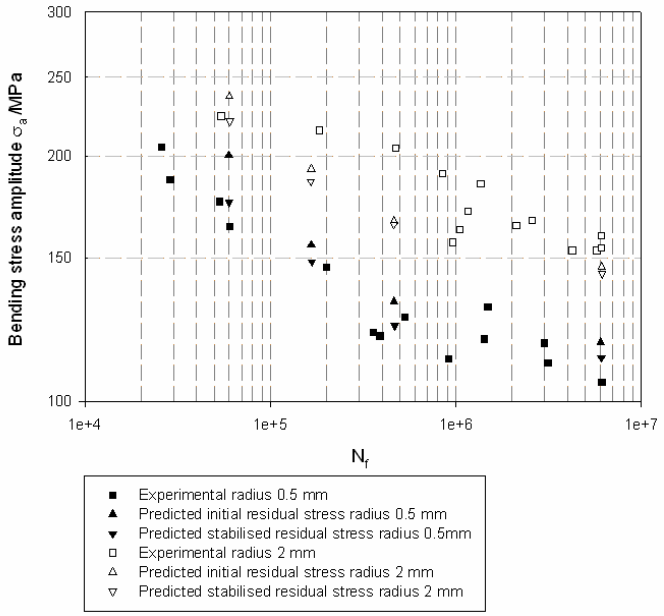

Figure 2- 21: Comparison of the predicted S-N curve using Sines criterion with experimental data for notched (radius 0.5 mm (K_t = 2.33) and 2 mm (K_t = 1.53)) shot peened (intensity = 4.5N, coverage = 100 %) Al 7075-T651 samples. After Benedetti *et al.* [136].

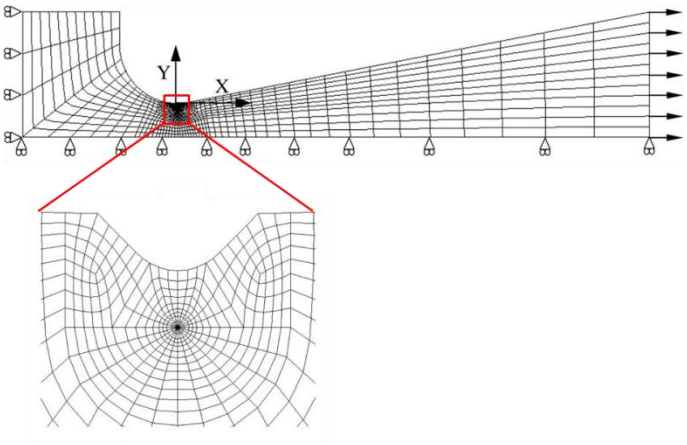

Figure 2- 22: An example of the mesh requirement for a 2D plane strain fracture mechanics analysis incorporating a crack in the washer specimen described in the caption to Figure 2-19. Reproduced from Cláudio *et al.* [133].

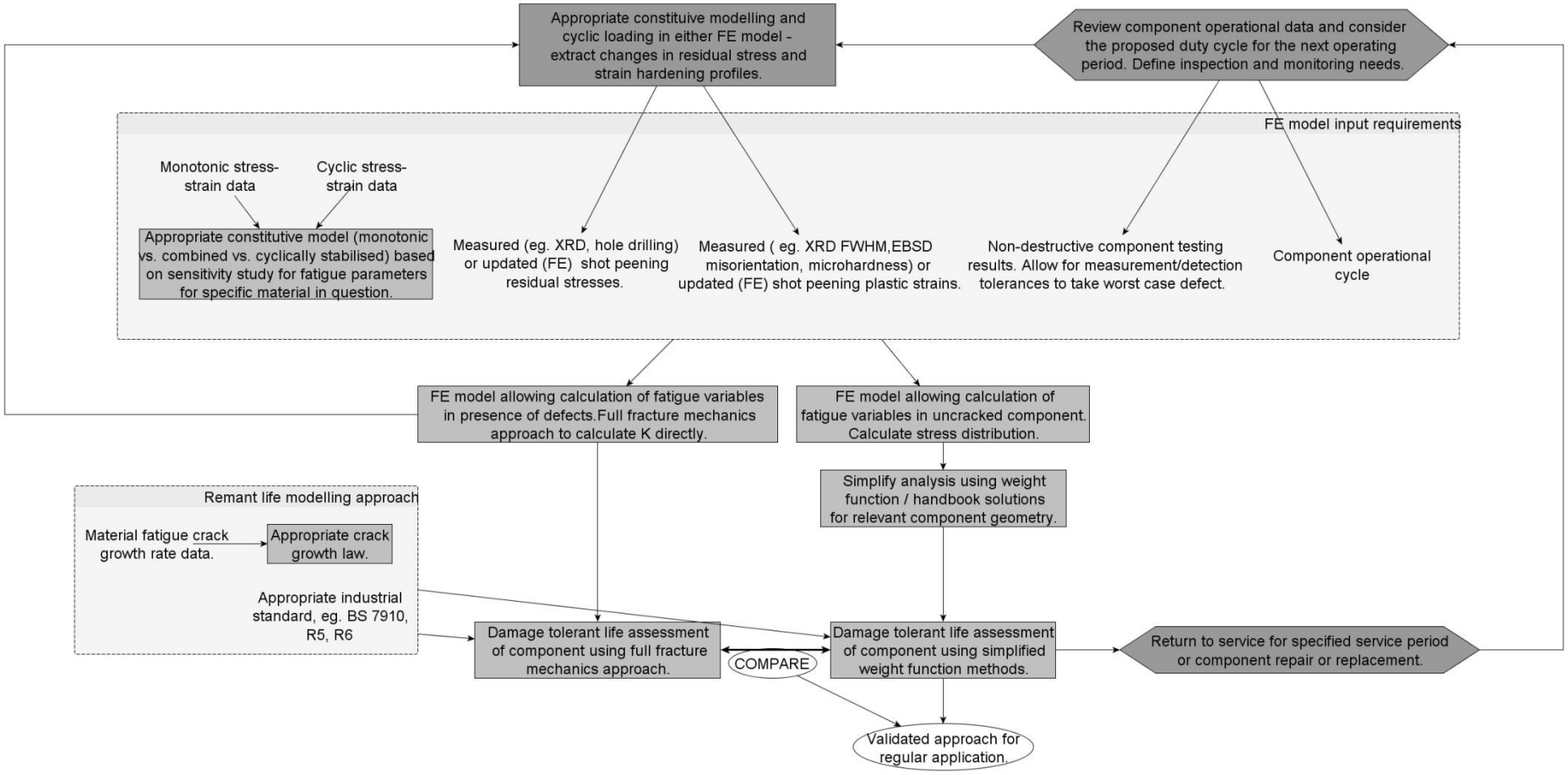

Figure 2- 23: An example component life assessment process which accounts for the effect of the shot peening process.

2.4. References

1. Suresh, S., *Fatigue of materials*. 2nd edn.; 2004, Cambridge, UK: Cambridge University Press.

2. Metal Improvement Company, *Shot peening applications*, 2005.

3. Meguid, S.A., Shagal, G., Stranart, J.C. and Daly, J. , *Three-dimensional dynamic finite element analysis of shot peening induced residual stresses.* Finite Elements in Analysis and Design, 1999. **31(**3): p. 179 - 191.

4. ESDU, *Guide to the effect of shot peening on fatigue strength*, 1992. ESDU Guide 92015.

5. Benedetti, M., Fontanari, V., Scardi, P., Ricardo, C.L.A. and Bandini, M., *Reverse bending fatigue of shot peened 7075-T651 aluminium alloy: The role of residual stress relaxation.* International Journal of Fatigue, 2009. **31**(8-9): p. 1225 - 1236.

6. Child, D.J., West, G.D. and Thomson, R.C., *Assessment of surface hardening effects from shot peening on a Ni-based alloy using electron backscatter diffraction techniques.* Acta Materialia, 2011. **59**(12): p. 4825 - 4834.

7. Clausen, R. and Stangenberg, J., *Roughness of shot peened surfaces - definition and measurement*, in *Proceedings of the 7th International Conference on Shot* Peening. 1999. Warsaw, Poland: International Scientific Committee on Shot Peening: p. 69 - 77.

8. Vaxevanidis, N.M., Manolakos, D.E., Koutsomichalis, A., Petropoulos, G., Panagotas, A., Sideris, I., Mourlas, A. and Antoniou, S.S., *The effect of shot peening on surface integrity and tribological behaviour of tool steels*, in *Proceedings of the International Conference on* Tribology. 2006. Parma, Italy: AITC-AIT.

9. Prevéy, P.S. *The measurement of subsurface residual stress and cold work distributions in nickel base alloys*, in *Proceedings of Residual Stress in Design, Process and Materials Selection*, Young, W.B., Editor. 1987. Metals Park, OH: ASM: p. 11 – 19.

10. Okolo, B., Pérez-Willard, F., Hawecker, J., Gerthsen, D. and Wanner, A., *Focussed ion beam study of the effects of shot peening on the subsurface microstructure of normalized pearlitic steel.* Journal of Materials Processing Technology, 2007. **183**(2-3): p. 160 - 164.

11. Fontanari, V., Frendo, F., Bortolamedi, T. and Scardi, P., *Comparison of the hole-drilling and X-ray diffraction methods for measuring the residual stresses in shot peened aluminium alloys.* Journal of Strain Analysis, 2005. **40**(2): p. 199 - 209.

12. Liu, G., Wang, S.C., Lou, X.F., Lu, J. amd Lu, K., *Low carbon steel with nanostructured surface layer induced by high energy shot peening.* Scripta Materialia, 2001. **44**(8-9): p. 1791 - 1795.

13. Liu, W.C., Dong, J., Zheng, X.W., Zhang, P., Ding, W.J., *Influence of shot peening on notched fatigue properties of magnesium alloy ZK60.* Materials Science and Technology, 2011. **27**(1): p. 201 - 207.

14. Altenberger, I., Scholtes, B., Martin, U. and Oettel, H., *Cyclic deformation and near surface microstructures of shot peened or deep rolled austenitic stainless steel AISI 304.* Materials Science and Engineering A, 1999. **264**(1-2): p. 1 - 16.

15. Kim, S.-B., Shackleton, J., Preuss, M., Withers, P.J., Evans, A. and Bruno, G., *Stress relaxation of shot-peened UDIMET 720Li under solely elevated-temperature exposure and under isothermal fatigue*. Metallurgical and Materials Transactions A, 2005. **36**(11): p. 3041 - 3053.

16. James, M.N., Hughes, D.J., Chen, Z., Lombard, H., Hattingh, D.G., Asquith, D., Yates, J.R. and Webster, P.J., *Residual stresses and fatigue performance.* Engineering Failure Analysis, 2007. **14**(2): p. 384 - 395.

17. Zimmerman, M., Klemenz, M. and Schulze, V., *Literature review on shot peening simulation.* International Journal of Computational Materials Science and Surface Engineering, 2010. **3**(4): p. 289 - 310.

18. McClung, R.C., *A literature survey on the stability and significance of residual stresses during fatigue.* Fatigue and Fracture of Engineering Materials and Structures, 2007. **30**(3): p. 173 - 205.

19. Withers, P.J. and Bhadeshia, H.K.D.H., *Residual stress. Part 1 - Measurement Techniques.* Materials Science and Technology, 2001. **17**(4): p. 355 - 365.

20. Prevéy, P.S., *X-ray diffraction residual stress techniques*, in *ASM Handbook Volume 10, Materials* Characterization. 1986. Metals Park, OH: ASM: p. 380 - 392.

21. Gao, Y.-K., Yao, M. and Li, J.-K., *An analysis of residual stress fields caused by shot peening.* Metallurgical and Materials Transactions A, 2002. **33**(6): p. 1775 - 1778.

22. Evans, A., Kim, S.-B., Shackleton, J., Bruno, G., Preuss, M. and Withers, P.J., *Relaxation of residual stress in shot peened Udimet 720Li under high temperature isothermal fatigue.* International Journal of Fatigue, 2005. **27**(10-12): p. 1530 - 1534.

23. Dalaei, K., Karlsson, B. and Svensson, L.-E., *Stability of residual stresses created by shot peening of pearlitic steel and their influence on fatigue behaviour.* Procedia Engineering, 2010. **2**(1): p. 613 - 622.

24. Benedetti, M., Bortolamedi, T., Fontanari, V. amd Frendo, F., *Bending fatigue behaviour of differently shot peened Al6082 T5 alloy.* International Journal of Fatigue, 2004. **26**(8): p. 889 - 897.

25. James, M.N., Newby, M., Hattingh, D.G. and Steuwer, A., *Shot-peening of steam turbine blades: Residual stresses and their modification by fatigue cycling.* Procedia Engineering, 2010. **2**(1): p. 441 - 451.

26. Bergström, J. and Ericsson, T., *Relaxation of shot peening induced compressive stress during fatigue of notched steel samples*. in *Proceedings of the 2nd International Conference on Shot* Peening. 1984. Chicago, USA: International Scientific Committee on Shot Peening: p. 241 – 248.

27. Martinez, S.A., Satish, S., Blodgett, M.P. and Shepard, M.J., *Residual stress distribution on surface-treated Ti-6Al-4V by X-ray diffraction.* Experimental Mechanics, 2003. **43**(2): p. 141 - 147.

28. Wang, S., Li, Y., Yao, M. and Wang, R., *Compressive residual stress induced by shot peening.* Journal of Materials Processing Technology, 1998. **73**(1-3): p. 64 - 73.

29. Zinn, W. and Scholtes, B., *Influence of shot velocity and shot size on Almen intensity and residual stress depth distributions,* in *Proceedings of the 9th International Conference on Shot Peening*. 2005. Paris, France: International Scientific Committee on Shot Peening: p. 379 – 384.

30. Torres, M.A.S. and Voorwald, H.J.C., *An evaluation of shot peening, residual stress and stress relaxation on the fatigue life of AISI 4340 steel.* International Journal of Fatigue, 2002. **24**(8): p. 877 - 886.

31. Dalaei, K., Karlsson, B. and Svensson, L.-E. *Stability of shot peening induced residual stresses and their influence on fatigue lifetime.* Materials Science and Engineering A, 2011. **528**(3): p. 1008 - 1015.

32. Menig, R., Pintschovius, L., Schulze, V. and Vöhringer, O., *Depth profiles of macro residual stresses in thin shot peened steel plates determined by X-ray and neutron diffraction.* Scripta Materialia, 2001. **45**(8): p. 977 - 983.

33. Ezeilo, A., Webster, G., Webster, P.J. and Webster, P.S., *Comparison of shot peening residual stress distributions in a selection of materials*. in *Proceedings of the 5th International Conference on Shot Peening*. 1993. Oxford, UK: International Scientific Committee on Shot Peening: p.275 – 282.

34. Mahagaonkar, S.B., Brahmankar, P.K. and Seemikeri, C.Y., *Effect of shot peening parameters on microhardness of AISI1045 and 316L material: An analysis using design of experiment.* International Journal of Advanced Manufacturing Technology, 2008. **38**(5-6): p. 563 - 574.

35. Guagliano, M. and Vergani, L., *An approach for prediction of fatigue strength of shot peened components.* Engineering Fracture Mechanics, 2004. **71**(4-6): p. 501- 512.

36. Li, J.K., Mei, Y. and Duo, W., *Mechanical approach to the residual stress field induced by shot peening.* Materials Science and Engineering A, 1991. **147**(2): p. 167 - 173.

37. Johnson, K.L., *Contact mechanics*. 1st edn.; 1985, Cambridge, UK: Cambridge University Press.

38. Shen, S. and Atluri, S.N., *An analytical model for shot peening induced residual stresses.* Computers Materials and Continua, 2006. **4**(2): p. 75 - 85.

39. Franchim, A.S., de Campos, V.S., Travessa, D.N., de Moura Neto, C., *Analytical modelling for residual stresses produced by shot peening.* Materials and Design, 2009. **30**(5): p. 1556 - 1560.

40. Fathallah, R., Inglebert, G. and Castex, L., *Prediction of plastic deformation and residual stresses induced in metallic parts by shot peening.* Materials Science and Technology, 1998. **14**(7): p. 631 – 639.

41. Le-Guernic, Y. and Eckersley, J.S., *Peenstress software selects shot peening parameters*. in *Proceedings of the 6th International Conference on Shot Peening*. 1996. San Francisco, CA, USA: International Scientific Committee on Shot Peening: p. 481 – 492.

42. Zarka, J., *Direct analysis of elastic-plastic structures with 'overlay' materials during cyclic loading.* International Journal for Numerical Methods in Engineering, 1980. **15**(2): p. 225-235.

43. Rouhaud, E., Ouakka, A., Ould, C., Chaboche, J.-L. and François, M., *Finite elements model of shot peening, effects of constitutive laws of the material*. in *Proceedings of the 9th International Conference on Shot Peening*. 2005. Paris, France: International Scientific Committee on Shot Peening: p. 107 – 112.

44. Frija, M., Hassine, T., Fathallah, R., Bouraoui, C. and Dogui, A., *Finite element modelling of the shot peening process: Prediction of the compressive residual stresses, the plastic deformations and the surface integrity.* Materials Science and Engineering A, 2006. **426**(1-2): p. 173 - 180.

45. Meguid, S.A., Shagal, G. and Stranart, J.C., *3D FE analysis of peening of strain-rate sensitive materials using multiple impingement model.* International Journal of Impact Engineering, 2002. **27**(2): p. 119 - 134.

46. ElTobgy, M.S., Ng, E. and Elbestawi, M.A., *Three-dimensional elastoplastic finite element model for residual stresses in the shot peening process.* Journal of Engineering Manufacture, 2004. **218**(Part B): p. 1471 - 1481.

47. Majzoobi, G.H., Azizi, R. and Alavi Nia, A., *A three-dimensional simulation of shot peening process using multiple shot impacts.* Journal of Materials Processing Technology, 2005. **164-165**: p. 1226 - 1234.

48. Meguid, S.A., Shagal, G. and Stranart, J.C., *Development and validation of novel FE models for 3D analysis of peening of strain-rate sensitive materials.* Journal of Engineering Materials Technology, 2007. **129**(2): p. 271 - 283.

49. Hong, T., Ooi, J.Y. and Shaw, B., *A numerical simulation to relate the shot peening parameters to the induced residual stresses.* Engineering Failure Analysis, 2008. **15**(8): p. 1097 - 1110.

50. Hong, T., Ooi, J.Y. and Shaw, B., *A numerical study of the residual stress pattern from single shot impacting on a metallic component.* Advances in Engineering Software, 2008. **39**(9): p. 743 - 756.

51. Klemenz, M., Schulze, V., Rohr, I. and Löhe, D., *Application of the FEM for the prediction of the surface layer characteristics after shot peening.* Journal of Materials Processing Technology, 2009. **209**(8): p. 4093 - 4102.

52. Achintha, M. and Nowell, D., *Eigenstrain modelling of residual stresses generated by laser shock peening.* Journal of Materials Processing Technology, 2011. **211**(6): p. 1091 - 1101.

53. Lemaitre, J. and Chaboche, J.-L., *Mechanics of solid materials*. 2nd edn.; 1990, Cambridge, UK: Cambridge University Press.

54. Totten, G., Howes, M. and Inoue, T., *Handbook of Residual Stress and deformation of* steel; 2002, Metals Park, OH: ASM.

55. Holzapfel, H., Schulze, V., Vöhringer, O. and Macherauch, E., *Residual stress relaxation in an AISI 4140 steel due to quasistatic and cyclic loading at higher temperatures.* Materials Science and Engineering A, 1998. **248**(1-2): p. 9 - 18.

56. Menig, R., *Randschichtzustand, Eigenspannungsstabilität und Schwingfestigkeit von unterschiedlich wärmebehandeltem 42 CrMo 4 nach modifizierten Kugelstrahlbehandlungen*. 2002, PhD Thesis: University of Karlsruhe.

57. Benedetti, M., Fontanari, V. and Monelli, B.D., *Numerical simulation of residual stress relaxation in shot peened high-strength aluminium alloys under reverse bending fatigue.* Journal of Engineering Materials and Technology, 2010. **132**.

58. Tosha, K. and Iida, K. *Residual stress and hardness distribution influenced by shot peening*, in *Proceedings of the 4th International Conference on Shot Peening*. 1990. Tokyo, Japan: International Scientific Committee on Shot Peening: p. 379 - 388.

59. Tan, L., Ren, X., Sridharan, K. and Allen, T.R., *Effect of shot-peening on the oxidation of alloy 800H exposed to supercritical water and cyclic oxidation.* Corrosion Science, 2008. **50**(7): p. 2040 - 2046.

60. Prevéy, P.S. *The uniformity of shot peening induced residual stress*. in *Proceedings of Residual Stress for Designers and Metallurgists*, Walle, L.J.V., Editor. 1981. Metals Park, OH: ASM: p. 151 – 168.

61. Prevéy, P.S., *X-Ray diffraction characterisation of residual stresses produced by shot peening*, in *Proceedings of Shot Peening Theory and Application*, Niku-Lari, A., Editor, 1990. Gournay-Sur-Marne, France: IITT International: p. 81-93.

62. Tosha, K., *Characteristics of shot peened surfaces and surface layers*, in *Proceedings of Asia-Pacific Forum on Precision Surface Finishing and Deburring* Technology, 2001, Singapore: Metal Industries Research and Development Centre: p. 193 - 201.

63. De los Rios, E.R., Trull, M. and Levers, A. *Modelling fatigue crack growth in shot-peened components of Al 2024-T351.* Fatigue and Fracture of Engineering Materials and Structures, 2000. **23**(8): p. 709 - 716.

64. Cahoon, J.R., Broughton, W.H. and Kutzak, A.R., *The determination of yield strength from hardness measurements.* Metallurgical Transactions, 1971. **2**(7): p. 1979 - 1983.

65. Srikant, G., Cohollacoop, N. and Ramamurty, U., *Plastic strain distribution underneath a Vickers indenter: Role of yield strength and work hardening exponent.* Acta Materialia, 2006. **54**(19): p. 5171-5178.

66. Chaudhri, M.M., *Subsurface strain distribution around Vickers hardness indentations in annealed polycrystalline copper.* Acta Materialia, 1998. **46**(9): p. 3047-3056.

67. Patterson, A.L., *The Scherrer formula for X-ray particle Saze determination.* Physical Review, 1939. **56**(10): p. 978 - 982.

68. Stokes, A.R. and Wilson, A.J.C., *The diffraction of X-rays by distorted crystal aggregates -1.* Proceedings of the Physical Society, 1944. **56**: p. 174 - 181.

69. Williamson, G.K. and Hall, W.H., *X-ray line broadening from filed aluminium and wolfram.* Acta Metallurgica, 1953. **1**(1): p. 22 - 31.

70. Yoda, R., Yokomaku, T. and Tsuji, N., *Plastic deformation and creep damage evaluations of type 316 austenitic stainless steels by EBSD.* Materials Characterization, 2010. **61**(10): p. 913 - 922.

71. Kamaya, M., Wilkinson, A.J. and Titchmarsh, J.M., *Measurement of plastic strain of polycrystalline material by electron backscatter diffraction.* Nuclear Engineering and Design, 2005. **235**(6): p. 713 - 725.

72. Kamaya, M., Wilkinson, A.J. and Titchmarsh, J.M., *Quantification of plastic strain of stainless steel and nickel alloy by electron backscatter diffraction.* Acta Materialia, 2006. **54**(2): p. 539 - 548.

73. Kamaya, M., *Measurement of local plastic strain distribution of stainless steel by electron backscatter diffraction.* Materials Characterization, 2009. **60**(2): p. 125 - 132.

74. Sáez-Maderuelo, A., Castro, L. and de Diego, G., *Plastic strain characterisation in austenitic stainless steels and nickel alloys by electron backscatter diffraction.* Journal of Nuclear Materials, 2011. **416**(1-2): p. 75 - 79.

75. ESDU, *The Effect of Surface Roughness on the Fatigue Limit of Steels at Zero Mean Stress*, 1974. ESDU Guide 74027.

76. Novovic, D., Dewes, R.C., Aspinwall, D.K., Voice, W. and Bowen, P., *The effect of machined topography and integrity on fatigue life.* International Journal of Machine Tools and Manufacture, 2004. **44**(2-3): p. 125 - 134.

77. Nwaogu, U.C., Tiedje, N.S., and Hansen, H.N. *A non-contact 3D method to characterize the surface roughness of castings.* Journal of Materials Processing Technology, 2013. **213**(1): p. 59 - 68.

78. Koster, W.B., *Effect of residual stress on fatigue of structural alloys*, in *Proceedings of the 3rd International Conference on Practical Application of Residual Stress Technology*, Rudd, C., Editor. 1991. Indianapolis, IN: ASM: p. 1-9.

79. Taylor, D. and Clancy, O.M., The f*atigue performane of machined surfaces.* Fatigue and Fracture of Engineering Materials and Structures, 1991. **14**(2-3): p. 329 - 336.

80. Withers, P.J., *Residual stress and its role in failure.* Reports on Progress in Physics, 2007. **70**(12): p. 2211 - 2264.

81. Webster, G.A. and Ezeilo, A.N., *Residual stress distributions and their influence on fatigue lifetimes.* International Journal of Fatigue, 2001. **23**(Supplement 1): p. 375 - 383.

82. De los Rios, E.R., Walley, A., Milan, M.T. and Hammersley, G., *Fatigue crack initiation and propagation on shot-peened surfaces in A316 stainless steel.* International Journal of Fatigue, 1995. **17**(7): p. 493 - 499.

83. Gao, Y.K. and Wu, X.R., *Experimental investigation and fatigue life prediction for 7475-T7351 aluminium alloy with and without shot peening-induced residual stresses.* Acta Materialia, 2011. **59**(9): p. 3737 - 3747.

84. Mutoh, Y., Fair, G.H., Noble, B. and Waterhouse, R.B., *The effect of residual stresses induced by shot peening on fatigue crack propagation in two high strength aluminium alloys.* Fatigue and Fracture of Engineering Materials and Structures, 1987. **10**(4): p. 261 - 272.

85. Zhu, X.Y. and Shaw, W.J.D., *Correlation of fatigue crack growth behaviour with crack closure in peened specimens.* Fatigue and Fracture of Engineering Materials and Structures, 1995. **18**(7-8): p. 811 - 820.

86. Song, P.S. and Wen, C.C., *Crack closure and crack growth behaviour in shot peened fatigued specimen.* Engineering Fracture Mechanics, 1999. **63**(3): p. 295 - 304.

87. Wagner, L. *Effect of mechanical surface treatments on fatigue performance of titanium alloys*. in *Proceedings of Fatigue Behaviour of Titanium Alloys*, Boyer, R.R., Eylon, D. and Lutjering, G., Editors. 1999. Warrendale, PA: TMS: p. 253 – 265.

88. Eleiche, A.M., Megahed, M.M. and Abd-Allah, N.M., *The shot-peening effect on the HCF behavior of high-strength martensitic steels.* Journal of Materials Processing Technology, 2001. **113**(1): p. 502 - 508.

89. Wagner, L., *Mechanical surface treatments on titanium, aluminium and magnesium alloys.* Materials Science and Engineering A, 1999. **263**(2): p. 210 - 216.

90. Song, X., Liu, W.C., Belnoue, J.P., Dong, J., Wu, G.H., Ding, W.J., Kimber, S.A.J., Buslaps, T., Lunt, A.J.G. and Korsunsky, A.M., *An eigenstrain-based finite element model and the evolution of shot peening residual stresses during*

fatigue of GW103 magnesium alloy. International Journal of Fatigue, 2012. **42**: p. 284 - 295.

91. Ferreira, J.A.M., Borrego, L.F.P., and Costa, J.D.M., *Effects of surface treatments on the fatigue of notched bend specimens.* Fatigue and Fracture of Engineering Materials and Structures, 1996. **19**(1): p. 111 - 117.

92. Dörr, T. and Wagner, L., *Influence of stress gradient on fatigue behaviour of shot peened Timetal 1100*, in *Proceedings of the 6th International Conference on Shot Peening*. 1996. San Francisco, CA: International Scientific Committee on Shot Peening: p. 223 - 232.

93. Meguid, S.A., Shagal, G. Stranart, J.C., Liew, K.M. and Ong, L.S., *Relaxation of peening residual stresses due to cyclic thermo-mechanical overload.* Journal of Engineering Materials and Technology, 2005. **127**(2): p. 170 - 178.

94. Zhuang, W.Z. and Halford, G.R., *Investigation of residual stress relaxation under cyclic load.* International Journal of Fatigue, 2001. **23**(Supplement 1): p. 31 - 37.

95. Morrow, J.D. and Sinclair, G.M., *Cycle-dependent stress relaxation*, in *STP 237, Basic Mechanisms of Fatigue*. 1958. Warrendale, PA: ASTM: p. 83 - 103.

96. Kodama, S. *The behaviour of residual stress during fatigue stress cycles*, in *Proceedings of the International Conference on Mechanical Behaviour of Metals II*, Gakkai, N.Z., Editor. 1972. Kyoto, Japan: Society of Material Science: p. 111 – 118.

97. Liu, J. and Yuan, H., *Prediction of residual stress relaxations in shot-peened specimens and its application for the rotor disc assessment.* Materials Science and Engineering A, 2010. **527**(24-25): p. 6690 - 6698.

98. Benedetti, M., Fontanari, V. and Bandini, M. *A simplified and fast method to predict plain and notch fatigue of shot peened high-strength aluminium alloys under reverse bending.* Surface Coatings and Technology, 2011, **Article in press: DOI:10.1016/j.surfcoat.2011.12.008**

99. Bathias, C., Bonnafe, J.P., Lebrun, J.L. and Maeder, G., *X-ray diffraction and acousitc emission study of fatigue damage in aluminium alloys*, in *STP 1004, Analytical and Experimental Methods for Residual Stress Effects in Fatigue,* Champoux, R.L., Underwood, J.H., and Kapp, J.A., Editors. 1988. Warrendale, PA: ASTM: p. 25 - 36.

100. Basquin, O.H., *The exponential law of endurance tests.* Proceedings of the American Society for Testing and Materials, 1910. **10**: p. 625 - 630.

101. Coffin, L.F., *A study of the effects of cyclic thermal stresses on a ductile metal.* Transactions of the American Society of Mechanical Engineers, 1954. **76**: p. 931 - 950.

102. Manson, S.S., *Behaviour of materials under conditions of thermal stress*, 1954. Cleveland, Lewis Flight Propulsion Laboratory: National Advisory Commission on Aeronautics. Report 1170.

103. Goodman, J., *Mechanics Applied to Engineering*. 1899, London, UK: Longmans Green.

104. Gerber, H., *Bestimmung der zulässigen Spannungen in Eisen-konstructionen.* Zeitschrift des Bayerischen Architeckten und Ingenieur-Vereins, 1874. **6**: p. 101-110.

105. Smith, K.N., Watson, P. and Topper, T.H., *A stress-strain function for the fatigue of materials.* Journal of Materials, 1970. **5**(4): p. 767 - 768.

106. Taylor, D., *The theory of critical distances.* Engineering Fracture Mechanics, 2008. **75**(7): p. 1696 - 1705.

107. El Haddad, M.H., Topper, T.H. and Smith, K.N., *Prediction of non-propagating cracks.* Engineering Fracture Mechanics, 1979. **11**(3): p. 573 - 584.

108. Kitagawa, H. and Takahashi, S., *Applicability of fracture mechanics to very small cracks or the cracks in the early stage*. in *Proceedings of the 2nd International Conference on Mechanical Behaviour of Materials*. 1976. Metals Park, OH: ASM: p. 627 – 631.

109. Carpinteri, A., de Freitas, M. and Spagnoli, A., Editors, *Biaxial/Multiaxial Fatigue and Fracture*, 2003. Amsterdam, The Netherlands: Elsevier. ESIS Publication 31.

110. Fatemi, A. and N. Shamsaei, *Multiaxial Fatigue: An Overview and Some Approximate Models.* International Journal of Fatigue, 2011. **33**(8): p. 948 – 958.

111. Crossland, B., *Effect of large hydrostatic pressures on the torsional fatigue strength of an alloy steel*, in *Proceedings of the International Conference on Fatigue of Metals*. 1956. London, UK: IMechE: p. 138 – 149.

112. Sines, G., *Behaviour of metals under complex static and alternating stresses*, in *Metal Fatigue*, Sines, G. and Waisman, J.L., Editors. 1959. New York, NY: McGraw-Hill: p. 145 - 169.

113. British Energy Generation Ltd., *R6 - Assessment of the integrity of structures containing defects, Revision 4*, 2001.

114. British Standard, *BS 7910:2005: Guide to methods for assessing the acceptability of flaws in metallic structures*, 2005.

115. Paris, P.C., Gomez, M.P. and Anderson, W.P., *A rational analytic theory of fatigue.* The Trend in Engineering, 1961. **13**: p. 9 - 14.

116. Paris, P.C. and Erdogan, F., *A critical analysis of crack propagation laws.* Journal of Basic Engineering, 1963. **85**(4): p. 528 - 534.

117. Xiang, Y. and Liu, Y., *Mechanism modelling of shot peening effect on fatigue life prediction.* Fatigue and Fracture of Engineering Materials and Structures, 2010. **33**(2): p. 116 - 125.

118. Vasudevan, A.K., Sadananda, K. and Glinka, G., *Critical parameters for fatigue damage.* International Journal of Fatigue, 2001. **23**(Supplement 1): p. 39 - 53.

119. British Energy Generation Ltd., *R5 - Assessment procedure for the high temperature response of structures. Issue 3*, 2003.

120. McClung, R.C., *Analysis of fatigue crack closure during simulated threshold testing*, in *STP 1372*, *Fatigue Crack Growth Thresholds, Endurance Limits, and Design,* Newman, J.C. and Poascik, R.S., Editors. 2000. West Conshohocken, PA: ASTM: p. 209 – 226.

121. Li, J.K., Mei, Y. and Duo, W., *An analysis of stress concentrations caused by shot peening and its application in predicting fatigue strength.* Fatigue and Fracture of Engineering Materials and Structures, 1992.**15**(12): p. 1271 – 1279.

122. Dowling, N.E., *Mechanical behaviour of materials - Engineering methods for deformation, fracture and fatigue*. 2nd edn.;1999, Upper Saddle, NJ: Prentice-Hall.

123. Bueckner, H.F., *A novel principle for the computation of stress intensity factors.* Zeitschrift für Angewandte Mathematik und Mechanik, 1970. **50**: p. 529 - 546.

124. Wu, X.R. and Carlsson, A.J., *Weight functions and stress intensity factor solutions.* 1991, Oxford, UK: Pergamon Press.

125. Knott, J.F., Bowen, P., Luo, J., Jiang, H. and Sun, H.L., *The structural integrity of cast aluminium automotive components subjected to fatigue loads.* Materials Science Forum, 2000. **331 - 337**: p. 1401 - 1412.

126. Winderlich, B., *Das konzept der lokalen dauerfestigkeit und seine anwendung auf martensitische randschichten, insbesondere laserhärtungsschichten.* Materialwissenschaft und Werkstofftechnik, 1990. **21**(10): p. 378 - 389.

127. Schulze, V., Hoffmeister, J. and Klemenz, M., *Correlation of mechanical surface treatments, induced surface states and fatigue performance of steel components.* Procedia Engineering, 2011. **19**: p. 324 - 330.

128. Lei, Y., O'Dowd, N.P. and Webster, G.A., *Fracture mechanics analysis of a crack in a residual stress field.* International Journal of Fracture, 2000. **106**(3): p. 195 - 216.

129. Korsunsky, A.M., *On the modelling of residual stresses due to surface peening using eigenstrain distributions.* Journal of Strain Analysis, 2005. **40**(8): p. 817 - 824.

130. Jun, T.-S., Venter, A.M. and Korsunsky, A.M., *Inverse eigenstrain analysis of the effect of non-uniform sample shape on the residual stress due to shot peening.* Experimental Mechanics, 2011. **51**(2): p. 165 - 174.

131. Jun, T.-S. and Korsunsky, A.M., *Evaluation of residual stresses and strains using the eigenstrain reconstruction method.* International Journal of Solids and Structures, 2010. **47**(13): p. 1678 - 1686.

132. Cláudio, R.A., Silva, J.M., Branco, C.M. and Byrne, J., *Fatigue life prediction of shot peened components.* Ciência e Technologia dos Materiais, 2008. **20**(1-2): p. 99 - 105.

133. Cláudio, R.A., Burgess, A., Branco, C.M. and Byrne, J., *Failure analysis of scratch damaged shot peened simulated components at high temperature.* Engineering Failure Analysis, 2009. **16**(4): p. 1208 - 1220.

134. Cláudio, R.A., Silva, J.M., Branco, C.M. and Byrne, J., *The ability of current models for fatigue life prediction of shot peened components.* Key Engineering Materials, 2010. **417 - 418**: p. 901 - 904.

135. Cláudio, R.A., Silva, J.M., Branco, J.M. and Byrne, J., *A fracture mechanics based approach to predict fatigue life of scratch damaged shot peened components.* Procedia Engineering, 2011. **10**: p. 2672 - 2677.

136. Benedetti, M., Fontanari, V., Santus, C. and Bandini, M., *Notch fatigue behaviour of shot peened high-strength aluminium alloys: Experiments and predictions using a critical distance method.* International Journal of Fatigue, 2010. **32**(10): p. 1600 - 1611.

137. Jun, T.-S., Venter, A.M., la Grange, C.P., Hofmann, F., Belnoue, J., van Heerden, P.R., Evans, A. and Korsunsky, A.M., *Eigenstrain analysis of non-uniformly shaped shot peened samples.* Procedia Engineering, 2009. **1**(1): p. 151 - 154.

138. Liu, J., Yuan, H. and Liao, R., *Prediction of fatigue crack growth and residual stress relaxations in shot-peened material.* Materials Science and Engineering A, 2010. **527**: p. 5962 - 5968.

139. Fathallah, R., Laamouri, A., Sidhom, H. and Braham, C., *High cycle fatigue behaviour prediction of shot-peened parts.* International Journal of Fatigue, 2004. **26**(10): p. 1053 - 1067.

140. Dang Van, K., *Sur la résistance à la fatigue des méteaux*. 1973, PhD Thesis: Scientifique et Technologique l'Armenent: Paris.

Chapter 3

Material characterisation

3.1. Introduction

Characterising the microstructure and mechanical properties of the material under investigation is an essential precursor to determining the effects of shot peening in Chapter 4 and subsequent fatigue in Chapter 5. An understanding of the material microstructure is required in developing electron backscatter diffraction (EBSD) techniques for measuring plastic strain and interpreting fracture surfaces; whilst data defining the mechanical properties (and calibrating appropriate constitutive models) is needed to determine the local stresses and strains in a sample or component under cyclic load.

In this chapter the microstructure of the material is investigated using standard metallographic techniques and compared with the microstructure expected in a 9-12 Cr steel (Section 1.2). Similarly, monotonic material properties are determined using standard techniques. The discussion regarding cyclic material properties in 9-12 Cr steels in Section 1.3.1 indicated that although cyclic softening is the common trend for the majority of life in these materials, this may be preceded in the first few cycles by either cyclic hardening or more rapid cyclic softening. Hence data defining the behaviour of the specific material in question is required in developing constitutive models which can account for this behaviour. Some aspects of the work detailed in this chapter have been published in the following paper:

K. A. Soady, B. G. Mellor, G. D. West, G. Harrison, A. Morris and P. A. S. Reed, *Evaluating surface deformation and near surface strain hardening resulting from shot peening a tempered martensitic steel and application to low cycle fatigue.* In press, International Journal of Fatigue, 2013, **DOI:10.1016/j.ijfatigue.2013.03.019**.

3.1.1. Determining cyclic stress-strain behaviour

Cyclic hardening and softening are best determined by consideration of the stress response to strain control loading (fully constrained loading conditions) since in components there is a degree of structural constraint at fatigue critical sites [1]. There are three strain controlled test methods commonly used to generate cyclic stress strain data, each with advantages and disadvantages in terms of test matrix size, material parameters and loading regimes which can be characterised with the resulting data.

Single step, constant strain amplitude tests offer the most comprehensive material characterisation for non-variable amplitude loading regimes. Multiple tests at different strain amplitudes are required; whilst there is some experimental scatter that may result from the use of many test samples the method provides full evolutionary details at each strain range as well as stabilised hysteresis loops [1, 2], the loci of which are used to determine the stabilised cyclic stress-strain curve. Assuming the material stabilises, the alternative multiple step and the incremental step methods [3] both allow the derivation of the stabilised cyclic stress-strain curve from multiple stabilised hysteresis loops at varying strain ranges from just one sample, reducing variability in the results. These approaches are unsuitable however when evolutionary coefficients for the hardening or softening response of the material are required. Strain control programmes for the three test procedures are illustrated in Figure 3- 1.

The multiple step test involves cycling a sample between constant strain limits until saturation is deemed to have occurred, this can be determined by closure of the hysteresis loops. The strain limits are then incremented until another stable hysteresis loop is obtained; the increment should be gradual to prevent the build-up of mean stresses and it is typically recommended that stable loops be obtained at each strain level under both increasing and decreasing strain amplitudes. The cyclically stabilised curve derived from the multiple step test has been shown to coincide well with that derived from single step tests [3-5].

The incremental step test imposes blocks of gradually and symmetrically increasing and decreasing total strain limits on a sample; each block consists of 20-30 cycles. Saturation is deemed to have occurred when the loci of successive blocks stabilise. Whilst this method was originally shown to result in similar behaviour to the single and multiple step tests [3], subsequent work has shown that the incremental step test results in a different cyclically stabilised curve [1, 4-6] (especially in low stacking fault energy alloys which exhibit planar slip [1]). This incremental step curve is more representative of the behaviour under variable amplitude loading and typically lies between the stress-strain curve from constant amplitude tests and the loading half hysteresis loop at the maximum strain. This is a result of the dependence of the cyclic stress-strain response on the dislocation structure and the transients in this structure with changing strain range [4-6]; indeed it has been shown that the stress-strain curve from the incremental step test is dependent on both the rate of strain amplitude change and the maximum strain amplitude [4, 6].

The present investigation is concerned only with constant amplitude loading; hence the incremental step test was not applied. Constant strain amplitude tests were selected as being appropriate for the derivation of evolutionary constants and an initial cyclically stabilised stress-strain curve; both of which are required for the sensitivity study

detailed in Chapter 5. Should the cyclically stabilised material model be demonstrated to be the most appropriate material model, multiple step tests could be used to derive the curve based on more data points and thus with improved reliability.

A statistical analysis of the first and second derivatives of the hysteresis loops from constant amplitude loading and comparison with dislocation structures imaged using transmission electron microscopy (TEM) can reveal the micro-mechanistic reasons for the specific response of a material [7]. Whilst this is beyond the scope of the present investigation (which is concerned with the development of constitutive models describing the cyclic mechanical response of the material and allowing for this in the determination of the local stress-strain response of components under fatigue loading), the dataset generated could be used to this end (with the addition of TEM micrographs) should, for example, the material response be significantly different at different total strains, or to that previously reported in the literature and a micro-mechanical explanation be required.

3.1.2. Constitutive models for components subjected to cyclic loads

There are two broad approaches to modelling cyclic stress-strain behaviour; model selection primarily depends on whether it is necessary to model the evolution of the stress-strain in a component or not. Where stabilised behaviour is sufficient, a simple law such as the cyclic Ramberg-Osgood relationship (Equation 3-1) can be defined relating strain range ($\Delta\varepsilon$) to stress range ($\Delta\sigma$) based on the stabilised cyclic stress-strain curve.

$$\frac{\Delta\epsilon}{2} = \frac{\Delta\sigma}{2E} + \left(\frac{\Delta\sigma}{2A'}\right)^{\frac{1}{n_f}} \quad (3\text{-}1)$$

Where E is the Young's modulus, n_f is the cyclic strain hardening exponent and A' is a constant. Although cyclic loading cannot be directly represented because the model is not expressed in incremental form, the cyclic Ramberg-Osgood relationship can be used to specify an appropriate material model which can be used to model local stress and strain parameters in a cyclically stabilised component. This approach has the benefit of not considering evolutionary behaviour and as such requires significantly less computational effort than the alternative approach which does allow for evolutionary behaviour but which requires each component cycle to be modelled.

Modelling evolutionary behaviour is usually only necessary in materials which continuously harden or soften, which show distinctly different behaviour at varying total strain amplitudes, or, when modelling components which experience only a few major cycles or which have isolated regions undergoing cyclic plasticity at different strain ranges [2]. Several constitutive relations have been developed [8], some of which

(for example the combined isotropic and kinematic hardening model) are readily available within commercial FE software such as Abaqus Standard [9]. Each model has different capabilities in terms of the aspects of the cyclic deformation response it can predict. These include the Bauschinger effect, elastic shakedown, cyclic hardening or softening before a stable hysteresis loop is developed, ratchetting under stress controlled fatigue and mean stress relaxation under strain controlled fatigue [1].

The Bauschinger Effect is characterised by a reduction in yield strength upon load reversal from continued forward deformation (Section 2.1.2); the effect may be significant in low cycle fatigue (LCF) situations and can be represented by kinematic hardening [2]. Elastic shakedown occurs when plastic deformation in the first cycle (or few cycles in cyclically hardening materials) causes residual stresses such that the local cyclic stress range is less than the cyclic yield strength leading to an elastic deformation response. Plastic shakedown occurs under non-cumulative plastic strain, i.e. zero net plastic strain in a cycle [1, 2]. Isotropic hardening predicts an elastic response under uniaxial cyclic loading with a non-zero mean stress whereas linear kinematic hardening predicts a state of alternating plastic flow after the first cycle of loading [10]. If the plastic deformation under loading is not opposed by an equal amount of yielding in the reverse direction, a situation which often arises under non-zero mean stress control, cyclic creep, or ratchetting, occurs in the direction of the mean stress. The cyclic accumulation of plastic strain with each load cycle can lead to failure by plastic collapse rather than by LCF [10, 11]. In an analogous manner, under conditions of unsymmetrical strain cycling, the mean stress may relax. Both ratchetting and mean stress relaxation can be predicted by non-linear kinematic hardening models [8, 9].

The approaches to modelling cyclic plasticity can be classified into four groups (parallel sub-element models, field of work hardening moduli, two-surface models and combined isotropic and kinematic hardening models). These are well introduced elsewhere, for example by Suresh [1] and only the combined model is considered further in the present work which is concerned mainly with assessing the significance of allowing for the evolution of cyclic behaviour in determining local stress and strain parameters for use in fatigue assessment. This model is already available within the Abaqus Standard software package [9] and does not require the use of user subroutines. Chaboche and collaborators are usually credited with the development of this model [2]; indeed Chaboche has written a recent review article [8] which provides a much more detailed mathematical consideration of the model than is discussed here. The present introduction to constitutive modelling is drawn primarily from Hales *et al.* [2] and the relevant sections of the Chaboche review [8], with reference to the Abaqus

user manual [9] since this defines the model that is to be employed in the sensitivity study in Chapter 5.

In constitutive modelling, the concept of the yield surface is introduced: The stress point remains on the yield surface as the material plastically deforms; to account for this the surface may expand, contract, translate or distort. Isotropic hardening is represented by a uniform expansion of the yield surface with no shape change or translation; kinematic hardening is represented by a translation of the yield surface in the direction of the outward normal. The Bauschinger effect is not present in an ideally isotropically hardening material model; elastic shakedown cannot be modelled by a purely kinematically hardening material model [1]. As a result, it is common for combined models to be implemented. The differences between these hardening models are illustrated in principal stress space assuming a circular von Mises yield surface in Figure 3- 2.

The yield surface is defined according to Equation 3-2.

$$F = f(\boldsymbol{\sigma} - \boldsymbol{\alpha}) - \sigma^0 \tag{3- 2}$$

Where $f(\boldsymbol{\sigma} - \boldsymbol{\alpha})$ is the equivalent Mises stress with respect to the backstress, $\boldsymbol{\alpha}$, and σ^0 is the size of the yield surface. The backstress represents the kinematic shift or the translation of the initial yield surface.

In combined models, the isotropic hardening component is represented by the change in σ^0 as a function of equivalent plastic strain $\bar{\epsilon}^{pl}$. This is typically specified using the exponential law in Equation 3-3.

$$\sigma^0 = \sigma|_0 + Q_\infty \left(1 - \exp^{-b\bar{\epsilon}^{pl}}\right) \tag{3- 3}$$

Where $\sigma|_0$ is the yield stress at zero plastic strain, Q_∞ is the maximum change in the size of the yield surface and b defines the rate at which the size of the yield surface changes as plastic strain accumulates. When the equivalent stress defining the size of the yield surface remains constant ($\sigma^0 = \sigma|_0$), the model reduces to a nonlinear kinematic hardening model. It is noted that should variable amplitude loading be significant, the resulting transient effects can be incorporated by making Q a function of q which evolves progressively with current plastic strain range such that Q_∞ is now $Q(q)$ [8].

The kinematic hardening component describes yield surface translation in terms of $\boldsymbol{\alpha}$. This component consists of a purely kinematic term and a relaxation term which introduces non-linearity, most commonly, non-linear kinematic hardening laws are based on the Armstrong-Frederick model [12]. Several backstresses may be superposed providing flexibility when fitting data and often improving the modelling

capability for the kinematic term [8], although with too many, the uniqueness of each becomes increasingly uncertain [2].

The hardening law (neglecting temperature and field dependencies) for each backstress is given in Equation 3-4. The overall backstress is calculated using Equation 3-5.

$$\dot{\boldsymbol{\alpha}}_k = C_k \frac{1}{\sigma^0}(\sigma - \alpha)\dot{\bar{\epsilon}}^{pl} - \gamma_k \boldsymbol{\alpha}_k \dot{\bar{\epsilon}}^{pl} \quad (3\text{-}4)$$

$$\boldsymbol{\alpha} = \sum_{k=1}^{N_\alpha} \boldsymbol{\alpha}_k \quad (3\text{-}5)$$

Where N_α is the number of backstresses, C_k are the initial kinematic hardening moduli, and γ_k determine the rate at which the kinematic hardening moduli decrease with increasing plastic deformation. When γ_k is zero, the kinematic term becomes linear. When both C_k and γ_k are zero, the model reduces to an isotropic hardening model. It is noted that the model also allows the input of initial conditions to prescribe an initial equivalent plastic strain value and/or the backstress tensor for a given element set. This capability may be useful when modelling material which has already been hardened, for example in the present work, by the shot peening process [9]. One identified drawback of this model is the tendency of non-linear kinematic hardening to over-predict ratchetting for some materials [2]; this can be improved by using several backstresses, one of which is linear and thus incapable of predicting ratchetting.

Many constitutive modelling methods which allow for improvements in the prediction of ratchetting for stress controlled cycling at non-zero mean stress have been developed (and are extensively reviewed in [13]), however they will not be considered further in the present work which is concerned with LCF in regions of high constraint and which are thus operated under strain control. Mean strain effects have been shown to have a negligible effect on LCF life which was dominated by strain amplitude in a tempered 42CrMo steel which showed similar cyclic softening behaviour as the 9-12Cr steels under present investigation [11]. It should be noted that this assumption is not valid for asymmetrical stress controlled cycling because ratchetting resulting from tensile mean stresses was shown to be detrimental to LCF life [11].

3.2. Experimental methods

3.2.1. Material microstructure

The 9-12 %Cr steel representative of those applied in low pressure turbine blades used throughout this work was FV448; barstock material was supplied by E.ON New Build and Technology. The nominal composition and the results of a spectrographic analysis

(carried out by Southdown Materials Testing Ltd.) are detailed in Table 3- 1. The material is typically austenitised at 1150 °C, oil quenched, tempered at 650 °C and then air cooled [14].

Samples were prepared to a 1 μm finish for microstructural analysis following the standard grinding and polishing method for steels. The final polishing stage used a 1 μm diamond paste on a Severn Sales S-Plan cloth with Struers DP-Lubricant purple. Vilella's Reagent (5 ml hydrochloric acid and 1 g picric acid in 100 ml ethanol) was used to etch the samples to reveal the microstructure. Optical micrographs were obtained using an Olympus BH2 Optical Microscope. Both plain polished and etched specimens were examined using both secondary electron imaging (SEI) and backscattered electron imaging (BEI) on a JSM 6500F field emission gun scanning electron microscope (FEG-SEM). Energy dispersive X-ray spectroscopy (EDX) was also used on areas of specific interest.

3.2.2. Mechanical properties

3.2.2.1. Baseline hardness and monotonic data

Microhardness testing was carried out in accordance with BS EN ISO 6507-1:2005 [16] using a Matsuzawa Seiki Co. tester. Indents were made under 200 g with 15 s dwell. For baseline material property characterisation, indent dimensions were measured using the ocular micrometer fitted to the test equipment. Before testing, a calibration was carried out using a standard test block and the sample results were adjusted using the appropriate linear correction factor.

Tensile testing was carried out to failure on two samples of dimension illustrated in Figure 3- 3a in accordance with BS EN 10002-1:2001 [17]. Testing was carried out on an electromechanical Instron 5569 fitted with a 50 kN load cell at an extension rate of 0.3 $mmmin^{-1}$. Ignoring load frame compliance effects, this extension rate corresponds to a strain rate of $1.8x10^{-4}$ s^{-1} on a sample of gauge length 28 mm. An extensometer of gauge length 12.5 mm was fitted to the centre of the parallel section in order to measure strain.

Compression testing was carried out on nine cylindrical samples (despite several being interrupted as described in Chapter 4, all contained sufficient data for determining Ramberg-Osgood coefficients) of dimension illustrated in Figure 3- 3b in accordance with ASTM E9-09 [18] at an extension rate of 0.1 $mmmin^{-1}$ using the same electromechanical Instron 5569. Ignoring load frame compliance effects, this compression rate corresponds to a strain rate of $2.5x10^{-4}$ s^{-1} on a sample of length 6.75 mm. Strain was measured using load frame load - displacement data corrected for

machine compliance; this measurement technique was verified using extensometer readings taken across the loading platens.

3.2.2.2. Cyclic stress-strain characteristics

Constant amplitude strain controlled axial fatigue tests were carried out at four total strain ranges ($\Delta\varepsilon$ = 0.0050, 0.0080, 0.0110, 0.0155); the lower strain ranges ensured that overall range covered the total strain ranges used in the S-N testing of notched samples described in Chapter 5 whilst the higher strain ranges were used to determine the influence of strain range on the cyclic behaviour. Tests were in accordance with BS 7270:2006 [19] and the recommendations provided by Hales *et al.* [2]; the geometry of the cylindrical samples used is illustrated in Figure 3- 4. Fatigue testing was carried out using a triangular waveform and a strain rate of $3\text{x}10^{-3}$ s^{-1}. Strain was controlled using a 12.5 mm gauge length extensometer; load and strain data were both recorded at a frequency such that a minimum of 500 data points were recorded per cycle.

Testing at the lowest strain range $\Delta\varepsilon$ = 0.0050 was at strain ratio R_ε = 0 since the material would not be expected to yield at the peak strain of 0.0025 that would be reached if testing was fully reversed at R_ε = -1. This dataset was used to demonstrate elastic shakedown. Once the peak strain under R_ε = -1 loading was sufficient to cause yielding (i.e. $\Delta\varepsilon$ = 0.0080, 0.0110, 0.0155), a combined isotropic and kinematic hardening material model was required, the development of which requires data obtained under R_ε = -1. Since fatigue loading in components (and the S-N fatigue test samples used in Chapter 5) often occurs under a tensile mean strain, an additional test at R_ε = 0 was carried out at the highest strain range implemented ($\Delta\varepsilon$ = 0.0155) to confirm that there was no effect on the cyclic stress-strain behaviour as suggested by Hales *et al.* [2] and shown by Kang and Liu [11]. No ramping was applied at start-up to eliminate any possible coaxing effects[1] described by other authors [20, 21]; instead the settings on the proportional-integral-derivative controller were carefully set to ensure that complete cycling with minimal overshoot began on the first cycle.

[1] Coaxing occurs in total strain controlled tests as a result of the dependence of the dislocation structure on the loading history. It has previously been shown [20] that the saturated plastic strain amplitude decreases as the duration of the ramp in numbers of cycles increases; alternatively this can be described as an increase in the fatigue limit by gradually increasing the load in small increments. Coaxing is most significant in strain ageing materials [21]: Although not identified in 9-12 %Cr steels in ambient conditions, serrated flow and dynamic strain ageing has been identified at intermediate temperatures ($250 < T < 400$ °C) [22]. Setting the test up in this manner would allow for the extension of the method to more service representative conditions.

3.3. Results

3.3.1. Material microstructure

Optical micrographs showing the material microstructure relative to barstock orientation (longitudinal (rolling direction), L, transverse, T and short-transverse, S directions) are shown in Figure 3- 5; these images are combined into a three dimensional representation of the material in Figure 3- 6. The microstructure is that of tempered martensite. The material microstructure can also be visualised using SEI on the SEM resulting in micrographs such as that illustrated in Figure 3- 7. In all three figures the prior austenite grain boundaries can be clearly identified; furthermore, despite it being possible to locate carbides at the grain boundaries, the intragranular carbides are much harder to visualise, even in the higher magnification SEI image shown in Figure 3- 7b.

To obtain information on the carbide distribution and to determine whether aluminium oxide stringers were present in the microstructure as had previously been reported for the similar FV566 [23], BEI was used on the SEM. The resulting micrographs relative to the barstock orientation are shown in Figure 3- 8.

There is no evidence of directionality in grains or aluminium oxide stringers in either Figure 3- 5 or Figure 3- 8. However, the scale of Figure 3- 8 is such that the distribution of smaller second phases cannot be easily identified. This distribution is shown more clearly in the longitudinal direction in Figure 3- 9.

The result of an EDX analysis on the particle shown in Figure 3- 9 is reported in Table 3- 2; it is noted that the average error for these measurements is ±1.35 %.

3.3.2. Monotonic mechanical properties and associated constitutive models

The Vickers hardness of the baseline material was found to be 301.0 ± 5.0. The monotonic tension and compression (shown as positive values) data in the transverse direction is shown in Figure 3- 10 a and b respectively. This direction was selected for analysis because it corresponded with the tensile axis in all the S-N testing (Chapter 5). Also shown are the associated constitutive models. The tensile experimental data showed good agreement between the two samples and the Ramberg-Osgood material model was developed based on the average of the two curves, noting that the average elongation at failure was 12 %. There are several other material models shown in Figure 3- 10a, these models were used in the sensitivity study described in Chapter 5 to determine the best material model for describing the local stress and strain at the notch root of a three point bend fatigue sample.

The elastic modulus found to be most representative for the material was 201.3 GPa. The Ramberg-Osgood model was used as the basis for an isotropic hardening material model specified by stress-plastic strain (σ – ε_p) pairs; to reduce errors, the first point was not the 0.2 % proof stress, $\sigma_{0.2}$, but the deviation from linearity (defined when ε_p = $1x10^{-4}$) at 652 MPa. The associated coefficients were A = 1152 MPa and monotonic strain hardening exponent, n_m = 0.05865. A kinematic hardening material model was also developed using just one backstress ($C_{k=1}$ = 15000 MPa and $\gamma_{k=1}$ = 40); although there is quite a large deviation from the experimental curve, this model was only used to determine the possible significance of the Bauschinger Effect and was not used in the analysis of any samples. Similarly, the 0.2 % proof stress and plastic data points was a simple material model based on specifying just the yield strength (and drawing a straight line back through the origin) and the stress-strain data for one experimental sample and was used only in the sensitivity study to show the significance of using the correct elastic modulus. The bilinear model (σ^0 = $\sigma_{0.2}$ = 806 MPa and strain hardening rate H_1 = 2264) was developed for application in the analytical and finite element models of the shot peening process described further in Chapter 4.

There was slightly more variation in the compressive curves than the tensile curves and the Ramberg-Osgood model was developed based on the modal curve (experimental curves for three samples were found to overlay the representative experimental curve shown). Also shown for comparison are the upper and lower bounding experimental curves between which the experimental curves for the remaining six samples fell. The compressive Ramberg-Osgood curve is compared with the tensile curve in Figure 3- 11. It is noted that n_m remains relatively constant at 0.05560 in compression compared with 0.05865 in tension but that A increases from 1152 MPa in tension to 1210 MPa in compression. This increase reflects the higher σ^0 in compression of 842 MPa compared with that in tension of 806 MPa.

Tensile data was also obtained in the longitudinal (rolling) direction from the first half cycle of the cyclic stress-strain test at $\Delta\varepsilon$ = 0.0155 (i.e. up to total strain ε_t = 0.00775. This direction was used as it was the only direction from which cyclic stress-strain samples of geometry shown in Figure 3- 4 could be obtained. Since the dataset was limited to low strains, the Ramberg-Osgood curve previously defined in the transverse direction was scaled by changing A and keeping n_m constant resulting in A = 1230 MPa and n_m = 0.05865. As for the transverse Ramberg-Osgood material model, this was used to specify an isotropic hardening material model (deviation from linearity at 697 MPa) in the longitudinal direction for application in the sensitivity study in Chapter 5. The increase in $\sigma_{0.2}$ from 806 MPa in the transverse direction to 858 MPa in the longitudinal direction is illustrated in Figure 3- 12; the significance of this difference is investigated further in Chapter 5.

3.3.3. Cyclic stress-strain characteristics

From the transverse tensile Ramberg-Osgood relationship it was clear that if testing at the lowest strain range, $\Delta\varepsilon$ = 0.0050 were to occur at R_ε = -1, then no yielding would occur since the maximum strain of 0.0025 is still within the elastic region in Figure 3-10a. The hysteresis loops for the first few cycles for the test conducted at R_ε = 0 are shown in Figure 3- 13a; the peak stresses in each cycle are shown up to cycle 1000 in Figure 3- 13b. There is clear plastic deformation in the first cycle; subsequent cycles behave elastically only and there are no significant changes in the peak stress through life (the variation between cycle 2 and cycle 1000 is -15 MPa). This is an example of elastic shakedown and a combined hardening material model is not required at this strain range. It was noted that in the first cycle there was a slight overshoot in strain of 3 % which has caused a drop in peak stress between cycle 1 and cycle 2; this overshoot is too small to affect material behaviour but was nonetheless corrected to < 0.5 % in the higher strain range tests to prevent overshoot being the cause of apparent softening in the first cycle.

All of the R_ε = -1 tests at $\Delta\varepsilon$ = 0.0080, 0.0110, 0.0155 showed cyclic softening behaviour throughout life. The plastic strain under both tensile and compressive loading can be most easily visualised at the highest plastic strain at $\Delta\varepsilon$ = 0.0155 and is shown in Figure 3- 14; the drop in peak stress with increasing cycles can also be identified. The development of the peak stresses through life for all three strain ranges up to cycle 3500 is shown in Figure 3- 15a; the graph in Figure 3- 15b shows the development of peak tensile stress near the beginning of life where softening is most significant.

At all strain ranges there is very clear cyclic softening through life; initially this softening is very rapid before slowing to a relatively constant through life rate. The rate of cyclic softening appears to be dependent on the strain range with a faster rate shown at higher strain ranges. Whilst this through life rate is still relatively rapid at higher strain rates, a quasi-plateau (Figure 1-5) appears to form at $\Delta\varepsilon$ = 0.0080 after 1500 cycles when the rate of softening becomes very low. The onset of cracking at $\Delta\varepsilon$ = 0.0110 and 0.0155 is clear in Figure 3- 15b; this sudden drop in peak stress was used to define the end of life.

This data was used to define a cyclic stress-strain curve for the material; since softening appears to continue throughout life, stabilisation was assumed to have occurred once the peak stress in a cycle was within 2 % of the peak stress at the end of life. The cycles at which stabilisation occurred and the associated life fraction are tabulated in Table 3- 3. The average life fraction at which the failure stress + 2 %

condition was met was 0.49; hence this approach is very similar to the alternative approach of taking the stress at half the fatigue life [6].

The hysteresis loops corresponding to the cycles listed in Table 3- 3 are shown in Figure 3- 16. The Ramberg-Osgood relationship was again scaled to minimise the error based on the three maximum tensile stress data points resulting in A' = 1100 MPa (a drop of 10.6 % compared to the monotonic data in the longitudinal direction) and n_f = 0.05865. The resulting maximum and minimum stresses predicted by the model for each strain range are also tabulated in Table 3- 3. This cyclically stabilised model was considered sufficiently well-defined for the sensitivity study detailed in Chapter 5; should this model prove the most appropriate for a given system, the multiple step test could be implemented to define the stabilised curve with improved accuracy.

A combined isotropic and non-linear kinematic hardening model was also developed for each strain range. The model development is detailed for $\Delta\varepsilon$ = 0.0155 because the process can be most clearly visualised at higher strain ranges. It is noted that the model is optimised for through life behaviour and the first experimental cycle is not considered due to anomalous behaviour in the first half cycle.

The yield surface was defined according to Equation 3-2. The isotropic and kinematic hardening components were defined according to Equations 3-3 and 3-4 respectively; the fitting of the isotropic and kinematic components is illustrated in Figure 3- 17a and Figure 3- 17b respectively. From Figure 3- 17a it can be seen that the change in yield surface is well modelled apart from at the end of life; this is not considered a problem as components would not be expected to operate in this regime. The use of just one backstress was found to be sufficient to represent the material behaviour well as illustrated in Figure 3- 17b.

Once calibrated, the model was implemented in Abaqus Standard as a single cell displacement controlled representation of the cyclic test $\Delta\varepsilon$ = 0.0155, R_ε = -1. An example hysteresis loop and the resulting peak stress development are compared with the experimental data in Figure 3- 18a and Figure 3- 18b respectively.

The example hysteresis loop in Figure 3- 18a shows how well the model represents the behaviour under cyclic load. It is, however, evident in Figure 3- 18b and Figure 3- 19a that the peak stress in the first cycle is not well modelled; other than this error, however, both the peak tensile and compressive stresses are well represented through life with maximum errors of 1.6 % and 2.7 % respectively.

The peak stress in the first cycle is not well represented because the model is optimised based on the behaviour in the second cycle. This modelling protocol was selected because of the apparent step change in maximum stress at all the strain

ranges shown in Figure 3- 15b. The overshoot in strain that caused this step change at $\Delta\varepsilon$ = 0.0050 was not the cause in Figure 3- 15b since there was no overshoot at $\Delta\varepsilon$ = 0.0080 or 0.0155 and only a 0.5 % overshoot at 0.0110. The cause of the error was investigated further by considering both the experimental and the model hysteresis loops for the first cycle shown in Figure 3- 19a.

It is clear from Figure 3- 19a that the first tensile half cycle is not well modelled using the constants optimised for cycle 2 and through life performance. Increasing the initial yield stress made optimising Q_∞ for through life performance difficult; it is also apparent that the shape of the plastic part of the cycle is incorrect, this is a result of a change in kinematic coefficients after one load reversal. This can be visualised by consideration of Figure 3- 19b; optimising the model based on the first cycle results in poor predictions of cyclic performance after one load reversal. Since this was true for all strain ranges under consideration, it was decided to optimise the models for fatigue applications at each strain range based on the behaviour exhibited from cycle 2 onwards. The resulting constants are tabulated in Table 3- 4 and the modelled through life peak stresses are compared with the experimental data in Figure 3- 20. The combined models predict through life peak stresses well for all but the $\Delta\varepsilon$ = 0.0110 sample in compression for the first 70 cycles; a statistical analysis of the models' performance against experimental data is given in Table 3- 5. Also tabulated are the statistical results of the cyclically stabilised model, assuming that the maximum and minimum stresses predicted (Table 3- 3) are the same in each cycle through life.

The average error in peak stress resulting from the combined model is less than 1.5 %. When comparing the average error, the cyclically stabilised model also appears to perform reasonably well with the highest average absolute error per cycle only 5.1 %. However, it is in the maximum absolute error in a half cycle that the combined model performs much better than the cyclically stabilised model; the maximum error in the combined model is 7.6 % whereas for the stabilised model it is 13.3 %. For both models, the highest error always occurs in the first cycle. However, error for the combined model is typically reduced to <2.5 % by the second cycle ($\Delta\varepsilon$ = 0.0110 excluded, it takes 40 cycles at this strain range), whereas for the stabilised model the error is much higher to begin with and reduces more slowly. This results in a greater standard deviation in the error for the stabilised model.

One test was also carried out at $\Delta\varepsilon$ = 0.0155, R_ε = 0 to determine the dependence of the model on R_ε and whether the material model derived from R_ε = -1 data was applicable at other strain ratios. The results are shown in Figure 3- 21; apart from the slightly anomalous initial hardening behaviour shown in the experimental compression data, the model optimised at R_ε = -1 is sufficient to describe the behaviour at higher strain ratios. A similar statistical comparison to that made for R_ε = -1 is made for this

dataset in Table 3- 6 noting that when loading is not fully reversed, the Ramberg-Osgood model in its original form (i.e. with no unloading criterion specified) can only predict loading behaviour for the first half cycle; this is a clear disadvantage of the stabilised model in this form so the curve was converted to an isotropically hardening material model allowing unloading and the determination of the minimum stress. The resulting maximum and minimum stresses were 846 MPa and -860 MPa respectively.

The maximum absolute error from the combined model when predicting $R_\varepsilon = 0$ behaviour is slightly greater than when predicting $R_\varepsilon = -1$ behaviour at 10.7 %. This error still occurs in the first cycle (this time as a result of the hardening behaviour in compression); the error is reduced to < 2.5 % after 7 cycles. It is noted that the average absolute error and standard deviation in the error is of the same order as when comparing the $R_\varepsilon = -1$ model with the $R_\varepsilon = -1$ experimental data in Table 3- 5. The maximum stress is not as well predicted by the stabilised model at $R_\varepsilon = 0$ as it was at $R_\varepsilon = -1$, since all three statistical parameters in Table 3- 6 are greater than those shown in Table 3- 5.

3.4. Discussion

3.4.1. Material microstructure

The microstructural images illustrated (Figure 3- 5 to Figure 3- 8) show similarities with those in the literature [23]. The scale of the images in Figure 3- 8 is sufficient that any aluminium oxide stringers present in FV448 (as reported by Perkins and Bache in FV566 [23]) would be visible. The lack of oxide stringers in the microstructure means that initiation life is not likely to be significantly different between the three directions as was the case in FV566 [23]. Despite there being no apparent differences in the microstructure with orientation in the barstock, as a result of the rolling process applied during manufacturing the material is slightly stronger in the longitudinal direction than in the transverse direction (Figure 3- 12), the difference is not thought to be significant enough to have an effect on fatigue life characteristics and as such the S-N data reported in Chapter 5 is all measured in the transverse direction.

The EDX analysis shown in Table 3- 2 is sufficient to conclude that the large particle analysed is niobium rich, however, the significant quantities of iron and chromium reported indicate that the spot size used during the analysis was too large to analyse the composition of individual particles, even for the relatively large niobium rich particle analysed. When attempted on the smaller particles shown in Figure 3- 9, the matrix dominated the results and it was not even possible to assess the type of particle present. Since it has previously been reported that quantitative EDX analysis on second phase particles in this material is difficult [24] this result was not entirely unexpected,

so an alternative theoretical analysis based on the precipitate appearance and the phases identified in Section 1.2.2 was used to at least identify the likely precipitate type.

The backscatter coefficient, η_i, was calculated based on the atomic number, *Z,* using Equation 3-6; for phases with more than one element, the total backscatter coefficient, η, was calculated using the rule of mixtures given in Equation 3-7 where f_i is the weight fraction. From this it was determined whether the particle appears darker or brighter than the matrix. Finally the contrast, C_{ph}, between two phases of backscattered coefficients η_A and η_B where $\eta_A < \eta_B$ was calculated as a percentage using Equation 3-8 [25]. The results for FV448 are detailed in Table 3- 7.

$$\eta_i = -0.0254 + 0.016Z - 1.86 \times 10^{-4}Z^2 + 8.3 \times 10^{-7}Z^3 \quad (3\text{- }6)$$

$$\eta = \sum f_i \eta_i \quad (3\text{- }7)$$

$$C_{ph} = \left(\frac{(\eta_B - \eta_A)}{\eta_B}\right) \times 100 \quad (3\text{- }8)$$

Based on the information in Table 3- 7 and the relative size of the particles, the likely composition of the second phase particles is summarised in Table 3- 8. The large bright particles were shown using EDX to be niobium rich; these are likely to be primary Nb(C,N) particles which remained undissolved during austenitisation and are known to be coarser than the secondary particles [26]. The large dark particles are most likely to be $Cr_{23}C_6$, which is known to be larger than the secondary MX and M_2X phases [24, 27-30]. No distinctions can be made between the small secondary phases other than whether they are bright or dark since the contrasts are so similar.

Given the typical tempering temperature of 650 ˚C, M_2X would be expected to dominate over MX, although it is noted that both may be present (Figure 1-4). The Mo:V ratio of FV448 is nominally 5 (Table 3- 1), although it is noted that in the spectrographic analysis, it was only 2 (Table 3- 1). Based on the work of Janovec *et al.* [31], given a ratio of 5, we would expect a weight percent ratio of Mo:Cr in M_2X of 3 and a thus a dominance of $Mo_2(C, N)$ particles over $Cr_2(C, N)$ particles; with the observed ratio of Mo:V reduced to 2, this dominance may be less pronounced.

3.4.2. Mechanical behaviour

There is a clear physical relationship between hardness, H_v, and yield strength; increasing yield strength results in an increased resistance to plastic deformation, a smaller indent and a higher hardness. Cahoon *et al.* [32] related hardness (in $kgfmm^{-2}$) to yield strength and strain hardening exponent, n_m, in steel using Equation 3-9 whilst Pavlina and van Tyne [33] used experimental data for 66 (tempered and untempered)

martensitic steels to generate the linear relationship in Equation 3-10 (hardness again in kgfmm^{-2}) with R^2 = 0.9088. Using the $H_{v0.2}$ value for FV448 of 301 kgfmm^{-2} results in σ^0 = 860 MPa and 866 MPa from Equations 3-9 and 3-10 respectively. These results are both within 1 % of the experimental σ^0 in the longitudinal direction of 858 MPa; given the triaxial stress field which results from indentation, it is not surprising that the yield strength in the strongest direction in the barstock is reflected by the hardness value.

$$\sigma^0 = \frac{9.81H_v}{3}(0.1)^{n_m} \quad (3\text{- }9)$$

$$\sigma^0 = 110.9 + 2.507H_v \quad (3\text{- }10)$$

Barstock material is typically manufactured by rolling or extrusion; it is therefore to be expected that the material shows different monotonic behaviour in the transverse and longitudinal directions. Whilst the 6.5 % difference in σ^0 may seem quite small, it may be significant when determining the local stress and strain characteristics in the fatigue samples and was one of the reasons why the sensitivity study (Chapter 5) was conducted.

The data in Figure 3- 11 suggests that FV448 is stronger in compression than in tension with a difference in σ^0 of 4.4 %. This conclusion is supported by the data taken from the cyclic stress-strain tests in the longitudinal direction in Table 3- 9 in which the peak stress is greater under compression than for tension for a given strain magnitude. It is clear that the peak stresses reached in compression are greater than those in tension; this is particularly apparent at the higher strain ranges, at the peak strain of 0.0040 in the $\Delta\varepsilon$ = 0.0080 test, the material is only just beyond yield and the resulting asymmetry effect is smaller. Indeed the asymmetry can be seen to be greatest in the $\Delta\varepsilon$ = 0.0110 test; this is the reason for the poor modelling of the compressive peak stresses by the combined model at this strain range since the isotropic component was modelled based on the tensile σ^0 behaviour. This tension-compression asymmetry was investigated extensively in many materials, particularly both untempered and tempered martensitic steels in the 1970s [34-37] and has more recently been reported in a similar 9Cr-1Mo steel where the increase in σ^0 in compression compared to tension was of a similar order to the present investigation at 3.8 % [38]. This phenomenon, also termed the strength-differential effect, has been said to be the result of an inhibiting effect of hydrostatic pressure (mean stress) on shear activated slip in grains [34, 39], although a more recent text indicates that this phenomenon is still not well understood [40].

Significant effort has been invested in developing constitutive relations which account for the strength differential (see for example [41-44]). Such models can account for behaviour under cyclic loading by incorporation with combined isotropic and kinematic

hardening behaviour, but are typically non-trivial as a result of their calibration requirements and user-subroutine implementation [43]. Such models do offer clear advantages over models which assume there is no difference in flow stress between tension and compression, for example, ratchetting is usually present under stress control when there is a non-zero mean stress, however it may occur at zero mean stress when tension-compression asymmetry is present [38] and can be predicted by constitutive models which incorporate these effects [44]. Such effects are most likely to be problematic under stress control [11]; under strain control the strength differential is more likely to manifest itself as a difference in peak stresses between tension and compression as shown in Table 3- 9.

These differences in peak stress in tension and compression do result in errors in the combined model which is formulated based on the Mises yield surface and is thus unable to account for the strength differential. The maximum absolute errors in the combined model reported in Table 3- 5 were always in the first cycle and were either the result of the poor modelling of the first half cycle or an under-prediction of peak compressive stress as a result of asymmetry and modelling based on the tensile cycle. Whilst the peak errors may seem large, in fatigue applications it is the error through life which is of greatest significance and the errors rapidly reduced resulting in a far more satisfactory average error of < 1.5 % for both R_ε = -1 and R_ε = 0 data. Since the combined model which has been developed can be readily included in Abaqus Standard analyses, does not result in significant errors at any of the strain ranges investigated and strain controlled loading best represents the condition in components at fatigue critical sites due to the structural constraint present [1], tension-compression asymmetry was not considered further in the constitutive modelling of FV448.

It is noted that the cyclic behaviour of FV448 at room temperature is softening only, with the most rapid softening occurring in the very early stages of life reflecting the second trend of cyclic behaviour in 9-12 %Cr steels identified in Section 1.3.1 (Figure 1-6). Comparing Figure 3- 21 with Figure 3- 20 shows that a variation in the mean strain did not influence the softening features (this result was also shown for a similar tempered steel [11]) or the ability of the material model developed based on R_ε=-1 to predict the peak stresses through life. Since the material appears to soften through life, especially at the higher strain ranges, the development of the cyclically stabilised model required an assumption to be made about the point at which the stress was stable. By assuming this point to be when the peak stress in a cycle was 2 % above the failure stress, the cyclically stabilised model results in the best predictions of stress around the mid-point of life; in fatigue lifing, a representative estimate of stress at this point might be considered more valuable than right at the start of life.

The cyclically stabilised model offers a good representation of peak stresses throughout life for all $\Delta\varepsilon$ and R_ε combinations investigated. The main drawback to this approach is the dependence of the constants in Table 3- 4 on the strain range. Hence the application of this model requires the selection of constants appropriate to the strain range predicted in the component; this could be achieved using a monotonic model such as in Figure 3- 10 or by defining a user subroutine which calculates the overall equivalent strain range for the last cycle and iterates a solution matching the material model with the calculated range. The most appropriate constants would be those interpolated between the tabulated values, however since there are no clear trends shown in Table 3- 4, interpolating a value for the constants based on the strain range under consideration is difficult. As a result, when the combined model is required, it is necessary to select the constants at the strain range which is closest to that under consideration; where the strain range distribution is non-uniform across the sample, it may also be possible to split the component model into several regions with different hardening models corresponding to different anticipated strain ranges.

Several material models were presented in Section 3.3; the available models are summarised in Table 3- 10. These models are used in Chapters 4 and 5 to analyse the shot peening process and local stress-strain parameters during fatigue testing respectively. Most notably, in Chapter 5, a sensitivity study is presented which determines whether the material model selection has a significant effect on the predicted stress in the notched fatigue samples investigated compared with a 5 % uncertainty in the load applied.

3.5. Conclusions

The baseline material microstructure and mechanical properties for FV448 have been established and can be summarised as follows:

- The microstructure is identified as tempered martensite with no clear directionality in relation to the barstock orientation or inclusion stringers. The prior austenite grain boundaries can be easily identified, however the precipitates could not be assessed using standard EDX techniques. The likely precipitates have been assessed using theoretical contrast based techniques to be $Cr_{23}C_6$, primary and secondary NbN and a combination of secondary Mo_2C, Mo_2N, Cr_2C, Cr_2N, NbC, VC and VN.
- FV448 shows tension- compression asymmetry, i.e. it is stronger in compression than in tension. Barstock FV448 is stronger in the rolling direction than in orthogonal directions. Several monotonic material models have been developed based on this data. If the stress range is less than the cyclic yield

strength, the material elastically shakes down. For R_ε = -1 the material shows cyclic softening behaviour, softening rapidly in the early stages of fatigue and then more slowly through life, in the range 0.0080 < $\Delta\varepsilon$ < 0.0155. Cycling at R_ε = 0 did not affect the softening behaviour.

- Two constitutive models have been derived describing the cyclic stress-strain behaviour. The combined model results in much lower peak and average absolute errors per half cycle than the cyclically stabilised model but is more data intensive in calibration and computationally expensive in application. Both the combined model and the cyclically stabilised model derived based on the R_ε = -1 data can be applied to R_ε = 0 situations, although the errors are slightly increased.

The significance of the use of the constitutive models derived in this chapter will be compared in more detail using a sensitivity study into the effect of material model as compared to uncertainty in the load applied on the local stress-strain parameters predicted in fatigue test samples in Chapter 5.

Material	C	Mn	Si	Ni	Cr	Mo	W	V	Nb	Fe	N
Nominal FV448 [14, 15]	0.13	1.0	0.5	-	10.5	0.75	-	0.15	0.45	Bal	0.05
Barstock FV448	0.12	0.94	0.31	0.74	11.0	0.58	< 0.01	0.31	0.34	Bal	-

Table 3- 1: Composition of FV448 in wt%.

Element	Weight %
V	1.2
Cr	10.3
Fe	57.8
Nb	30.8

Table 3- 2: Quantitative EDX analysis for a niobium rich particle.

$\Delta\varepsilon$	Tensile stabilisation stress /MPa	Stabilisation cycle (N/N_f)	Predicted maximum and minimum stress /MPa
0.0080	682	1479 (0.38)	706 / -706
0.0110	788	128 (0.57)	758 / -758
0.0155	793	141 (0.52)	794 / -794

Table 3- 3: Stabilisation stress and corresponding cycle for cyclic stress-strain curve.

Strain range	$\sigma\|_0$ /MPa	$C_{k=1}$ /GPa	$\gamma_{k=1}$	Q_∞ /MPa	b
All - first cycle	700	141	792	48	40
0.008	493	710	2165	-71	0.695
0.011	501	340	1053	-56	0.693
0.0155	508	191	506	-79	1.078

Table 3- 4: Combined isotropic and kinematic hardening model constants.

Strain range	Model	Average absolute error per half cycle /%	Standard deviation error per half cycle /%	Maximum absolute error in an half cycle /%
0.008	Combined	1.0	0.64	5.4
	Stabilised	2.2	1.36	6.4
0.0110	Combined	1.4	1.66	7.6
	Stabilised	5.1	2.41	13.3
0.0155	Combined	1.3	0.74	6.2
	Stabilised	2.2	2.00	10.4

Table 3- 5: Statistical comparison of combined and stabilised model peak stresses against experimental data for $\Delta\varepsilon$ = 0.0080, 0.0110, 0.0155, R_ε = -1.

Strain range	Model	Average absolute error per half cycle /%	Standard deviation error per half cycle /%	Maximum absolute error in an half cycle /%
0.0155	Combined	1.3	1.14	10.7
	Stabilised	7.1	2.41	12.3

Table 3- 6: Statistical comparison of combined and stabilised model peak stresses against experimental data for $\Delta\varepsilon$ = 0.0155, R_ε = 0.

Phase	η	vs. Fe	Colour vs. Fe	C_{ph}
Fe matrix	0.279	-	-	-
$Cr_{23}C_6$	0.252	Lower	Darker	9.95
VC	0.218	Lower	Darker	21.99
VN	0.216	Lower	Darker	22.63
NbC	0.340	Higher	Brighter	17.70
NbN	0.336	Higher	Brighter	16.87
Mo_2C	0.361	Higher	Brighter	22.67
Mo_2N	0.359	Higher	Brighter	22.25
Cr_2C	0.242	Lower	Darker	13.28
Cr_2N	0.241	Lower	Darker	13.78

Table 3- 7: Analysis of contrast expected between precipitates and Fe matrix in FV448.

Large bright	Large dark	Small bright	Small dark
Primary NbN	$Cr_{23}C_6$	Secondary NbN NbC Mo_2C Mo_2N	VC VN Cr_2C Cr_2N

Table 3- 8: Classification of second phase particles based on their contrast and size illustrated in Figure 3- 9.

Strain range	Maximum stress /MPa	Minimum stress /MPa
0.0080	740	-746
0.0110	812	-865
0.0155	860	-880

Table 3- 9: Maximum and minimum stresses in cycle 2 for $\Delta\varepsilon$ = 0.0080, 0.0110, 0.0155, R_ε = -1 loading.

Monotonic	Cyclic
Tensile normal to rolling, isotropic.	Fully reversed parallel to rolling, combined at $\Delta\varepsilon$ = 0.0080, 0.0110, 0.0155.
Tensile normal to rolling, kinematic.	Fully reversed parallel to rolling, cyclically stabilised isotropic.
Tensile normal to rolling, $\sigma_{0.2}$ and plastic data points.	
Tensile normal to rolling, bilinear.	
Tensile parallel to rolling, isotropic.	

Table 3- 10: Summary of material models available.

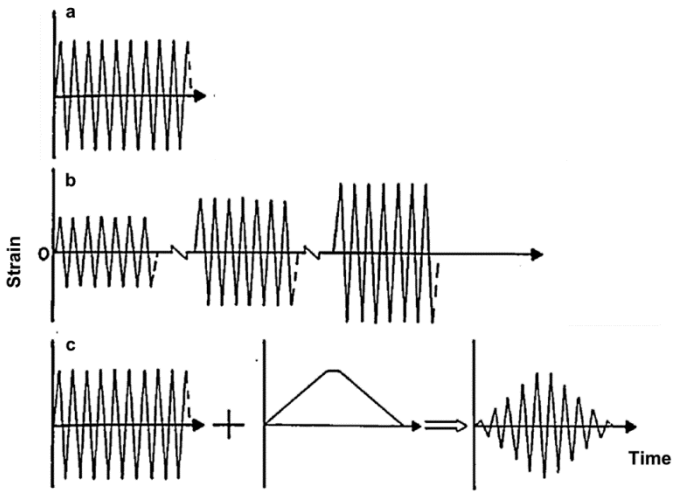

Figure 3- 1: Strain control programmes for cyclic stress-strain testing showing (a) single step, (b) multiple step and (c) incremental step. After Landgraf *et al.* [3].

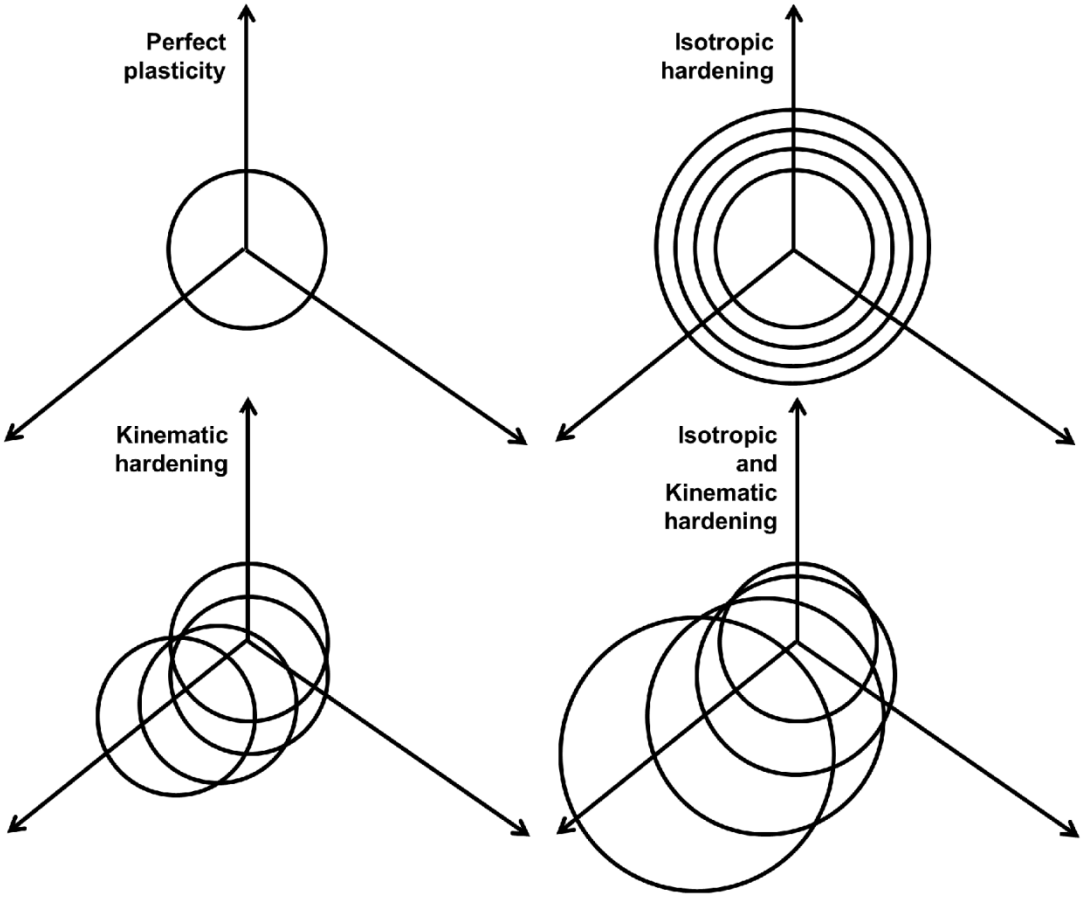

Figure 3- 2: von Mises yield surfaces illustrating isotropic and kinematic hardening in principal stress space.

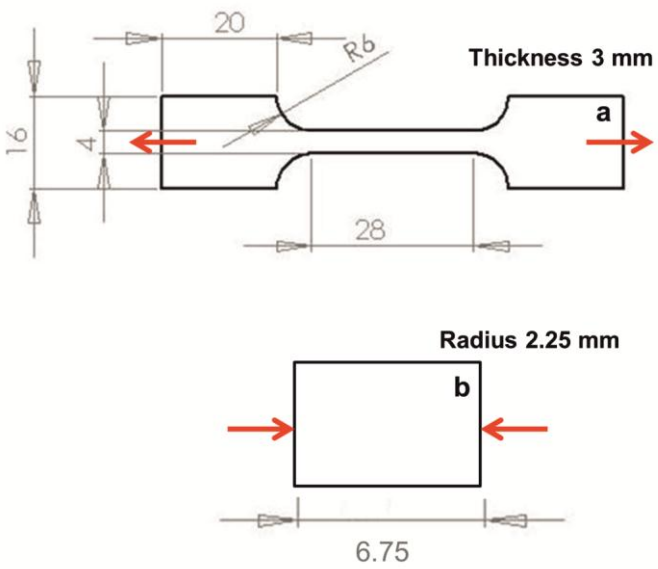

Figure 3- 3: (a) Tensile and (b) compression test sample dimensions in mm.

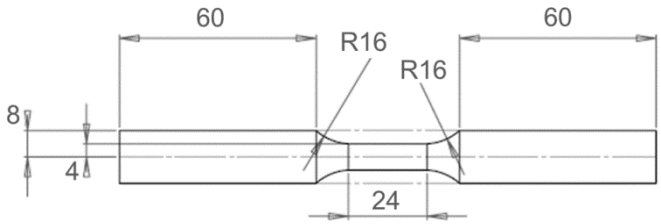

Figure 3- 4: Cyclic stress strain test sample dimensions in mm.

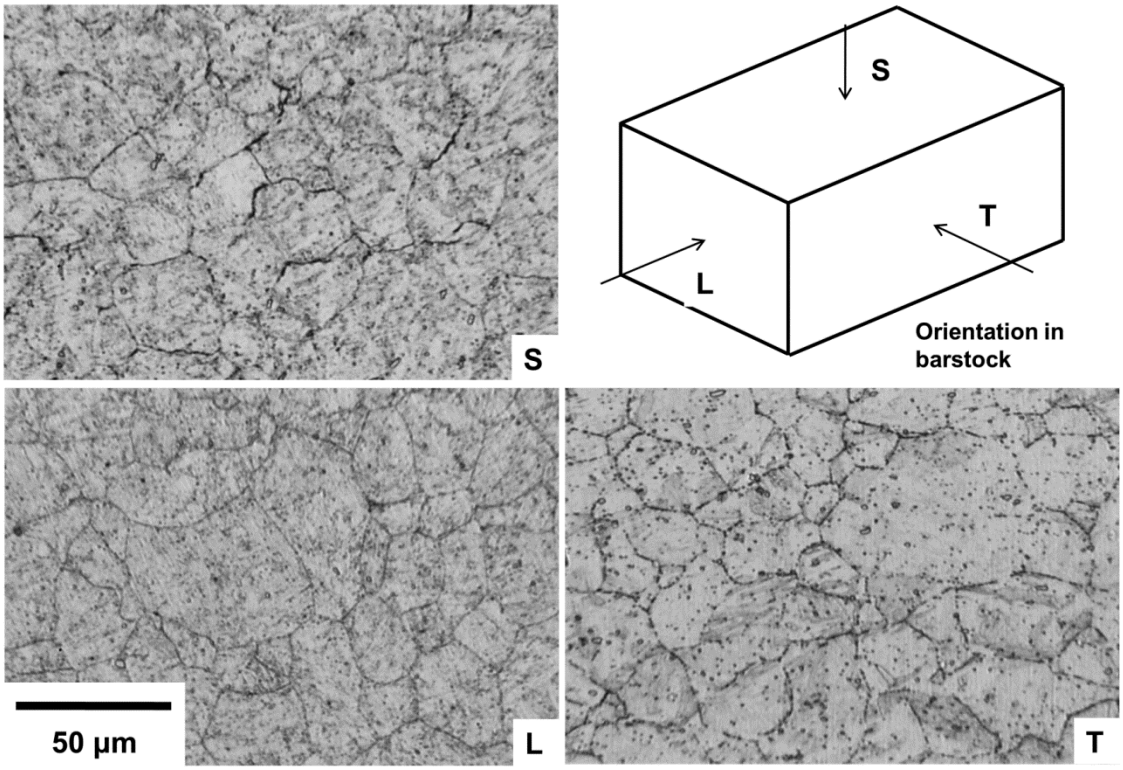

Figure 3- 5: Optical micrographs of etched FV448 showing microstructural directionality.

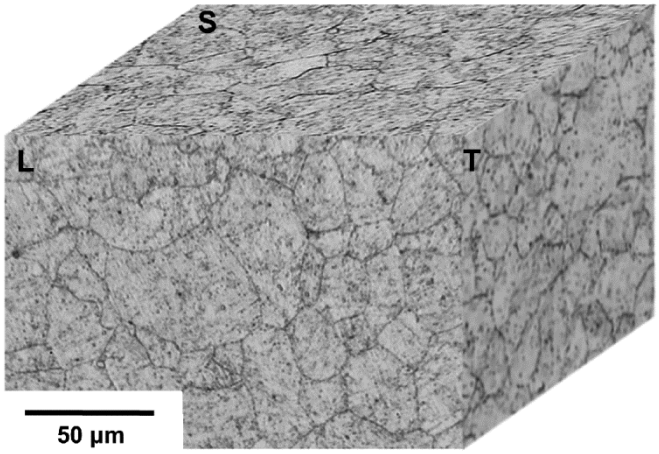

Figure 3- 6: Microstructural directionality 3D reconstruction.

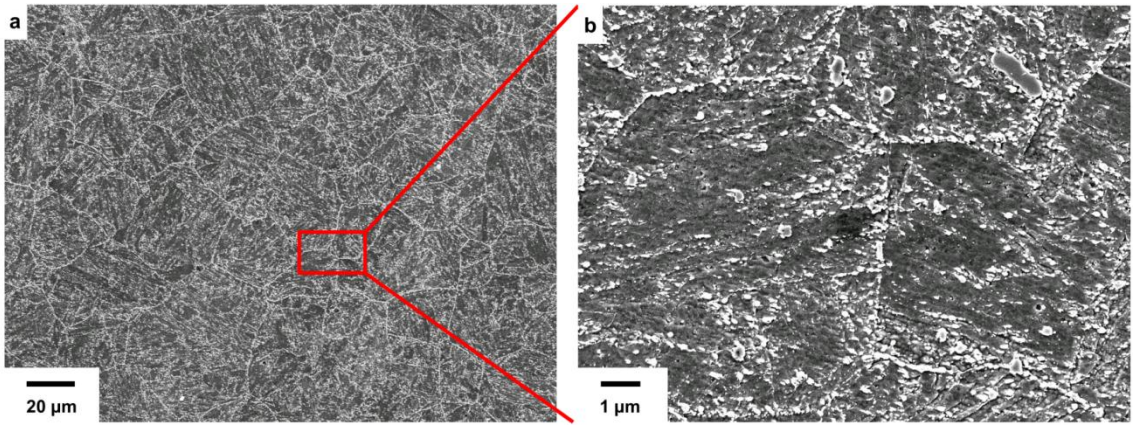

Figure 3- 7: SEI micrograph of etched FV448 in longitudinal direction at (a) low magnification and (b) higher magnification.

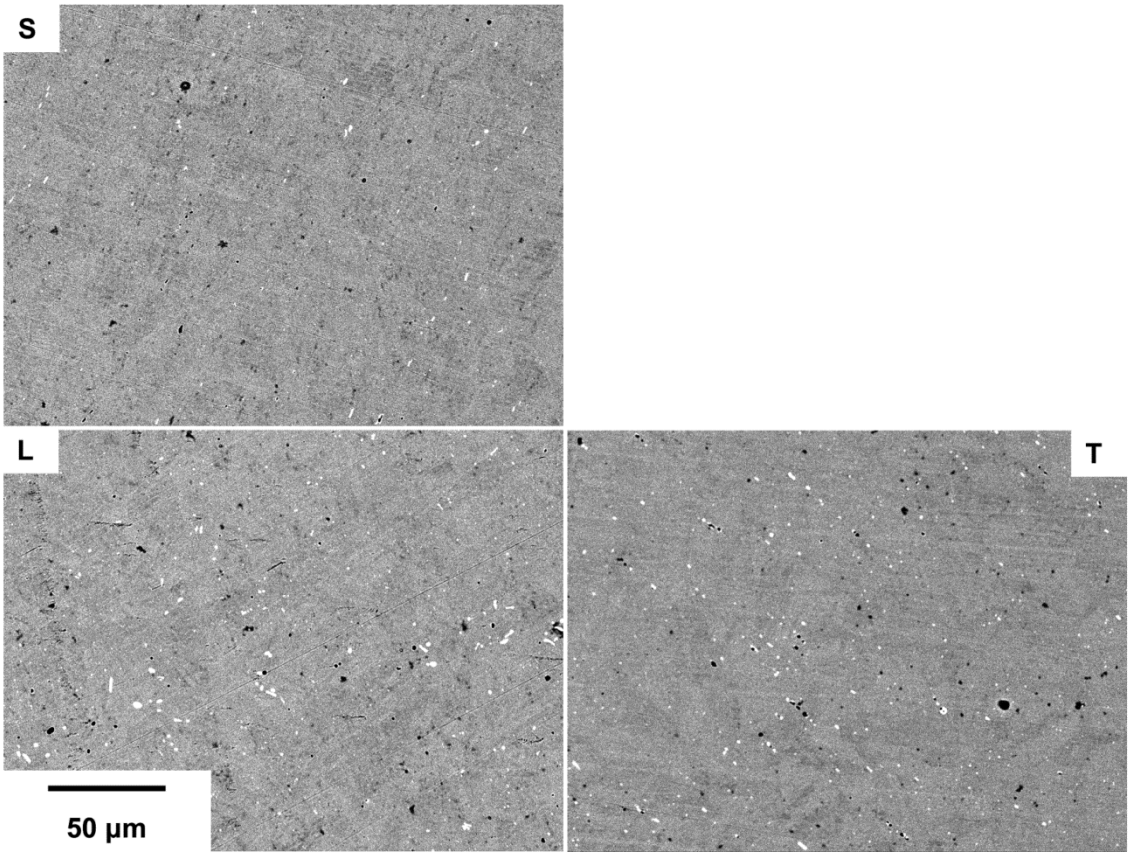

Figure 3- 8: BEI micrographs of polished FV448 illustrating second phases present in the microstructure in all three directions.

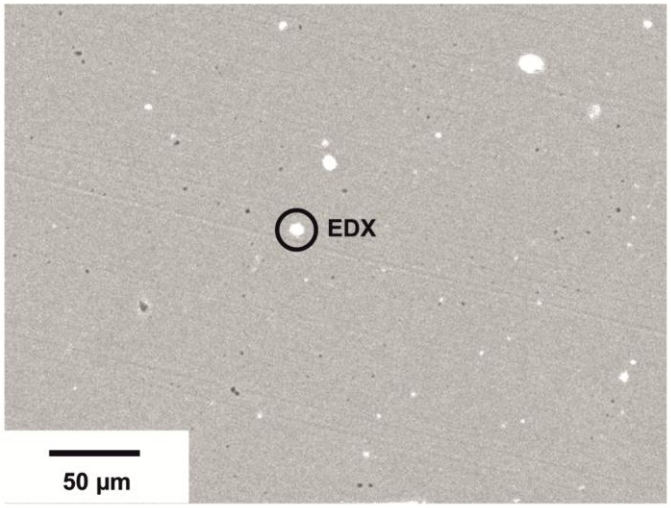

Figure 3- 9: BEI micrograph of polished FV448 in the longitudinal direction illustrating second phase particles.

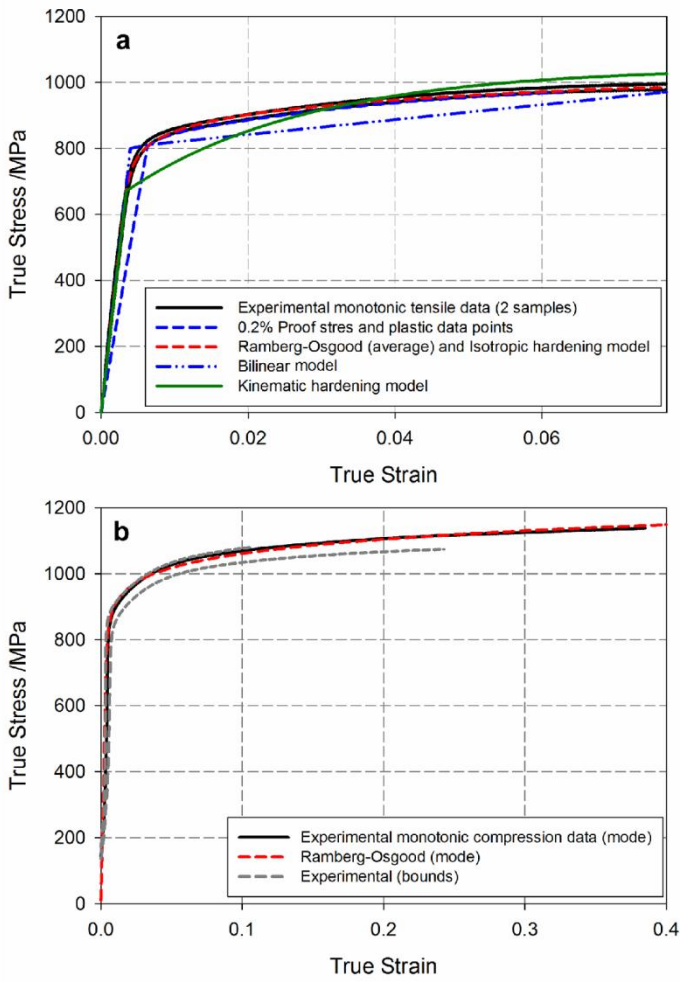

Figure 3- 10: Experimental uniaxial monotonic data in transverse direction and corresponding constitutive models for (a) tensile testing and (b) compression testing.

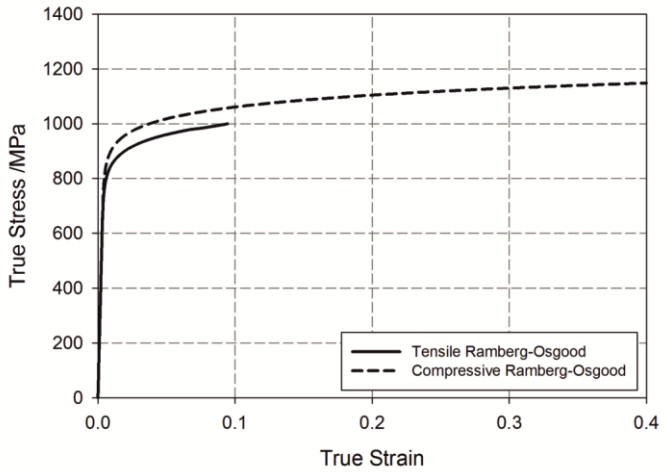

Figure 3- 11: Comparison of Ramberg-Osgood material models for uniaxial monotonic testing in the transverse direction in tension and compression.

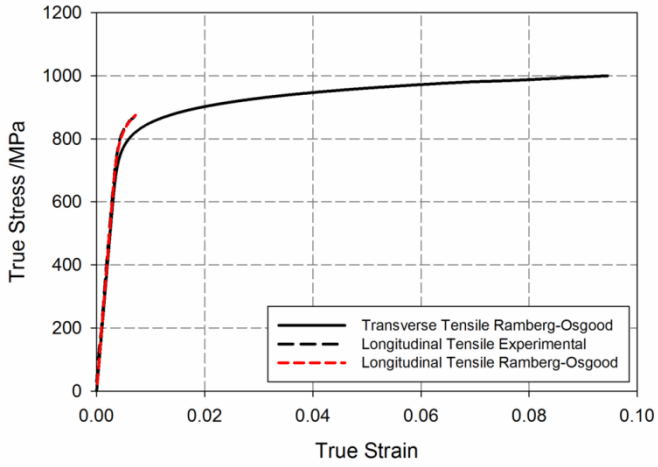

Figure 3- 12: Comparison of tensile behaviour in the longitudinal and transverse directions.

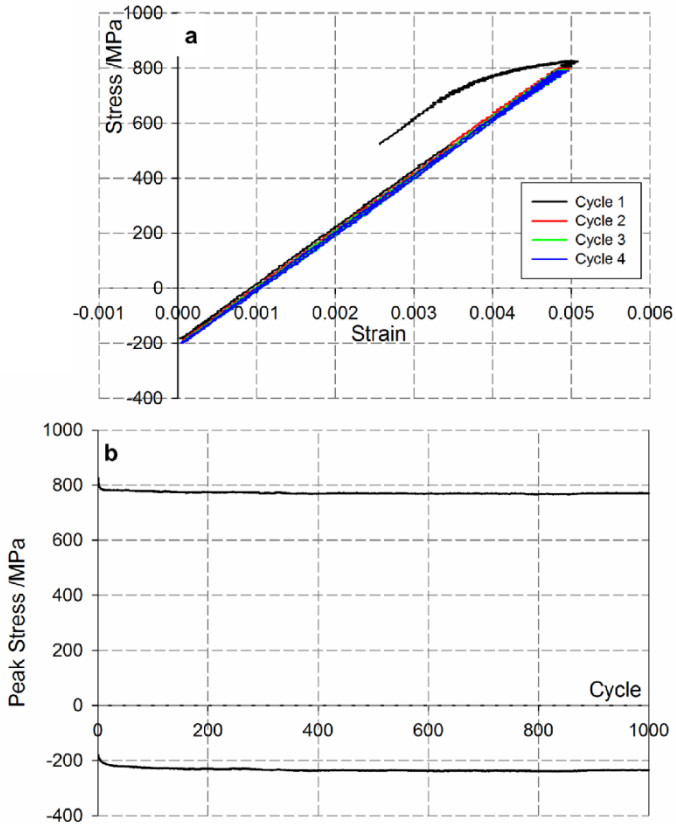

Figure 3- 13: Cyclic behaviour at $\Delta\varepsilon$ = 0.0050, R_ε = 0 showing (a) hysteresis loops for the first four cycles and (b) peak stresses for the first 1000 cycles.

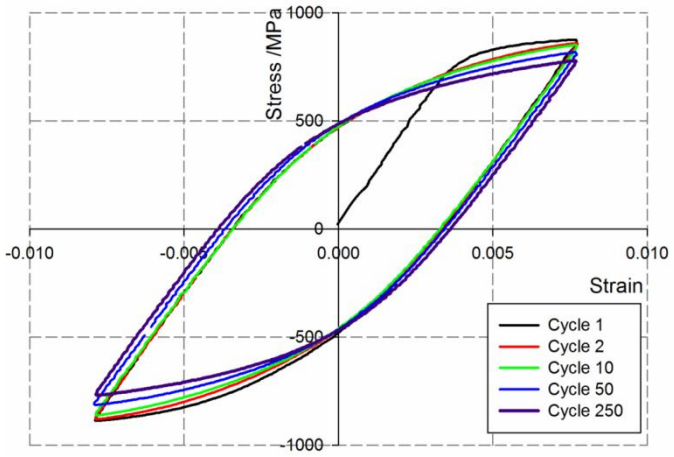

Figure 3- 14: Hysteresis loops at $\Delta\varepsilon$ = 0.0155, R_ε = -1.

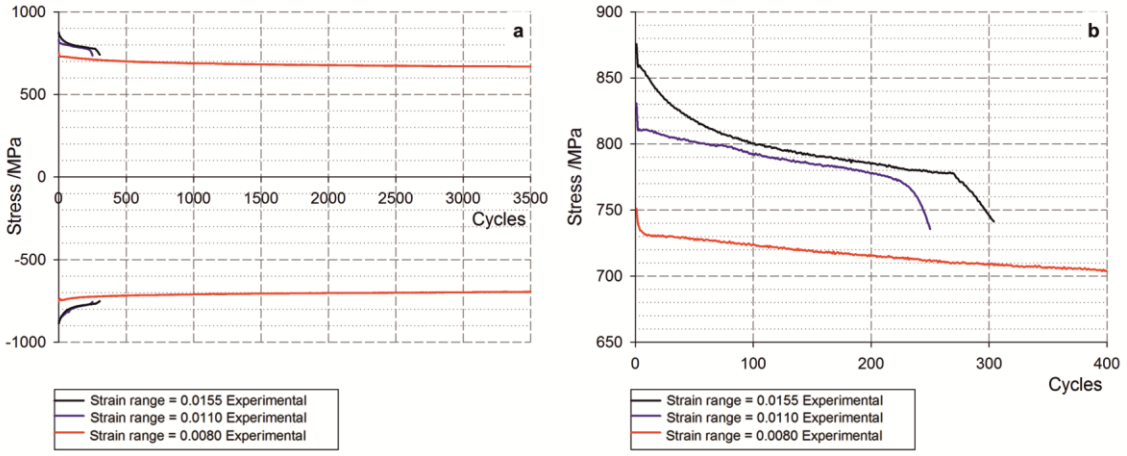

Figure 3- 15: Development of peak stresses through life at $\Delta\varepsilon$ = 0.0080, 0.0110, 0.0155, R_ε = -1 showing (a) through life behaviour and (b) tensile behaviour at the start of life.

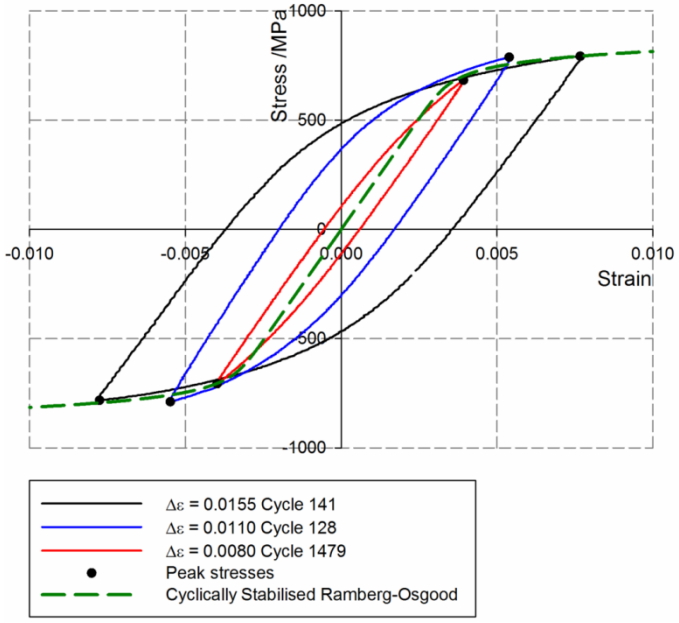

Figure 3- 16: Cyclically stabilised hysteresis loops and stress-strain curve based on R_ε = -1 tests.

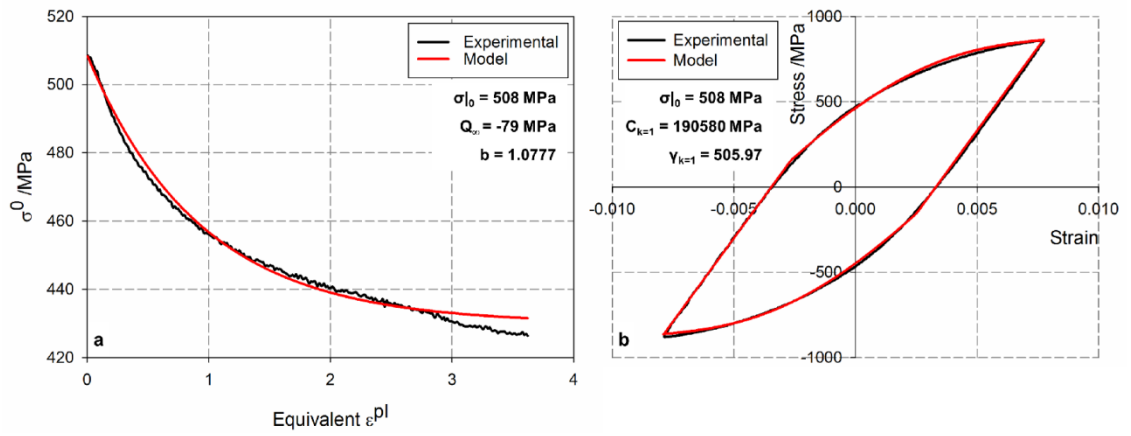

Figure 3- 17: Development of the combined material model for $\Delta\varepsilon$ = 0.0155, R_ε = -1 illustrating (a) calibration of the isotropic component based on cycle 2 onwards and (b) calibration of the kinematic component based on cycle 2.

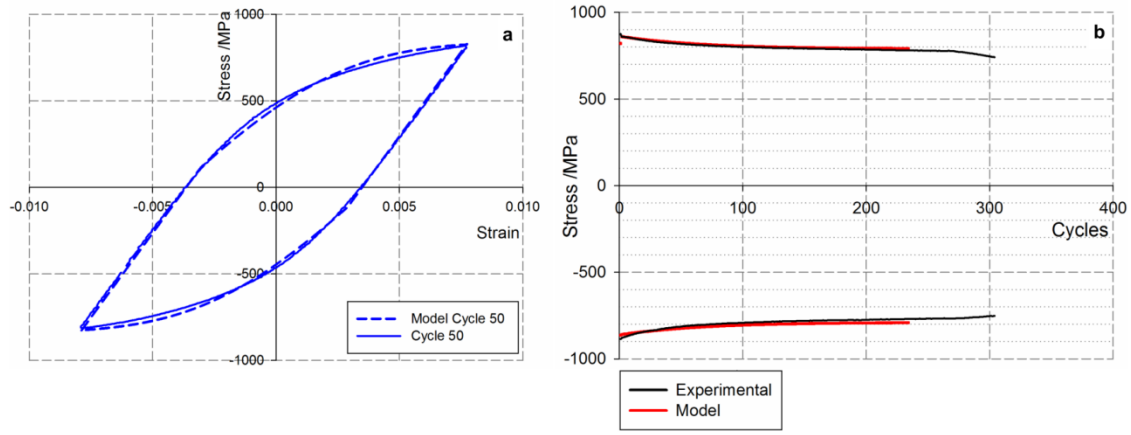

Figure 3- 18: Comparison of the combined model with experimental data at $\Delta\varepsilon$ = 0.0155, R_ε = -1 illustrating (a) hysteresis loops at cycle 50 and (b) through life peak tensile and compressive stresses.

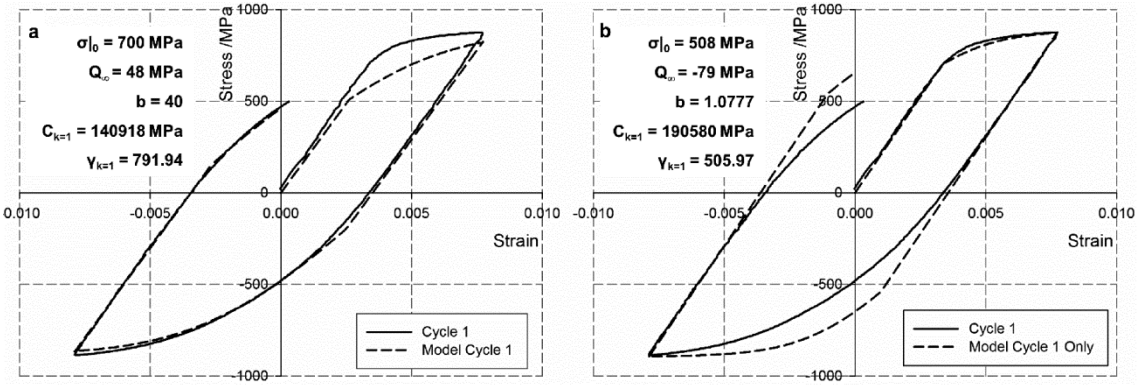

Figure 3- 19: Comparison of experimental and combined model hysteresis loops for cycle 1 at $\Delta\varepsilon$ = 0.0155, R_ε = -1 showing (a) combined model optimised for through life performance and (b) combined model optimised for first tensile half cycle.

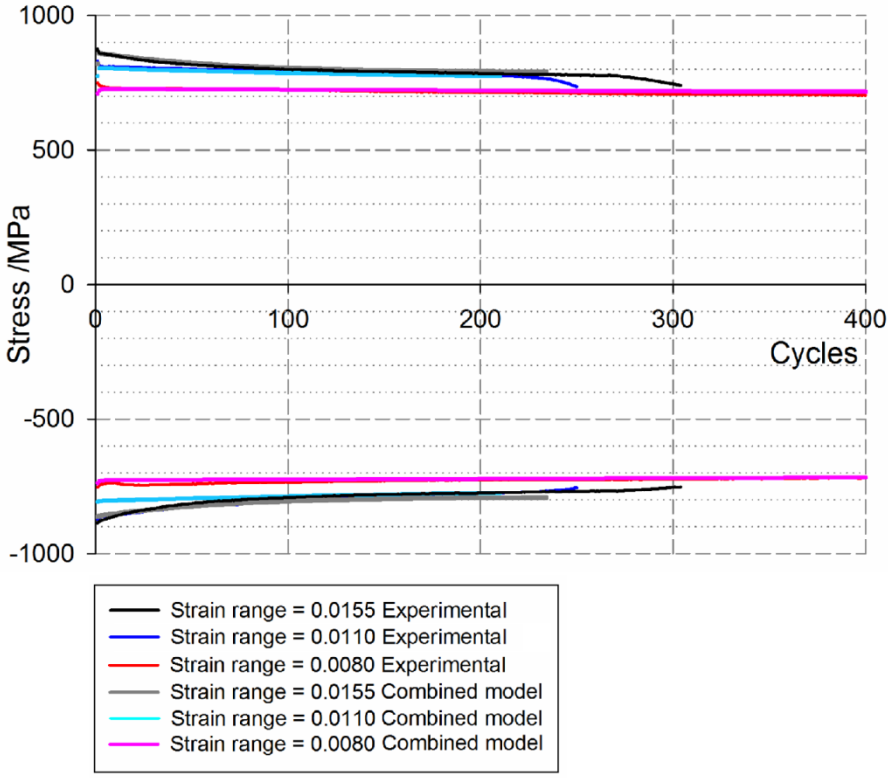

Figure 3- 20: Peak experimental stresses for $\Delta\varepsilon$ = 0.0080, 0.0110, 0.0155, R_ε = -1 compared with the corresponding values predicted using the combined isotropic and kinematic hardening models.

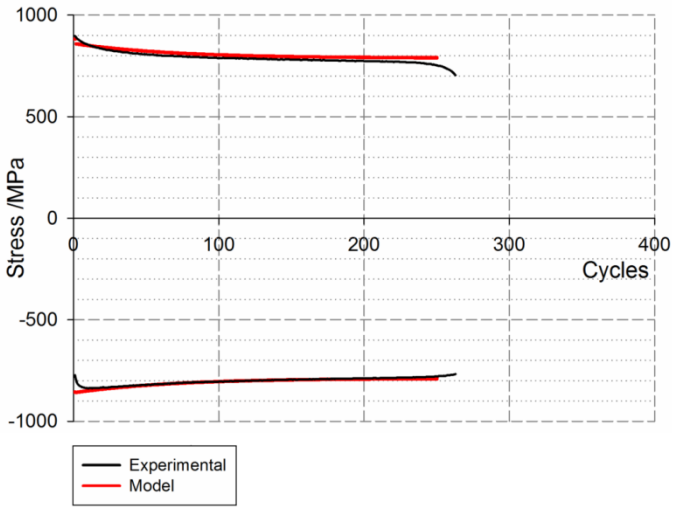

Figure 3- 21: Comparison of the combined model with experimental data at $\Delta\varepsilon$ = 0.0155, R_ε = 0 showing through life peak tensile and compressive stresses.

3.6. References

1. Suresh, S., *Fatigue of materials*. 2nd edn.; 2004, Cambridge, UK: Cambridge University Press.

2. Hales, R., Holdsworth, S.R., O'Donnell, M.P., Perrin, I.J. and Skelton, R.P., *A code of practice for the determination of cyclic stress-strain data.* Materials at High Temperatures, 2002. **19**(4): p. 164-185.

3. Landgraf, R.W., Morrow, J.D., and Endo, T., *Determination of the cyclic stress-strain curve.* Journal of Materials, 1969. **4**(1): p. 176 - 188.

4. Polák, J., Klesnil, M. and P. Lukáš, *On the cyclic stress-strain curve evaluation in low cycle fatigue.* Materials Science and Engineering, 1977. **28**(1): p. 109 - 117.

5. Mughrabi, H. and Christ, H.-J., *Cyclic deformation and fatigue of selected ferritic and austenitic steels: Specific aspects.* ISIJ International, 1997. **37**(12): p. 1154 - 1169.

6. Polák, J. and Hájek, M., *Cyclic stress-strain curve evaluation using incremental step test procedure.* International Journal of Fatigue, 1991. **3**(3): p. 216 - 222.

7. Polák, J., Fardoun, F. and Degallaix, S., *Analysis of the hysteresis loop in stainless steels I. Austenitic and ferritic steels.* Materials Science and Engineering A, 2001. **297**(1-2): p. 144 - 153.

8. Chaboche, J.L., *A review of some plasticity and viscoplasticity constitutive theories.* International Journal of Plasticity, 2008. **24**(10): p. 1642 - 1693.

9. Simulia, *Abaqus version 6.10 user manual*, 2010.

10. Abdel-Karim, M., *Review: Shakedown of complex structures according to various hardening rules.* International Journal of Pressure Vessels and Piping, 2005. **82**(6): p. 427 - 458.

11. Kang, G. and Liu, Y., *Uniaxial ratchetting and low-cycle fatigue failure of the steel with cyclic stabilising or softening feature.* Materials Science and Engineering A, 2008. **472**(1-2): p. 258 - 268.

12. Armstrong, P.J. and Frederick, C.O., *A mathematical representation of the multiaxial Bauschinger effect*, 1966. Berkeley, UK. CEGB Report RD/B/N731.

13. Kang, G., *Ratchetting: Recent progresses in phenomenon observation, constitutive modelling and application.* International Journal of Fatigue, 2008. **30**(8): p. 1448 - 1472.

14. Fujita, T., *Review: Current progress in advanced high Cr ferritic steels for high-temperature applications.* ISIJ International, 1992. **32**(2): p. 175 - 181.

15. Davis, J.R., *Stainless steels*. 2nd edn,; 1994, Materials Park, OH: ASM.

16. British Standard, *BS EN ISO 6507-1:2005*: *Metallic materials - Vickers hardness test - Part 1: Test method,* 2005.

17. British Standard, *BS EN 10002-1:2001*: *Metallic materials - Tensile testing - Part 1: Method of test at ambient temperature,* 2001.

18. ASTM, *ASTM E9-09. Standard test methods of compression testing of metallic materials at room temperature*, 2009.

19. British Standard, *BS 7270:2006: Metallic materials - Constant amplitude strain controlled axial fatigue - Method of test*, 2006.

20. Lukáš, P. and Kunz, L., *Cyclic plasticity and substructure of metals.* Materials Science and Engineering A, 2002. **322**(1-2): p. 217 - 227.

21. Sinclair, G.M., *An investigation of the coaxing effect in fatigue of metals.* Proceedings of ASTM, 1952. **52**: p. 743 - 751.

22. Choudhary, B.K., *Influence of strain rate and temperature on serrated flow in 9Cr-1Mo ferritic steel.* Materials Science and Engineering A, 2013. **564**: p. 303 - 309.

23. Perkins, K.M. and Bache, M.R., *The influence of inclusions on the fatigue performance of a low pressure turbine blade steel.* International Journal of Fatigue, 2005. **27**(6): p. 610 - 616.

24. Gustafson, A. and Hättestrand, M., *Coarsening of precipitates in an advanced creep resistant 9% chromium steel - Quantitative microscopy and simulations.* Materials Science and Engineering A, 2002. **333**(1-2): p. 279 - 286.

25. Goodhew, P.J., Humphreys, J. and Beanland, R., *Electron microscopy and analysis*. 3rd edn.; 2001, London, UK: Taylor and Francis.

26. Kuboň, Z., Foldyna, V. and Vodárek, V., *Optimized chemical composition of 9-12% Cr steels with respect to maximum creep resistance*, in *Proceedings of the 6th Liège Conference in Materials for Advanced Power Engineering*, Lecomte-Beckers, J., Schubert, F. and Ennis, P.J., Editors. 1998. Liège, Belgium: Forschungszentrum Jülich: p. 311 – 320.

27. Hald, J. and Straub, S., *Microstructural stability of 9-12%CrMo(W)VNbN-steels*, in *Proceedings of the 6th Liège Conference in Materials for Advanced Power Engineering*, Lecomte-Beckers, J., Schubert, F. and Ennis, P.J., Editors. 1998. Liège, Belgium: Forschungszentrum Jülich: p. 155 - 169.

28. Kasl, J. and Kaska, V., *Microstructural investigation of advanced creep resistant 10% Cr steel*, , in *Proceedings of the 6th Liège Conference in Materials for Advanced Power Engineering*, Lecomte-Beckers, J., Schubert, F. and Ennis, P.J., Editors. 1998. Liège, Belgium: Forschungszentrum Jülich: p. 585 – 591.

29. Kadoya, Y., Dyson, B.F. and McLean, M., *Microstructural stability during creep of Mo - and/or W - bearing 12Cr steels*, in *Proceedings of the 6th Liège Conference in Materials for Advanced Power Engineering*, Lecomte-Beckers, J.,

Schubert, F. and Ennis, P.J., Editors. 1998. Liège, Belgium: Forschungszentrum Jülich: p. 593 - 602.

30. Hofer, P., Cerjak, H. and Warbichler, P., *Quantitative evaluation of precipitates in the martensitic cast steel G-X12CrMoWVNbN10-1.1*, in *Proceedings of the 6th Liège Conference in Materials for Advanced Power Engineering*, Lecomte-Beckers, J., Schubert, F. and Ennis, P.J., Editors. 1998. Liège, Belgium: Forschungszentrum Jülich: p. 549 - 557.

31. Janovec, J., Svoboda, M., Kroupa, A. and Výrostková, *Thermal induced evolution of secondary phases in Cr-Mo-V low alloy steels.* Journal of Materials Science, 2006. **41**(11): p. 3425 - 3433.

32. Cahoon, J.R., Broughton, W.H. and Kutzak, A.R., *The determination of yield strength from hardness measurements.* Metallurgical Transactions, 1971. **2**(7): p. 1979 - 1983.

33. Pavlina, E.J. and Van Tyne, C.J., *Correlation of yield strength and tensile strength with hardness for steels.* Journal of Materials Engineering and Performance, 2008. **17**(6): p. 888 - 893.

34. Drucker, D.C., *Plasticity theory, strength-differential (SD) phenomenon, and volume expansion in metals and plastics.* Metallurgical Transactions, 1973. **4**(3): p. 667 - 673.

35. Rauch, G.C. and Leslie, W.C., *The extent and nature of the strength-differential effect in steels.* Metallurgical Transactions, 1972. **3**(2): p. 373 - 385.

36. Chait, R., *Factors influencing the strength differential of high strength steels.* Metallurgical Transactions, 1972. **3**(2): p. 365 - 371.

37. Spitzig, W.A., Sober, R.J. and Richmond, O., *Pressure dependence of yielding and associated volume expansion in tempered martensite.* Acta Metallurgica, 1975. **23**(7): p. 885 - 893.

38. Yaguchi, M. and Takahashi, Y., *Ratchetting of viscoplastic material with cyclic softening, part 1: Experiments on modified 9Cr-1Mo steel.* International Journal of Plasticity, 2005. **21**(1): p. 43 - 65.

39. Casey, J. and Jahedmotlagh, H., *The strength-differential effect in plasticity.* International Journal of Solids and Structures, 1984. **20**(4): p. 377 - 393.

40. Hosford, W.F., *Iron and* Steel. 2012: New York, NY: Cambridge University Press.

41. Iyer, S.K. and Lissenden, C.J., *Multiaxial constitutive model accounting for the strength-differential in Inconel 718.* International Journal of Plasticity, 2003. **19**(12): p. 2055 - 2081.

42. Kuroda, M. and Kuwabara, T., *Shear-band development in polycrystalline metal with strength-differential effect and plastic volume expansion.* Proceedings of the Royal Society A, 2002. **458**(2025): p. 2243 - 2259.

43. Verma, R.K., Kuwabara, T., Chung, K. and Haldar, A.,, *Experimental evaluation and constitutive modeling of non-proportional deformation for asymmetric steels.* International Journal of Plasticity, 2011. **27**(1): p. 82 - 101.

44. Yaguchi, M. and Takahashi, Y., *Ratchetting of viscoplastic material with cyclic softening, part 2: Application of constitutive models.* International Journal of Plasticity, 2005. **21**(4): p. 835 - 860.

Chapter 4

Shot peening process effects

4.1. Introduction

In order to include the effects of the shot peening process in a fatigue lifing protocol, it is essential that there are well defined procedures for establishing the resulting surface roughness, strain hardening and residual stresses. It became apparent from the review in Chapter 2 that whilst the procedure for measuring residual stresses using X-ray diffraction (XRD) is well defined, the procedures for measuring surface topography and cumulative plastic strain are not.

This chapter characterises the shot peening process which is applied to steam turbine blades (T0 = MI230R 13A 200 %). Residual stresses are measured using laboratory XRD and several methods are investigated for determining plastic strain: microhardness, XRD line broadening and electron backscatter diffraction (EBSD) local misorientation measurements. The surface topography is characterised both in two and three dimensions. The optimum analysis method for both surface topography and plastic strain is discussed as a first step towards standardising the analysis methods for shot peening surface roughness and strain hardening as a precursor to their inclusion in life assessment methods.

As a comparison, the surface topography and plastic strain resulting from three other peening processes are characterised: one at higher intensity, one at lower intensity and one at the same intensity achieved using a larger shot at lower velocity.

This chapter is largely based on two papers, with some additional analysis which has not previously been published. The two papers are detailed below. The chapter is structured as a paper such that this introduction (which also contains a brief theory of the XRD $\sin^2\psi$ method for residual stress measurement and a more detailed discussion of the surface roughness and plastic strain characterisation tools than was included in Chapter 2) is followed by methods, results, a discussion and conclusions.

K. A. Soady, B. G. Mellor, J. Shackleton, A. Morris and P. A. S. Reed, *The effect of shot peening on notched low cycle fatigue*. Materials Science and Engineering A, 2011. **528**(29-30): p. 8579 – 8588.

K. A. Soady, B. G. Mellor, G. D. West, G. Harrison, A. Morris and P. A. S. Reed, *Evaluating surface deformation and near surface strain hardening resulting from shot*

peening a tempered martensitic steel and application to low cycle fatigue. In press, International Journal of Fatigue, 2013, **DOI: 10.1016/j.ijfatigue.2013.03.019**.

4.1.1. XRD for measuring residual macrostresses

The most common experimental method for determining shot peening residual stress profiles is laboratory XRD with incremental layer removal by electropolishing. It offers better spatial and depth resolution than mechanical methods [1] and is preferred to non-linear ultrasonic, magnetic and electrical methods because of the requirement for stress free samples and the errors introduced by grain size, preferred orientation and cold work for these techniques [2]. Not only does XRD reduce these errors, but it is able to differentiate between the macrostresses and the microstresses which result from strains over distances of the order of or less than crystal dimensions (which are introduced, for example, by cold work [1]) which can be measured using the line broadening techniques discussed later in this chapter. The most common technique for determining residual macrostresses, and that employed in the present investigation, is the $\sin^2\psi$ method; a full theoretical derivation of this is well described elsewhere [3-5] and as such is only briefly shown here.

Bragg's Law (Equation 4.1) describes when interference between diffracted X-rays is constructive and forms the basis for XRD.

$$n\lambda = 2d\sin\vartheta \qquad (4\text{- }1)$$

Where λ is the X-ray wavelength, d is the interplanar spacing, 2θ is the peak position and n is an integer.

The interplanar spacing of a material that is free from strain produces a characteristic diffraction pattern for that material. When the material is strained, Poisson's ratio effects lead to elongations and corresponding contractions within the crystal lattice which change the interplanar spacing of the {hkl} planes. Equation 4-1 implies that this results in a change in θ and the diffraction pattern is shifted. From this shift, the strain in the material can be deduced, essentially using the atomic planes as strain gauges. Figure 4- 1 illustrates the angular definitions used in XRD analysis and shows how tilting the sample can bring planes into a position such that they satisfy Bragg's Law.

Using elasticity theory for a macroscopically isotropic crystalline material, the strain in the direction defined by φ (the angle between a fixed direction in the plane of the sample and the projection in that plane of the normal to the diffracting plane) and ψ (the angle between the sample normal and the diffracting plane normal), $\varepsilon_{\varphi\psi}$, is given by Equation 4-2. Assuming the stress state is biaxial at the surface ($\sigma_{13} = \sigma_{23} = \sigma_{33} = 0$), this results in Equation 4-3.

$$\varepsilon_{\phi\varphi} = S_1[\sigma_{11}+\sigma_{22}] + \frac{1}{2}S_2[\sigma_{11}cos^2\phi + \sigma_{22}sin^2\phi + \sigma_{12}sin2\phi]sin^2\varphi + \frac{1}{2}S_2[\sigma_{13}cos\phi + \sigma_{23}sin\phi]sin2\varphi \quad (4\text{- }2)$$

$$\frac{d_{\phi\psi}-d_0}{d_0} = S_1[(\sigma_{11}+\sigma_{22})] + \frac{1}{2}S_2[(\sigma_{11}cos^2\phi + \sigma_{22}sin^2\phi)sin^2\psi] \quad (4\text{- }3)$$

Where $d_{\varphi\varphi}$ is the interplanar spacing in the direction defined by φ and ψ and d_0 is the strain free interplanar spacing. Using the definitions of the X-ray elastic constants specific to the family of planes {hkl}, $S_1 = \frac{-\nu}{E}$ and $\frac{1}{2}S_2 = \frac{1+\nu}{E}$, Equation 4-3 can be rearranged, yielding Equation 4-4, which is the basis for the $\sin^2\psi$ method of residual stress determination.

$$d_{\phi\psi} = \left[\frac{1+\nu}{E}\sigma_\phi d_0 sin^2\psi\right] - \left[\frac{\nu}{E}d_0(\sigma_{11}+\sigma_{22})\right] + d_0 \quad (4\text{- }4)$$

Experimental data is obtained for $d_{\varphi\varphi}$ at varying ψ and $d_{\varphi\varphi}$ vs. $\sin^2\psi$ is plotted as a straight line, from which gradient and intercept values (Equation 4-5) are found.

$$\frac{\partial d_{\phi\psi}}{\partial sin^2\psi} = \frac{1+\nu}{E}\sigma_\phi d_0 \quad \text{and} \quad d_{\phi 0} = d_0\left[1 - \frac{\nu}{E}(\sigma_{11}+\sigma_{22})\right] \quad (4\text{- }5)$$

Where d_0 is typically unknown; however, since $E \gg (\sigma_{11}+\sigma_{22})$, $d_{\phi 0}$ differs from d_0 by ≤1 %. The residual stress in direction φ, σ_φ, can be found from the resulting data with no stress free references required using Equation 4-6.

$$\sigma_\phi = \left(\frac{E}{1+\nu}\right)\left(\frac{1}{d_{\phi 0}}\right)\left(\frac{\partial d_{\phi\psi}}{\partial sin^2\psi}\right) \quad (4\text{- }6)$$

Since X-ray penetration is usually limited to a few micrometres, the assumption of the biaxial residual stress state is generally valid. However, for the general stress state $\begin{bmatrix}\sigma_{11} & \sigma_{12} & \sigma_{13}\\ \sigma_{12} & \sigma_{22} & \sigma_{23}\\ \sigma_{13} & \sigma_{23} & \sigma_{33}\end{bmatrix}$ $d_{\varphi\varphi}$ vs. $\sin^2\psi$ is no longer linear. Whilst at the surface, only $\begin{bmatrix}\sigma_{11} & \sigma_{12} & 0\\ \sigma_{12} & \sigma_{22} & 0\\ 0 & 0 & 0\end{bmatrix}$ is possible, within the interior of the sample there is no requirement for this. Both σ_{13} and σ_{23} show $\sin^2\psi$ dependence in Equation 4-2; when present, they result in ψ-splitting and a non-linear relationship between $d_{\varphi\varphi}$ and $\sin^2\psi$, when this occurs the relationship is elliptical [6].

When measuring residual stresses resulting from shot peening, a depth profile is typically required. Given the limited penetration of laboratory XRD, incremental layer removal is required; material is typically removed in thin layers from the specimen by electropolishing; after each increment the residual stresses are redistributed. It may be necessary to correct for these redistributed residual stresses: In some cases finite element solutions are required (for example in coated materials with varying elastic properties [7] or for complex removal geometries which are not covered by analytical

solutions [8]); however for relatively simple geometries, approximation using the well-known analytical solutions for tubes and flat plates derived by Moore and Evans [9] is often sufficient (see for example [10, 11]). Whilst some researchers [12] routinely apply the depth correction, others [13] argue that it is only applicable once the effect moves the residual stress value outside experimental error.

4.1.2. Measuring surface deformation and associated strain hardening

Many parameters can be defined to describe surface roughness based on line profiles; despite some indications that describing other parameters such as peak to valley measurements, R_z or R_t (which can capture worst case defect data) or profile skewness, R_{sk}, and kurtosis, R_{ku}, (which can capture more statistical information about the surface profile) [14], the arithmetical mean vertical deviation of the assessed profile from the mean line, R_a, remains the parameter of choice in the majority of papers considering shot peening surface roughness effects; R_t is also sometimes reported (see for example [15] and Section 2.1.1).

However, in a recent study, Child *et al.* [16] characterised the surface roughness resulting from shot peening in three dimensions. This is indicative of the recent drive towards three dimensional topographical characterisation of surfaces with new standards defining areal equivalent parameters such as S_a and S_z [17] and the tactile and optical methods which can be used to characterise them [18]. Child *et al.* [16] used white-light interferometry to determine S_a; however the relationship between the areal parameters and linear parameters was not confirmed. This relationship may be critical if such measurements are to be used in determining roughness induced stress concentration factors for inclusion in component life assessment procedures.

The strain hardening profile resulting from shot peening can be characterised (see for example [13, 16, 19-23]). Any changes to the dislocation distribution during low cycle fatigue (LCF) should also be considered since this rearrangement is strongly related to the relaxation of residual stresses and can help identify locations where initiation is likely [13, 19, 24]. There are three well recognised methods for determining the extent of cumulative plastic strain, namely microhardness, XRD line broadening (typically measured using full width at half maximum (FWHM) data) and EBSD image quality or misorientation analyses.

It was noted in Chapter 2 that for shot peened components, these plastic strain measures are commonly quoted ‘as is’ and not converted to a plastic strain magnitude (see for example uncalibrated hardness [20], laboratory XRD FWHM [13] and EBSD [16]); this conversion is essential if the varying yield strength near the surface of a shot peened component is to be considered in life assessment.

The relationship between microhardness and yield strength has been presented in several papers; the causal link between the two processes is clear: strain hardening and the associated increase in dislocation density increases the resistance to plastic deformation. Whilst in some cases, no attempt is made to define a mathematical relationship and plastic strain is calibrated from hardness by interpolation based on constant strain range axial fatigue tests [25, 26], in other cases a mathematical relationship is presented; various relationships have been reported: Cahoon *et al.* [27] related hardness to yield strength in aluminium and steel using the strain hardening exponent whilst Fontanari *et al.* [28] suggest that the ratio of elevated yield strength to bulk yield strength in aluminium alloys is the same as the measured hardness ratio. Also in aluminium alloys, de los Rios *et al.* [29] suggest a linear relationship between flow stress and hardness; this is equivalent to the models of Srikant *et al.* [30] developed in aluminium alloys and Chaudhri [31] for copper alloys which relate hardness to plastic strain using a power law; indeed for power law hardening materials this would be expected to be the most physically representative model.

Neglecting instrumental effects, diffraction peaks can be broadened by reductions in crystallite size and the presence of microstrains. For diffraction profiles that are known with high statistical significance, complex deconvolution analyses can be used to separate the crystallite size and strain effects [32]; these techniques are now often implemented in commercial diffraction peak analysis software, such as TOPAS [33].The Williamson-Hall approach can also be used to separate size and strain effects and has been demonstrated for shot peened samples by Tan *et al.* [34]. However, the laboratory XRD systems used to investigate shot peened materials (typically for residual stresses) are often not optimised for such complex analyses and as such deconvolution is not always possible.

When relative values will suffice, the calibration approach described by Prevéy for nickel based alloys can be applied [12, 21]. Peak width was related to plastic strain by an exponential relationship; the plastic strain can then be used to determine the variation of yield strength as a function of depth [12].

EBSD techniques have recently been growing in popularity for measuring plastic strain. Geometrically necessary dislocations resulting from crystallographic slip result in crystal orientation changes within the material which can be detected [35, 36]. Two parameters are affected: image quality and intragranular misorientation. Early work quantified the 'diffuseness' of the Kikuchi line pairs using the gradient of the pixel grey level on traversing the line [37] or measurement based on the power spectrum [38]. This was calibrated to plastic strain using tensile samples manufactured from 316H stainless steel, although the scatter bands were quite large and at plastic strain, ε_p > 15 %, there were no further changes in grey level gradient making application of

this method to high plastic strains difficult [37]. However, measurements on aluminium tensile samples made using the first moment of the power spectrum showed a linear relationship to plastic strain to ε_p = 20 % [38] so the use of image quality parameters may be used up to plastic strains of 20 %.

More recently, image quality parameters have been used qualitatively only (since they may be influenced by other effects such as interaction volume, sample surface and sample tilt [35]), with quantitative methods focussing on crystallographic misorientation parameters. This is typically quantified as the spread in crystallographic orientation within a grain and has been shown to be independent from measurement conditions such as the EBSD system, grain size and step size, although camera resolution and electron beam conditions remain important considerations [39]. Linear relationships between misorientation and plastic strain have been developed for 304 austenitic stainless steel [35, 39], nickel alloy 600 [39] and 316 stainless steel [40]. Local (non-grain based) misorientation methods have also been employed in 316 stainless steel [41], 304L stainless steel and nickel alloy 690 [42] and also show a linear relationship. Given possible saturation effects [42], it is crucial to extend the calibration beyond the maximum of 20 % reported in these studies if the method is to be extended to analysing the plastic strain distribution resulting from shot peening where strains are typically in excess of 20 % and in the extreme may reach 50 % [21].

Examples of the indicated plastic strain distributions resulting from each measurement technique are given in Table 4- 1 which is based on the data presented in Table 2-2 and details the plastic strain measured in shot peened (6-8A) Udimet 720Li by two different research groups using different methods. The results from the microhardness technique show reasonable repeatability; the indicated depth by the laboratory XRD technique is somewhat reduced whilst the depth measured by the EBSD technique is around half that measured by the microhardness technique. A similar comparison between uncalibrated EBSD grain based misorientation and synchrotron XRD FWHM plastic strain indicators after rapid metal cutting in Inconel 178 also showed discrepancies in the affected depth (EBSD ~175 μm and XRD ~375 μm) [43]. This is clear evidence of the need for the systematic comparison of the three techniques presented in this chapter; a comparison which, to the best of the author's knowledge, has not been previously presented.

4.2. Experimental methods

4.2.1. Sample preparation

The baseline shot peening process used throughout this study is the industrially applied T0 process; this process is the most extensively documented and all three

(roughness, residual stress and strain hardening) peening effects are quantified. Furthermore, the optimum surface roughness and cumulative plastic strain characterisation methods are developed for this process. The results were compared against samples which met the industrial machined component and pre-peen specification of R_a < 0.8 µm.

As a means of comparison, three other processes have also been considered; these are detailed in Table 4- 2. The use of three intensities (4A, 13A and 18A) allowed consideration of the effect of the magnitude of the intensity; the two processes at 13A allowed consideration of the effect of shot size and velocity selection in achieving a given intensity. Time and cost constraints meant the residual stresses were only measured for the T0 process, however, inferences on the residual stress profiles are made based on the surface topography and plastic strain profiles recorded for these processes.

Several sample geometries were used in the characterisation of the shot peening process. The simplest flat geometry was used to develop surface roughness and plastic strain characterisation methods and also to determine the residual stresses expected as a result of this process. Since all the fatigue testing detailed in Chapter 5 is carried out in notched samples using three point bend, it was also essential to demonstrate that the effects of the shot peening process applied in the present investigation are independent of the notch geometry as it has been suggested by other authors that in certain situations this may not necessarily be the case [44]; to this end, the roughness, residual stress and plastic strain was also quantified in the baseline fatigue geometry discussed further in Chapter 5. Furthermore, the roughness was quantified in each of the geometry variations used in the fatigue testing.

Samples were machined from barstock using electro-discharge machining (EDM). In order to ensure that any metallurgical, mechanical or geometrical modifications (which can lead to surface tensile stresses, microcracks, roughness and reduced lifetime) did not affect results, 250 µm was ground from the cut face before the sample preparation process began. Appendix A to this chapter details how this grinding depth was established. The surface finish after this grinding process was that required (R_a < 0.8 µm) both pre-peen and in the ground samples used as the baseline comparison.

Plastic strain calibration samples were deformed using an electromechanical Instron 5569 using monotonic uniaxial tension (at low ε_p) at extension rate 0.3 mmmin^{-1} and compression (at high ε_p) at extension rate 0.1 mmmin^{-1}. Tensile testing was in accordance with BS EN 1002-1:2001 [45] and compression testing was in accordance with ASTM E9-09 [46] using molybdenum disulphide as a lubricant to reduce barrelling effects. Extensometer readings were used to determine remnant plastic strain in the

tensile samples. Compression samples were much smaller and load frame load-displacement data was corrected for machine compliance and used in conjunction with sample gauge length measurements to determine the remnant plastic strain.

Microhardness testing, XRD profiles and EBSD area scans were performed on calibration samples and shot peened samples in the region near the peened surface (Figure 4- 2) to obtain residual stress and calibrated plastic strain profiles. Estimates of the variation in yield strength near the shot peened surface were obtained from plastic strain profiles using the monotonic Ramberg-Osgood model perpendicular to rolling developed in Chapter 3. Furthermore, the deformed microstructures were revealed using the same surface preparation and optical microscopy techniques as were detailed in Chapter 3. This approach requires the assumption that cold work induced crystal deformation and dislocation formation induced by shot peening affects crystallite size and strain (and associated misorientations) in the same way as uniaxial deformation.

4.2.2. Surface topographical characterisation

Both a Taylor Hobson Form Talysurf 120L stylus profilometer and an Alicona Infinite Focus optical (focus variation) profilometer were used to determine surface roughness average parameters (R_a and S_a) and peak to valley heights (R_z and S_z) [17, 47] for each surface condition. To ensure comparability between results, both tactile and optical profile lengths and filters were selected according to BS ISO 4288:1996 [48]; filters for optical areal data were set in accordance with best practice guidelines ensuring that surface form was removed [49]. Tactile horizontal resolution is dependent on the stylus tip radius which was 3 μm; vertical resolution was 12.8 nm. The vertical resolution on the Infinite Focus was set to 200 nm for shot peened surfaces and 100 nm for the ground surface in accordance with best practice recommendations [49]. Due to the relatively coarse shot peened surface profile with indent diameters of the order of tens of micrometres, a horizontal resolution of 3.5 μm was deemed sufficient for roughness analysis. All optical data was processed to remove spikes from the surface and fill holes with values interpolated from nearby data points; the reference plane was set appropriately.

Tactile data was taken from a minimum of 32 line profiles, 8 on each of four samples. Optical data was taken from five area scans measuring 1.4 mm x 1.1 mm; line profiles were zig-zagged across the area to ensure sufficient profile length. For T0 the average R_a and S_a of the five small scans were checked against a larger scan (in which fewer repeat zig-zags were required) of dimension 3.9 mm x 1.1 mm and the error in both found to be less than 2 %. Thus data from five small scans was considered appropriate and allowed data to be collected from different surface locations to check coverage.

Two approaches were applied to measuring the average indent size resulting from shot peening:

i. Optical micrographs were taken of the 200 % coverage surface using an Olympus BH2 optical microscope. Bi-directional indent diameters were measured in accordance with Figure 4- 3 using Image J image processing software. 24 random indents were measured from a minimum of four images for each peening process.

ii. The Alicona Infinite Focus was used to measure the indent size on 20 % coverage samples (peened for less time using the same shot and velocity). 15 indent areas were measured for each peening process from a minimum of three scans such as that illustrated in Figure 4- 4. The indent was defined as the area beneath the reference plane for each indent and the corresponding diameter calculated for a circular indent.

4.2.3. XRD to measure residual stresses

Measurements appropriate to the $\sin^2\psi$ method were made using a Proto iXRD device and incremental layer removal was achieved by an electropolishing method; an extensive optimisation study was carried out based on the suggestions of Fitzpatrick *et al.* [4] to ensure a good reaction but limit the amount of pitting and prevent undesirable insoluble deposits or etching on the surface. The electrolyte was 8 % (by volume) of 60 % perchloric acid solution mixed in solution with 92 % (by volume) of glacial acetic acid. The solution start temperature was 15 ˚C to minimise the polishing rate and pitting and the voltage was 60 V. A magnetic stirrer was used to ensure good mixing; it was ensured that the whirlpool was away from the sample to avoid cavitation. These optimised conditions are noted to be very similar to those used in the preparation of TEM foils in similar 9-12 %Cr steels [50].

The polishing was carried out in one minute increments and the sample was cleaned after each increment using methanol to remove the anodic film. Lacomit varnish was used so only the desired area was polished; this enabled the use of a stylus profilometer (Mitutoyo Contracer CV-3100) to measure changes in the notch profile relative to the unpolished end tabs. Near the surface, depth increments were approximately 30 µm, although one measurement was always made within 20 µm of the surface. Once the maximum residual stress had been recorded, the increments were increased to a maximum of approximately 100 µm at the greatest depths.

A Cr-Kα X-ray source was used with a wavelength of 2.291 Å and measurements were taken on the {211} diffraction peak which was recorded at a 2θ angle of approximately 156˚. The diffraction elastic constant $½S_2$ was $5.92\text{x}10^{-6}$ MPa^{-1}. In order to minimise

error associated with taking residual stress measurements on a curved surface, the smallest collimator available (0.5 mm diameter) was used. The X-ray penetration depth in ferrite was estimated using data taken from the literature [4] for Cr radiation on the {211} peak at $\psi = 0^{\circ}$ (i.e. where penetration is at its greatest) to be $z_p = 5$ µm. The irradiated area was less than 0.4 times the radius of curvature of the analysed surface in the direction of the stress component [3]. At the beginning of each working day a 'gain' or flat field correction was carried out to account for the variation in efficiency across the 512 positions on each detector and between the two detectors. The profile was corrected by dividing the peak by gain.

Data was collected for both notched and flat samples in two orthogonal directions as illustrated in Figure 4- 5. When the beam was rotating in the axial direction, there were no notch shadowing effects, and thus fourteen ψ angles varying from -39 to +39° were considered across two detectors. When the beam was rotating in the radial direction however, notch shadowing effects became more significant and the fourteen ψ angles measured only ranged from -30 to +30°.

Given the equibiaxiality of the shot peening residual stress field when the impinging shot is normal to the surface, significant macro-shear stresses were not expected to be present in the samples [51-53]. Once this was confirmed for this specific peening process using a flat shot peened sample (by considering the linearity of the $d_{\varphi\varphi}$ vs. $\sin^2\psi$ relationship), any ψ splitting detected in the notched samples' (which manifested as an apparent elliptical fit in the $d_{\varphi\psi}$ vs. $\sin^2\psi$ data indicating the presence of shear stress components) radial direction was considered to be a result of notch curvature and associated beam splitting and an appropriate correction was applied to remove the shear component from the data [6]. This correction was applied using the algorithms supplied in the Proto control and analysis package XRDWIN.

The error was determined by calculating the sample standard deviation over 5 bi-directional measurements (10 data points) at different locations on the surface of the flat shot peened sample. The standard deviation was 25 MPa; as a result the 95 % confidence range was ±50 MPa. Due to time constraints and equipment availability, this was assumed to be the confidence with which all data could be quoted rather than carrying out repeat measurements for each notched sample data point.

Although the samples had a slight curvature, an appropriate analytical depth correction solution was that for a flat plate [9]. It was assumed that the relaxation stress had a linear distribution over the cross section of the remaining material with the same integrated force and moment as the stress in the removed layer but of opposite sign. It was found that at the greater depths the corrections were as great as 80 MPa, this is outside the experimental error and indicates that the correction was required.

Strong stress gradients can result in curvature in the $d_{\varphi\psi}$ vs. $\sin^2\psi$ plots; however there was no evidence of this in the present investigation. The conditions in which XRD measurements can be used in the presence of stress gradients are given in Equation 4-7 [3]:

$$\frac{\partial\sigma}{\partial Z} < \frac{1}{z_p}.\frac{1}{0.5S_2}.\frac{1}{500} < \frac{1}{5\mu m}.\frac{1}{5.92x10^{-6}MPa^{-1}}.\frac{1}{500} < 67.6MPa\mu m^{-1} \quad (4\text{-}7)$$

This condition is not exceeded at any point in the present data set and as a result the method is deemed appropriate. No correction has been made for the presence of stress gradients.

4.2.4. Plastic strain measurement techniques

4.2.4.1 Microhardness

Microhardness profiles were obtained for each surface condition based on four traverses of indents separated by 10 μm on the polished face indicated in Figure 4- 2. Testing was in accordance with BS EN ISO 6507-1:2005 using 200 g load for 15 s dwell. The image analysis protocol illustrated in Figure 4- 6 was implemented in Image J to analyse the microhardness indents and their position with respect to the surface mean line. Indents on a traverse were imaged such that successive images contained two overlapping indents, allowing a montage to be mathematically created based on indent centroids.

Images were binarised by making use of the 'Autothreshold' plug-in; the 'Minimum' method [54] was found to be the most reliable method for segmenting the data. Once binarised, the 'Measure ROI PA' plugin [55] was used to measure the diagonal lengths and location of the indents; any noise remaining after the thresholding process was removed at this stage by seeking only 'particles' in the size range anticipated. When used in conjunction with data pertaining to the sample edge mean line, the indent size, and hence microhardness (calibrated in the same manner as described previously in Chapter 3), as a function of depth beneath the peened surface could be accurately calculated. This image processing technique was validated against measurements made using an ocular micrometer also described in Chapter 3. Data for multiple traverses were smoothed using a Loess function with a polynomial of degree 1 and sampling proportion of 0.3 to ensure any waviness in the data was removed.

4.2.4.2 XRD

Data from the aforementioned laboratory based XRD $\sin^2\psi$ method was reanalysed to consider microstrain in the crystal lattice. The $\psi = 0^\circ$ data was used to determine the

line broadening depth profiles (defined by the FWHM of a Gaussian profile fit) that had occurred as a result of the shot peening process.

Despite variations in the residual stress profile with measurement direction (Section 4.3.3), as expected there was no significant directionality found in the plastic strain profiles measured in either the calibration or flat or notched T0 samples and as such the profiles were averaged. The error was approximated in an analogous manner to that for residual stresses: the sample standard deviation was calculated based on 5 bi-directional measurements on the surface of the flat T0 sample; the resulting 95 % confidence in FWHM measurements was ±0.12˚.

4.2.4.3 EBSD

All cross sections for EBSD analysis were ground and polished to a 1 μm finish before final preparation using colloidal silica of 0.04 μm grain size. Data were collected using an EDAX Hikari EBSD camera operating at 300 fps used with a FEI Nova 600 Nanolab field emission gun scanning electron microscope operating at an accelerating voltage of 20 kV and a nominal current of 24 nA. Uncleaned data was processed in OIM vs. 5.2 and the patterns were indexed according to an α-iron structure.

All data was collected on an area measuring at least 200 x 200 μm using a step size of 0.4 μm (the shot peened samples were positioned with the edge such that with a scan size 200 x 250 μm, the sample area for collection was ~200 x 200 μm). This step size was validated by also collecting data at 0.2 μm for calibration samples and one T0 shot peened sample and comparing the analysed profile with those obtained at 0.4 μm. Two T0 samples were analysed at step size 0.4 μm, for each sample two different near surface areas were examined.

In the first instance, the same grain based method that was successfully applied in shot peened nickel based superalloy Udimet 720Li was used [16]. The results of this approach are illustrated in Figure 4- 7a. Although the colour coded map indicates that there is an increase in misorientation as measured by grain orientation spread (GOS) near the shot peened surface, the change in the smoothed data is too small as to be able to confidently define the strain hardened region. This is a result of the high degree of intrinsic misorientation in this tempered martensitic material and as a result the application of a local misorientation method was investigated. This intrinsic misorientation is revealed by underlaying the image quality parameter in greyscale in Figure 4- 7a.

Several local parameters were investigated, including kernel average misorientation (KAM), local average misorientation (LAM) and local orientation spread (LOS) [56]. Figure 4- 8 shows that KAM exhibited the largest variation across the strain hardened

region minimising calibration error; this variation is illustrated in Figure 4- 7b. To calculate KAM, the misorientation between a point at the centre of the kernel and all points at the perimeter of the kernel (based on first nearest neighbour, second nearest neighbour etc.) are measured, excluding any points exceeding a specified tolerance value. The KAM assigned to the centre point is the average of these misorientations. A schematic illustrating this is shown in Figure 4- 9; it should be noted that this measurement can be affected by step size, thus step size independence should be verified when using this approach [56].

This kernel approach resulted in many more data points than the original grain based approach. Any data points with a KAM of 5˚ or greater were considered to represent block boundaries and removed [41] since it was found that although the number of highly misoriented points increased near the peened surface the analysis was less reproducible between analysis areas. The mean KAM at each depth (based on the sample surface mean line) was then calculated and the data were smoothed using the same procedure as for the hardness data. The strain hardened region can be clearly identified in Figure 4- 7b when the smoothed line is compared with the upper and lower unstrained bounds as identified from unstrained mean ± 2 times unstrained standard deviation.

4.3. Results

4.3.1. Microstructural changes

The changes in microstructure induced by compression are illustrated in Figure 4- 10. As the plastic strain increases, the grain structure changes with elongated pancake grains more evident. The prior austenite grains on the top surface appear to get larger as strain increases and become flatter on the front and side surfaces.

The changes in microstructure near the shot peened surface are compared with those resulting from the grinding process in Figure 4- 11. Due to the roughness induced at the shot peened surface, microstructural inspection was performed on the cross section indicated only.

Some grain refinement is evident in the near surface region of the shot peened samples when compared with the ground sample. The microstructure resulting from the T1 process with small shot at low velocity appears unchanged, although the T0 process does appear to have refined the surface microstructure over a region extending to approximately 70 μm; this is evidenced by heavier etching in the near surface region, which would be expected to correspond to work hardened material. This is particularly evident in the region highlighted under a shot peening dent. The T2

process which has resulted in the same Almen intensity as the T0 process using larger shot at a lower velocity has resulted in a microstructure where these changes are no longer evident. The T3 process with high Almen intensity (larger shot at a similar velocity to the T0 process) also shows a region of heavier etching, again under a peening dent.

The images in Figure 4- 11 have all been taken away from the edges of the shot peened samples where significant deformation can be identified. Figure 4- 12 shows the shear deformation that has taken place in the edge region of an etched shot peened (T0) sample. This large shear deformation is not representative of that in the bulk material, but indicates a need for caution when selecting the area of interest for residual stress and plastic strain analysis. Furthermore, the resulting stress concentration feature may lead to an increase in the propensity for fatigue initiation from fatigue sample edges; this is discussed further in Chapter 5.

4.3.2. Surface topography

4.3.2.1 Surface roughness and indent diameters

3D reconstructions of the surface topography for each sample surface condition are shown in Figure 4- 13a-e. Figure 4- 14 compares the line profile roughness parameters R_a and R_z with the areal equivalents S_a and S_z; there is no significant difference between optical and tactile line measurement techniques. It is clear that whilst the measurement of average amplitude parameters seems consistent when comparing areal and profile measurements, the areal measurement of maximum peak to valley height is significantly greater than the line measurement. This is indicative of the greater probability of finding a significant surface feature using areal scanning compared to line scanning.

The indent diameters resulting from shot peening are quantified using the two different approaches in Figure 4- 15; there are no apparent significant differences between the two measurement approaches.

Both measurements of surface roughness parameters and indent diameters tend to show that process T1 results in significantly less surface deformation than processes T0, T2 and T3. Furthermore, it appears that there is no significant difference in surface roughness between the two 13A processes and the 18A process. This result is similar to that in Udimet 720Li where S_a increased between 5A and 8A processes before reaching a plateau [16].

4.3.2.2 Verifying the shot peening process in notched geometries

Figure 4- 14 shows the inherent variability in the R_a measured using the Talysurf resulting from shot peening process T0. For this process, the mean value (with error quoted as 95 % confidence range) was obtained from 144 measurements as R_a = 3.39 ± 1.06 µm (±32 %). The maximum absolute deviation from the mean was 1.64 µm (48 %). This variability in roughness is greater than that which was previously reported by Clausen and Stangenberg [57]. The non-directionality of the surface roughness was confirmed by performing roughness measurements on 10 % of the flat surfaces measured in a perpendicular direction to that used for all other measurements; the mean R_a in this direction was found to be 3.27 µm.

R_a was measured at varying points around the notch for each of the fatigue test geometries (Chapter 5) peened using process T0. The measurement locations are indicated in Figure 4- 16. Since it was expected that there would be a difference in the results of the shot peening process between left and right sides of the notch caused by the slight angle at which the nozzle was inclined to the flat surface during the shot peening process, the data was first processed to separate left and right sides into 'On' and 'Off' sides based on whether the average R_a for levels 1 and 2 (notch positions which are equiangular from base and surface) from the left side was higher or lower than levels 1 and 2 from the right side. The higher average was assumed to be the 'On' side and the lower the 'Off' side.

Based on the raw data set, three core observations were made:

- On side R_a > Off side R_a in 6 of the 8 cases (where the on side is expected to be that aligned most perpendicular to the impeding shot).
- Level 2 R_a > Level 1 R_a in 5 of the 8 cases.
- Base R_a > Level 1 R_a in 6 of the 8 cases. Base R_a > Level 2 R_a in 7 of the 8 cases.

These results are presented graphically as cumulative probability curves in Figure 4-16. The t-test was used to test the significance of these results; none of the observations were found to be statistically significant.

Figure 4- 16 illustrates that all but two measurements of notch R_a lie within the absolute range observed for flat R_a. It is noted that both measurements outside the range have R_a greater than those measured for the flat surfaces and are thus not thought to be a result of notch shielding. Furthermore, apart from the measurements taken for the 10.5 x 3 mm notch, all mean values for notch R_a are greater than the flat mean of R_a = 3.39 µm and even those for the 10.5 x 3 mm notch measurements are still greater than the lower 95 % flat confidence limit.

Thus, on the basis of surface roughness measurements, it can be concluded that the inherent variability in the shot peening process is greater than that which is caused by the notch profile geometry.

4.3.3. Residual stress

The residual stress profiles measured in ground and both flat and notched shot peened (T0) samples are shown in Figure 4- 17.

Since the shot peened samples were all pre-ground to the same specification, consideration was made of the residual stresses present in the material before the application of the shot peening process. All grinding took place in the transverse direction; in this direction at the surface no residual stress has been recorded. This is in contrast to the longitudinal direction where there is an apparent surface compressive residual stress. In both cases the residual stress increases to a maximum tensile stress at approximately 25 μm; the magnitude of this tensile stress is greater in the longitudinal direction. The residual stress then decays to a balancing tensile stress.

Given the expected measurement variability, there is no significant difference between the stress distributions resulting from shot peening in both directions in the flat sample and the stress distribution in the transverse direction in the notched sample (the maximum stress was -630 MPa or $-0.8\sigma_{0.2}$); however the stress distribution in the notched sample longitudinal direction appears to be more compressive (with a maximum at -780 MPa). The depth to which the elevated compressive stress extends is, however, unchanged with the stress beginning to increase towards zero in all four cases at approximately 200 μm. The total depth of the compressive residual stresses in all cases was 340 μm.

Whilst the increased magnitude of longitudinal compressive residual stress may not have been anticipated in the notch root given the potential shadowing effect of the notch in preventing shot impinging at the base of the notch, these results are in line with previous work [58] and the slight increase in mean R_a found at varying locations around the notch in this geometry (Figure 4- 16).

4.3.4. Plastic strain

4.3.4.1 Compression samples

The results of the plastic strain indicators for the calibration samples are shown in Figure 4- 18. A power law least squares regression resulted in the most appropriate calibration curve for the percentage change in microhardness data shown in Figure 4-

18a; this is not surprising given the Ramberg-Osgood behaviour shown by FV448 shown previously in Chapter 3.

The 95 % confidence bars are based on 20 measurements for each calibration sample; however there are clear issues with repeatability reflected by the large error bars and the low R^2 value. It was ensured that there was no variation in hardness with location on each sample to eliminate barrelling effects as the cause of this scatter. The resulting difficulty in quantifying the error in the calibration was one reason for the development of the other techniques as it meant that no error bounds could easily be placed on the calibrated data from shot peened samples.

Two least squares regressions were applied to the XRD FWHM data shown in Figure 4-18b, both resulted in considerably higher R^2 values than the microhardness calibration. There was found to be no significant difference between the plastic strain profiles once they were applied. The power law (allowing a constant term for instrumental broadening) was selected rather than the exponential law (previously used by Prevéy [12, 21] in nickel base alloys), since the fit was almost as good, was easier to apply as no numerical solution was required and allowed a more consistent comparison with the microhardness measurements. The error bars shown are constant at 0.12˚ as previously discussed and were not calculated for each measurement point; they are shown to indicate the order of the error existing in FWHM measurements on strained samples. Since this error is not well defined and R^2 was so high for this calibration, no error bounds were placed on the calibrated data from shot peened samples.

Using EBSD techniques, the KAM vs. plastic strain graph shown in Figure 4- 18c was determined for the calibration samples. There was no clear power law fit and so a straight line fit was applied. The EBSD data is more averaged than the other two approaches and the 95 % confidence bars for each sample were based on 250,000 data points. The upper and lower bounds shown were calculated based on the average error across the 12 calibration samples; whilst the confidence in the fit is much better than for the microhardness data, it is lower than for the XRD data. This is exemplified by the mean points for two of the calibration samples lying outside the calibration error bounds. The high density data allowed account to be taken of this error. The unstrained KAM shown is known with a high degree of confidence, since it is the average of all the data points taken in the unstrained regions of the shot peened samples. Hence a linear shift was used to force the correct unstrained KAM in the calibration for each shot peened sample.

4.3.4.2 Shot peened samples

Figure 4- 19 compares the repeatability of the EBSD measurement technique. The results of four scans on T0 samples at 0.4 μm step size are shown and compared with the result of the scan at 0.2 μm step size. The high level of repeatability in the data is clear and the profile of Sample 1a was selected as representative of the T0 process. Applying the error bounds shown in Figure 4- 18c resulted in a far wider band than is required based on the data shown. Instead, in the present analysis all calibrated plastic strains were adjusted by 20 %, this is equivalent to the worst case deviation from the mean line of the calibration sample at ε_p = 0.2 and resulted in the bounding curves shown in Figure 4- 19. The lower bound curve gives the lowest prediction of yield strength for a given misorientation and is considered representative for this data set; the lower bound is applied to all EBSD data presented from this point forwards.

The plastic strain in notched and flat samples resulting from process T0 was compared using XRD and the results are shown in Figure 4- 20 along with the results for the ground comparison sample. The results are consistent and there is no indication that the notch geometry has had an effect on the plastic strain resulting from shot peening.

The near surface plastic strain profiles after shot peening process T0 measured by the three techniques under consideration are compared in Figure 4- 21a. The corresponding yield strength profiles determined using the monotonic tensile Ramberg-Osgood relationship are compared in Figure 4- 21b. The XRD profile is very similar to the EBSD profile, although the measurement of the surface plastic strain is higher using XRD; once calibrated to yield strength, the error at this point appears less significant; this is a result of the shape of the Ramberg-Osgood curve. Although at the first point of measurement, the yield strength determined by microhardness is not too dissimilar to that measured using the other two approaches, the profile extends much further into the sample. Indeed comparison with the residual stress data presented in Figure 4- 17 indicates that the plastic strain profiles measured using XRD and EBSD correlate very well with the depth of the maximum compressive residual stress at 150 μm; that measured using the hardness traverse extends to 250 μm which is closer to the overall depth of the compressive residual stresses at 340 μm.

The plastic strain profiles resulting from each peening process are shown in Figure 4- 22. Unlike the XRD data shown in Figure 4- 20, measurements on ground samples did not detect any significant plastic strain profile although there was an upwards trend in misorientation (that remained within the mean ± 95 % confidence bounds) in the 15 μm nearest the surface indicating that there may have been some near surface plastic deformation. This is in keeping with the XRD results and the presence of a tensile residual stress near the surface of the ground samples.

It is clear that the industrial 13A process (T0) resulted in the highest plastic strain in the near surface region. Increasing the intensity of the process to 18A (T3) resulted in a flatter profile near the surface but the same depth of profile, although the plastic strain remained high to a greater depth than in the industrial 13A process. Decreasing the intensity of the process to 4A (T1) resulted in a lower surface plastic strain and shallower profile. Increasing the shot size and reducing the velocity and maintaining the intensity at 13A (T2) resulted in a shallower profile with lower surface plastic strain compared to the industrial process.

4.4. Discussion

4.4.1. Optimal surface deformation measurement techniques

Greater areal maximum peak to valley measurements than line measurements have previously been reported for much rougher surfaces (R_a ~ 20 µm) [59]. This trend is also present in the shot peened surfaces (R_a ~ 3 µm) presented here. The implication for component lifing is clear: Using the optical R_z data reported for T0 in the stress concentration assessment approach of Li *et al*. [60] and assuming that peaks are separated by the average indent diameter, the elastic stress concentration factor, K_t = 1.26 based on an average indent of 168 µm measured optically. Using the same empirical relationship for S_z data results in K_t = 1.43, an increase of 13.6 %. Despite the original paper [60] being based on finite element analyses and thus well-defined dent geometries, the approach is most typically applied using line profiles [51] which may not detect the worst case defect. The application of areal profiles increases the chance of picking up the worst case stress concentration and would represent a more conservative approach.

Indent diameter measurements were made using two different approaches. It was thought that measurements made on a 200 % coverage surface might be influenced by neighbouring impacts and that the crude method of measuring maximum feret diameters might be an oversimplification. Furthermore, it was relatively difficult to identify indents from the resulting images, partly due to the limited depth of field of the Olympus optical microscope. However, comparison with the Alicona results taken from measuring the indent diameter on a surface where individual indents could be readily identified and imaged in three dimensions, allowing the reference plane position to be taken into account, did not result in significant differences in measured diameter. Given that there is no significant difference in results between the two measurement techniques, it is concluded that measurements on a full coverage surface using a simple optical microscope are sufficient and are preferred, since the approach

does not require the additional peening of low coverage samples and is quicker and simpler than the more complex three dimensional technique.

The accurate description of near surface strain hardening is important, especially if it is to be used in finite element models determining component stress and strain distributions for application in life assessment (for example following the procedure described by Benedetti *et al.* [44]). Of the three approaches to measuring cumulative plastic strain presented in this work, despite the difference in sample volume (XRD being greater than EBSD [37]), EBSD and XRD techniques are the most consistent. Although easy to use, there are several drawbacks to the microhardness technique, the first being that constraint effects prevent indents being placed immediately next to the peened surface of interest. The other major drawback to the approach is the increase in indicated plastic strain depth resulting in a deeper elevated yield strength profile which could lead to non-conservative estimates of component remnant life. This might be a result of the influence of residual stresses on hardness measurements [23]. It is generally considered that plastic strain has the greatest influence on hardness, indeed interpolation based on the results of Xu and Li [61] indicates that in the present case, at the maximum residual stress ~-0.8$\sigma_{0.2}$ and $E/\sigma_{0.2}$ = 250, the variation in hardness caused by residual stresses would be expected to be just 5 %. However, given the sensitivity of the power law calibration at low plastic strains and the shape of the Ramberg-Osgood curve, even small changes in hardness could lead to increases in the estimated yield strength.

For this reason, the microhardness technique was not applied further in the present investigation. EBSD is advantageous over XRD in that many more data points are collected and results are more averaged, increasing confidence in the data. Since the XRD data is produced from discrete data points, the confidence in individual data points is lower. However, the calibration R^2 value was higher for XRD and although time consuming, FWHM data is typically available from the same data set as that used for residual stress measurements, so the approach could be applied if residual stress measurements were required with no further data collection requirements. A key indication from the results is that a mix and match approach can be used depending on which method is more appropriate to a given situation. Indeed this mix and match approach has been used in the present work, applying the EBSD technique to compare the different peening processes where incremental layer removal XRD would have been too time consuming, and applying the XRD technique to investigate the effect of fatigue on dislocation distribution since the data was already available after residual stress analysis; the effects of fatigue are reported further in Chapter 5.

As expected, based on the work of Child *et al.* [16], peening at a higher intensity resulted in high plastic strains extending to a greater depth whilst peening at a lower

intensity resulted in lower plastic strains and a shallower profile. However, the comparison of T0 and T2 is of interest in the present case. It is not just the intensity of the shot peening process which is important, but also the manner in which that intensity is achieved as this affects the resulting plastic strain profile. This new plastic strain data supports the previous conclusions based on surface microhardness [62], residual stress measurements [22, 63] and rotating bend fatigue life [64]. This emphasises the requirement for strain hardening and residual stress profiles for each target material – shot peening process system if the effects of the peening process are to be included in component lifing protocols. Furthermore, the need for a well optimised process is clear, despite the lower yield strength resulting from process T2 than T0, the worst case defect as measured by S_z is increased, indicating that the initiation life of samples peened using process T2 would be worse than those peened using T0.

4.4.2. Residual stress and cumulative plastic strain profiles

The shape of the post-grinding residual stress profile is similar to that which has been reported previously [65]. The 'more tensile' residual stress at the surface in the transverse (grinding) direction would be expected [65-67]; however, the higher maximum tensile residual stress in the longitudinal direction is contrary to previous work [65, 66]. This may be a result of the need to balance the surface compressive residual stress; this change of sign near the surface in the longitudinal direction has also not been reported in other work.

There are three mechanisms of generating residual stresses during grinding: mechanical deformation, thermally induced deformation and phase transformations in hardened steels [66]. One possible explanation for the sign change is an increased dominance of the mechanical residual stress creation mechanism at the notch surface (stress concentrator) and a resulting compressive residual stress despite the high temperature of the grinding process which has resulted in tensile residual stresses at greater depths.

One other possible explanation would be the attainment of temperatures in excess of that required to form austenite during the grinding process and the formation of untempered martensite at the sample surface with a corresponding compressive residual stress; overtempered material would be present in subsurface layers with a corresponding tensile residual stress. The formation of untempered martensite at the sample surface would, however, be associated with both a more significant variation in local misorientation near the surface than was observed and discernible variation in the microstructure near the ground surface illustrated Figure 4- 11. Hence phase change was eliminated as the cause of the grinding residual stress.

It is clear from Figure 4- 17 that the shot peening process applied has been sufficient to remove all evidence of the grinding residual stress profiles, converting to a compressive profile of the form generally expected from shot peening. In order to validate the profile, comparisons have been made with several empirical and analytical prediction methods previously developed and published in the open literature and described briefly below. Where the method requires materials properties data, monotonic data in the direction perpendicular to rolling (as described in Chapter 3) is used for consistency with the model applied further in Chapter 5. Where indent diameters are required, the measurements made on the 200 % coverage surface with the Olympus microscope are used.

The empirical equations developed by Gao *et al.* [68] (Equations 2-1 to 2-4) were first used to predict the key parameters describing the residual stress profile. Initial analytic estimates have also been calculated based on the work of Al Hassani [69] and Hills and Waterhouse [70]. The maximum stress allowed was based on the von Mises yield criterion. The depth of the residual stress field was approximated using the analysis of Al Hassani [69] which represents the stress field beneath each dent as that in an elastic/plastic medium containing a spherical cavity. The plastic solution for the stress distribution under the indent $\sigma(z)$ is given in Equation 4-8 and was extrapolated to find the point at which the predicted residual stress first reached zero. The plate of thickness h was allowed to elastically unload to obtain the resulting residual stress; the point at which this reached zero was found. This is sufficient as a first approximation for the depth of the residual stress field.

$$\frac{\sigma(z)}{\sigma^0} = 1 - 2\ln\left(\frac{h_p+R_{shot}}{z+R_{shot}}\right) - 2\left[1-\left(\frac{h_p+R_{shot}}{h+R_{shot}}\right)^3\right] \quad \text{where} \quad z \leq h_p \tag{4- 8}$$

Where h_p is the depth of the plastic zone and the shot radius is R_{shot}. Al Hassani [69] defined the plastic boundary using the maximum shear stress contour. After much analysis, it was shown that the depth of the plastic boundary could be related to R_{shot} and the depth of indentation ($D_{z,shot}$) by Equation 4-9. Approximating the dynamic collision by a quasi-static analysis resulted in Equation 4-10.

$$\frac{h_p}{R_{shot}} = 2.57\left(\frac{D_{z,shot}}{R_{shot}}\right)^{\frac{1}{2}} \tag{4- 9}$$

$$\frac{h_p}{R_{shot}} = 2.57\left(\frac{2}{3}\right)^{\frac{1}{4}}\left(\frac{\rho_{shot}{v_{shot}}^2}{P_{mean}}\right)^{\frac{1}{4}} \tag{4- 10}$$

Where ρ_{shot} is the shot density, v_{shot} is the shot velocity and P_{mean} is the mean Hertzian contact pressure.

The analytical model developed by Li *et al*. [71] has also been applied using the bilinear material model described in Chapter 3. The classical elastic, frictionless contact theory of Hertz can be modified to account for elastic impact by considering it a quasi-static event with deformation restricted to the vicinity of the contact area and ignoring the effects of elastic waves. The simplest consideration is for a collinear impact; the maximum Hertzian contact pressure (P_0) can be calculated from Equation 4-11 whilst a_{Hz} can be calculated from Equation 4-12 [72].

$$P_0 = \frac{3}{2\pi}\left(\frac{4E^*}{3R^{*0.75}}\right)^{\frac{4}{5}}\left(\frac{5}{4}m_{shot}{v_{shot}}^2\right)^{\frac{1}{5}} \tag{4-11}$$

$$a_{Hz} = \frac{\pi P_0 R^*}{2E^*} \tag{4-12}$$

Where m_{shot} is the mass of the shot, $\frac{1}{E^*} = \frac{1-{\nu_{target}}^2}{E_{target}} + \frac{1-{\nu_{shot}}^2}{E_{shot}}$ and $\frac{1}{R^*} = \frac{1}{R_{target}} + \frac{1}{R_{shot}}$; R_{target} is the radius of the target, which tends to infinity.

The elastic von Mises equivalent stress distribution, σ_{eq}^e, beneath a single impact was calculated using Equation 4-13. Hooke's Law (Equation 4-14) was used to convert this to an equivalent elastic strain distribution, ε_{eq}^e. In order to account for plastic deformation, α, a coefficient relating calculated elastic indent diameter $2a_{Hz}$ to that measured experimentally, D_d was employed. Thus Equation 4-15 was used to convert the elastic strain distribution to an elastic plastic one; the materials model was then used to determine the elastic plastic stress distribution in accordance with Equation 4-16.

$$\sigma_{eq}^e = P_0\left[\frac{3}{2}A_3 - (1+\upsilon)B_2\right] \text{ where } A_3 = \left[1+\left(\frac{z}{a_{Hz}}\right)^2\right]^{-1} \text{ and } B_2 = 1 - \frac{z}{a_{Hz}}\tan^{-1}\left(\frac{a_{Hz}}{z}\right) \tag{4-13}$$

$$\varepsilon_{eq}^e = \frac{\sigma_{eq}^e}{E_{target}} \tag{4-14}$$

$$\varepsilon_{eq} = \begin{cases} \varepsilon_{eq}^e & \text{for } \varepsilon_{eq}^e \le \varepsilon^0 \\ \varepsilon^0 + \alpha\left(\varepsilon_{eq}^e - \varepsilon^0\right) & \text{for } \varepsilon_{eq}^e > \varepsilon^0 \end{cases} \quad \text{where} \quad \alpha = \frac{D_d}{2a_{Hz}} \tag{4-15}$$

$$\sigma_{eq} = \begin{cases} E\varepsilon_{eq} & \text{for } \varepsilon_{eq} \le \varepsilon^0 \\ \sigma^0 + H_1\left(\varepsilon_{eq} - \varepsilon^0\right) & \text{for } \varepsilon_{eq} > \varepsilon^0 \end{cases} \tag{4-16}$$

The residual stresses after unloading a single impact, $\sigma_{res11,22}^{sing}$, were calculated based on the assumptions that the amount of deformation was small, unloading is an elastic process until reversed yielding starts and hydrostatic stress does not induce plastic deformation (Equation 4-17). Some stress relaxation is allowed in accordance with Hooke's Law to ensure that the derived equations satisfy the equilibrium conditions for steady and continuous shot peening; the resulting in plane residual stress resulting

from multiple impacts, $\sigma_{res11,22}^{multi}$, is calculated from Equation 4-18. Figure 4- 23 illustrates these calculation stages for process T0.

$$\sigma_{res11}^{sing} = \sigma_{res22}^{sing} = \begin{cases} 0 & \text{for } \sigma_{eq}^{e} < \sigma^{0} \\ \frac{1}{3}\left(\sigma_{eq} - \sigma_{eq}^{e}\right) & \text{for } \sigma^{0} \leq \sigma_{eq}^{e} \leq 2\sigma_{eq} \\ \frac{1}{3}\left(\sigma_{eq} - 2\sigma_{eq} - \Delta\sigma_{eq}\right) & \text{for } \sigma_{eq}^{e} \geq 2\sigma_{eq} \end{cases} \quad (4\text{- }17)$$

$$\sigma_{res11}^{multi} = \sigma_{res22}^{multi} = \frac{1+v}{1-v}\sigma_{res11}^{sing} \quad (4\text{- }18)$$

The results of these comparisons for the residual stress resulting from the T0 process are shown in Figure 4- 24. Also shown are the residual stresses predicted by Metal Improvement Company using their in-house software Peenstress®.

The Peenstress® results show maximum residual stresses greater than the monotonic yield stress in FV448; this result is both unrealistic and very different to both the experimental results and the other prediction procedures applied (Figure 4- 24). The over-prediction of the residual stress magnitude by Peenstress® was unexpected given the under-prediction shown in other work in the literature [16]; this apparent unreliability was the main reason for the application of the other predictive approaches.

The magnitude of residual stress predicted by the model after Li *et al.* [71] results in much better correlation with experimental results than the Peenstress® profile with a conservative prediction of maximum compressive residual stress within 20 % of the experimentally measured value and an excellent prediction of profile depth. The predicted residual stress profile is, however, flat, with no distinction between surface residual stress and maximum compressive residual stress; this was also observed by Franchim *et al.* [73] when using a similar material model and could be modified by using a Ramberg-Osgood type material model with appropriate unloading criteria. However, since the purpose of the analytical model in the present case was to validate the experimental profile, this additional computation is not considered necessary in the present case.

The predictions of maximum compressive residual stress and profile depth after Al Hassani [69] serve to increase the confidence in the experimental and full analytical procedure after Li *et al.* [71]. The empirical method of Gao *et al*. [68] results in a good prediction of the magnitude of the surface compressive residual stress and although the estimated profile depth is slightly shallow, the approach could be used as a first approximation of the expected residual stress profile. The analytical approach of Li *et al.* [71] was subsequently applied to the other shot peening processes investigated; the resulting predicted residual stress profiles are shown in Figure 4- 25.

The trends shown by these predictions are in line with expectation based on the work of Meguid *et al.* [74] and Hong *et al.* [75], that is that increasing intensity increases the depth of the residual stress profile, but not the maximum compressive residual stress that is achieved. Changing the way in which the intensity is achieved (T0 vs. T2) results in only a slight change in the predicted residual stress profile. A summary of the key parameters (maximum compressive residual stress, σ_{mcrs}, depth of the maximum compressive residual stress, z_m and overall compressive profile depth, z_0) predicted is given in Table 4- 3. This data is compared with the overall measured depths of cumulative plastic strain shown in Figure 4- 22.

Table 4- 3 indicates that it is not possible to use a ratio of the measured cumulative plastic strain profile to make direct inferences on the residual stress profile and vice versa. This means that in order to include both strain hardening and residual stress profiles it is necessary to measure (or predict) both. The present investigation has shown that residual stresses can either be measured using XRD or predicted using the analytical model of Li *et al.* [71] and cumulative plastic strain can be measured using EBSD or XRD approaches.

For completeness, it is noted here that an attempt was made to develop a finite element (FE) protocol building upon work already carried out on modelling both the shot peening process [76] solid particle erosion (SPE) process [77] with the aim of establishing all nine stress components rather than the in-plane stress results provided by experimental and analytical methods. This would be advantageous if importing initial residual stresses for life assessment directly. Despite the axisymmetric approach used being validated against the results for an idealised system presented in the literature [76], upon application to the present system, several difficulties were encountered which meant the predicted residual stresses were not in good agreement with those experimentally determined. In fact, the maximum in plane compressive residual stress predicted to result from a single impact was -1000 MPa, and the depth of the profile was 0.24 mm; comparison with Figure 4- 24 indicates that these numerical results were more closely correlated with the Peenstress® results than with the experimental data. The FE approach is considered in greater detail in Appendix B to this chapter.

It is believed that the key parameter responsible for the difference between the numerically simulated residual stress profile and the experimental result is the modelling of plasticity in the target material. Both the FE approach and the Peenstress® approach directly account for plasticity, in this case using monotonic data, unlike the procedure based on Li *et al.* [71] which uses a plasticity correction factor. It is thought that whilst simplistic, this plasticity correction factor allows any differences resulting

from strain rate sensitivity and the cyclic softening that have not been accounted for in the Peenstress® or FE approaches to be implicitly included.

In order to optimise the shot peening process for a given target material – shot peening process system and assess the sensitivity of the results to variation in process parameters, an approach to predict the residual stresses that does not require extensive experimentation or computational analysis is desirable. However, the results presented suggest that this may only be achievable once full account of the target material behaviour is taken, such as by implementing the combined hardening model suggested by Klemenz *et al.* [78]. However, the application of this approach to a sensitivity study is not possible for two reasons: Firstly, the data required to generate these material models require extensive experimentation and are thus non-trivial to obtain and secondly, the computational expense of running such a multiple impingement model is too great for application in a sensitivity study. As a result, an appropriate prediction tool for use in a sensitivity analysis is still required.

4.4.3. Quality assurance for the shot peening process

4.4.3.1 Shot peening process control

Shot peening is a dynamic process which requires close process control in order to achieve the desired results. Typically controlled parameters include the shot used, intensity and coverage [79]. The shot used is controlled by a specification such as MIL-S-851D [80]; a sieve system is employed to remove media of the incorrect size and a spiral separation system is often used to ensure broken media is removed. It is important to correctly understand the tolerances on shot being used for a given process as inconsistently sized shot can result in a non-uniform compressive layer and damaged shot can result in a poor surface finish [79]. Intensity is typically controlled using Almen strips as described in Section 2.1.1; the time required for 100 % coverage in a given system can be determined either visually for soft materials where the dimples are easily distinguishable or by using a fluorescent dye which is removed by impacting shot [79].

It has become apparent from the results presented in Section 4.3 that it is not only intensity which affects the outcome of the shot peening process but also the combination of shot size and velocity selected. Once the peening process has been optimised, specific shot size and tolerance are known, so control of intensity is sufficient to ensure a consistent outcome. The standard Almen strip approach to intensity control should be applied to all peened components, including those peened on-site.

4.4.3.2 Verification of the peening process

For components peened on-site, a system whereby the peening process can be verified is desirable. Whilst the experimental approaches discussed thus far are useful tools in the optimisation process and generate the surface roughness, strain hardening and residual stress data that are essential in incorporating the shot peening process in life assessment procedures, they are destructive either because they require layer removal or because they require the component to be sectioned before testing. To this end, a surface load variance hardness testing procedure [81, 82] was investigated for its potential to distinguish between different surface plastic strains sufficiently (when used in conjunction with a portable hardness testing system [83]) as to be able to indicate whether the peening process has been performed within the required tolerance. Further details of the load variance approach can be found in Appendix C to this chapter.

Whilst data from the surface load variation hardness procedure showed the general trend of decreasing indicated microhardness with increasing depth of indentation, the accuracy of the laboratory micro hardness system used in the present investigation was not sufficient to resolve the different peening processes; thus the approach is not appropriate for application in acceptance criteria for peening processes. This was due to the large variation in repeat hardness measurements under each load resulting from indenting a dimpled surface compared with the relatively small expected variation in plasticized depth for each peening process. Whilst the error could possibly be reduced sufficiently so as to be able to resolve the different peening processes by polishing the surface before indentation and using a nano-indentation system which is able to provide load-displacement data, this modified technique would not be representative of an on-site repair process and could not be applied to service components. Hence an approach for verifying on-site peening processes is still required.

4.4.3.3 Recommendations to operators

The current recommendation to operators is that the process be optimised for a given target material as best as possible in conjunction with suppliers using Peenstress® (or an alternative in-house equivalent). Several test runs should be carried out around the optimal point with subsequent areal analysis of surface roughness and inference of surface stress concentration factors, optical analysis of indent size and EBSD analysis of plastic strain and inference of strain hardening. The indent size data can be used in conjunction with the analytical model based on the work of Li *et al.* [71] to predict the residual stress in each case and allow a final decision on the process parameters. If the residual stress profile is to be included in fatigue lifing protocols, residual stress analysis by laboratory XRD should be carried out to verify the residual stress profile for

the selected process. Where a new supplier is used for the first time to apply a previously optimised process, it is also recommended that the process is verified using surface profile analysis and EBSD local misorientation analysis as a minimum and additionally XRD residual stress analysis as the gold standard.

4.5. Conclusions

This chapter focussed on determining the specific surface topographical, strain hardening and residual stress profiles resulting from the industrial shot peening process T0. Comparisons have also been drawn with the profiles resulting from shot peening processes at different intensities. The optimum experimental approach for defining the surface roughness and strain hardening profile with a view to including the corresponding stress concentration factors and variation in near surface yield strength in fatigue life assessments was investigated; this represents a significant step towards standardising an approach for including such effects in remnant life estimates. The following conclusions can be drawn:

- Component shape has no effect on the efficacy of the shot peening process as measured by the induced surface roughness, residual stress and plastic strain profiles.
- Shot peening results in a dimpled surface topography; the size of the indents can be satisfactorily measured using optical microscopy directly on a 200 % coverage surface. Both tactile and optical instruments can be used to determine roughness parameters based on line profiles; such profiles can be used to qualitatively compare processes. Where data on peak to valley height is required to determine elastic stress concentration factors for use in fatigue life assessment, areal data should be used since the most significant surface features in the area of interest will be assessed. Increasing process intensity tends to increase both indent diameter and surface roughness, although both effects tend to saturate at higher intensities.
- The grinding process used in sample preparation caused tensile residual stresses in the very near surface region; the T0 shot peening process was sufficient to convert these residual stresses to compressive stresses of the form expected from shot peening. The best model for predicting these residual stresses is a physical model employing a simple bilinear material model and a correction factor allowing for plasticity. The T0 residual stress profile was predicted to within 20 % of the experimental profile.
- Shot peening induces microstructural changes in the near surface region. Microhardness, EBSD local misorientation and XRD FWHM measurements can all be used in conjunction with a series of calibration samples to calculate the yield

strength profile resulting from shot peening. EBSD and XRD approaches showed the most consistent results with microhardness traverses tending to overestimate the extent of the strain hardened region. EBSD misorientation maps consist of more data points so the data is more averaged and the confidence is high, however, despite being more time consuming and only resulting in discrete data points, the XRD calibration R^2 value was higher than that of the EBSD method and the technique can be applied to data already collected for residual stress measurements.

- Increasing the intensity above an industrially optimised process may not necessarily increase the depth of the plastic strain profile but may result in higher plastic strains being retained deeper in the profile. Reducing the intensity of the shot peening process tends to reduce the magnitude and depth of the plastic strain profile. The plastic strain profile is not just dependent on intensity, but also on the combination of shot size and velocity.
- The measured strain hardening affected region for process T0 extends to approximately half the depth of the compressive residual stresses. However, comparisons of measured plastic strain for the other peening processes with predicted residual stresses indicate that the measured plastic strain profile cannot be used to directly infer the residual stress profile and vice versa. Hence the inclusion of strain hardening and residual stress in the component finite element models used for fatigue life assessment (allowing determination of the resulting changes in local stress and strain parameters) requires both effects to be determined independently.
- Optimisation of the shot peening process requires some experimental data to verify the prediction tool in use. The recommended minimum is as follows:
    - Surface roughness data is used to infer stress concentration features at the surface.
    - Indent size is used to infer the residual stress profile using the physical model.
    - EBSD data is used to infer the plastic strain profile.

The strain hardening and residual stress data detailed in this chapter is sufficient for inclusion in component FE models allowing the consideration of shot peening. However, additional data on the stability of these profiles under operational conditions is also required; the material model implemented in the FE model must be capable of predicting these changes. Furthermore, experimental data is also required on the effect that shot peening has on fatigue life in simple component geometries allowing validation of the lifing protocol under development. These issues are discussed further in the next chapter.

Method	Depth /μm	Source
Microhardness	120	Kim *et al.* [13]
Laboratory XRD FWHM	100	Kim *et al.* [13]
Microhardness	100	Child *et al.* [16]
EBSD grain based misorientation	70	Child *et al.* [16]

Table 4- 1: Comparison of indicated plastic strain depths resulting from shot peening (6-8A) Udimet 720Li.

Process	Label	Intensity	Coverage /%	Shot diameter /mm	Shot hardness /HRC	Shot velocity /ms^{-1}
MI110R 04A 200%	T1	4A	200	0.28	45-52	26
MI230R 13A 200%	T0	13A	200	0.58	45-52	57
MI330R 13A 200%	T2	13A	200	0.84	45-52	35
MI330R 18A 200%	T3	18A	200	0.84	45-52	54

Table 4- 2: Shot peening process parameters; all shot peening was carried out by Metal Improvement Company Derby Division.

Process	Bilinear model based on Li *et al.* [71]			EBSD measured h_p /mm	h_p / z_0
	σ_{mcrs}/MPa	z_m /mm	z_0 /mm		
T1	-499	0.0650	0.1000	0.037	0.37
T0	-499	0.2275	0.3350	0.15	0.45
T2	-499	0.2425	0.3575	0.086	0.24
T3	-499	0.3200	0.4675	0.154	0.33

Table 4- 3: Comparison of predicted residual stress profiles with measured cumulative plastic strain profile depths.

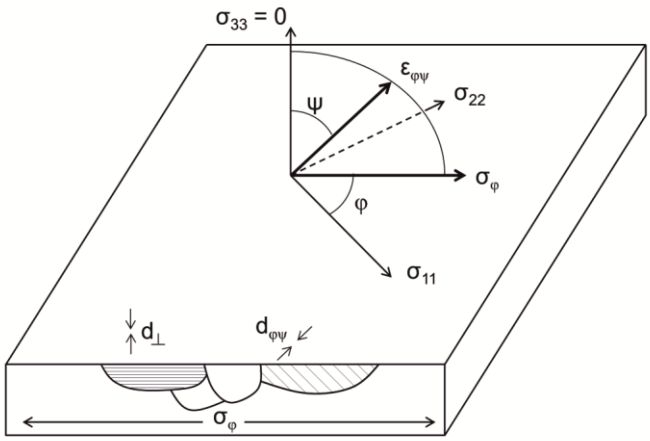

Figure 4- 1: Schematic showing diffraction planes parallel to the surface and at an angle $\varphi\psi$. After Fitzpatrick *et al.* [4].

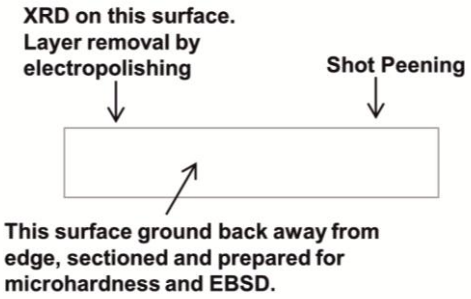

Figure 4- 2: Sample preparation.

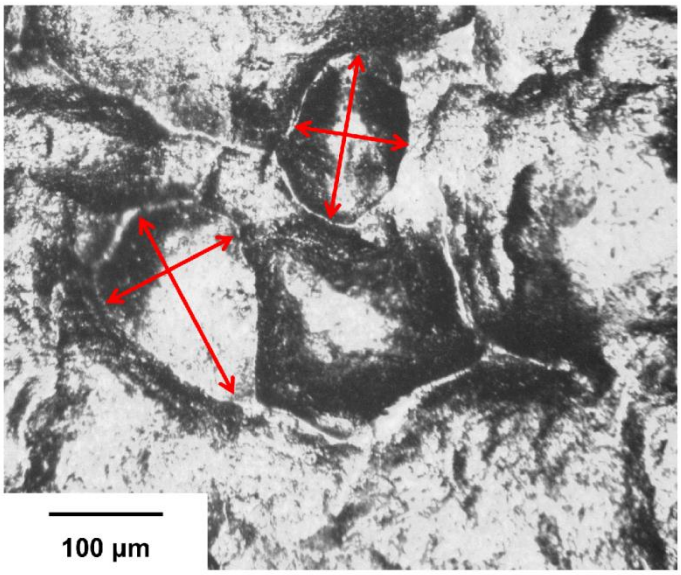

Figure 4- 3: Optical micrograph of a shot peened (T0) surface illustrating dent diameter measurement.

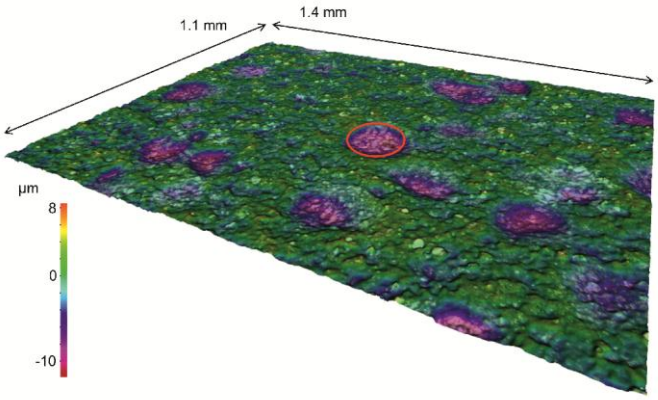

Figure 4- 4: Alicona Infinite Focus 3D view of a shot peened (T0) surface illustrating dent diameter measurement.

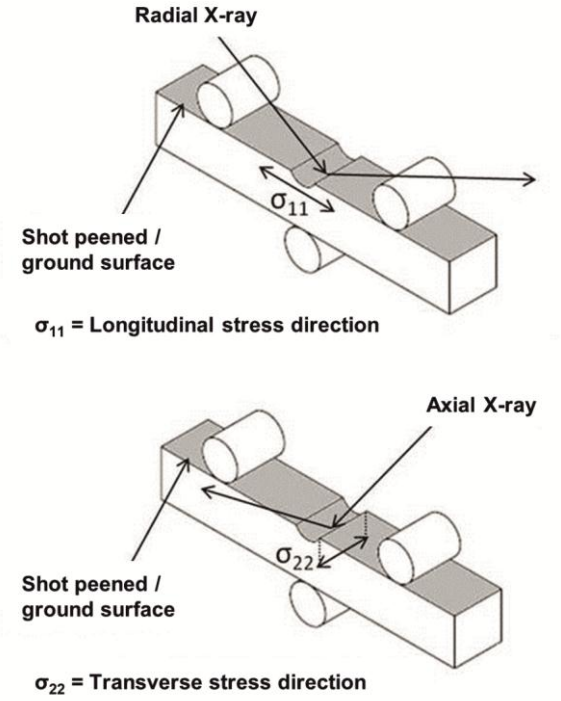

Figure 4- 5: XRD setup.

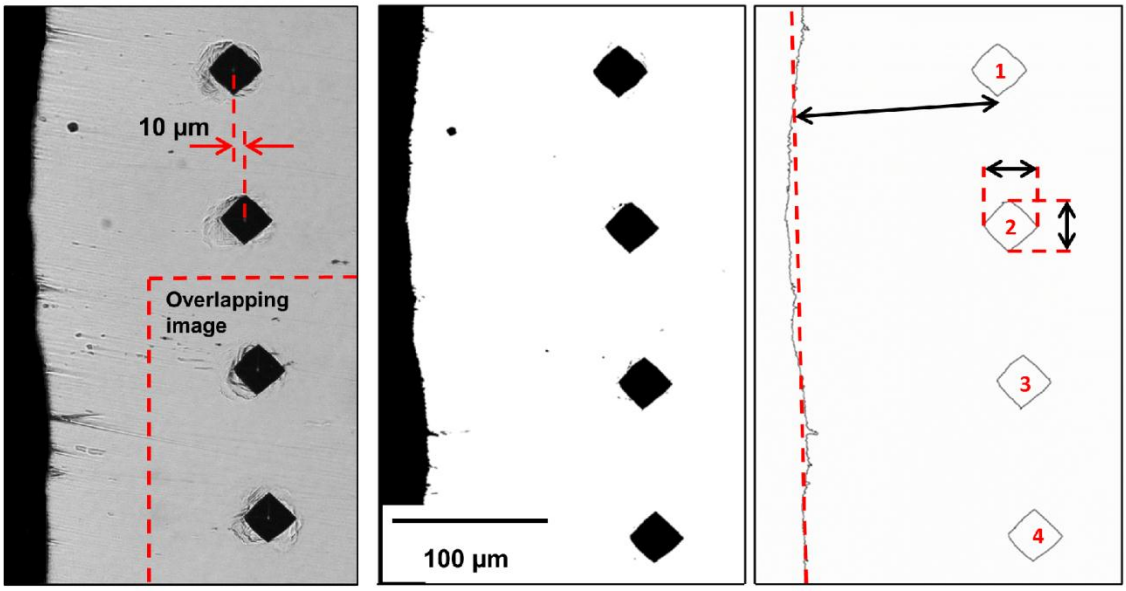

Figure 4- 6: Microhardness traverse technique.

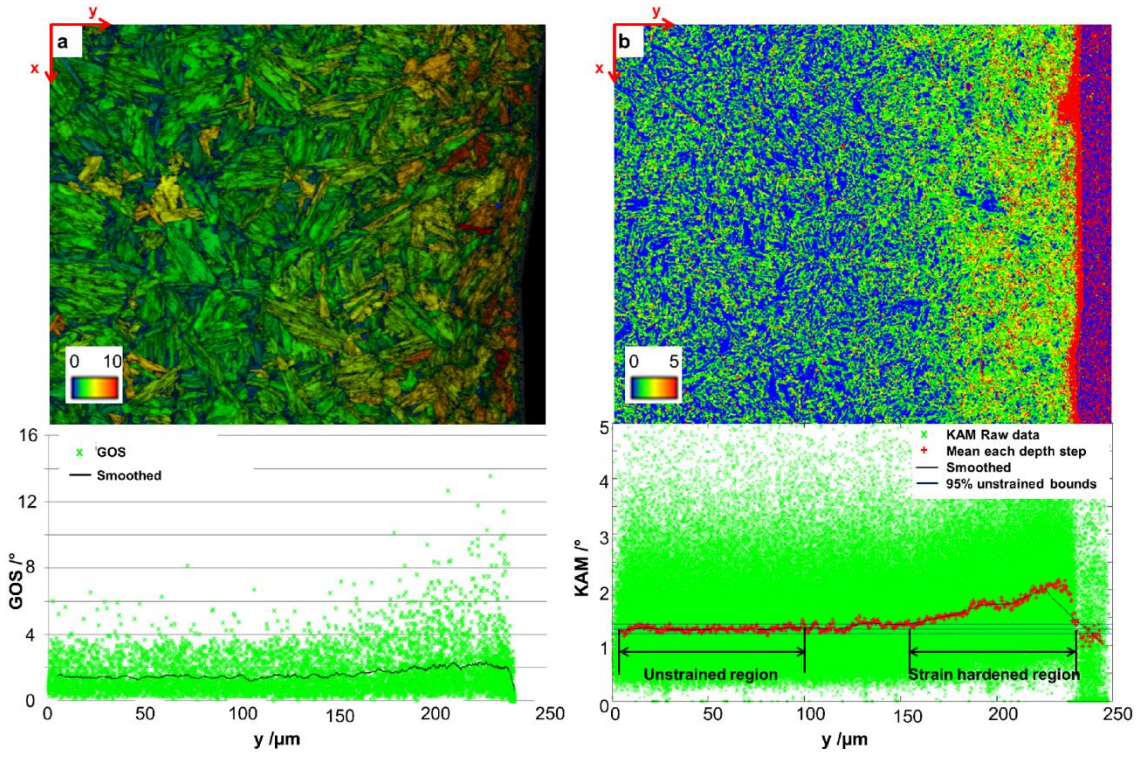

Figure 4- 7: Colour coded map indicating (a) grain orientation spread (with image quality in greyscale) and (b) kernel average misorientation for shot peening process T0 indicating the strain hardened region as identified by the local misorientation approach.

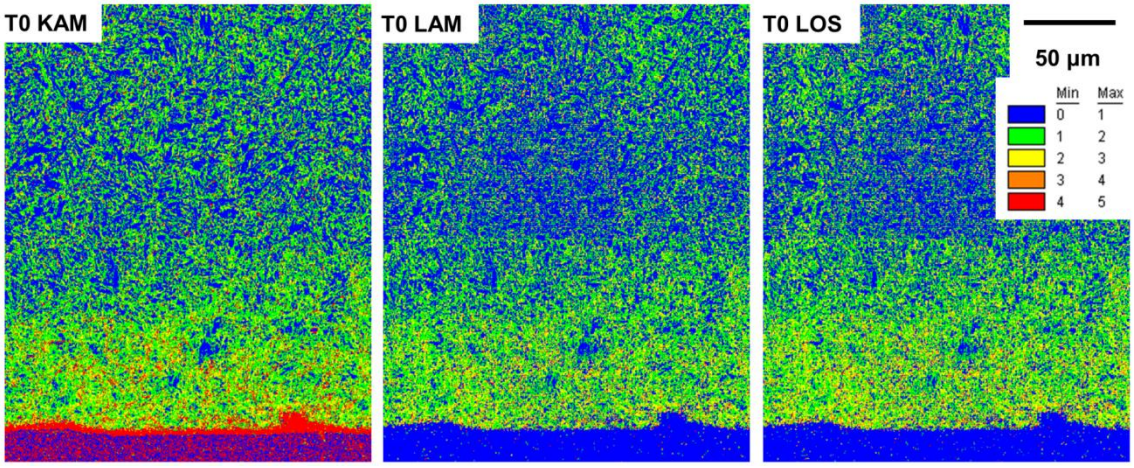

Figure 4- 8: Colour coded maps indicating the spread of the local misorientation parameters investigated as part of this study for shot peening process T0.

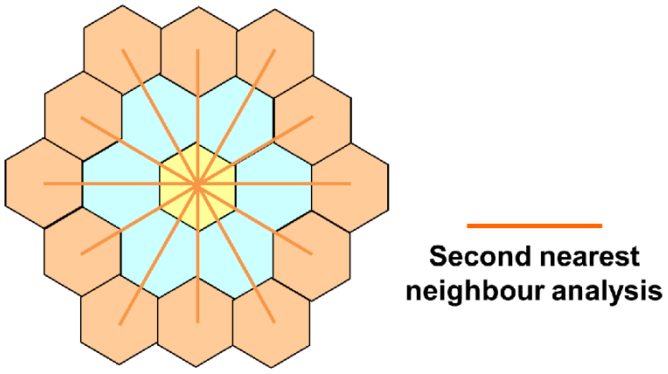

Figure 4- 9: Schematic illustrating second nearest neighbour KAM analysis: The misorientations between the kernel centre and all points on the kernel perimeter are averaged. After [56].

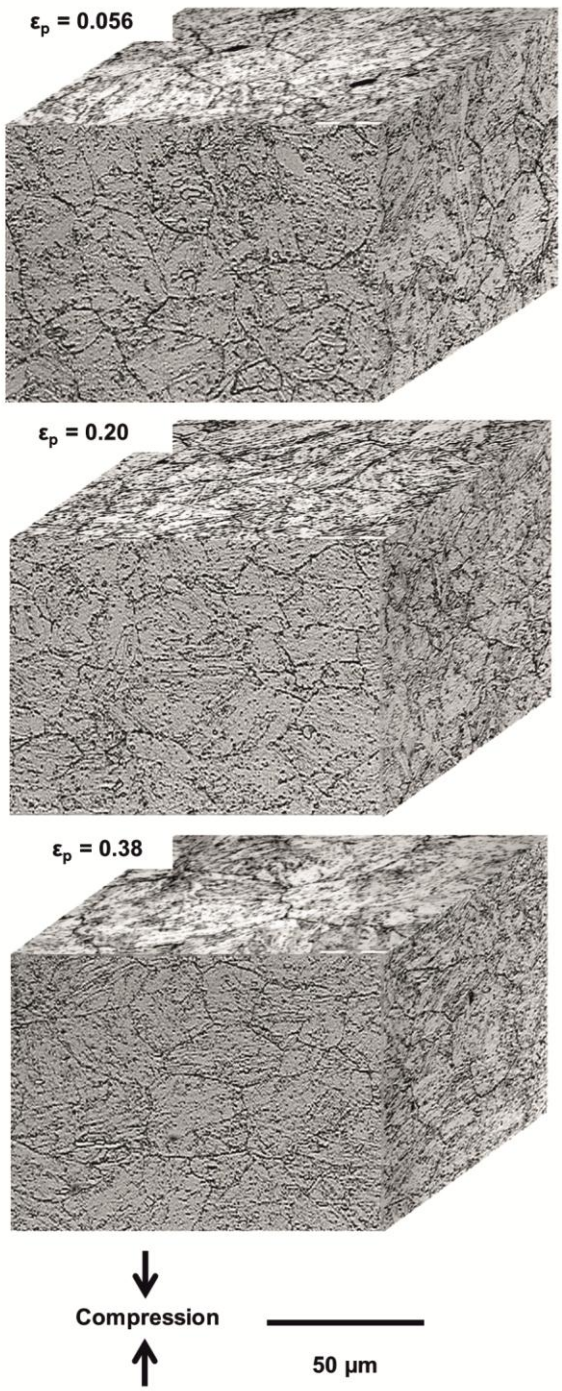

Figure 4- 10: Microstructure in calibration samples after compression to known plastic strains illustrating the development of elongated pancake grains.

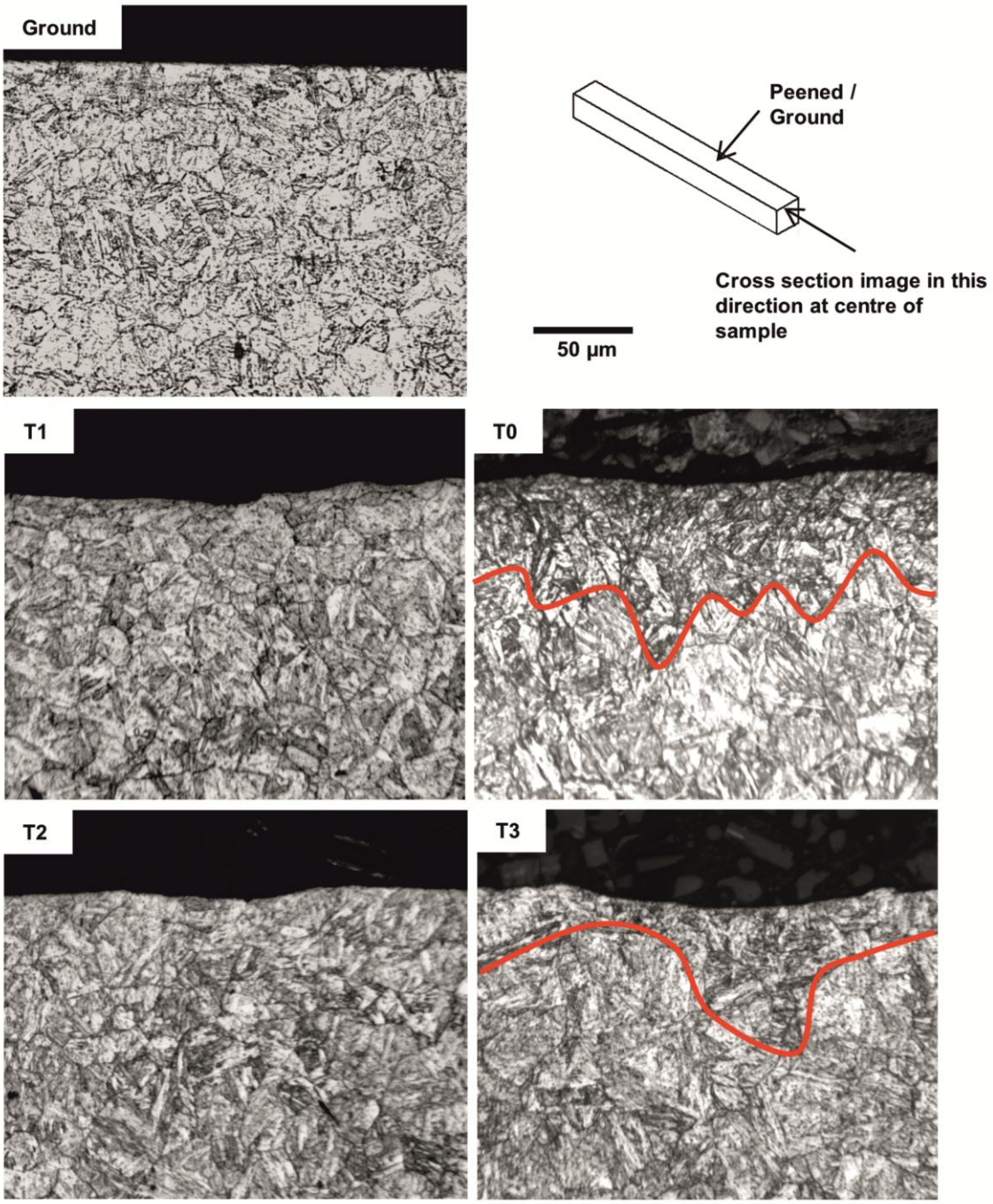

Figure 4- 11: Effect of grinding and varying shot peening processes on near surface microstructure.

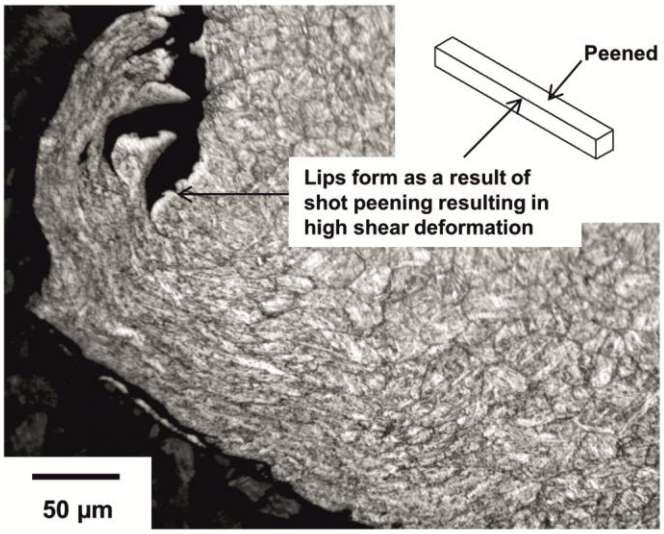

Figure 4- 12: Shot peened (T0) sample illustrating shear deformation in edge region.

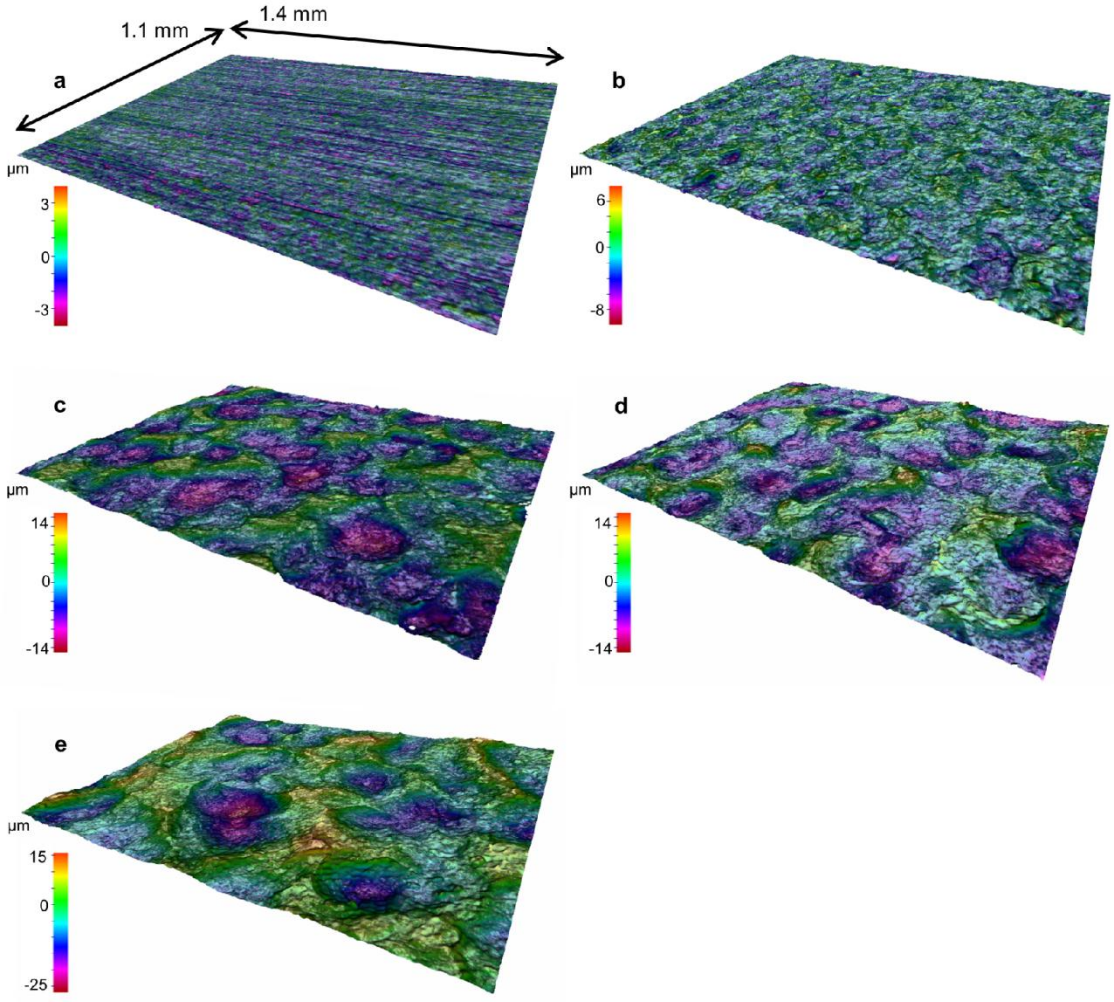

Figure 4- 13: 3D surface deformation generated by each surface preparation technique ((a) ground, (b) T1, (c) T0, (d) T2, (e) T3).

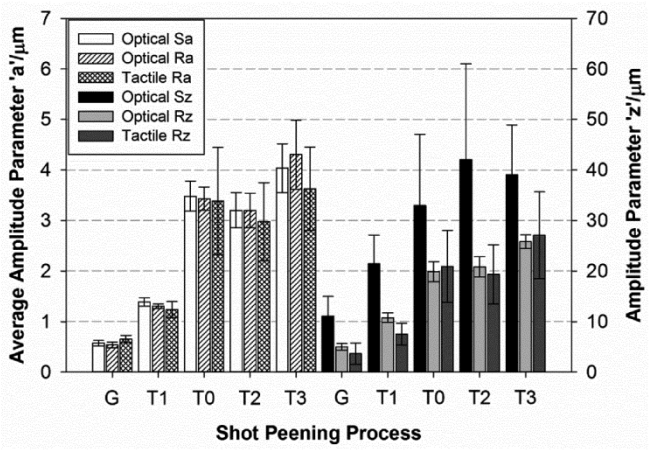

Figure 4- 14: Comparison of surface roughness measurements for each surface condition indicating the 95 % confidence range.

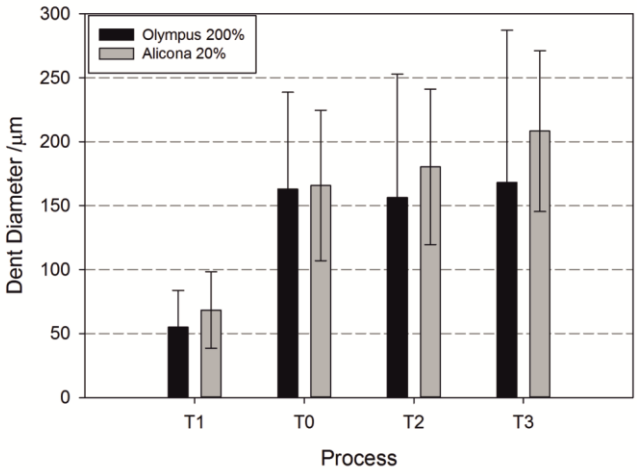

Figure 4- 15: Comparison of dent diameter measurements resulting from each shot peening process indicating the 95 % confidence range.

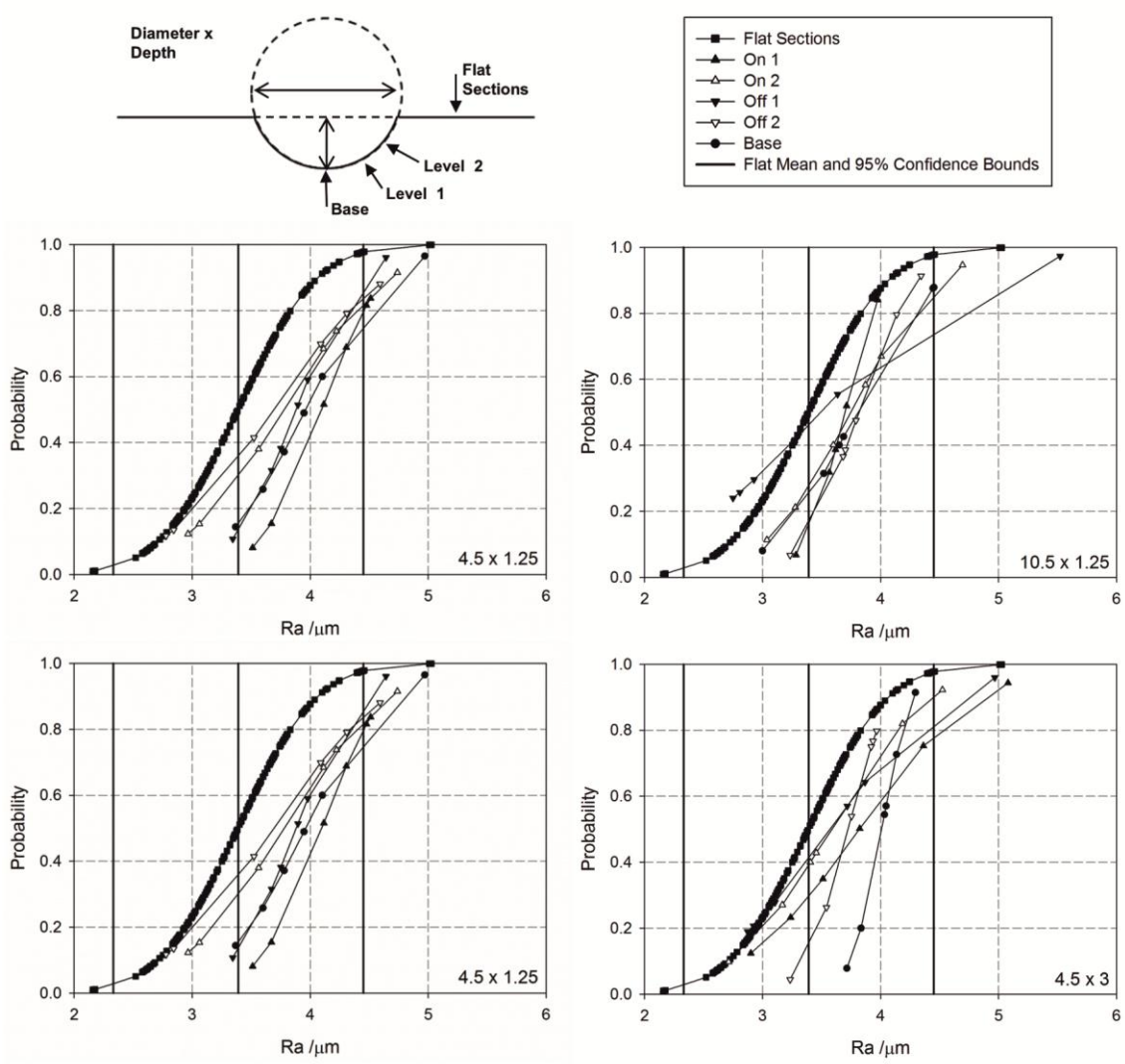

Figure 4- 16: Cumulative probabilities (assuming normal probability density function) illustrating variation in surface roughness around notches of differing geometry.

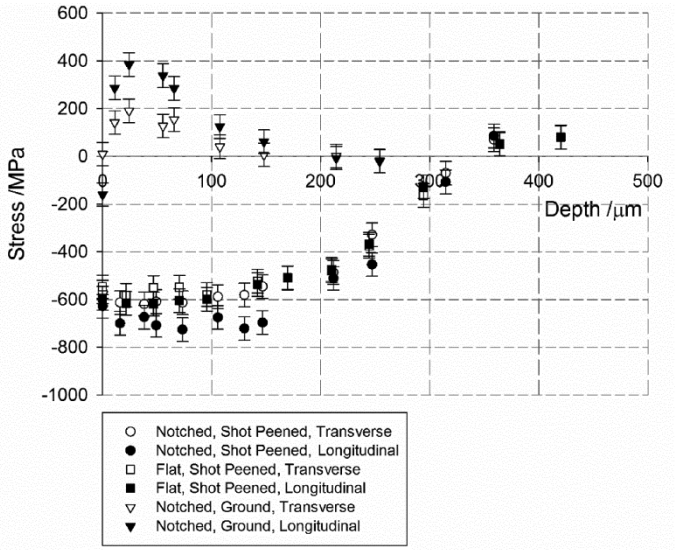

Figure 4- 17: Residual stresses resulting from pre-peen grinding and T0 shot peening.

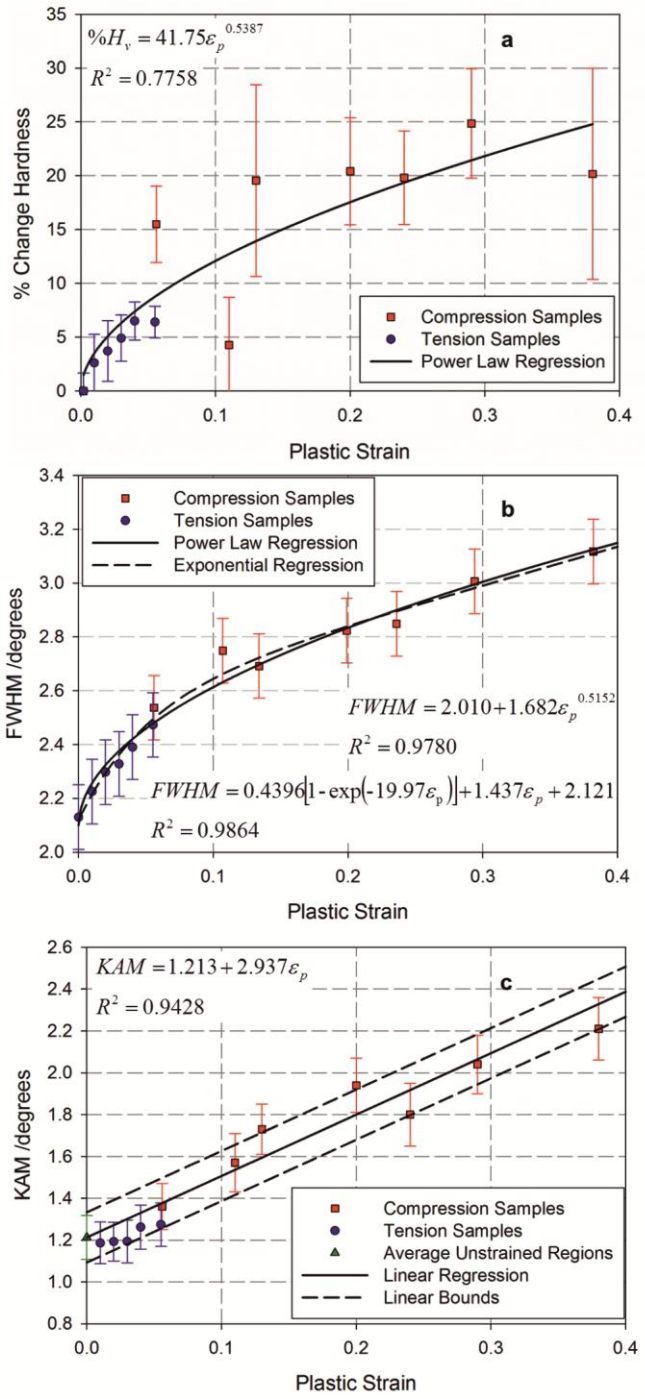

Figure 4- 18: Calibration equations for monotonic uniaxial tension and compression samples relating (a) % change in microhardness, (b) XRD FWHM and (c) EBSD KAM to plastic strain.

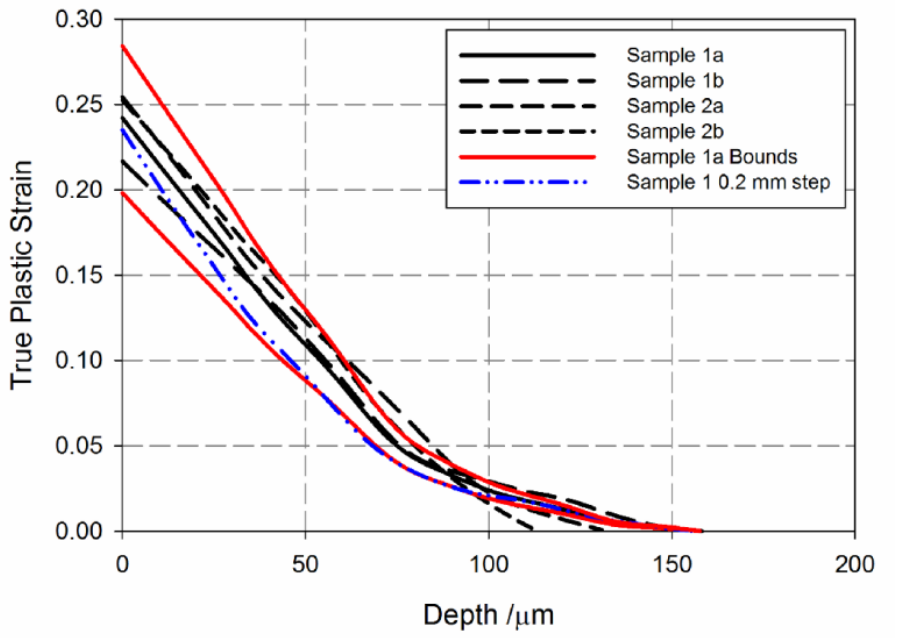

Figure 4- 19: EBSD profiles in T0 samples comparing 0.4 μm and 0.2 μm step size data and illustrating the lower bound consideration of error.

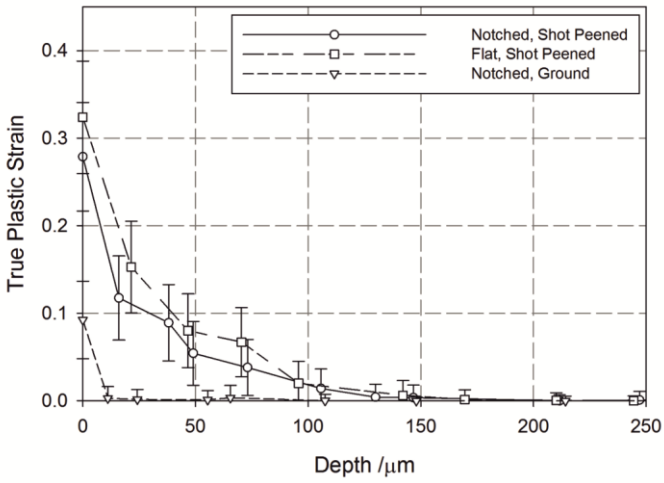

Figure 4- 20: Comparison of plastic strain profiles resulting from shot peening process T0 in flat and notched samples using XRD technique.

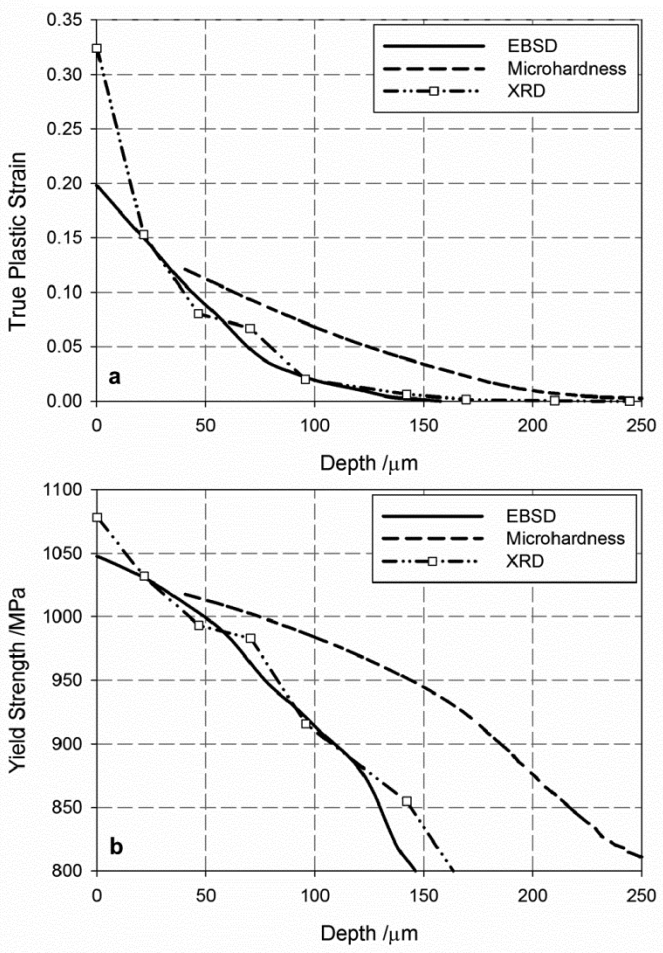

Figure 4- 21: Comparison of (a) plastic strain measured by the three different methods on flat samples and (b) the corresponding yield strength distributions calculated using the Ramberg-Osgood relationship resulting from shot peening process T0.

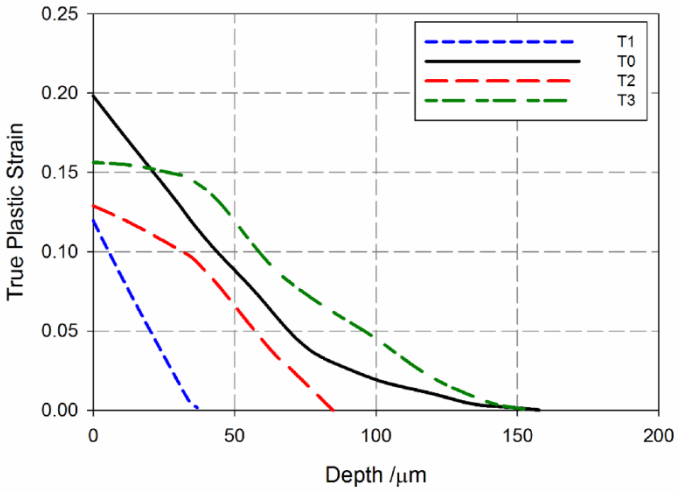

Figure 4- 22: Comparison of the plastic strain resulting from the four peening processes measured using the lower bound EBSD technique.

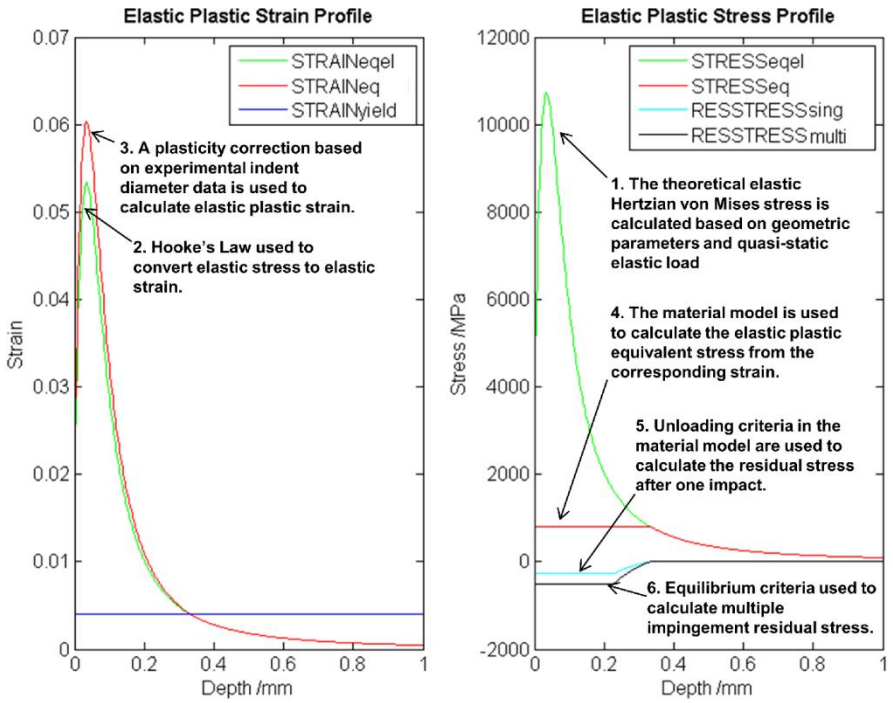

Figure 4- 23: Analytical model after Li *et al.* [71] determining residual stress resulting from shot peening process T0 in bilinear FV448.

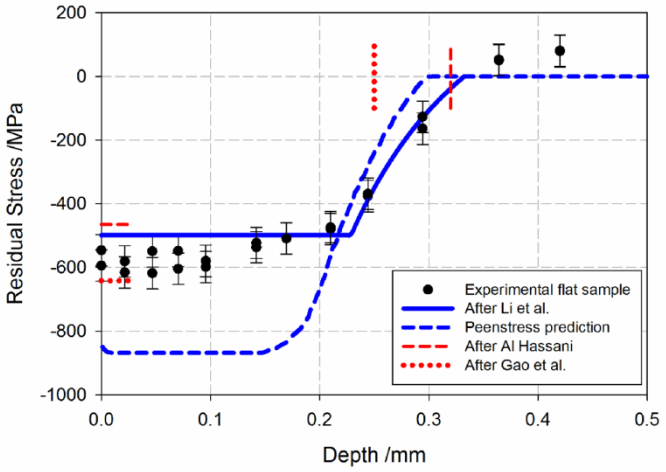

Figure 4- 24: Comparison of experimental and predicted residual stresses resulting from shot peening process T0.

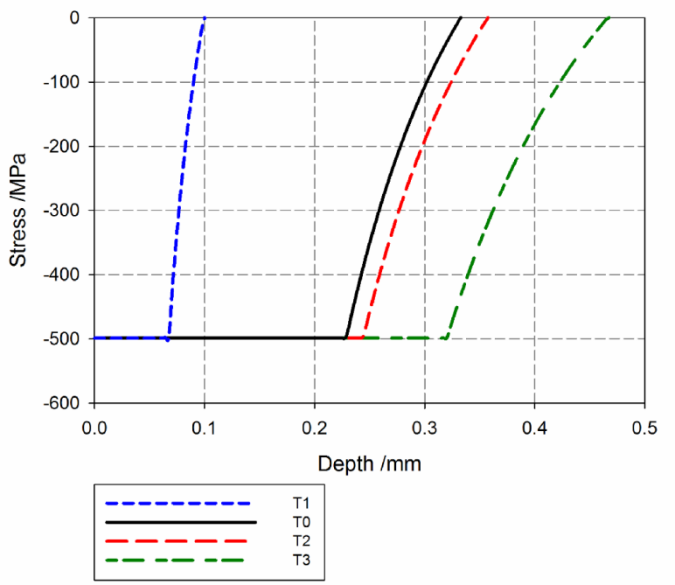

Figure 4- 25: Prediction of the residual stress profile of samples after varying shot peening processes using the analytical model after Li *et al.* [71].

4.6. References

1. Prevéy, P.S., *X-ray diffraction residual stress techniques*, in *ASM Handbook Volume 10, Materials* Characterization. 1986. Metals Park, OH: ASM: p. 380 - 392.

2. Withers, P.J. and Bhadeshia, H.K.D.H., *Residual stress. Part 1 - Measurement Techniques.* Materials Science and Technology, 2001. **17**(4): p. 355 - 365.

3. British Standard, *BS EN 15305:2008: Non-destructuve testing - Test method for residual stress analysis by X-ray diffraction*, 2008.

4. Fitzpatrick, M.E., Fry, A.T., Holdway, P., Kandil, F.A., Shackleton, J. amd Suominen, L.,*Determination of residual stresses by X-ray diffraction*, 2005. National Physical Laboratory Measurement Good Practice Guide No. 52.

5. Cullity, B.D. and Stock, S.R., *Elements of X-ray diffraction.* 3rd edn.; 2001, Upper Saddle River, NJ: Prentice Hall.

6. Dölle, H., *The influence of multiaxial stress states, stress gradients and elastic anisotropy on the evaluation of (residual) stresses by X-rays.* Journal of Applied Crystallography, 1979. **12**(6): p. 489 - 501.

7. Pederson, T.F. and Hansson, I.L.H., *Finite element calculations for correction of residual stress profiles of coated and uncoated materials measured by X-ray diffraction.* NDT International, 1989. **22**(6): p. 347 - 352.

8. Savaria, V., Bridier, F. and Bocher, P., *Computational quantification and correction of the errors induced by layer removal for subsurface residual stress measurements.* International Journal of Mechanical Sciences, 2012. **64**(1): p. 184 - 195.

9. Moore, M.G. and Evans, W.P., *Mathematical correction for stress in removed layers in XRD residual stress analysis.* SAE Transactions, 1958. **66**: p. 340 - 345.

10. Benedetti, M., Fontanari, V., Höhn, B.-R., Oster, P. and Tobie, T.,, *Influence of shot peening on bending tooth fatigue limit of case hardened gears.* International Journal of Fatigue, 2002. **24**(11): p. 1127 - 1136.

11. Salio, M., Berruti, T. and De Poli, G., *Prediction of residual stress distribution after turning in turbine disks.* International Journal of Mechanical Sciences, 2006. **48**(9): p. 976 - 984.

12. Prevéy, P.S., *X-Ray diffraction characterisation of residual stresses produced by shot peening*, in *Proceedings of Shot Peening Theory and Application*, Niku-Lari, A., Editor, 1990. Gournay-Sur-Marne, France: IITT International: p. 81-93.

13. Kim, S.-B., Shackleton, J., Preuss, M., Withers, P.J., Evans, A. and Bruno, G., *Stress relaxation of shot-peened UDIMET 720Li under solely elevated-temperature exposure and under isothermal fatigue*. Metallurgical and Materials Transactions A, 2005. **36**(11): p. 3041 - 3053.

14. Novovic, D., Dewes, R.C., Aspinwall, D.K., Voice, W. and Bowen, P., *The effect of machined topography and integrity on fatigue life.* International Journal of Machine Tools and Manufacture, 2004. **44**(2-3): p. 125 - 134.

15. Vaxevanidis, N.M., Manolakos, D.E., Koutsomichalis, A., Petropoulos, G., Panagotas, A., Sideris, I., Mourlas, A. and Antoniou, S.S., *The effect of shot peening on surface integrity and tribological behaviour of tool steels*, in *Proceedings of the International Conference on* Tribology. 2006. Parma, Italy: AITC-AIT.

16. Child, D.J., West, G.D. and Thomson, R.C., *Assessment of surface hardening effects from shot peening on a Ni-based alloy using electron backscatter diffraction techniques.* Acta Materialia, 2011. **59**(12): p. 4825 - 4834.

17. British Standard, *BS EN ISO 25178-2:2012: Geometrical product specifications (GPS) - Surface texture: Areal. Part 2: Terms, definitions and surface texture parameters*, 2012.

18. British Standard, *BS EN ISO 25178-6:2010: Geometrtical product specifications (GPS) - Surface texture: Areal. Part 6: Classification of methods for measuring surface texture*, 2010.

19. Dalaei, K., Karlsson, B. and Svensson, L.-E. *Stability of shot peening induced residual stresses and their influence on fatigue lifetime.* Materials Science and Engineering A, 2011. **528**(3): p. 1008 - 1015.

20. Harada, Y. and Mori, K., *Effect of processing temperature on warm shot peening of spring steel.* Journal of Materials Processing Technology, 2005. **162-163**: p. 498 - 503.

21. Prevéy, P.S. *The measurement of subsurface residual stress and cold work distributions in nickel base alloys*, in *Proceedings of Residual Stress in Design, Process and Materials Selection*, Young, W.B., Editor. 1987. Metals Park, OH: ASM: p. 11 – 19.

22. Zinn, W. and Scholtes, B., *Influence of shot velocity and shot size on Almen intensity and residual stress depth distributions,* in *Proceedings of the 9th International Conference on Shot Peening*. 2005. Paris, France: International Scientific Committee on Shot Peening: p. 379 – 384.

23. Tosha, K., *Characteristics of shot peened surfaces and surface layers*, in *Proceedings of Asia-Pacific Forum on Precision Surface Finishing and Deburring* Technology, 2001, Singapore: Metal Industries Research and Development Centre: p. 193 - 201.

24. Kamaya, M., *Characterization of microstructural damage due to low-cycle fatigue by EBSD observation.* Materials Characterization, 2009. **60**(12): p. 1454 - 1462.

25. Benedetti, M., Fontanari, V., Scardi, P., Ricardo, C.L.A. and Bandini, M., *Reverse bending fatigue of shot peened 7075-T651 aluminium alloy: The role of residual stress relaxation.* International Journal of Fatigue, 2009. **31**(8-9): p. 1225 - 1236.

26. Benedetti, M., Fontanari, V. and Monelli, B.D., *Numerical simulation of residual stress relaxation in shot peened high-strength aluminium alloys under reverse bending fatigue.* Journal of Engineering Materials and Technology, 2010. **132**.

27. Cahoon, J.R., Broughton, W.H. and Kutzak, A.R., *The determination of yield strength from hardness measurements.* Metallurgical Transactions, 1971. **2**(7): p. 1979 - 1983.

28. Fontanari, V., Frendo, F., Bortolamedi, T. and Scardi, P., *Comparison of the hole-drilling and X-ray diffraction methods for measuring the residual stresses in shot peened aluminium alloys.* Journal of Strain Analysis, 2005. **40**(2): p. 199 - 209.

29. De los Rios, E.R., Trull, M. and Levers, A., *Modelling fatigue crack growth in shot-peened components of Al 2024-T351.* Fatigue and Fracture of Engineering Materials and Structures, 2000. **23**(8): p. 709 - 716.

30. Srikant, G., Cohollacoop, N. and Ramamurty, U., *Plastic strain distribution underneath a Vickers indenter: Role of yield strength and work hardening exponent.* Acta Materialia, 2006. **54**(19): p. 5171-5178.

31. Chaudhri, M.M., *Subsurface strain distribution around Vickers hardness indentations in annealed polycrystalling copper.* Acta Materialia, 1998. **46**(9): p. 3047-3056.

32. Balzar, D., *Voigt-function model in diffraction line-broadening analysis*, in *Intenational Union of Crystallography Monographs on Crystallography 10: Microstructure Analysis from Diffraction*, Snyder, R.L., Bunge, H.J. and Fiala, J., Editors. 1999. Oxford, UK: Oxford University Press. p. 94 – 124.

33. Bruker AXS GmbH, *DIFFRAC plus TOPAS 4.2 Technical* Reference, 2009.

34. Tan, L., Ren, X., Sridharan, K. and Allen, T.R., *Effect of shot-peening on the oxidation of alloy 800H exposed to supercritical water and cyclic oxidation.* Corrosion Science, 2008. **50**(7): p. 2040 - 2046.

35. Kamaya, M., Wilkinson, A.J. and Titchmarsh, J.M., *Measurement of plastic strain of polycrystalline material by electron backscatter diffraction.* Nuclear Engineering and Design, 2005. **235**(6): p. 713 - 725.

36. Brewer, L.N., Field, D.P, and Merriman, C.C., *Mapping and assessing plastic deformation using EBSD*, in *Electron backscatter diffraction in materials science*, Schwartz, A.J., Kumar, M., Adams, B.L. and Field, D.P., Editors. 2nd edn,; 2009, New York, NY: Springer: p. 251 - 262.

37. Buchanan, P.J., Randle, V. and Flewitt, P.E.J., *A simple procedure for the assessment of plastic strain in electron back-scatter diffraction patterns.* Scripta Materialia, 1997. **37**(10): p. 1511 - 1518.

38. Wilkinson, A.J. and Dingley, D.J., *Quantitative deformation studies using electron back scatter patterns.* Acta Metallurgica et Materialia, 1991. **39**(12): p. 3047 - 3055.

39. Kamaya, M., Wilkinson, A.J. and Titchmarsh, J.M., *Quantification of plastic strain of stainless steel and nickel alloy by electron backscatter diffraction.* Acta Materialia, 2006. **54**(2): p. 539 - 548.

40. Yoda, R., Yokomaku, T. and Tsuji, N., *Plastic deformation and creep damage evaluations of type 316 austenitic stainless steels by EBSD.* Materials Characterization, 2010. **61**(10): p. 913 - 922.

41. Kamaya, M., *Measurement of local plastic strain distribution of stainless steel by electron backscatter diffraction.* Materials Characterization, 2009. **60**(2): p. 125 - 132.

42. Sáez-Maderuelo, A., Castro, L. and de Diego, G., *Plastic strain characterisation in austenitic stainless steels and nickel alloys by electron backscatter diffraction.* Journal of Nuclear Materials, 2011. **416**(1-2): p. 75 - 79.

43. Brewer, L.N., Othon, M.A., Gao, Y., Hazel, B.T., Buttrill, W.H. and Zhong, Z., *Comparison of diffraction methods for measurement of surface damage in superalloys.* Journal of Materials Research, 2006. **21**(7): p. 1775 - 1781.

44. Benedetti, M., Fontanari, V., Santus, C. and Bandini, M., *Notch fatigue behaviour of shot peened high-strength aluminium alloys: Experiments and predictions using a critical distance method.* International Journal of Fatigue, 2010. **32**(10): p. 1600 - 1611.

45. British Standard, *BS EN 10002-1:2001*: *Metallic materials - Tensile testing - Part 1: Method of test at ambient temperature,* 2001.

46. ASTM, *ASTM E9-09. Standard test methods of compression testing of metallic materials at room temperature*, 2009.

47. British Standard, *BS EN ISO 4287:2000: Geometrical product specification (GPS) - Surface texture: Profile method - Terms, definitions and surface texture parameters*, 2000.

48. British Standard, *BS ISO 4288:1998: Geometric product specification (GPS) - Surface texture - Profile method: Rules and procedures for the assessment of surface texture*, 1998.

49. Alicona, *Alicona InfiniteFocus IFM Manual IFM 2.1.5. EN 16.06.*2008, 2008.

50. Pešička, J., Kužel, R., Dronhofer, A. and Eggeler, G., *The evolution of dislocation density during heat treatment and creep of tempered martensite ferritic steels.* Acta Materialia, 2003. **51**: p. 4847 - 4862.

51. Benedetti, M., Bortolamedi, T., Fontanari, V. amd Frendo, F., *Bending fatigue behaviour of differently shot peened Al6082 T5 alloy.* International Journal of Fatigue, 2004. **26**(8): p. 889 - 897.

52. Prevéy, P.S. *The uniformity of shot peening induced residual stress*. in *Proceedings of Residual Stress for Designers and Metallurgists*, Walle, L.J.V., Editor. 1981. Metals Park, OH: ASM: p. 151 – 168.

53. Martinez, S.A., Satish, S., Blodgett, M.P. and Shepard, M.J., *Residual stress distribution on surface-treated Ti-6Al-4V by X-ray diffraction.* Experimental Mechanics, 2003. **43**(2): p. 141 - 147.

54. Landini, G., *Auto Threshold (Image J) vs. 1.14 User Guide*, 2011. Available from http://fiji.sc/wiki/index.php/Auto_Threshold; Accessed 30/10/2012.

55. Dougherty, B., *Measure_Roi_PA.java*, 2005. OptiNav, Inc. Available from http://www.optinav.com/Measure-Roi.htm; Accessed 30/10/2012.

56. EDAX-TSL, *OIM vs. 5.2 User Manual*.

57. Clausen, R. and Stangenberg, J., *Roughness of shot peened surfaces - definition and measurement*, in *Proceedings of the 7th International Conference on Shot* Peening. 1999. Warsaw, Poland: International Scientific Committee on Shot Peening: p. 69 - 77.

58. Bergström, J. and Ericsson, T., *Relaxation of shot peening induced compressive stress during fatigue of notched steel samples*. in *Proceedings of the 2nd International Conference on Shot* Peening. 1984. Chicago, USA: International Scientific Committee on Shot Peening: p. 241 – 248.

59. Nwaogu, U.C., Tiedje, N.S., and Hansen, H.N. *A non-contact 3D method to characterize the surface roughness of castings*. Journal of Materials Processing Technology, 2013. **213**(1): p. 59 - 68.

60. Li, J.K., Mei, Y. and Duo, W., *An analysis of stress concentrations caused by shot peening and its application in predicting fatigue strength.* Fatigue and Fracture of Engineering Materials and Structures, 1992.**15**(12): p. 1271 – 1279.

61. Xu, Z.-H. and Li, X., *Influence of equi-biaxial residual stress on unloading behaviour of nanoindentation.* Acta Materialia, 2005. **53**(7): p. 1913 - 1919.

62. Mahagaonkar, S.B., Brahmankar, P.K. and Seemikeri, C.Y., *Effect of shot peening parameters on microhardness of AISI1045 and 316L material: An analysis using design of experiment.* International Journal of Advanced Manufacturing Technology, 2008. **38**(5-6): p. 563 - 574.

63. Guagliano, M. and Vergani, L., *An approach for prediction of fatigue strength of shot peened components.* Engineering Fracture Mechanics, 2004. **71**(4-6): p. 501- 512.

64. Mahagaonkar, S.B., Brahmankar, P.K. and Seemikeri, C.Y., *Effect on fatigue performance of shot peened components: An analysis using DOE technique.* International Journal of Fatigue, 2009. **31**(4): p. 693 - 702.

65. Flavenot, J.F. and Skalli, N., *Effects of grinding conditions on fatigue behaviour of 42CD4 grade steel; comparison of different fatigue criteria incorporating residual stresses*, in *STP 993, Mechanical Relaxation of Residual Stresses,* Mordfin, L., Editor. 1988. Philadelphia, PA: ASTM. p. 91 - 111.

66. Balart, M.J., Bouzina, A., Edwards, L. and Fitzpatrick, M.E., *The onset of tensile residual stresses in grinding of hardened steels.* Materials Science and Engineering A, 2004. **367**(1-2): p. 132 - 142.

67. Poggie, R.A. and Wert, J.J., *The influence of surface finish and strain hardening on near-surface residual stress and the friction and wear behaviour of A2, D2 and CPM-10V tool steels.* Wear, 1991. **149**(1-2): p. 209 - 220.

68. Gao, Y.-K., Yao, M. and Li, J.-K., *An analysis of residual stress fields caused by shot peening.* Metallurgical and Materials Transactions A, 2002. **33**(6): p. 1775 - 1778.

69. Al-Hassani, S.T.S., *Mechanical aspects of residual stress development in shot peening*, in *Proceedings of the 1st International Conference on Shot Peening*. 1981. Paris, France: International Scientific Committee on Shot Peening: p. 583 – 602.

70. Hills, D.A., Waterhouse, R.B. and Noble, B., *An analysis of shot peening.* Journal of Strain Analysis for Engineering Design, 1983. **18**(2): p. 95 - 100.

71. Li, J.K., Mei, Y. and Duo, W., *Mechanical approach to the residual stress field induced by shot peening.* Materials Science and Engineering A, 1991. **147**(2): p. 167 - 173.

72. Johnson, K.L., *Contact mechanics*. 1st edn.; 1985, Cambridge, UK: Cambridge University Press.

73. Franchim, A.S., de Campos, V.S., Travessa, D.N., de Moura Neto, C., *Analytical modelling for residual stresses produced by shot peening.* Materials and Design, 2009. **30**(5): p. 1556 - 1560.

74. Meguid, S.A., Shagal, G. and Stranart, J.C., *3D FE analysis of peening of strain-rate sensitive materials using multiple impingement model.* International Journal of Impact Engineering, 2002. **27**(2): p. 119 - 134.

75. Hong, T., Ooi, J.Y. and Shaw, B., *A numerical study of the residual stress pattern from single shot impacting on a metallic component.* Advances in Engineering Software, 2008. **39**(9): p. 743 - 756.

76. Meguid, S.A., Shagal, G., Stranart, J.C. and Daly, J. , *Three-dimensional dynamic finite element analysis of shot peening induced residual stresses.* Finite Elements in Analysis and Design, 1999. **31(**3): p. 179 - 191.

77. Zanjani, M. and Ogden, S., *PI 02/01: TSB collaborative project: Sealing and surface engineering technlogies for ultra super critical steam turbine plant (700-760C)*, 2011. E.ON New Build and Technology report ENT/11/TSP/SA/1014/R.

78. Klemenz, M., Schulze, V., Rohr, I. and Löhe, D., *Application of the FEM for the prediction of the surface layer characteristics after shot peening.* Journal of Materials Processing Technology, 2009. **209**(8): p. 4093 - 4102.

79. Metal Improvement Company, *Shot peening applications*, 2005.

80. US Department of Defense, *MIL-S-851D: Military specification steel grit, shot, and cut-wire shot; and iron grit and shot-blast cleaning and peening*, 1989.

81. Čekada, M., Panjan, M., Panjan, P. and Kek-Merl, D., *Microindentation depth profiling of selected hard coatings.* Surface and Coatings Technology, 2006. **200**(22-23): p. 6554-6557.

82. Barbieri, F.C., Otani, C., Lepienski, C.M., Urruchi, W.I., Maciel, H.S. and Petraconi, G., *Nanoindentation study of Ti6Al4V alloy nitrided by low intensity plasma jet process.* Vacuum, 2002. **67**(3-4): p. 457-461.

83. Mulvihill, P., *Determination of the threat of in-service cracking to the integrity of LP blades: Progress report*, 2005. Power Technology report PT/05/BB36/R..

84. Ekmekci, B., *Residual stresses and white layer in electric discharge machining (EDM).* Applied Surface Science, 2007. **253**(23): p. 9234 - 9240.

85. Rebelo, J.C., Morao Dias, A., Kremer, D. and Lebrun, J.L.,, *Influence of EDM pulse energy on the surface integrity of martensitic steels.* Journal of Materials Processing Technology, 1998. **84**(1-3): p. 90 - 96.

86. Ghanem, F., Braham, C. and Sidhom, H., *Influence of steel type on electrical discharge machined surface integrity.* Journal of Materials Processing Technology, 2003. **142**(1): p. 163 - 173.

87. Cusanelli, G., Hessler-Wyser, A., Bobard, F., Demellayer, R., Perez, R. and Flükiger, R., *Microstructure at submicron scale of the white layer produced by EDM technique.* Journal of Materials Processing Technology, 2004. **149**(1-3): p. 289 - 295.

88. British Standard, *BS EN ISO 6507-1:2005*: *Metallic materials - Vickers hardness test - Part 1: Test method,* 2005.

89. Bray, D., *Development of life assessment methods for power generation turbine disc and blade materials*. 2011, PhD 9 month report: University of Southampton.

90. Woytowitz, P.J. and Richman, R.H., *Modelling of damage from multiple impacts by spherical particles.* Wear, 1999. **233-235**: p. 120 - 133.

91. Rouhaud, E., Ouakka, A., Ould, C., Chaboche, J.-L. and François, M., *Finite elements model of shot peening, effects of constitutive laws of the material*. in *Proceedings of the 9th International Conference on Shot Peening*. 2005. Paris, France: International Scientific Committee on Shot Peening: p. 107 – 112.

92. Woytowitz, P.J. and Richman, R.H., *Solid mechanics modelling of erosion damage*, in *STP 1315: Applications of Continuum Damage Mechanics to Fatigue and Fracture*, McDowell, D.W., Editor. 1997. ASTM: p. 186 - 199.

93. Bielawski, M. and Beres, W., *FE modelling of surface stresses in erosion-resistant coatings under single particle impact.* Wear, 2007. **262**(1-2): p. 167 - 175.

94. Simulia, *Abaqus/Explicit: Advanced Topics Course Notes*, 2007.

95. ElTobgy, M.S., Ng, E. and Elbestawi, M.A., *Three-dimensional elastoplastic finite element model for residual stresses in the shot peening process.* Journal of Engineering Manufacture, 2004. **218**(Part B): p. 1471 - 1481.

96. ASTM, *ASTM E140-07: Standard hardness conversion tables for metals relationship among Brinell hardness, Vickers hardness, Rockwell hardness, superficial hardness, Knoop hardness and scleroscope hardness*, 2007.

97. Pavlina, E.J. and Van Tyne, C.J., *Correlation of yield strength and tensile strength with hardness for steels.* Journal of Materials Engineering and Performance, 2008. **17**(6): p. 888 - 893.

98. Hong, T., Ooi, J.Y. and Shaw, B., *A numerical simulation to relate the shot peening parameters to the induced residual stresses.* Engineering Failure Analysis, 2008. **15**(8): p. 1097 - 1110.

99. Meguid, S.A., Shagal, G. and Stranart, J.C., *Development and validation of novel FE models for 3D analysis of peening of strain-rate sensitive materials.* Journal of Engineering Materials Technology, 2007. **129**(2): p. 271 - 283.

100. Premack, T. and Douglas, A.S., *Three-dimensional analysis of the impact fracture of 4340 steel.* International Journal of Solids and Structures, 1995. **32**(17-18): p. 2793 - 2812.

101. British Standard, *BS EN ISO 14577-1:2002: Metallic materials - Instrumented indentation test for hardness and materials parameters - Part 1: Test method*, 2002.

4.7. Appendices

4.7.1. Appendix A: Sample removal by EDM

During the EDM process, material is removed from the workpiece by use of consecutive electric sparks, each of which can cause local melting, evaporation and even ionisation of the material. All of the evaporated and some of the molten material is quenched and flushed away by the dielectric liquid; the remaining melt is recast on the surface and called the white layer. Between the white layer and the base material lies a heat affected zone (HAZ) formed by the rapid heating and quenching cycles [84]. The resulting near surface layers in ferritic materials are illustrated in a simple schematic in Figure 4-A- 1a.

These microstructural changes result in significant surface hardening, this is a result of an increase in the carbon content at the surface due to pyrolysis of the dielectric [85] and the formation of the hard martensite phase [86]. High tensile residual stresses of thermal origin also occur near the EDM cut; these high stresses can lead to microcracks near the surface and result in stress relaxation [86]. An example of the surface hardening and residual stresses is shown in Figure 4-A- 1b. As a result of these considerations it was considered necessary to investigate the depth of and remove the modified surface layer prior to any surface treatment (grinding or shot peening) and testing.

Microhardness traverses were used on two cut faces to approximate the depth of the affected layer after sample removal in FV448. Testing was in accordance with BS EN ISO 6507-1:2005 [88] using 200 g load for 15 s at 20 μm intervals. The resulting change in hardness near the surface is shown in Figure 4-A- 2. Given the error in baseline hardness of ±1.7 % (Chapter 3), 250 μm was removed by a grinding process from the EDM cut surface of interest. This depth seems appropriate given the depth scales reported in the literature (Figure 4-A- 1) and should be sufficient to remove both the white layer and HAZ as well as any possible microcracks that are associated with the EDM surface (although none were observed in the test specimens).

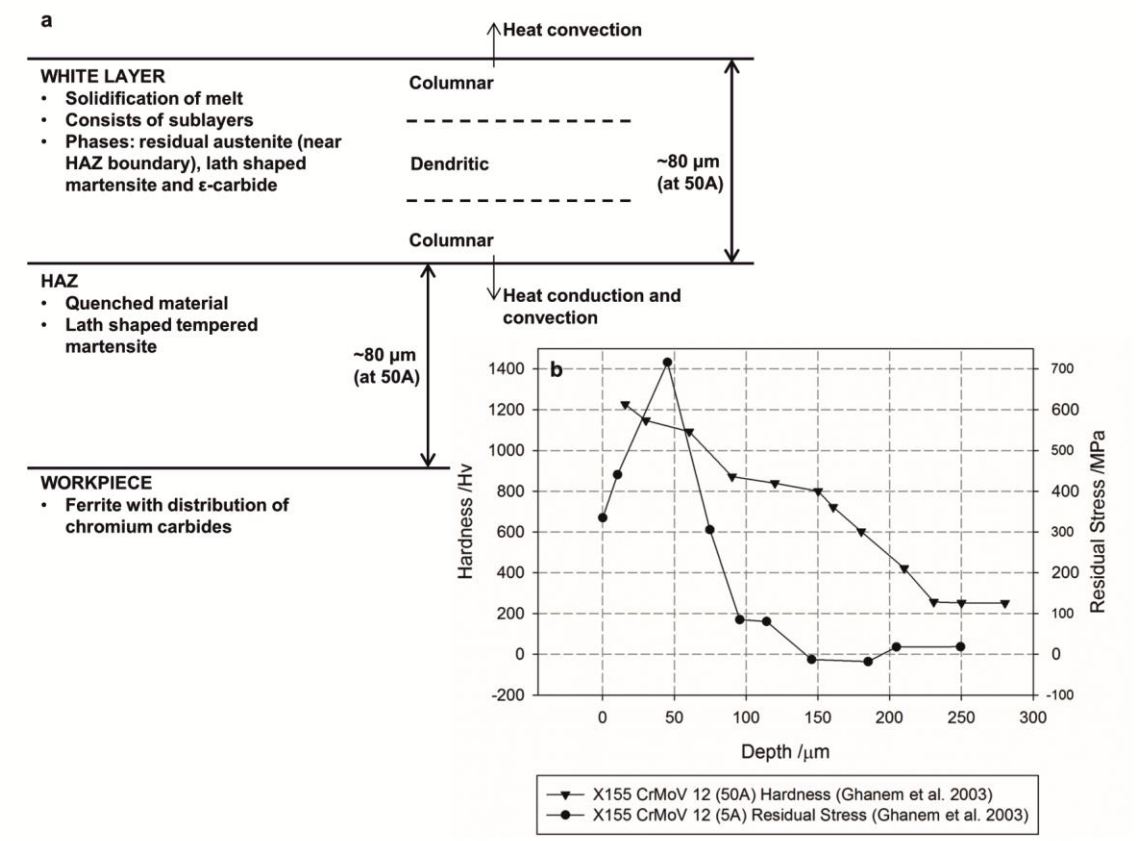

Figure 4-A- 1: (a) Schematic illustrating near surface microstructural changes resulting from EDM and (b) hardness and residual stress profiles resulting from EDM on a 1.6 C 12 Cr hardenable ferritic steel (note the different machining currents). After Cusanelli *et al.* [87] and Ghanem *et al.* [86].

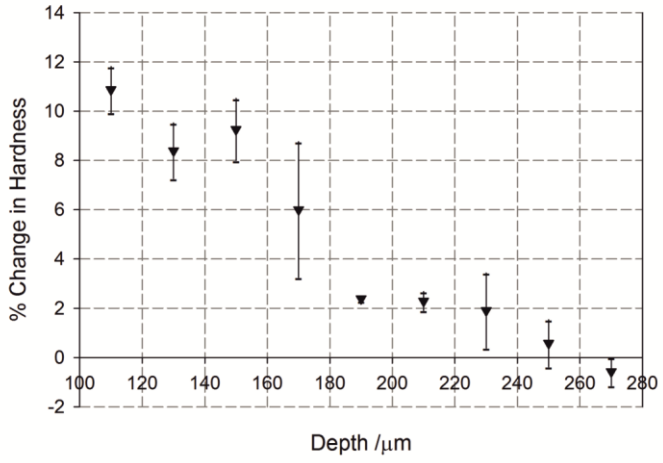

Figure 4-A- 2: % change in microhardness cause by EDM. Upper and lower absolute values from the two traverses are shown to indicate scatter.

4.7.2. Appendix B: FE modelling of the shot peening process

This appendix details the work undertaken to assess the applicability of FE analysis using the commercial software package Abaqus Explicit in assessing the residual stress profile resulting from shot peening process T0.

4.7.2.1 Development of the modelling approach

A single impact 3D model (Figure 4-B- 1 [89]) was developed for validation of the approach against results available in the literature [76]. The target was set as an 8 x 8 x 8 mm block of high strength steel, ρ_{target} = 7800 kgm^{-3} with E_{target} = 200 GPa, v_{target} = 0.3 σ^{0}_{target} = 600 MPa and bilinear hardening law with strain hardening rate H_{target} = 800 MPa. The shot was assumed to be rigid, this condition was achieved by applying a very high stiffness to the elastic material model of E_{shot} = 200,000 GPa; ρ_{shot} = 7800 kgm^{-3}. An initial translational velocity of 100 ms^{-1} was imposed on the 0.5 mm radius shot; boundary conditions were imposed on nodes on the bottom of the substrate to prevent rigid body motion.

The model was made up of 193536 linear elements (C3D8 – an 8 node linear brick and C3D6 – a 6 node linear triangular prism) and 205034 nodes. Since the highest strain gradients in the substrate are found at the top surface (which is also the region of interest), a higher mesh density was applied in this region. The coefficient of friction used in the contact pair analysis was 0.25 [76]; the linear and quadratic bulk viscosity coefficients in the model were set to zero. The contact condition applied was kinematic. The analysis was run for a total of 4x10^{-6} s, after which point the energies (internal, kinetic, strain, plastic dissipation and frictional dissipation) remained constant and the model was considered to be stable. However, after this time, there were still some fluctuations in maximum compressive residual stress caused by stress waves still present in the target.

Since the final application for such a FE approach would be in sensitivity studies optimising the shot peening process, the models must be computationally efficient. Such approaches include 2D plane strain and axisymmetric models. A brief attempt was made to apply a 2D plane strain model to the same impact case as for the 3D model previously described keeping all modelling parameters constant. Physically the plane strain model represents impact by a long cylinder; despite the area under the curve being similar, the maximum compressive residual stress was under-predicted and the overall depth over-predicted when compared with the 3D model. This is not surprising given the difference in contact area between a cylinder and a sphere; indeed Woytowitz and Richman showed that a 2D model was insufficient in modelling the solid particle erosion (SPE) process when compared in terms of damage [90].

Whilst the axisymmetric approach has not been applied extensively to the shot peening process, perhaps owing to its insufficiency in modelling multiple adjacent impacts, it has been applied by other researchers when investigating impacts at a single location with application to both shot peening [91] and SPE [92, 93]. An axisymmetric model was developed for use in the present case (Figure 4-B- 2).

The model was made up of elements of type CAX3 (3 node linear axisymmetric elements) and CAX4R (4 node bilinear axisymmetric elements with reduced integration and hourglass control). The same physical target and shot parameters were used as were used in the 3D model. Discussion of the modelling parameters selected in the model is made below:

- Contact Condition: The contact condition used in the 3D modelling was kinematic. This is the default condition in Abaqus and achieves precise compliance with the contact conditions, but cannot be used in cases of conflict with other types of constraints, such as in the axisymmetric case, where there was a conflict with the symmetry condition. As a result of this, the penalty condition was used which allows for the treatment of more general types of contact as a result of less stringent enforcement of the contact constraints [94].

- Coefficient of Friction: The coefficient of friction used in this analysis was μ_{cf} = 0.25. This is in line with the conditions used in the literature [76, 95] and is a result of the significant frictional effects near the surface for $0 \leq \mu_{cf} \leq 0.1$ and negligible differences for $0.1 \leq \mu_{cf} \leq 0.5$ [74].

- Mesh Refinement: Two mesh densities were assessed to determine whether the results were mesh dependent. The coarse model consisted of 4232 nodes and 4121 elements with refinement in the target in the region of contact. The refined model consisted of 22500 elements and 22680 nodes. The difference in maximum compressive residual stress was 1.3 % and the difference in overall profile depth was 0.96 %. Hence the coarse mesh was accepted.

- Duration of Simulation: Given the lack of stability in the peak compressive stress in the 3D model, the duration of the simulation was increased to 12×10^{-6} s. However, the stresses still did not stabilise with a standard deviation based on 16 data points at 0.6×10^{-6} s intervals between 3×10^{-6} and 12×10^{-6} s of 19.6 MPa. As a result of this, the damping mechanisms available in Abaqus Explicit were investigated.

- Damping: Data presented in [95] confirms that with no damping implemented, non-stabilisation in the residual stress magnitude after 12x10^{-6} s from impact is a problem. Two damping options were presented: numerical damping introduced by bulk viscosity parameters (which damps shock waves and helps control high frequency oscillations) or by artificial material damping (in Abaqus this is Rayleigh damping). In this work [95], it was demonstrated that the Mises stress stabilised to the same level in all cases.

  A sensitivity study was run using no damping, using bulk viscosity only and using bulk viscosity and material damping. Bulk viscosity was set so the linear coefficient was 0.06 and the quadratic coefficient was 0.12. Material damping was set using Equation 4-B-1 [74].

  $$\alpha_d = 2\omega_0\xi \qquad (4\text{-B- } 1)$$

  Where α_d is the mass dependent damping coefficient, ζ_d is the modal damping parameter and $\omega_0 = \frac{1}{Z_h}\sqrt{\frac{2E_{target}}{\rho_{target}}}$ where Z_h is the height of target. For ζ_d = 0.5 (as in Meguid *et al.* [74]), α_d =895144 s^{-1}. Stiffness dependent damping was set equal to that in [74] at β_d = 2x10^{-9} s. Bulk viscosity reduced the standard deviation in the results slightly to 16.6 MPa; the addition of material damping removed all the fluctuations completely by the end of the time step, but increased the magnitude of the maximum compressive stress. As a result of these considerations, the model containing bulk viscosity and no material damping has been selected for use in the present work.

  Increasing the time step yet further might be expected to allow for stabilisation in the stresses. The model was run to 80x10^{-6} s; there was no effect on the mean peak compressive stress measured over time, with only a slight reduction in the standard deviation to 15.1 MPa. Given the analysis time was 8.5 times longer than the shorter analysis, the shorter time step model was accepted.

- Element Distortion Control: The default element distortion control was used throughout the analysis. This constraint activates when a rectangular element under uniaxial compression undergoes 90 % nominal strain, i.e. negative element volumes and other excessive distortion are prevented from occurring during an analysis.

The in-plane stress depth distributions for the axisymmetric model are compared with those of the 3D model and the validation case [76] in Figure 4-B- 3. The 3D model resulted in a maximum compressive stress of -898 ±12 MPa and a compressive stress depth of 0.705 mm; a 6.9 % and 4.7 % error compared with those reported in the

literature (-965 MPa and 0.740 mm [76]) respectively. Other than the small tensile stress predicted near the surface, the axisymmetric model closely matches the validation case with a maximum compressive residual stress of -998 MPa and compressive stress depth of 0.725 mm (3.4 % and 2.0 % error respectively). The occurrence of this peak in tensile stress is thought to be a result of the overly stiff particle behaviour; it does not appear to affect the maximum compressive residual stress and compressive stress depth, the two parameters of most significance in an optimisation study.

In order to more closely represent the shot peening process, the effect of using deformable shot was considered by reducing the overly stiff value for E to a value representative of steel shot, i.e. E_{shot} = 200 GPa. Since the shot are typically significantly harder than the target, a value for σ^0_{shot} = 1000 MPa was appropriate in this development stage. To allow representative plastic deformation, the hardening parameter was the same as the target material, i.e. H_{shot} = 800 MPa. The in-plane stress results using a deformable particle are compared with those using the (pseudo)-rigid particle in Figure 4-B- 4a. There is very little change in the residual stress profile except for a slight reduction in the maximum compressive residual stress and the removal of the near surface tensile peak. This is reflected by consideration of the energy balance throughout the impact (Figure 4-B- 4b). Reducing the stiffness of the shot and allowing some plastic deformation has reduced the overall plastic dissipation energy. The peak strain energy has remained relatively constant since there is now also strain in the particle. The final strain energy is reduced as the strain in the shot was mostly elastic and recovered after impact. In order to achieve energy balance, due to the reduced plastic dissipation, there is an associated increase in kinetic energy of the rebounding shot. The reduced plastic dissipation energy in the system (and hence the target) explains the slight reduction in maximum compressive residual stress.

4.7.2.2 Approximation of the industrial T0 shot peening process

It was essential to establish whether the single impact simplification was capable of predicting the residual stresses resulting from a full coverage process. To this end the axisymmetric model with plastically deforming shot was used to simulate the T0 process. The simple bilinear material model developed in Chapter 3 and used in the analytical approaches discussed in Section 4.4.2 was used for the FV448 target. Using the shot specification supplied by Metal Improvement Company [80], the hardness of the cast steel shot was 42<*HRC*<52; the lower bound value of *HRC* = 42 was used in further analysis. Using the methodology described in [96], the minimum hardness was converted to H_v = 410. Using the linear relationship developed in [97], this was found to correspond to a yield strength of 1088 MPa. Given the empiricism involved in these

conversions, it was decided that the material properties of the hard shot in the original deformable shot analysis were appropriate in the present case.

The residual stresses predicted in the single impact case are compared with the experimental and other predicted results originally shown in Figure 4- 24 in Figure 4-B-5. The profile predicted by the FE model is closer to that predicted by Peenstress® than it is to the experimental profile with the maximum compressive residual stress predicted to be -992 MPa, although it is noted that the overall predicted depth of the profile is less than that predicted by Peenstress.

There is a large discrepancy between the peak compressive stress predicted by the axisymmetric model and the peak experimental compressive stress of -619 MPa (a 60 % error). Similarly there is a large discrepancy in the overall depth of the compressive residual stress profile (0.24 mm predicted by FE model compared with 0.34 mm experimental results in a 29 % error). Indeed if allowances were to be made for multiple impingements as in the analytical model, the residual stress predicted by FE is moved even further from the experimental data. However, the work of Hong *et al.* [98] suggests that after multiple impacts, the depth of the compressive residual stress layer may increase by 30 %. The addition of this factor to the present depth results in a predicted depth of 0.31 mm, which compares much more favourably with the experimental results.

It is believed that the key parameter responsible for the difference between the simulated residual stress profile and experimental residual stress profiles is the manner in which the target material is represented. In the original two works of Meguid [74, 76], no in-plane residual compressive stresses less than yield were reported; this is unrepresentative of experimental results typically reported. The residual stress profile resulting from the FE simulation in the present work is the result of application of a bilinear material model based on the same monotonic dataset as the Peenstress® model. Both the FE and the Peenstress® methods differ from the analytical model generated by the present author based on the work of Li *et al.* [71] in that plasticity is directly considered rather than using a simple plasticity correction factor determined from measurements of indent size. This plasticity correction factor implicitly allows for strain rate effects and cyclic materials behaviour, both of which have previously been shown to be significant considerations in modelling the shot peening process [74, 78, 95, 99]. The strain rate during shot peening is much higher ($\sim 10^5$ s^{-1} [74]) than that during uniaxial tensile deformation and as such σ^0 would be expected to increase (based on data for AISI 4340 steel [100]), reducing the plasticity on impact. This would tend to reduce the residual stresses and would be in line with the present observation that Explicit FE modelling using monotonic tensile data tends to over-predict residual stresses.

Klemenz *et al.* [78] applied a combined isotropic and kinematic materials model to a cyclically softening target material subjected to a multiple impingement shot peening process. Relatively good correlation was shown with experimental data; the peak normalised compressive residual stress was of the order -0.6. This can be compared with the peak normalised compressive residual stress measured by XRD in the present of -0.77. Hence it might be expected that moving to the combined material model and multiple impingement process might significantly improve the correlation between predicted and experimental results in the present work. However, this would be both data intensive and computationally expensive and would impede the application of the FE approach to a sensitivity study.

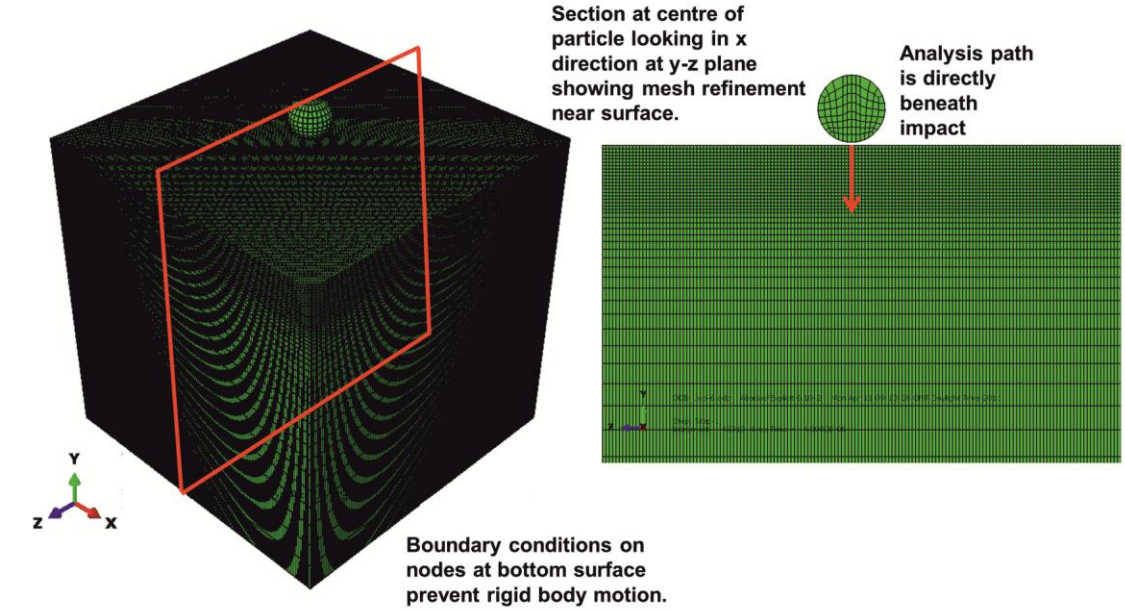

Figure 4-B- 1: Set up and mesh of 3D shot peening model.

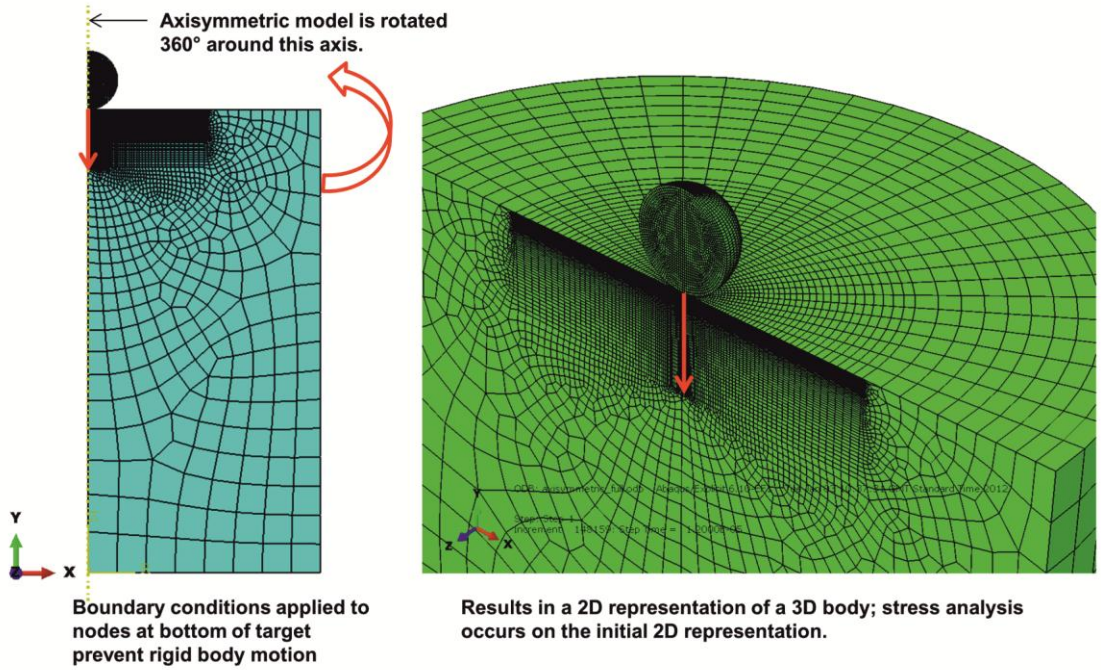

Figure 4-B- 2: Set up and coarse mesh of axisymmetric shot peening model.

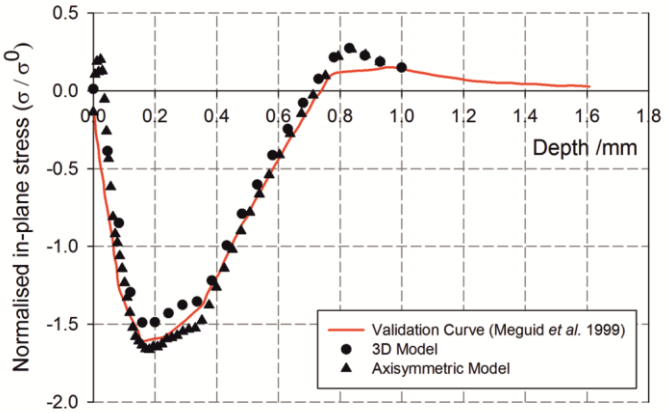

Figure 4-B- 3: 3D and axisymmetric undeformable particle shot peening FE model in-plane stress variation with depth directly beneath impact. Validation is against data after Meguid *et al.* [76].

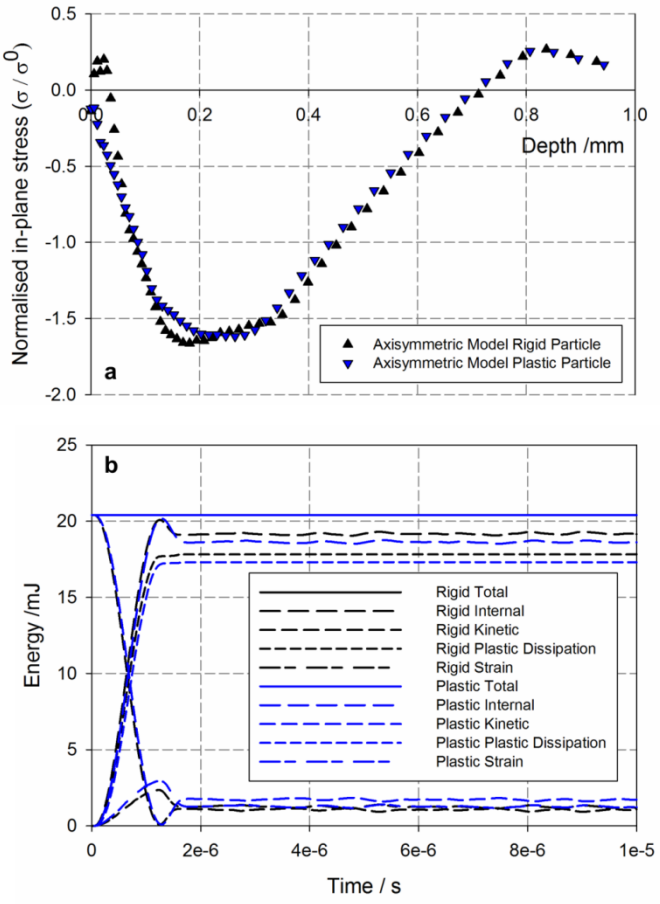

Figure 4-B- 4: Comparison of axisymmetric model results using rigid and plastically deforming single impact particles showing (a) in-plane stresses and (b) energy development.

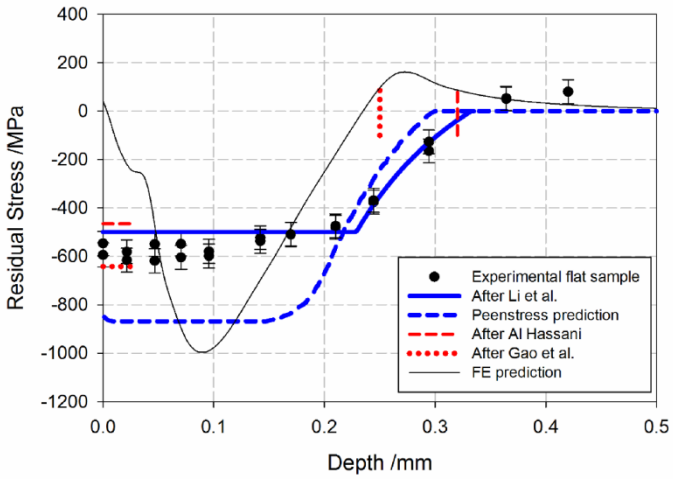

Figure 4-B- 5: Comparison of the residual stress predicted to result from peening process T0 using the FE approach with experimental, analytical and empirical predictions.

4.7.3. Appendix C: Quality assurance using the surface load variance method

The basic premise of the load variance technique is that by carrying out the hardness test with increasing load (penetration depth), an increased volume is plasticized and the hardness is indicated over a greater depth. If the shot peening process is considered as resulting in a functionally graded coating with decreasing yield strength with depth (Figure 4- 21b), the indicated hardness will decrease as the load increases.

The technique has previously been used in analysing hard coatings [81]. In the untreated material, there is no dependence on load; this is a fundamental assumption of the standard hardness testing approach. The introduction of a hard surface coating typically results in the load dependence illustrated in Figure 4-C- 1.

Under low load, the hardness measured is that of the hard coating (region a). However, once the load is such that the indent penetration is approximately $1/7^{th}$ of the coating thickness, the lower hardness of the substrate begins to affect the measured hardness; further increases in the load cause the measured hardness to tend towards that of the baseline substrate (region b). This is noted to be in keeping with the ISO standard 14577-1:2002 [101] which states that to measure coating properties, the indentation depth must be at most $1/10^{th}$ the depth of the coating thickness. In multilayer coating systems (which are more representative of a functionally graded material than a single coating layer), the analysis becomes much more complex as indents interact with more than two layers. Whilst there are clear variations in hardness as the load increases corresponding to measurements in different layers, the interactions are typically too complex for quantitative assessment of the hardness in each layer [81].

The technique has also been applied to nitrided components [82]. This process results in a strain hardening profile of similar shape to the shot peening process with increased surface microhardness which reduces with increasing depth. Barbieri *et al.* [82] were able to show clear differences in the hardness vs. load profiles of plasma jet nitrided titanium alloys using nano-indentation loads up to 5 g.

The method has previously only been described using nano-indentation loads up to 10 g [81]. The purpose of the present work was to investigate whether similar trends are discernible using laboratory based micro-hardness testing since this technique could be applied on-site using the Equotip portable hardness tester [83]. The intention was not to determine the hardness variation with depth but to develop an approach which indicates whether the peening process applied was that intended; to this end a comparison against the hardness vs. load of the ideal case would be sufficient.

4.7.3.1 Load variation microhardness method

Vickers microhardness testing was carried out using loads varying from 100 g to 1 kg (1 to 10 N) with a dwell of 15 s under load. In this development stage, indents were measured using an ocular micrometer and calibrated in the same manner as described in Chapter 3. Since the filters used in processing indent images on a polished surface were insufficient to remove surface roughness features. Where possible, testing was in accordance with British (ISO) Standard 6507-1:2005 [88]; however, in the present situation, removing the surface roughness would also remove some of the strain hardened region under investigation and be unrepresentative of the test conditions under which the actual verification procedure on-site would occur. British (ISO) Standard 14577-1:2002 for nano-indentation suggests that in order to minimize the effect of surface roughness, penetration depth of the Vickers indenter $D_{z,Hv} > 20R_a$; however, in the present steel samples this would require a load in excess of 100 N and most of the effect of load variation would be dominated by baseline material behaviour. Hence measurements were made of ten valid indents (made directly on the shot peened surface as illustrated in Figure 4-C- 2) at each load. Figure 4-C- 2 illustrates that some indents were excessively elongated as a result of the surface contours; furthermore, some were difficult to measure due to optical microscope depth of field constraints. These invalid indents were disregarded in the analysis. Any indents that were possible to measure but that were of sufficiently different dimension as to lie outside the range 'Mean H_v -100 < H_v < Mean H_v +100' were also disregarded in further analysis.

4.7.3.2 Load variation microhardness results and discussion

The hardness variation with indent load results for the four peening processes are compared with those for ground and polished samples in Figure 4-C- 3a.

Both T1 and T0 show the expected profile of decreasing measured hardness with increasing load. It is also noted that the ground sample shows a slight increase in hardness under low load; this tends to support the data presented previously in Section 0 suggesting that there is some very near surface plastic deformation resulting from grinding. The profiles for both T2 and T3 above 3 N load show the expected trend, however, the measurements at 2 N and 1 N are lower than those at 3 N. This may be a result of systematic measurement errors for small indents indicated for the polished sample at 1 N, which, as anticipated, otherwise shows no variation in indicated hardness with load. Figure 4-C- 3b shows the surface hardness variation with intensity under 3 N load. Apart from a slightly high measured hardness for the T1 process, the trend of increasing hardness with intensity is as expected.

However, the variation of hardness with intensity under one load condition does not provide sufficient data as to be able to accept or reject a peening process. The measurement will be subject to error and it is possible that different plastic strain profiles could result in the same surface hardness under one load. This is why the verification must take place based on the hardness vs. indentation load curves. From the measurements presented in Figure 4-C- 3a, the different peening processes cannot be resolved.

To investigate the reason for the difficulty in resolving the peening processes further, the depth of the plasticized zone beneath the hardness indent was determined for each peening process – load combination. This was based on a modification to the approach developed by Srikant *et al.* [30] for determining the extent of the plastic strain beneath a Vickers indenter to allow for variations in yield strength at the shot peened surface; the parameters used in the model are illustrated in Figure 4-C- 4.

The plastic zone beneath a Vickers indent has been shown to be elliptical in shape [30, 31]. This ellipticity ($\frac{\delta_z}{\delta_x}$) was shown to be dependent on the strain hardening exponent; assuming a linear relationship between the data points presented by Srikant *et al.* [30], and assuming FV448 shows the same dependency as the Al7075 for which data was available resulted in an ellipticity of 1.88. Equation 4-C-1 was used to determine δ_x.

$$\frac{\delta_x}{a_{Hv}} = \left[\frac{3P_{Hv}}{2\pi\sigma^0}\right]^{\frac{1}{2}} \qquad (4\text{-C- }1)$$

Where P_{Hv} is the indentation load and a_{Hv} is the semi width of the contact ($a_{Hv} = D_{x,Hv}/2$). δ_z could then be calculated based on the ellipticity. In order to consider the different affected depths for each of the peening processes, the plastic strain variation after each peening process shown in Figure 4- 22 was used to determine the near surface yield strength variation. An iterative procedure was used to calculate the depth of the plasticized region based on the average yield strength in the same region. The results are presented in Figure 4-C- 5; it is noted that in this first approximation the yield strength is averaged with equal weight over the whole plastic depth, a more precise calculation might give more weight to the surface region based on measurements of the precise shape of the plastic zone beneath the indent where available.

The reducing affected depth with increasing peening intensity would be expected based on the areas under the curves shown in Figure 4- 22; however the differences in affected depth between the peening processes are relatively small. This reflects the inability to distinguish between the different processes based on the data shown in Figure 4-C- 3a; the experimental scatter in the indicated hardness vs. load curves is greater than the differences caused by the varying surface layer yield strength. Since the Equotip microhardness system that would be used on-site has been shown to result

in the same statistical variance as a standard laboratory microhardness technique [83], the scatter in the laboratory data is expected to be representative of that which would be found during on-site testing. The experimental error in the laboratory could potentially be reduced by removing the dimpled surface and using a nano-indentation system, resulting in more accurate load-displacement data; however this modified process would not be representative of an on-site repair process and could not be applied to service components.

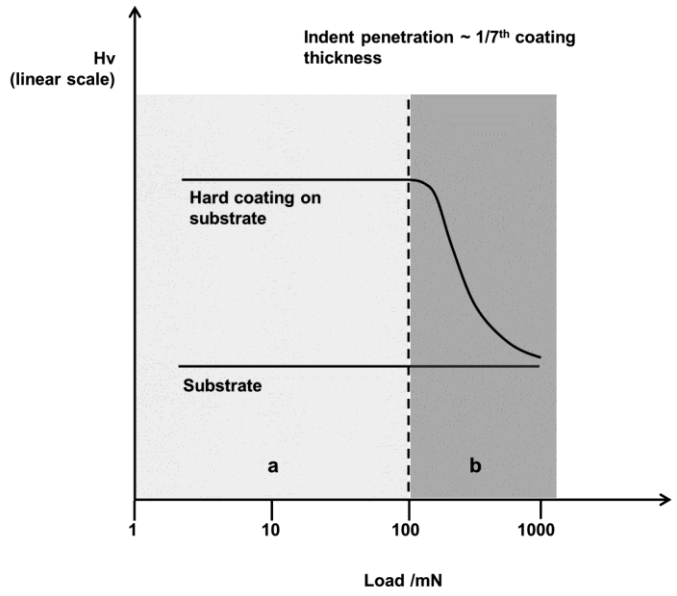

Figure 4-C- 1: Load variation method applied to a hard coating. After Čekada *et al.* [81].

Figure 4-C- 2: Surface microhardness indents on the T0 shot peened surface under varying applied load.

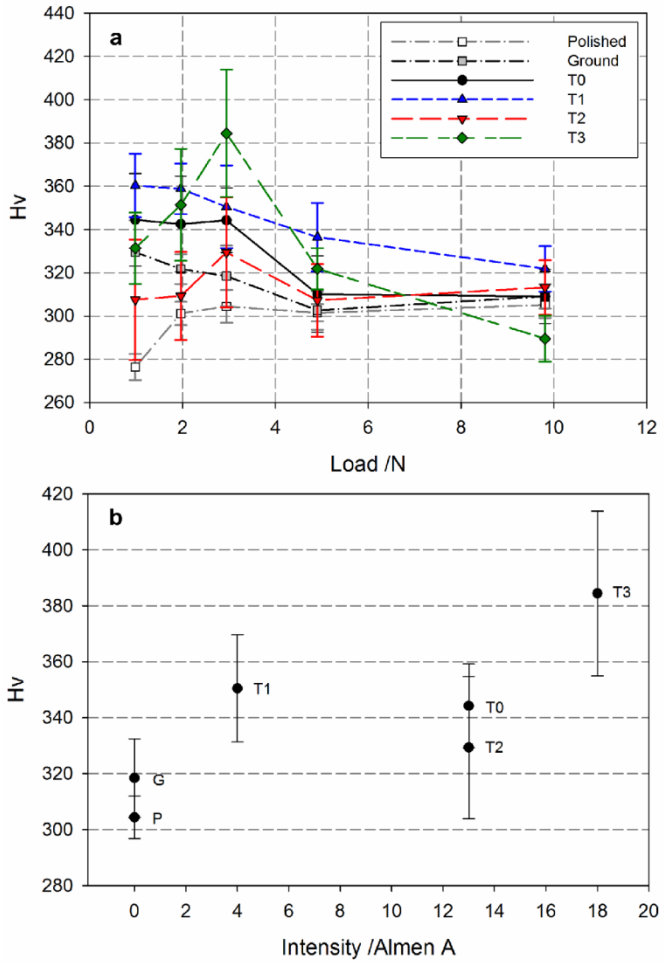

Figure 4-C- 3: Measured surface hardness variation with (a) indent load under varying surface preparation conditions and (b) shot peening intensity under 0.3 N load.

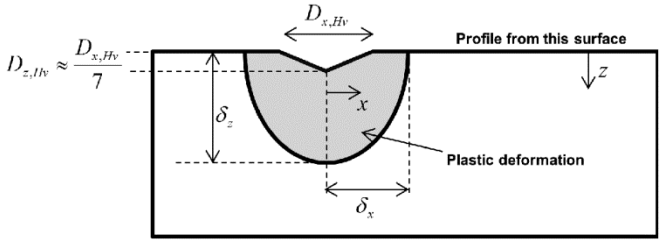

Figure 4-C- 4: Schematic showing the extent of plasticity beneath a Vickers indent.

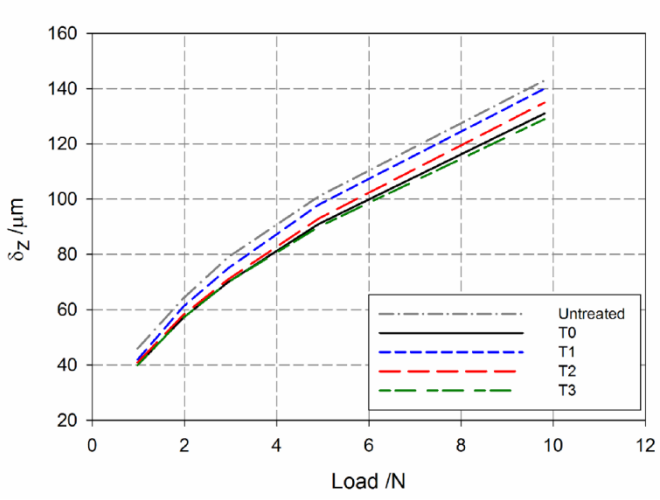

Figure 4-C- 5: Variation in the depth of the plastic zone beneath hardness indents under varying load after various surface preparation processes.

Chapter 5

The shot peening – fatigue interaction

5.1. Introduction

The review presented in Chapter 2 highlighted that it is not only the start of life residual stress, strain hardening and surface roughness profiles which influence the fatigue behaviour of a component but rather the complex interaction between the shot peening process effects (detailed in Chapter 4), the material behaviour under cyclic load (detailed in Chapter 3) and the service conditions which may result in changes to the residual stress and strain hardening profiles.

One of the research questions resulting from the literature review first presented in Section 2.1.3.2 was:

'*How do the residual stress distributions interact with the specific applied loading conditions and are there certain combinations in which the residual stresses do not relax, allowing the maintenance of the shot peening benefit to high applied stress?'*

It is this question which this chapter primarily seeks to answer. S-N data for notched and un-notched samples tested in three point bend are used to determine whether shot peening is still beneficial under bending low cycle fatigue (LCF) loads in certain geometries. By investigating a range of notch geometries, the efficacy of the shot peening process with respect to the fatigue life could be investigated in addition to the investigation based on post-peen surface roughness, residual stress and plastic strain presented in Chapter 4. Furthermore, the effect of varying the shot peening process parameters on fatigue life is investigated; this investigation highlights the need to include the strain hardening and residual stresses resulting from shot peening.

Changes in the residual stress and plastic strain profiles resulting from both shot peening process T0 and the pre-peen grinding processes with LCF are investigated in notched geometries using X-ray diffraction (XRD). The results are discussed in the light of the applied stress distributions and the material's cyclic behaviour and are used in analysing the mechanistic reasons for differences in fatigue behaviour of the different geometries.

The experimental data presented in this chapter will also form part of the validation dataset for the fatigue lifing protocol presented in Figure 2-23. The calculation of changes in the residual stress and strain hardening profiles after fatigue cycling which

are predicted using the finite element (FE) model and fed back into the calculation at each inspection interval must be validated using the XRD data presented for simple geometries. Furthermore, the damage tolerant remnant life calculation must be validated against total life data for the geometries investigated here. It is also noted that the damage tolerant remnant life calculation requires the input of fatigue crack growth rate data; this baseline crack propagation data is also presented in this chapter. Development of the lifing protocol is on-going and further discussion of the development of the lifing procedure and its validation is made in Chapter 7 which describes both the current and future directions of the work.

Similarly to Chapter 4, this chapter is largely based on the first two papers detailed below with the addition of some previously unpublished data and analysis. Additional discussion is also drawn from part of the third paper also listed below.

K. A. Soady, B. G. Mellor, J. Shackleton, A. Morris and P. A. S. Reed, *The effect of shot peening on notched low cycle fatigue*. Materials Science and Engineering A, 2011. **528**(29-30): p. 8579 – 8588.

K. A. Soady, B. G. Mellor, G. D. West, G. Harrison, A. Morris and P. A. S. Reed, *Evaluating surface deformation and near surface strain hardening resulting from shot peening a tempered martensitic steel and application to low cycle fatigue.* In press, International Journal of Fatigue, 2013, **DOI: 10.1016/j.ijfatigue.2013.03.019**.

B. He, K. A. Soady, B. G. Mellor, A. Morris, P. A. S. Reed, *The effects of shot peening on short crack growth rate and resulting low cycle fatigue behaviour in a low pressure turbine blade material*. In press, Materials Science and Technology, 2013.

5.2. Experimental methods

5.2.1. Crack propagation

Two single edge notch bend (SENB) samples (illustrated in Figure 5- 1) were tested under three point bend in order to determine the characteristic crack growth rate vs. stress intensity factor range (log da/dN vs. log ΔK) graph for FV448, the Paris Law coefficients (C and m) and an indication of the threshold stress intensity factor range, ΔK_{th}. Samples were aligned so the crack was growing in the longitudinal direction. Fatigue loads were applied using a servo-hydraulic Instron 8502 fitted with a 50 kN load cell in ambient conditions using a sinusoidal waveform of frequency 20 Hz and a load ratio, R_p = 0.1.

The direct current potential drop (DCPD) method was applied to monitor the crack length continuously. A constant current was imposed across the sample and the crack

length, a : sample width, W, ratio was calibrated to the potential difference, V : datum potential difference, V_0, ratio for each sample.

Crack growth rate measurements were in accordance with BS ISO 12108:2002 [1] and ASTM E647 [2]. An initial ΔK of 17 MPam$^{0.5}$ was used to initiate crack growth. Given that the samples have standard SENB3 geometry [1], for outer roller span $4W$, the sample compliance, $g\left(\frac{a}{W}\right)$, was calculated according to Equation 5-1; hence the initial load range, ΔP, was calculated according to Equation 5-2:

$$g\left(\frac{a}{W}\right) = \frac{6\frac{a}{W}^{\frac{1}{2}}}{\left[\left(1+2\frac{a}{W}\right)\left(1-\frac{a}{W}\right)^{\frac{3}{2}}\right]}\left[1.99 - \frac{a}{W}\left(1-\frac{a}{W}\right)\left(2.15 - 3.93\frac{a}{W} + 2.7\frac{a}{W}^{2}\right)\right] \quad (5\text{-}1)$$

$$\Delta P = \frac{\Delta K B W^{\frac{1}{2}}}{g\left(\frac{a}{W}\right)10^{1.5}} \quad (5\text{-}2)$$

A load shedding procedure was used to determine fatigue crack growth rates in the near threshold region and an approximation for ΔK_{th}. ΔK was stepped down in 9 % increments until da/dN < 10^{-7} mmcycle^{-1}. It was ensured that sufficient crack growth was allowed at each ΔK to minimise retardation effects caused by the crack growing through the plastic zone generated at the previous load step. Thus it was ensured that the crack extension at a given ΔK was at least six monotonic plastic zone sizes calculated using Equation 1-3. In order to maintain quasi-constant ΔK at ± 2 % between each major step down, small step downs in ΔP of <2 % were required as the crack length increased.

Once ΔK_{th} was identified, ΔK was increased to 14 MPam$^{0.5}$ (so some overlap was obtained with the precracking ΔK levels). The crack was then grown out under constant load to failure which typically occurred around a/W = 0.75; this allowed an estimation of fracture toughness (K_{Ic}) to be made. Fracture surfaces were examined using a JSM 6500F field emission gun scanning electron microscope (FEG-SEM) in secondary electron imaging (SEI) mode.

5.2.2. S-N sample preparation

All S-N sample notches were manufactured with circular profile notch geometries defined by their depth and diameter. The sample preparation process used was the same as that described in Section 4.2.1, i.e. the samples were machined from barstock using electo-discharge machining and 0.25 mm was removed from the surface by a grinding process such that the surface roughness met the industrial machined component (and pre-peen) specification of surface roughness R_a < 0.8 µm.

To investigate the effect of varying component geometry on the efficacy of the shot peening process, notch geometry was varied in accordance with the elastic stress concentration factors, K_t and service relevance detailed in Table 5- 1 (all samples had total width in the direction of crack growth W = 7.75 mm and breadth B = 8.00 mm). The elastic stress concentration factors were calculated by comparing the stress parallel to the tensile axis, σ_{11}, (resulting from an elastic FE analysis using the models detailed in Section 5.3) with the equivalent elastic stress calculated using Equation 5-3.

$$P_{max} = \frac{BW^2\sigma_{nom}}{3s} \quad (5\text{- }3)$$

Where P_{max} is the maximum load applied, s is the loading span and σ_{nom} is the nominal bending stress at the surface under tension. Comparisons were made against un-notched plain bend bar (PBB) samples also with W = 7.75 mm and B = 8.00 mm. The shot peening process used was T0, i.e. the process employed during the peening of turbine blade components.

To investigate the effect of varying the shot peening process parameters, the blade connection simulation geometry was used. The effect of varying intensity was considered by using the same three shot peening processes of varying intensity (4A, 13A, 18A) as were previously detailed in Table 4-2. The effect of the means of achieving a given intensity by varying shot diameter and velocity on fatigue life was considered by using two shot peening processes at the same intensity (13A).

5.2.3. Low cycle fatigue conditions

Since the maximum service temperature of low pressure (LP) turbines of 250 ˚C is outside the creep regime for this material, consideration of the creep-fatigue interaction is not required in the life assessment process for these components. Hence ambient behaviour is considered representative for the development of the approach, with the provision that upon application to components, the material properties at the operating temperature are used when determining local stress and strain parameters.

All S-N fatigue testing was carried out using a sinusoidal waveform of frequency of 20 Hz and a load ratio R_p = 0.1 using the same servo hydraulic Instron 8502 as was used for SENB testing. On PBB samples, the test was carried out in four point bend using a load roller separation of 10 mm and support roller separation of 40 mm (i.e. s =15 mm); this ensured the most uniform stress distribution in the region of maximum stress [3]. In notched samples, three point bend is sufficient to ensure the maximum stress occurs beneath the notch; s was held constant at 15 mm resulting in the test set up illustrated in Figure 5- 2.

All S-N testing was carried out in load control; an elastic-plastic finite element model was developed to determine the true stress and strain ranges experienced at the notch root. The development of this model is presented in Section 5.3 together with the details of the sensitivity study that was carried out to investigate the significance of using the different material constitutive models developed in Chapter 3 compared with a 5 % variation in the applied load. This variation is representative of uncertainties in both the applied load and component geometry which may arise when analysing older plant.

Replica techniques were used on one polished PBB sample tested at maximum σ_{11} = $0.95\sigma^0$ (i.e. 95 % of yield stress) to obtain information on crack propagation behaviour and verify the data obtained using SENB samples. The surface of the PBB was cleaned using acetone; acetone was also used to soften the acetate replica, which was then applied (under pressure) to the surface of the PBB and allowed to harden. Testing was initially interrupted every 10,000 cycles and acetate replicas of the surface loaded in tension were taken with the sample held at the mean load. Once a crack was identified in the replicas using optical microscopy, the interruption frequency was increased to every 1,000 cycles and again to 500 cycles as the crack accelerated towards failure. The surface crack lengths were then traced back through the replicas using optical microscopy and measured post-test using Image J.

5.3. Calculating notch root stresses and strains

5.3.1. Effect of material model on local stress/strain in fatigue samples

A sensitivity study was carried out to determine the significance of the material model selection in determining the stress and strain parameters for the three point bend notched fatigue samples. The variations in the stress and strain parameters (defined in Table 5- 2) caused by changing the material model were compared with those caused by a load variation of ±5 %.

The material models under consideration for FV448 were summarised in Table 3-10. The monotonic and cyclically stabilised materials models applied to single element strain ratio R_ε = 0 tension-release models controlled by nodal displacement in a single direction (to simulate a monotonic uniaxial tensile test followed by monotonic unloading) in the FE package Abaqus Standard are illustrated in Figure 5- 3a. The directions ‘parallel’ and ‘perpendicular’ in the caption to Figure 5- 3 are with respect to the rolling direction in the barstock material and correspond to ‘L’ and ‘T’ in Figure 3-5 respectively. The development in peak stress with increasing number of cycles determined for the combined model in use using single element fully reversed

displacement controlled R_ε = -1 tension-compression models is illustrated in Figure 5-3b.

The sensitivity study was carried out on the 4.5 x 1.25 geometry using the same loads as were applied to the fatigued samples analysed for residual stress and strain hardening distributions after fatigue using XRD; hence the nominal elastic stress, σ_{nom}^{e}, calculated using Equation 5-3 was 1034 MPa. The combined material model constants were those at the strain range closest to the strain range evaluated at the surface of the notch using the monotonic material models; hence the constants determined for $\Delta\varepsilon$ = 0.0080 were used.

The finite element model of the fatigue sample is illustrated in Figure 5- 4. Symmetry conditions were applied such that a quarter model was sufficient. The load roller was simulated by an appropriate pressure load defined over an area approximated using an elastic Hertzian analysis for the contact between an 8 mm roller and a flat body; the support roller was simulated by restricting displacement in the vertical direction over an equivalent area. An elastic material model was used in the region of the rollers to avoid non-convergence in the model and sequential static analyses were applied using R_p = 0.1 and the *amplitude command. For monotonic material models, 1 cycle was applied; for the combined material models, 1000 cycles were applied and data was extracted after 1, 2, 3, 10, 20, 50, 100, 200, 500 and 1000 cycles.

The model was partitioned so that the element dimensions in the near-notch region (to depths below the surface of 2 mm) could be controlled such that the element edge length was 0.1 mm; a relatively coarse mesh was desired as applying a fine mesh when implementing the combined material model and multiple cycles would be highly computationally expensive. The automatic meshing tool in Abaqus was used to mesh the remainder of the sample with global element edge length 0.75 mm. All elements were C3D20R, i.e. 20 node reduced integration three dimensional brick elements. These elements were selected because reduced integration in the element stiffness matrix means element assembly is around 3.5 times less costly than in the full integration element because there are only 8 integration points rather than 27. In Abaqus Standard the reduced integration elements generally yield more accurate results than the corresponding fully integrated elements. There are no hourglassing issues in 2nd order reduced integration elements. Furthermore, shear locking only occurs in 1st order fully integrated elements subjected to bending whilst volumetric locking is less likely in reduced integration 2nd order elements as more significant straining is required in almost incompressible materials than for fully integrated elements. The mesh was validated by comparing the results from the mesh shown in Figure 5- 4 with one implementing elements in the notch region of half the size at the

baseline load. There was no significant variation in resulting stresses and strains as illustrated in Figure 5- 5 and the coarse mesh was accepted.

It is clear from the data presented in Figure 5- 5 that the behaviour of this geometry under bend load is dominated by the stresses and strains along the tensile axis; hence from this point forwards all the stresses and strains reported will be in terms of σ_{11} and ε_{11}. The greatest differences are observed in the stresses under peak load; however, since in fatigue assessment it is typically the stress and strain ranges which are needed in calculations, this is not a significant issue in the present work; furthermore it is noted that in damage tolerant calculations it is typically the opening stress which is used. However, should the work be extended to take account of the mean stress in S-N curves, analysis in terms of the equivalent stress may become important.

The results from the material model sensitivity study can be seen in Figure 5- 6; the models are compared in terms of the stress and strain parameters at the notch surface; this is typically referred as a 'hot spot approach'. Considering the peak stress in the loading direction which occurs under maximum load using monotonic material models indicates that the materials model selection plays a more significant role in the stress magnitude than a 5 % load error. These errors are far less significant however when considering the peak strain under maximum load using monotonic material models. However, when using the combined hardening material model, it is clear that both the peak stress and strain vary significantly at the notch surface with increasing number of cycles and thus equivalent plastic strain (equivalent plastic strain is accumulated on a cycle by cycle basis). However, in considering the results of the combined material model in this way, significant simplifications are made; the development of stress and strain parameters with the number of cycles and equivalent plastic strain in this model is presented in more detail in Appendix A to this chapter allowing the mechanistic reasons for these variations to be elucidated.

It was previously mentioned that in the present work, it is the stress and strain ranges which are considered to be of greatest significance. The errors induced by material model selection are far less significant than when considering the peak stresses and strains apart from the error introduced at high loads when implementing the kinematic hardening model and allowing for the Bauschinger Effect (shown in Figure 5- 6b). It is also noted that use of the material model normal to rolling which is based on 0.2 % proof stress, $\sigma_{0.2}$, and the plastic data points whilst not introducing significant differences in the stress range, causes significant differences in the strain range, with a surface strain range of 0.011 reported at σ^{e}_{nom} = 1034 MPa. This model is thus not considered further in the present study.

5.3.2. Selection of material model for further application

It is intuitive that for fatigue analysis, cyclic material properties should be considered. However, it should also be noted that the collection of sufficient data to obtain a cyclically stabilised stress-strain curve is non-trivial and as in the present case for the cyclically stabilised Ramberg-Osgood curve, often requires some element of fitting based on monotonic materials data.

For FV448 in this three point bend system, the isotropic perpendicular model was selected for further application. The sample removal schematic shown in Figure 5- 7 illustrates that the fatigue samples were in fact loaded primarily in this direction (making the isotropic parallel material model unsuitable). Furthermore, the perpendicular monotonic tensile data was the dataset upon which the Ramberg-Osgood model coefficients were originally based and thus known with the greatest confidence. The cyclically stabilised data was obtained in the parallel direction because this was the only direction from which samples of appropriate geometry for axial LCF testing could be machined. Whilst it would be possible to scale the monotonic perpendicular isotropic hardening model using the ratio of stress relaxation observed in the parallel direction, since the cyclically stabilised model firstly does not result in significant differences as compared to the monotonic model in the same parallel direction and secondly is based on only three data points and already fitted using monotonic Ramberg-Osgood parameters making any further fitting increasingly unreliable, this model was not used further.

The kinematic material model clearly begins to show an effect at the higher load where the Bauschinger Effect is active, however the error introduced is not considered significant in the present study because it was only significant at the very highest S-N stress ranges above those used for residual stress and strain hardening analysis. Furthermore, since it was developed using a simplistic single backstress model which under-predicted stresses in the yield region, it is possible that even at these higher stress ranges the Bauschinger Effect would not be so significant once the number of backstresses was increased to improve the fit of the model.

The material is in fact unlikely to be purely kinematic or purely isotropic, it is more likely to be a combination of the two; this is verified by the fit to experimental data that can be obtained when applying this model (Figure 3-20). This combined model was implemented only at the baseline load due to the computational expense of running repeated cycles on the sample. However, due to the errors in modelling the behaviour on the first cycle (previously discussed in Chapter 3), the peak stress and stress range reported fall short of those predicted using the monotonic parallel model (with which this material model should be compared) meaning that although fatigue is

typically considered the result of the average stress/strain cycle through life, there is a chance of missing the worst case cycle (where changes in the residual stress and strain hardening profiles resulting from shot peening may occur) in a FE analysis. These errors, combined with the computational expense of running such a model make it unsuitable for further routine application, however, the implications of cyclic softening indicated by the model should be qualitatively considered when analysing the monotonic data.

In summary, the purely isotropic material model was selected over the purely kinematic material model since the load at which this sensitivity study was carried out resulted in one of the higher equivalent elastic stresses used in S-N testing and so for the majority of the remaining samples, the Bauschinger Effect can be considered to be insignificant. For those few samples which were tested at higher load, there may be some error in the stress range introduced by this assumption. However, at such high stress ranges, fatigue is typically low cycle in nature and thus is generally considered to be governed by strain range, a parameter which is not significantly affected by the choice between purely isotropic or purely kinematic hardening. The errors noted in peak surface stress are likely to affect the mean stress observed during fatigue cycling, and so will affect any analysis which makes consideration of this, such as when applying the Goodman or Gerber approximations. However, should mean stresses be required in the S-N analysis, it would be possible to use this study to judge the magnitude of the error in using the monotonic material model in the present system.

Lastly, it is important to remember that this sensitivity study is only valid for this material – load combination. The significance of the material model selected may be greater or less when analysing different systems, such as when looking at residual stress and strain hardening changes through life or when using different materials or different strain ranges. This is because the material may cyclically harden or soften to a greater or lesser degree than FV448 at $\Delta\varepsilon$ = 0.0080 where the maximum change in the size of the yield surface, Q_∞, was just -71 MPa.

5.3.2.1. Calculation of local stresses and strains in S-N fatigue samples

The model described in Section 5.3.1 was adapted to the four different geometries tested under three point bend (Table 5- 1). The element edge length in the notch region of interest was retained at 0.1 mm; the resulting models are illustrated in Figure 5- 8. It is noted that the mesh is not so uniform in the 4.5 x 3.00 mm geometry; this is a result of the non-circular nature of the notch; attempting to force a more uniform mesh of the same dimension resulted in some elements being of a non-optimised geometry; hence the application of the mesh indicated.

The aim was to develop an analysis protocol which could predict the applied stresses and strains at the centre of the notch surface without using finite element analysis each time but still allowing for slight variations in measured notch geometry in each sample after manufacture. In the first instance, it was assumed that by plotting the stresses and strains calculated for the ideal sample geometry using FE (Figure 5- 9) against the nominal stress and accounting for the actual sample geometry by using the measured remaining ligament on each individual sample in the nominal elastic stress calculation, the curves could be used to determine the notch stresses and strains.

This method implies that slight changes to the notch radius do not result in significant changes to the stress concentration factor and that it is the size of the remaining ligament that is the critical factor. A further study was carried out into the reliability of this method by varying the notch radius and keeping the centre of the notch at the same height above the flat sample surface (hence in this case, both the notch radius and the remaining ligament vary).

Each geometry was analysed at a range of peak loads in order to generate relationships for stress and strain parameters vs. nominal elastic stress which spanned the range of equivalent elastic stresses in the experimental samples. The range of equivalent stresses investigated using FE is detailed in Table 5- 3; the calibrations are only valid within these ranges. The results set for $\Delta\sigma_{11}$ and $\Delta\varepsilon_{11}$ are shown in Figure 5- 9 a and b respectively; the results are compared with those for a PBB with no stress concentration feature. Since the unloading in the isotropic material model used was elastic, both the stress and strain ranges show a linear dependency, this is a useful feature when calibrating in this manner and means this approach is helpful when considering stress and strain ranges. Lines were fitted such that the stress/strain parameters could be described as a function of equivalent elastic stress, and thus the relevant parameter found for each experimental S-N sample.

In order to validate this FE approach, σ_{11} under maximum load was also extracted from the analyses of the notched components and compared with the results of the biaxial Neuber and elastic strain energy density (ESED) approaches. The K_t values used in the analysis were those detailed in Table 5- 1.

In these two approaches, the notch tip stress and strain fields under maximum load can be related to nominal far field loading using K_t. The Neuber approach [4] is based on the relationship in Equation 5-4; when combined with the Ramberg-Osgood relationship (constants E, A and n_m), Equation 5-5 can be used to determine the local stress at the notch root.

$$K_t^{\,2} = K_\sigma K_\varepsilon \qquad (5\text{- }4)$$

$$\frac{(\sigma_{nom}K_t)^2}{E} = \frac{{\sigma_{11}}^2}{E} + \sigma_{11}\left(\frac{\sigma_{11}}{A}\right)^{\frac{1}{n_m}} \quad (5\text{- }5)$$

Where K_σ is the stress concentration factor and K_ε is the strain concentration factor. The ESED approach (Equation 5-6) is based on the work of Molski and Glinka [5, 6]; it is assumed that local stresses and strains hold an elastic strain energy density equivalence with the nominal loading conditions. Implementation of the definitions of strain energy per unit volume and the Ramberg-Osgood relationship results in Equation 5-7.

$$w_{\sigma_{nom}}{K_t}^2 = w_\sigma \quad (5\text{- }6)$$

$$\frac{(\sigma_{nom}K_t)^2}{2E} = \frac{{\sigma_{11}}^2}{2E} + \frac{\sigma_{11}}{n_m+1}\left(\frac{\sigma_{11}}{A}\right)^{\frac{1}{n_m}} \quad (5\text{- }7)$$

Where $w_{\sigma_{nom}}$ is the strain energy per unit volume due to the nominal remote stress and w_σ is the strain energy per unit volume due to local stress and strain at the notch root. Equations 5-4 to 5-7 are valid under plane stress conditions (i.e. when the stress state at the notch root is reduced to a uniaxial stress state) and when the nominal stress does not exceed the limit of proportionality (although this can be accounted for by also applying the Ramberg-Osgood relation to the nominal stress). Under plane strain conditions, there is a biaxial stress state at the notch tip as a result of component thickness. Both the Neuber and ESED methods can be modified [6] by replacing σ_{11} with σ_{11}'' using the translation of the uniaxial stress strain curve into the analogous plane strain relation (based on Poisson's ratio, ν, plastic strain, ε_p, and E) according to Equations 5-8 to 5-10 [7]. The Ramberg-Osgood relationship can still be used to relate stresses and strains, however a new regression analysis must be performed to determine the biaxial equivalent constants, A'' and n_m''.

$$\sigma_{11}'' = \frac{\sigma_{11}}{\sqrt{1-\mu+\mu^2}} \quad (5\text{- }8)$$

$$\varepsilon_{11}'' = \frac{\varepsilon_{11}(1-\mu^2)}{\sqrt{1-\mu+\mu^2}} \quad (5\text{- }9)$$

$$\mu = \frac{\nu+\frac{E\varepsilon_p}{2\sigma_{11}}}{1+\frac{E\varepsilon_p}{\sigma_{11}}} \quad (5\text{- }10)$$

The results of the biaxial Neuber and ESED analyses are shown in Figure 5- 10. It is clear that the ESED approach results in the best approximation in the present case, which can be shown to be tending towards plane strain by the calculation of the ratio of strain across the sample to strain in the tensile axis at the centre of the notch to be $\frac{\varepsilon_{22}}{\varepsilon_{11}} = -0.115$ at σ_{nom}^e = 1034 MPa and hence closer to zero than $-\nu$ [8]. This conclusion is thus in line with those of other authors [8-10] who have shown that the ESED

prediction gives the best prediction of notch root stresses and strains under plane strain monotonic and cyclic loads. A statistical analysis showing the maximum error between the FE data point and the ESED curve is given in Table 5- 4. The error in σ_{11} at the notch surface under maximum load is always less than 5 % between the FE analysis and the ESED approach; this result is sufficient to validate the FE approach in current use. The higher predictions of σ_{11} by the Neuber analysis compared to the ESED approach are not surprising given the only difference between Equations 5-5 and 5-7 is the factor $\frac{2}{n_m+1}$. This difference is perhaps more clearly understood when the physical meaning of the two approaches shown schematically in Figure 5- 11 is considered. The ESED method requires point A to be found such that area OCAB = K_t^2area OCD whereas the Neuber method required point A' to be found such that triangle area OA'B' = K_t^2 area OCD.

Ye *et al.* [11] show that the Neuber method is equivalent to the ESED method when the dissipation of heat energy at the notch root during plastic deformation is neglected and conclude that since this dissipation cannot be avoided, Neuber's rule overestimates the local stress when the elastic limit is exceeded. This overestimation has been shown by a number of other authors [6, 8-11] for notches under both uniaxial tension and bending and is especially pronounced in plane strain conditions; hence the ESED method is the more physically representative of the two. It should be noted that whilst not apparent in the present investigation, under certain circumstances, the ESED method may underestimate the local stresses and strains, especially at high σ_{nom} and K_t as a result of local stress redistribution by plastic yielding at the notch tip and that corrections are available which allow for this [11, 12].

It was postulated that it would be possible to use an ESED calculation of maximum surface σ_{11} to determine the resulting strain range with a calibration approach. The results and cubic fit to the finite element data shown in Figure 5- 12 indicate that there is no significant variation in the calibration with notch geometry; however, in order to demonstrate the maximum accuracy achievable with the method, in the first instance, individual quadratic fits for each geometry were obtained. This calibration was then applied to the maximum σ_{11} calculated using the ESED method for the same loading conditions as were applied to the original FE analyses. The maximum percentage error in the resulting $\Delta\varepsilon_{11}$ when compared with the $\Delta\varepsilon_{11}$ resulting from the FE results for each geometry is detailed in Table 5- 5. These errors are considered too high and the $\Delta\varepsilon_{11}$ and $\Delta\sigma_{11}$ calibrations based on FE for each geometry are the most appropriate for application to S-N samples.

Finally, a sensitivity study was carried out in order to assess the error introduced by assuming constant notch radius when varying the sample geometry. Five finite element

models were generated, each of slightly varying geometry described in Table 5- 6; a variation in notch geometry of ± 1mm was used since this is representative of the variation in notch geometries observed in experimental S-N samples. The load was held constant at 7766 N, which is the load required for σ_{nom}^{e} = 1034 MPa in 4.5 x 1.25 mm samples. This was the σ_{nom}^{e} calculated in the samples used for residual stress analysis. For consistency, element edge lengths in the near notch region were held constant at 0.1 mm and all models were implemented in the manner discussed previously.

Stress and strain parameters were calculated using both the calibration approach for 4.5 x 1.25 mm samples discussed previously and directly from the FE models. The results are tabulated in Table 5- 6 and the percentage differences between the two methods are tabulated in Table 5- 7.

The results for the 4.5 x 1.25 mm notch indicate the error introduced by the calibration curves alone; this error is negligible. It is clear that for a notch radius difference of 0.1 mm, a tolerance which can be reasonably expected from the manufacturing process, there is no significant difference in the results calculated using the calibration method and the FE method. Thus the calibration method is considered acceptable for the calculation of stress and strain parameters in samples whose equivalent elastic stresses lie within the present investigated range.

In summary, it was concluded that the most appropriate material model for analysing the stress and strain ranges in the direction of bend loading, $\Delta\sigma_{11}$, and $\Delta\varepsilon_{11}$ respectively, was the isotropically hardening model based on the monotonic tensile data obtained in the direction perpendicular to rolling. Calibration curves based on the FE results which related $\Delta\sigma_{11}$ and $\Delta\varepsilon_{11}$ to the nominal elastic stress, calculated based on the measured remaining ligament in each sample, σ_{nom}^{e}, were found to be sufficient to describe the local stress and strain ranges at the notch surface.

5.4. Results

5.4.1. Baseline crack propagation behaviour

DCPD monitoring of crack propagation in SENB samples resulted in potential difference vs. time data which was converted into a/W vs. N for each sample. During the grow-down phase, discrete data points for da/dN were obtained at each ΔK based on the gradient of a linear fit on a graph of a vs. N; the use of the linear fit successfully suppressed any noise in the data. The R^2 for the linear fit at each ΔK was always >0.9 and the average R^2 was 0.98.

During the grow-out under constant load phase, da/dN vs. ΔK could be determined directly by applying the secant method (Equation 5-11) to the raw data since ΔK increased with increasing a under constant load.

$$\frac{\mathrm{d}a_j}{\mathrm{d}N} = \frac{a_j - a_{j-1}}{N_j - N_{j-1}} \quad \text{at} \quad a_{javg} = \frac{a_j + a_{j-1}}{2} \tag{5-11}$$

There was particularly marked noise in the data at intermediate ΔK ($14 < \Delta K < 25$) which resulted in erroneous da/dN results, hence several methods of noise reduction in the original V/V_0 vs. N data were compared; the data smoothing and digitizing approaches considered and the resulting da/dN vs. ΔK are discussed further in Appendix B to this chapter. At higher $\Delta K > 25$ MPam$^{0.5}$, the rate of increase in V/Vo was such that the noise became much more insignificant and the secant method could be applied directly. The grow-out SENB data shown in Figure 5- 13 is a combination of the secant method applied to digitized data for $14 < \Delta K < 25$ MPam$^{0.5}$ regime and the secant method applied directly to the raw data when $\Delta K > 25$ MPam$^{0.5}$. From this SENB dataset, the Paris Law (Equation 2-16) for FV448 was determined as $C = 1.66\text{x}10^{-9}$ mmcycle^{-1} and $m = 3.3$; K_{IC} was estimated at 55.3 MPam$^{0.5}$ and ΔK_{th} at 5.5 MPam$^{0.5}$. Upper and lower limit Paris Laws were defined by holding m constant and changing C; the resulting range was $6.74\text{x}10^{-10} < C < 4.1543\text{x}10^{-9}$ mmcycle^{-1}.

Replicas taken from the polished PBB sample where the primary crack was first observed at 213373 cycles (0.933 N_f) and just before failure at 228386 cycles (0.999 N_f) are shown in Figure 5- 14 and Figure 5- 15 respectively. Failure occurred when the primary and secondary cracks joined together.

Fatigue life was dominated by corner initiation in this particular configuration; indeed it was observed that initiation in all PBB occurred at the edge of the sample despite careful bevelling to try and alleviate this propensity (an example is shown in Figure 5-16). Initiation from the corner of the sample meant Equation 5-12 (based on FE stress intensity solutions for quarter-circular corner cracks [13]) was used to determine K_{max} and hence ΔK in the polished PBB replica sample.

$$K_{\max} = M_G M_B M_S \mathrm{F}(\sigma_{\max}) \Phi(\pi c)^{\frac{1}{2}} \tag{5-12}$$

Where M_G is a general correction factor allowing for crack type (in this case corner) and crack front position. M_B and M_S are back face and side face correction factors respectively allowing for the intersection, or otherwise, of a free surface by a line drawn from the centre of the crack through the crack front position in question. The correction factor was determined as a function of incrementing surface length, c, using the empirical relations detailed in Pickard [13]. F(σ) accounts for the effect of a complex stress field; F$(\sigma)/\sigma_{max}$ vs. $c/0.5B$ data given at surface positions for linear

bending [13] was used in combination with the applied loading parameters to allow for the applied stress distribution in the present case. Φ is an ellipticity correction factor which allows for the aspect ratio of the crack and can be calculated from $\Phi = 1/E(k)$. Pickard [13] details two methods of calculating $E(k)$; both are dependent on the crack aspect ratio of width, a, to surface length, c, $k = a/c$. The aspect ratio was taken to be $k = 0.7$; this was based on semi-elliptical crack shape observations in the literature [14, 15] and was verified in other failed PBB tested during the course of this investigation (for the sample exemplified in Figure 5- 16, $k = 0.696$). The two methods of calculating $E(k)$ and hence Φ were evaluated; the results were consistent at $\Phi = 0.52$ and in line with the expected result based on the Φ vs. k curves presented in Pickard [13].

Data for the two cracks observed in the replication test are also shown in Figure 5- 13; initiation from the corner of the sample meant the crack was already in the long crack regime once detected. Data for the primary crack is very close to the data obtained using the SENB technique, increasing confidence in the data. The increased crack growth rate shown by the secondary crack is the result of interaction between the stress fields of the primary and secondary cracks.

The fracture surfaces of an SENB sample were examined at the different locations shown in Figure 5- 17. At the end of the threshold region (Figure 5- 18) the fracture surface has a feathery appearance indicating that failure is transgranular. This could be either the result of failure on particular martensitic laths or the discontinuous microstructurally dependent growth which is a feature of near-threshold crack growth. At intermediate ΔK (Figure 5- 19), the fracture surface has a more blocky appearance; although evidence of failure on laths is still present, secondary cracking could also be identified in the micrographs. As final failure was approached at high ΔK (Figure 5- 20), there is evidence of microvoid coalescence at carbides, indicating the presence of some monotonic failure modes. The scale of the striations observed at high ΔK correlate well with the crack growth rate determined using the DCPD method; measurements made using Image J based on higher magnification images such as that illustrated in Figure 5- 21 reveal a striation separation of ~0.35 μm, comparison with the Paris Law prediction of 0.34 μm per cycle indicates that these striations represent crack growth on a cycle by cycle basis.

5.4.2. Total life fatigue test data and fracture surfaces

The S-N curve shown in Figure 5- 22 shows total life for both notched and PBB shot peened (using the industrial T0 process) and ground samples. The data is shown in this format as opposed to as a Coffin-Manson plot ($\Delta\varepsilon_p$ vs. $2N_f$) because yield was not exceeded in the compressive direction using the simple isotropic hardening material model (Section 0); hence there is no cyclic plastic strain predicted.

It is noticeable that removing the lip from the edges of the shot peened PBB samples (where large shear deformation was identified in Figure 4-11) significantly increased the beneficial effect of the shot peening process by removing the associated stress concentration effects. The beneficial effects of shot peening on PBB samples (including those with the ground top surface) are most evident at lower strain ranges, whereas at higher strain ranges ($\Delta\varepsilon_{11}$ > 0.005), where significant yielding occurs on the first cycle, the beneficial shot peening effect appears to be lost.

This behaviour can be compared with that of the notched samples which showed a greater fatigue life than the PBB samples under the same hot spot strain range. It is evident that shot peening is still beneficial even at 0.005 < $\Delta\varepsilon_{11}$< 0.008 in this more highly constrained notched system, although the benefit does appear to reduce as $\Delta\varepsilon_{11}$ increases.

A similar comparison is made for the samples of varying notch geometry in Figure 5-23. In the same way as PBB appeared to have a shorter life than the 4.5 x 1.25 mm notched samples, samples with notches of 10.5 mm diameter appear to show a lower fatigue life than the samples containing 4.5 mm diameter notches for a given $\Delta\varepsilon_{11}$.

Fatigue life data for notched (4.5 x 1.25 mm) samples shot peened using the four different processes under investigation is compared with the fatigue life after grinding in Figure 5- 24. The 4A T1 process offers very little improvement in total life over that of the ground samples in LCF conditions. Increasing the intensity from the industrial standard 13A to 18A in the T3 process did not improve the fatigue life, even though the compressive residual stress profiles are expected to be deeper (Figure 4-24). Indeed the fatigue life appears to be slightly lower than that for the optimised T0 process at lower strain ranges. Using larger shot at a lower velocity to develop the same intensity has resulted in a similar effect to the higher intensity process.

The fracture surfaces were examined to establish the initiation sites for each sample geometry. As mentioned previously, initiation from the corner was observed for all PBB samples, as shown in Figure 5- 25a. Centre initiation dominated in notched samples, as exemplified in Figure 5- 25b; furthermore, the ratchet marks were much easier to identify in notched samples than in PBB. The number of initiation sites as determined from the number of ratchet marks observed on the surface for each sample geometry peened using process T0 is shown in Figure 5- 26. As the strain range increases there is an increase in the number of initiation sites. The propensity for corner initiation means that the number of initiation sites for PBB samples at a given strain range is relatively low compared to notched samples. It was this tendency for corner initiation in PBB that the presence of a lip resulting from the shot peening process was considered to be important in PBB samples, but of much less significance in the

notched samples where centre initiation was dominant. In the notched samples, there are no apparent differences in the number of initiation sites with notch geometry.

A comparison of the fracture surfaces obtained on samples with different surface preparations is shown in Figure 5- 27. It appears that there are more initiation sites in the samples peened using processes T0, T2 and T3 than in the ground or low intensity T1 samples. This trend is also shown in Figure 5- 28; samples prepared by grinding or process T1 tend to have a lower number of initiation sites than those prepared by the higher intensity peening processes, between which there do not appear to be any significant differences.

5.5. Discussion

5.5.1. Crack propagation behaviour

5.5.1.1. Ambient temperature

The crack propagation behaviour for FV448 is shown to be very similar to data previously published for two similar materials as shown in Figure 5- 29. Indeed the Paris Law reported is very similar to that reported by Chaswal *et al.* [16] in which $C = 3.012\text{x}10^{-9}$ mmcycle^{-1} and $m = 3.092$. Furthermore, the ΔK_{th} was within the range of values reported for the normalised and tempered condition of $4.3 < \Delta K_{th} < 5.95$.

The dominance of transgranular fracture surfaces have also been reported by different authors for similar materials in ambient conditions [16, 18]; this fracture mode was retained in samples tested at higher temperatures up to 600 ˚C [18, 19]. The formation and growth of microvoids ahead of the crack tip which are associated with precipitates has been reported to be the dominant transgranular mechanism in the Paris regime [16]; these microvoids act as stress concentration features and have also been reportedly associated with secondary cracks [18]; examples of both can be seen in FV448 at intermediate and high ΔK in Figure 5- 19 and Figure 5- 20. In the near-threshold regime, where the plastic zone ahead of the crack tip is much smaller, transgranular failure is dominated by bursts of micro-cleavage between inter-precipitate ligaments ahead of the crack [16]. Since there is no evidence of microvoids or secondary cracks at lower ΔK in Figure 5- 18, it is assumed that the same microcleavage mechanism operates in FV448 at low ΔK.

The Paris Law and crack propagation behaviour has been shown to be in keeping with that expected for this class of material; hence the Paris Law constants reported for FV448 in Section 5.4.1 are sufficient for application in the fatigue lifing protocol

development process in ambient conditions; furthermore, ΔK_{th} data can be used to predict situations of non-propagating cracks.

5.5.1.2. Effect of temperature on crack propagation

Where the Paris Law is derived based on material behaviour in ambient conditions, application of the model to components operating at elevated temperature may result in a change in constants; e.g. if elevated temperatures cause a change in E and σ^0, the range of crack tip opening displacement, $\Delta\delta_t$, (Equation 5-13) is changed and as a result da/dN for a given ΔK may change since $\Delta\delta_t$ at the crack tip can be assumed to represent the strain accommodated by crack advance and hence be related to da/dN [20]. Furthermore, since Stage I crack growth is dependent on dislocation motion on the slip plane under the highest shear stress, changes in material yield strength and thus resistance to dislocation motion would be expected to have an effect on ΔK_{th}. Hence the component lifing procedure must be based on Paris Law constants derived at the temperature in question.

$$\Delta\delta_t = \frac{0.5\Delta K^2}{2E\sigma^0} \qquad (5\text{-}13)$$

The effect of the maximum LP turbine service temperature of 250 ˚C on $\Delta\delta_t$ can be estimated as follows: The variations in σ^0 and E with temperature in P91, a tempered martensitic 9 Cr steel (0.10 C, 8.75 Cr, 0.95 Mo, 0.22 V), are shown in Figure 5- 30 a and b respectively; the magnitude of the drop in σ^0 appears reasonable after comparison with the reductions in tensile peak stress with temperature in this class of material shown in Figure 1-6. Percentage variations with temperature based on the known values under ambient conditions can be used to show that at 250 ˚C there is a 12.1 % drop in σ^0 and a 6.8 % drop in E (based on the monotonic isotropic hardening material model perpendicular to rolling this results in σ^0 = 573 MPa and E = 187.7 GPa at 250 ˚C). When implemented in Equation 5-13, this results in an estimated increase in $\Delta\delta_t$ of 22 % for equivalent ΔK levels and illustrates the need for applying material data obtained at the correct temperature in any component analysis, even when, as in the present case, creep-fatigue interactions are negligible.

5.5.2. S-N behaviour

All SENB testing was carried out at R_p = 0.1, the same load ratio as was used for three point bend S-N fatigue testing of notched samples. However, the FE analysis described in Section 5.3 revealed that due to the nature of loading, the stress ratio, R_σ, was not constant through the sample and furthermore at the surface, was negative (Figure 5-31). The depth of the transient region in R_σ is noted to correspond with that of the initial notch plastic zone defined by the equivalent plastic strain after the first half

cycle, $\bar{\epsilon}^{pl}$. It is unknown at this stage whether the notch plastic zone and any crack closure effects in the subsequent elastic cyclic loading will influence the ability of the current Paris Law to predict crack propagation behaviour in notched samples; should this be the case, additional fatigue crack propagation testing will be required to determine the Paris Law for FV448 in terms of the effective stress intensity factor range, ΔK_{eff}. Further discussion of the implications of the presence of notches on damage tolerant fatigue lifing is made in the introduction to current and future work in Chapter 7.

The increased propensity for initiation from the corner of PBB samples despite bevelling compared to notched samples can be explained by consideration of the stress distributions across the samples when loaded beyond the elastic limit (Figure 5-32). The σ_{11} at the edge of the PBB sample under maximum load is 4 % lower than that at the centre of the sample; however, the σ_{11} at the edge of the 4.5 x 1.25 mm notched sample under maximum load is 14 % lower than at the centre of the sample. Whilst bevelling was not accounted for in the model, the effect is still significant enough to mean that much smaller defects at the edges of the PBB are sufficient to promote initiation at the edge compared with the notched samples. Furthermore, the length over which these defects could occur is greater for the PBB sample as the σ_{11} is relatively constant between the load rollers compared with the notched sample in which the σ_{11} decreases rapidly with increasing circumferential distance away from the notch. Based on this discussion and the stress distributions shown for the ideal axial sample in Figure 5- 32, it would be expected that axially loaded samples would show the greatest propensity for edge initiation; initiation at the sample edge was indeed observed in the cylindrical axial fatigue samples described in Chapter 3.

The stress distributions shown in Figure 5- 32 can also be used to explain the variation in fatigue life shown between PBB and 4.5 x 1.25 mm notched samples in Figure 5- 22. In PBB samples the high tensile stresses above yield resulting from bending extend to around three times the depth they extend to in 4.5 x 1.25 mm notched samples. Indeed these elevated stresses extend to a depth far beyond that of the residual stresses from the shot peening process; the larger sampling volume at elevated stress increases the probability of fatigue initiation.

A similar argument based on the stress distributions shown in Figure 5- 33 can be used to explain the lower fatigue life observed in wider notches in Figure 5- 23. The variation in fatigue life with geometry is thus not considered to be a result of variations in the efficacy of the shot peening process (if the effect was due to notch shadowing, we would expect the lower life in the most severe 4.5 x 3 mm notch) but a result of the high tensile stresses resulting from bending extending to greater depths below wider notches.

It was shown in Figure 5- 24 that the low intensity 4A shot peening process offers very little improvement over that of the ground samples in LCF conditions. This is thought to be a result of the very shallow residual stress depth predicted in Chapter 4 (Figure 4-24) to be only 100 μm and the strain hardening depth profile of just 37 μm. The industrial 13A (T0) process has been shown to result in much improved life in notched samples representative of fir tree blade-disc connections, even in the LCF regime up to $\Delta\varepsilon_{11} < 0.008$. Despite the increase in compressive residual stress depth predicted to result from increasing the intensity of the process to 18A (T3), there has not been an improvement in fatigue life; indeed at lower $\Delta\varepsilon_{11}$, there appears to have been a slight reduction in life. This may be a result of the higher strain hardening at the surface resulting from process T0 (Figure 4-21) compared with process T3 (despite the higher plastic strains extending to a greater depth after process T3) slowing initiation in the HCF regime where initiation is known to play a more significant role than in the HCF regime.

Using larger shot at a lower velocity to develop the same intensity (T2 compared to T0) results in no significant difference in fatigue life at high $\Delta\varepsilon_{11}$, however at lower $\Delta\varepsilon_{11}$ the fatigue life is slightly reduced in the T2 samples. In an analogous manner to the T3 vs. T0 comparison, this is thought to be the result of initiation being facilitated by a lower surface plastic strain in the T2 samples compared with the T0 samples. This evidence confirms that it is not just the intensity which is important when considering the effect of shot peening on component life but also the combination of shot size and velocity and the resulting strain hardening and residual stress profiles. This conclusion is similar to that of Guagliano and Vergani [24] who demonstrated that different residual stress profiles resulted from peening a 39NiCrMo3 low alloy steel at 12A using shot of diameter 0.3 mm and 0.6 mm. Their work showed that the larger diameter shot resulted in greater residual stresses and a finite element analysis showed that as a result a lower ΔK_{eff}would be expected to result from a crack of a given length in a notched rotating bend sample and hence it was implied that fatigue crack propagation would be slower in these samples. No S-N data was presented, and it is possible that despite the stronger residual stress profile in the sample peened with the larger shot (as was predicted in the present work in Figure 4-24) the fatigue life is dominated by the initiation characteristics resulting from the combination of surface roughness and strain hardening, neither of which were investigated in their work [24].

Examination of the fracture surfaces revealed that there were more initiation sites in samples peened using the higher intensity processes (T0, T2 and T3) compared with the T1 and ground samples. This is thought to be a result of the increased surface roughness (in terms of all the parameters shown in Figure 4-13) in these samples compared with ground and T1 samples. There appears to be no significant difference

between the number of initiation sites in the T0, T2 and T3 processes; this may be a result of the surface roughness parameters reaching a plateau. This plateau effect is clear when the average surface roughness parameters S_a and R_a are considered, although the effect is less clear when considering the peak surface roughness parameters S_z and R_z. There is, however, a more significant increase in R_z resulting from intensities 4A and 13A than 13A and 18A indicating the trend may be plateauing. Furthermore, the S_z parameter (which was previously concluded in Section 4.4.1 to be the more important parameter) shows no significant difference from 13A to 18A; indeed there is a slight decrease in S_z. This analysis is in terms of surface roughness because it was found that the empirical approach based on the work of Li *et al.* [25] used previously in Chapter 4 resulted in higher values of the elastic stress concentration factor, K_t, for the T1 process than for the higher intensity processes because of the relatively low values of indent diameter, D_d (Table 5- 8). For this reason, caution must be exerted when using this empirical approach to draw conclusions on the initiation characteristics resulting from a given shot peening-target material system.

In terms of fatigue life in the present study, the detrimental surface roughness effect appears to be negated by the beneficial residual stress and strain hardening profiles. Whilst detrimental surface roughness effects are often considered to be insignificant in systems with $2.5 < R_a < 5$ μm which are dominated by residual stress and strain hardening [26], if the life assessment procedure explicitly accounts for residual stresses and strain hardening, it would be prudent to also consider the effects of surface roughness, possibly by taking account of the stress concentration factor K_t, calculated using the empirical approach of Li *et al.* [25]. This is particularly important in operating conditions where significant stress relief and changes to the dislocation profile resulting from shot peening occur (as a result of operating temperature and applied stress distributions) [27, 28], since surface roughness may become a more dominant factor in assessing fatigue life. For example, in stress relieved AISI 4140, even a surface roughness of $R_a < 1.4$ μm ($R_t < 14$ μm) had a detrimental effect compared to polished samples of $R_a = 0.3$ μm ($R_t < 5$ μm) [29].

Should mechanical residual stress relief and changes in the dislocation structure after fatigue be a feature of the specific operating conditions, surface roughness must be considered as a factor affecting initiation life; in modelling approaches which include a strain life to initiation, this must be considered. Hence the inclusion of surface roughness in the life assessment model is dependent on residual stress relaxation, changes in the dislocation profile and the modelling approach in use. The present study considers changes in both residual stress (in Section 5.5.3) and the strain hardening profile (in Section 5.5.4) under service replicating conditions to determine whether surface roughness is a significant consideration in the present system.

It is clear from Figure 5- 22 that shot peening can still be beneficial under bending LCF, for highly constrained geometries, although the relative magnitude of the beneficial effect is reduced as the strain range increases. This reduction may be a result of changes in the residual stress and strain hardening profiles under high $\Delta\varepsilon_{11}$. In order to elicit further information on the possible mechanism for retention of shot peening benefit in notched samples, residual stress changes were investigated in these samples at σ^{e}_{nom} = 1034 MPa ($\Delta\varepsilon_{11}$ = 0.0068). This strain range was selected because there is a clear retention of shot peening benefit with a doubling of life shown to result from shot peening notched samples at this strain range in Figure 5- 22. This effect can be compared with the lack of improvement in life resulting from shot peening PBB samples even at lower strain ranges of $\Delta\varepsilon_{11}$ = 0.0054.

5.5.3. Changes in residual stress with LCF

5.5.3.1. Changes in shot peening induced residual stresses

Residual stress data was collected using the same XRD technique as was described previously in Chapter 4. In addition to the sample tested after shot peening, two additional samples were tested in each surface condition (ground and shot peened) at a different total life fraction (uncycled, one cycle and estimated 50 % total life).

The effect of applying fatigue cycles to notched shot peened samples on near surface residual stresses is illustrated in Figure 5- 34. In order to simplify the graph the error bars are not shown but are assumed to be constant at 50 MPa as previously discussed in Section 4.2.3 In the transverse direction (Figure 5- 34a) there is a reduction in the residual stress magnitude after the application of fatigue cycles but no change in the overall depth of the compressive stress field and after approximately 250 μm the uncycled shot peened profile is retained. This trend is not shown in the longitudinal direction (Figure 5- 34b) where the original residual stress profile is retained after fatigue cycling. There is no additional change in the residual stress profile in either direction after the first cycle.

The relaxation of post-shot peen residual stresses in the transverse direction is thought to be a direct result of the quasi-static mechanism reported in Section 2.1.3.2. Under loading, residual stresses combine with applied stresses to cause local plastic yielding and reduce the plastic misfit which caused the presence of the residual stresses.

The surface stress relaxation to 78 % of its original value can be compared with similar work [30] (in this case, the measurement was taken after 1000 cycles in a material which does show some logarithmic relaxation with increasing cycles) where a flat

(aluminium alloy) sample was loaded to a maximum stress greater than yield under four point bend with R_σ = 0.1. In this case the stress relaxed to 82 % of its initial value; this shows good correlation with the present results. However, whilst not explicitly defined, it is assumed that the direction of stress measurement in this work [30] was parallel to the loading direction. In the present work, there is no stress relaxation observed in the longitudinal loading direction.

It has been noted in several works (see for example [28, 31]) that the relaxation is greatest in the direction parallel to the applied load rather than perpendicular to it. This effect is not apparent in the present investigation. The material near the surface which is yielded in tension develops a compressive residual stress after unloading as a result of constraint by the elastically deformed material beneath. This constraint opposes any relaxation which may occur in the loading phase of the fatigue cycle because the unloading still produces a superposing compressive residual stress. In addition the initial load-induced tensile stress needs to overcome the residual compressive stress from shot peening, and the local effect of work hardening from the shot peening may also be expected to affect the stress distribution.

The stress distribution beneath the notch surface shown in Figure 5- 32 shows that the maximum σ_{11} in these samples is above $\sigma_{0.2}$ over the first 0.96 mm. For PBB samples this is true over the first 3.25 mm and for axially loaded samples, this would be true through the entire sample thickness. It is noted that residual stress relaxation has been reported in both geometries typically to a lesser extent in PBBs than in axial samples (Section 2.1.3.2). Since the stress distribution in the PBB samples sits somewhat in-between that of the notched sample and the equivalent uniaxial sample, it is likely that the residual stresses in the PBB geometry have relaxed more than those in the notched geometry, given that the high stresses in the PBB sample extend further beyond the limit of the compressive residual stress region (340 μm) than in the notched sample. This observation goes some way to explaining the retention of the beneficial effects of shot peening in the notched sample at strain ranges where for the PBB sample the benefit is lost.

5.5.3.2. Changes in grinding induced residual stresses

Measurements of changes in the residual stress profile resulting from the initial grinding process are shown in Figure 5- 35. After fatigue cycling, in the transverse direction there has been a reduction in the tensile residual stress magnitude; indeed at the surface the residual stresses are now compressive. This effect is even more marked in the longitudinal direction. In both cases, the resulting residual stresses are the same after one cycle and half the expected total life; this indicates that the change in residual stress occurs after the first cycle.

The relaxation of both longitudinal and transverse grinding residual stresses has been reported previously [32-34]. In the present case, unloading from high tensile stresses above σ^0 on the first cycle has resulted in a compressive residual stress field. This is in line with the work of Quesnel *et al.* [34] who found that the initial residual stress profile from machining was relaxed within the first tensile half cycle and from that point onwards at each strain reversal (±1 %) the residual stress changed in the direction opposing the previously applied stress.

The material near the surface is yielded under tension, and yet the material beneath is not; upon release of the load, the elastically deformed material places the near surface plastically deformed material under compression. This mechanism is a direct result of the loading under three point bend and is similar to that which is present in the shot peened samples; furthermore, this would perhaps not be expected to be so significant in axially loaded samples where the bulk would also deform plastically under maximum σ_{11}. Since the grinding residual stresses are of both lower magnitude and shallower depth (Figure 4-16), and the variations in material properties resulting from strain hardening are less severe (Section 4.3.4), the ground sample data is helpful in developing FE models which can predict residual stress relaxation.

In order to demonstrate this potential, the residual stress present at the notch root in the longitudinal (11) and transverse (22) directions generated by unloading after the application of one stress cycle (in material with no residual stress or variation in material properties) was determined (Figure 5- 36). The stress distributions after unloading have also been shown in conjunction with the experimental results on the ground samples in Figure 5- 35. The high bending stresses under maximum load in the longitudinal direction shown in Figure 5- 36a result in a compressive residual stress at the surface after load release. The correlation between experimental and computational results is sufficient to add confidence to both datasets. For this simple case, the method clearly shows potential for modelling the residual stress distributions after loading and it is in developing this approach in components containing residual stresses and strain hardening from shot peening where future modelling efforts (Chapter 7) will be focussed.

5.5.4. Changes in plastic strain with LCF

The XRD data was also analysed to elicit information on changes in line broadening and hence dislocation arrangement and strain hardening. The results for both shot peened and ground samples are shown in Figure 5- 37. Again, error bars are not shown, however, the error in FWHM would be ±0.12° as discussed in Section 4.2.4.2 and once calibrated to plastic strain, of the same order as shown in Figure 4-19.

The initial cold work levels associated with both surface preparation processes have been reduced by the application of one fatigue cycle. Continued cycling does not appear to have had a significant further effect on the profile. The dislocation distribution after LCF can be compared with the cyclic softening behaviour reported in Chapter 3. The cyclic softening in FV448 is associated with the sweeping of dislocations into a cellular structure; it is thought that it is this rearrangement of dislocations near the surface under the first cycle of load which results in the measured reduction in plastic strain. This mechanism was also reported by Quesnel *et al.* [34] to be responsible for the reductions in diffraction peak width in a high strength low alloy steel.

In FV448, the rate of softening reduces after the first load cycle; this explains the lack of continued logarithmic softening measured between the first cycle and 50 % of life. This result can be compared with that of Dalaei *et al.* [27] in a pearlitic steel in which a logarithmic reduction in FWHM with fatigue cycling was reported and Kim *et al.* [28] in a Ni-base superalloy in which no change in FWHM profile was found at moderate temperatures; both other works employed a similar strain range to that under investigation here. Since these changes are dependent on the material cyclic stress-strain behaviour and the specific loading geometry, it is essential when considering the application of plastic strain and residual stress data in fatigue life assessments that any possible changes in the specific system are accounted for in the simulation.

In FV448 the rate of softening reduces after the first load cycle (Figure 3-15); this explains the lack of continued logarithmic softening measured between the first cycle and 50 % of life. This also correlates well with the observation that the residual stress profiles after one cycle and half the samples' expected total life are the same in both the ground and shot peened conditions; hence there is a causal link between the cyclic behaviour of the material and the changes in the residual stress and plastic strain profiles under fatigue.

Since there was no significant change in residual stress or strain hardening with LCF, it is thought that surface roughness is likely to have only a very small effect on fatigue behaviour in the present system where residual stresses and strain hardening will dominate. However, as previously mentioned, this will not always be the case and this should be a consideration of any analyst performing a remnant life assessment for a shot peened component.

5.6. Conclusions

The baseline fatigue behaviour of FV448 and the interactions with the effects of shot peening can be summarised as follows:

- Long crack propagation in FV448 can be modelled using a conventional Paris Law approach; hence the Paris Law constants selected in a fatigue crack propagation analysis must be appropriate for the component operating temperature. Crack propagation is transgranular in nature.
- Shot peening notched samples increases the total fatigue life, even when operating in LCF conditions.
- The notch shape does not affect the efficacy of the shot peening process in terms of fatigue life, but there are intrinsic lifetime effects resulting from increased sampling volume effects in PBBs and samples with wider notches.
- The need to separate the beneficial effects of strain hardening and compressive residual stresses from shot peening before including the effects of shot peening in lifing estimates has been established by investigating the S-N behaviour after different peening processes. Where strain hardening and residual stresses are significant throughout the component life, surface roughness is not considered to be a significant factor in the damage tolerant lifing process.
- Cyclic plastic deformation of a notched shot peened component manufactured from FV448 under three point bend and unloading from tension results in:
    - The retention of any near surface compressive residual stresses (for example resulting from the shot peening process) in the direction of loading and relatively small quasi-static relaxation in the orthogonal direction (to approximately 80 % of the original value).
    - The conversion of near surface tensile residual stresses (for example resulting from a grinding process) to compressive residual stresses in the direction of loading.
    - There is a slight reduction in the near surface plastic strain after one load cycle and no further appreciable changes through life. This behaviour correlates well with the rapid initial cyclic softening followed by slight through life softening observed in FV448 and is in good agreement with the observed residual stress relaxation characteristics.

These effects can be directly explained by the interaction of the specific stress distribution resulting from loading notched samples in three point bend and the residual stresses and plastic strains resulting from shot peening. The retention of the compressive residual stresses resulting from shot peening is a result of the high stress gradients near the notch. The material near the surface is yielded under tension, and yet the material beneath is not; upon release of the load, the elastically deformed material places the near surface plastically deformed material under compression. This effect has been demonstrated using FE modelling for ground samples.

- The lack of relaxation of residual stresses in the constrained notched geometry and only very slight modifications to the strain hardening profile may explain the observed continued retention of shot peening benefit, even to LCF, compared with the reduction in shot peening benefit in PBB samples.

The results presented in this chapter are sufficient to conclude that before the application of a peening process to a component, consideration must be given to the manner in which the shot peening process effects are likely to interact with the applied cyclic stresses. The FE model in its present state can account for the loading type and various material constitutive models (a sensitivity study similar to that conducted in Section 5.3.1 should be conducted for each loading configuration – material system, including the addition of residual stresses and strain hardening to the FE model to predict the residual stresses after unloading), but cannot account for the residual stresses and strain hardening resulting from shot peening. Furthermore, the lifing procedure under development is largely based on the assumption that it is the change in local stress and strain distributions in the component caused by shot peening that controls the improvement in fatigue life and that the changes in fatigue micro-mechanisms are negligible. Work on developing the FE model to incorporate the shot peening process effects and to establish the micromechanisms of fatigue crack initiation and growth in the layers affected by shot peening is on-going and is detailed further in Chapter 7.

Samples are defined as diameter x depth, e.g. 4.5 x 1.25 mm.		Notch diameter / mm	
		4.5	10.5
Notch depth / mm	1.25	K_t = 1.6. Simulate blade connection geometry.	K_t = 1.3. Simulate repair like geometry.
	3.00	K_t = 1.5. Simulates a deeper notch.	K_t = 1.2. Completes test matrix.

Table 5- 1: Service relevance and K_t values for the varying notch geometries.

Parameter	Definition
σ_{11}	Stress (true) in the direction of applied bending stress. It is noted that in fracture mechanics damage tolerant analysis it is the crack opening stress which is typically of most significant interest.
ε_{11}	Total logarithmic (true) strain in the direction of applied stress.
σ_{eq}	Von Mises Equivalent stress, allowing for stresses in all three directions. Where the range (denoted by Δ) is calculated, the range of each stress component is used in place of the absolute value. It is noted that in fatigue initiation analysis, it is typically the equivalent stress which is considered most important. The standard definition is given in Equation 5-14: $\sigma_{eq} = \frac{1}{\sqrt{2}}[(\sigma_{11}-\sigma_{22})^2 + (\sigma_{22}-\sigma_{33})^2 + (\sigma_{33}-\sigma_{11})^2 + 6({\tau_{12}}^2 + {\tau_{23}}^2 + {\tau_{31}}^2)]^{0.5}$ (5- 14)
ε_{eq}	Equivalent strain, allowing for strains in all three directions. The standard definition is applied to elastic and plastic components of strain and the elastic and plastic equivalent strains are summated to result in the overall equivalent strain. Where the range is calculated, the range of each strain component is used in place of the absolute value. The standard definition is given in Equation 5-15: $\varepsilon_{eq} = \frac{1}{\sqrt{2}(1+\upsilon)}\left[(\varepsilon_{11}-\varepsilon_{22})^2 + (\varepsilon_{22}-\varepsilon_{33})^2 + (\varepsilon_{33}-\varepsilon_{11})^2 + \frac{3}{2}({\gamma_{12}}^2 + {\gamma_{23}}^2 + {\gamma_{31}}^2)\right]^{0.5}$ where $\nu = \begin{cases} 0.3 & \text{elastic} \\ 0.5 & \text{plastic} \end{cases}$ (5- 15)

Table 5- 2: Definition of the stress and strain parameters used in fatigue analysis.

Geometry /mm	Lower validity σ^e_{nom}/MPa	Upper validity σ^e_{nom}/MPa
4.5 x 1.25	533	1265
4.5 x 3	561	1620
10.5 x 1.25	641	1198
10.5 x 3	670	1745

Table 5- 3: Range of validity for calibration curves.

Geometry /mm	Maximum % error in σ_{11}
4.5 x 1.25	3.3
4.5 x 3	3.2
10.5 x 1.25	4.6
10.5 x 3	4.4

Table 5- 4: Maximum error in surface σ_{11} between FE data points and ESED approach for each notch geometry.

Geometry /mm	Maximum % error in $\Delta\varepsilon_{11}$
4.5 x 1.25	10.4
4.5 x 3	10.7
10.5 x 1.25	14.9
10.5 x 3	14.1

Table 5- 5: Maximum errors in surface $\Delta\varepsilon_{11}$ between calculations based on the ESED plus calibration method and FE results for each geometry.

Geometry /mm	Notch radius /mm	Remaining ligament /mm	σ^{e}_{nom} /MPa	4.5 x 1.25 mm calibration curve		FE analysis	
				$\Delta\varepsilon_{11}$	$\Delta\sigma_{11}$	$\Delta\varepsilon_{11}$	$\Delta\sigma_{11}$
4.3 x 1.15	2.15	6.60	1003	6.64e-3	1409	6.73e-3	1428
4.4 x 1.20	2.20	6.55	1018	6.74e-3	1431	6.79e-3	1441
4.5 x 1.25	2.25	6.50	1034	6.85e-3	1452	6.85e-3	1454
4.6 x 1.30	2.30	6.45	1050	6.95e-3	1475	6.92e-3	1467
4.7 x 1.35	2.35	6.40	1066	7.06e-3	1498	6.98e-3	1481

Table 5- 6: Stress and strain results for geometry sensitivity study calculated using calibration curves and FE methods.

Geometry /mm	% Error $\Delta\varepsilon_{11}$	% Error $\Delta\sigma_{11}$
4.3 x 1.15	-1.26	-1.30
4.4 x 1.20	-0.69	-0.70
4.5 x 1.25	-0.09	-0.09
4.6 x 1.30	0.50	0.53
4.7 x 1.35	1.11	1.16

Table 5- 7: Error in notch shape sensitivity study results obtained using calibration curves compared to results from FE analysis.

Process	D_a/ μm	Optical S_z/μm	K_t
T1	55	21	1.82
T0	163	33	1.43
T2	156	42	1.56
T3	168	39	1.49

Table 5- 8: Elastic stress concentrations resulting from each peening process calculated using the empirical approach developed by Li *et al.* [25].

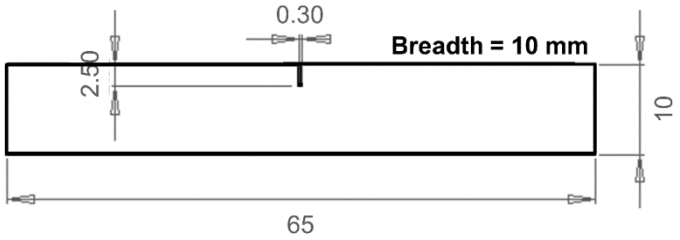

Figure 5- 1: SENB fatigue test sample, dimensions are shown in mm.

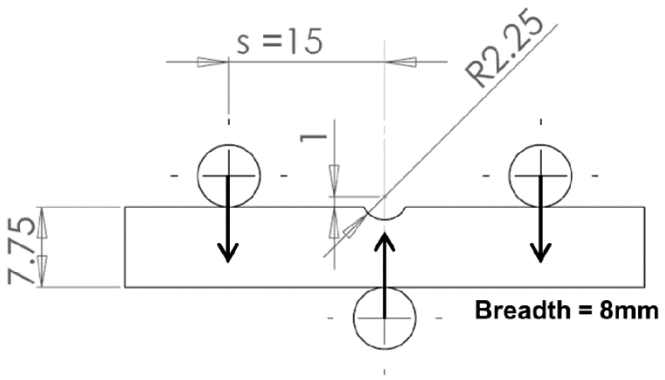

Figure 5- 2: Notched three point bend fatigue test setup for 4.5 x 1.25 mm sample; dimensions are shown in mm.

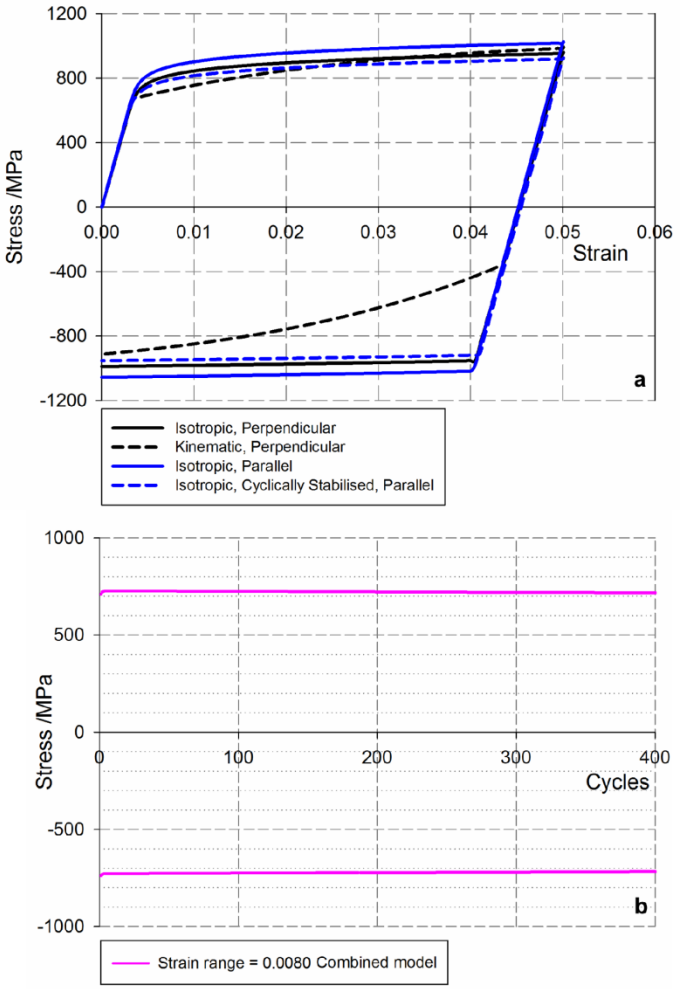

Figure 5- 3: Materials models implanted in Abaqus showing (a) static material models under R_ε = 0 and (b) combined cyclically softening material model at $\Delta\varepsilon$ = 0.0080, R_ε = -1.

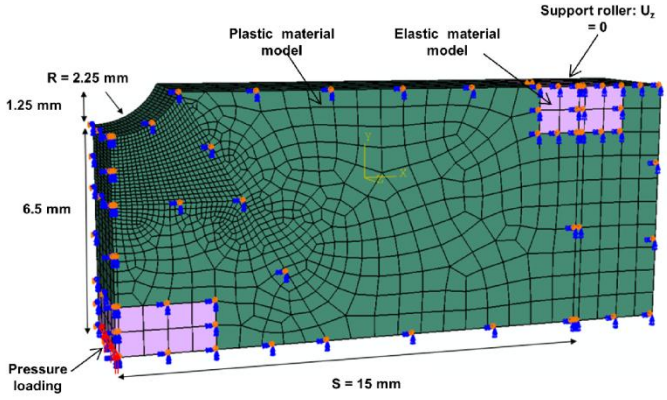

Figure 5- 4: The coarse mesh quarter model used in FE analysis of local stresses and strains in 4.5 x 1.25 mm three point bend fatigue sample.

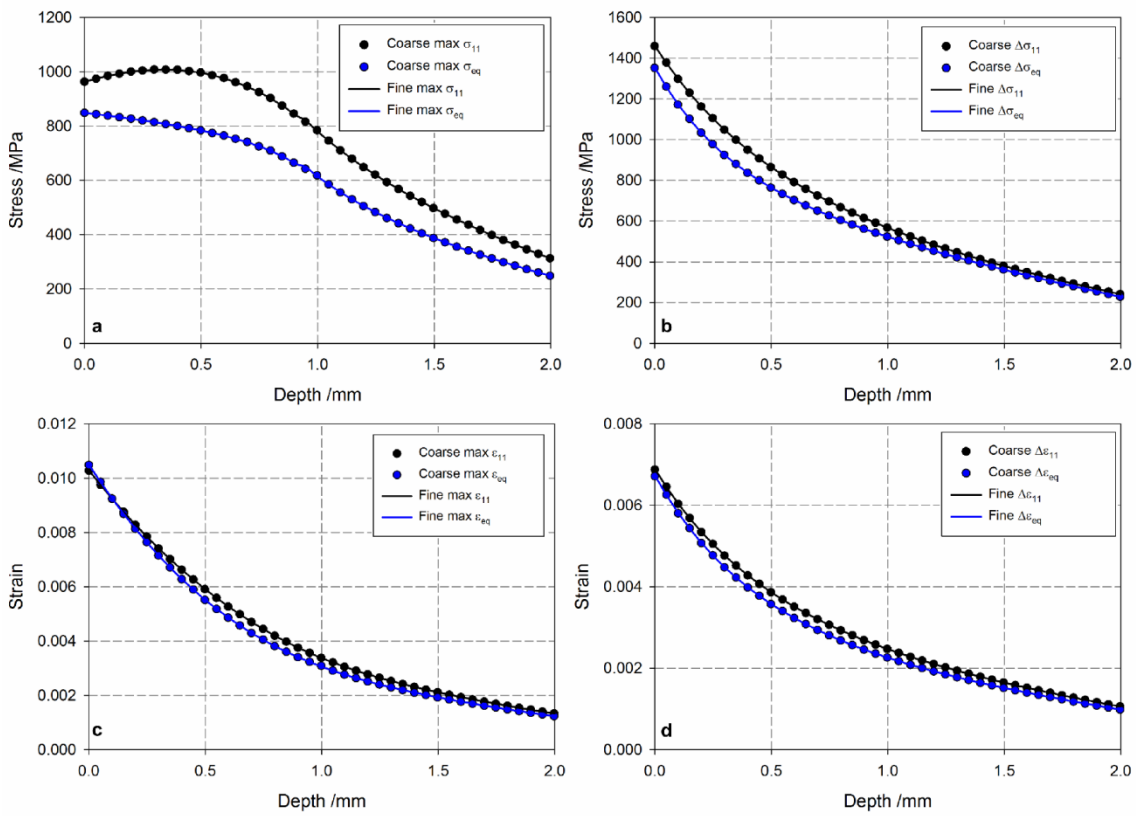

Figure 5- 5: Mesh validation in 4.5 x 1.25 mm geometry at σ^{e}_{nom} = 1034 MPa using normal to rolling tensile isotropic hardening material model illustrating (a) stresses at peak load, (b) stress range under R_p = 0.1 load, (c) strains at peak load and (d) strain range under R_p = 0.1 load.

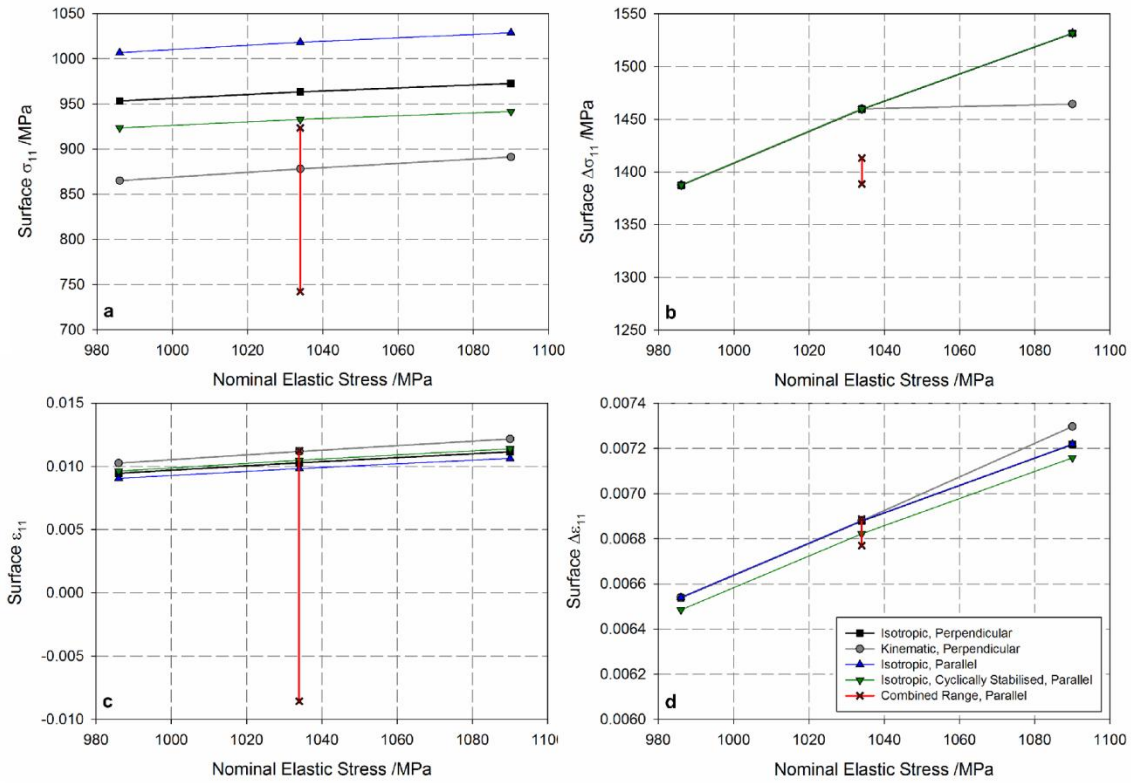

Figure 5- 6: Material model sensitivity results at the surface of the 4.5 x 1.25 mm notch at σ^{e}_{nom} = 1034 MPa on the first tensile half cycle illustrating (a) σ_{11}, (b) $\Delta\sigma_{11}$, (c) ε_{11} and (d) $\Delta\varepsilon_{11}$.

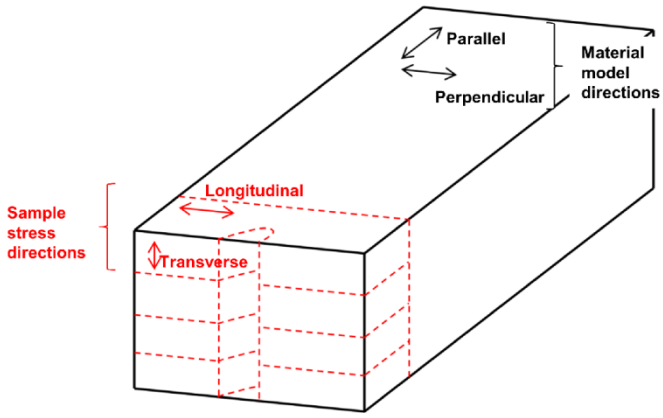

Figure 5- 7: Sample removal from barstock.

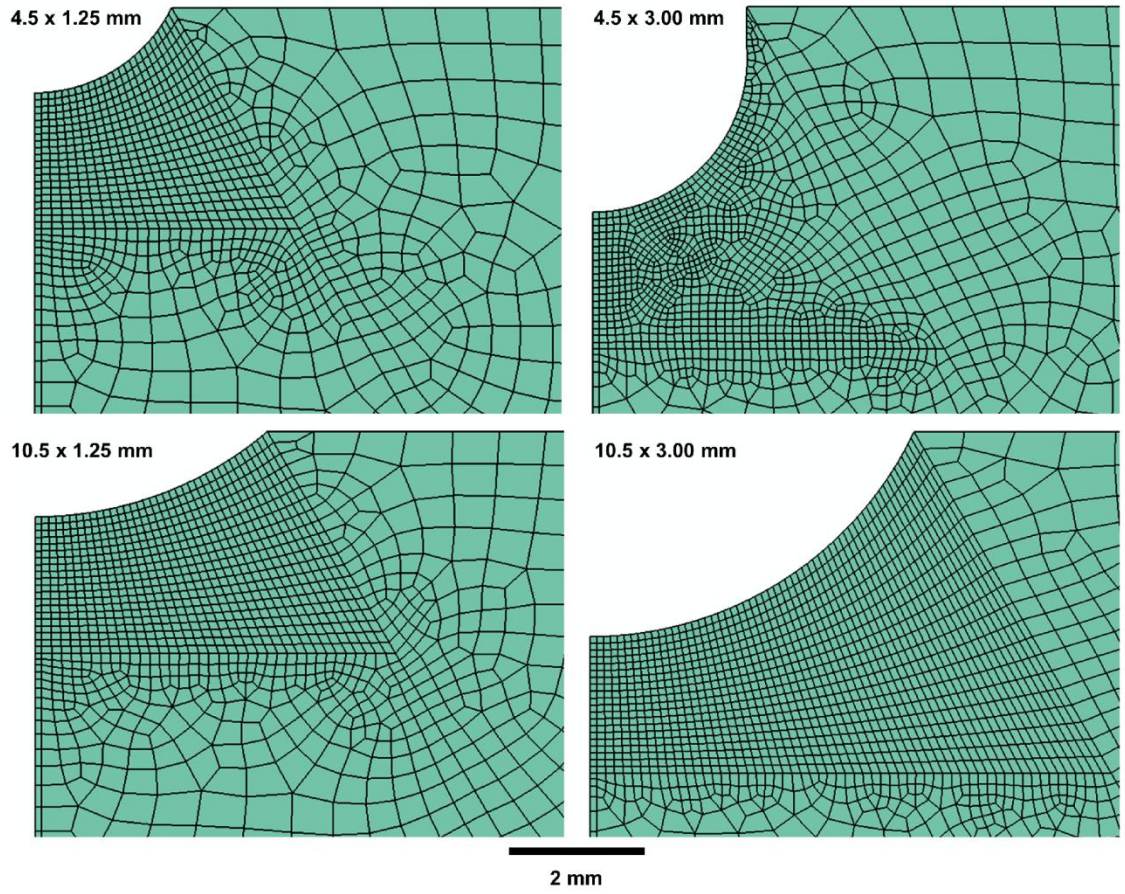

Figure 5- 8: Near notch mesh geometry in notches of varying geometry.

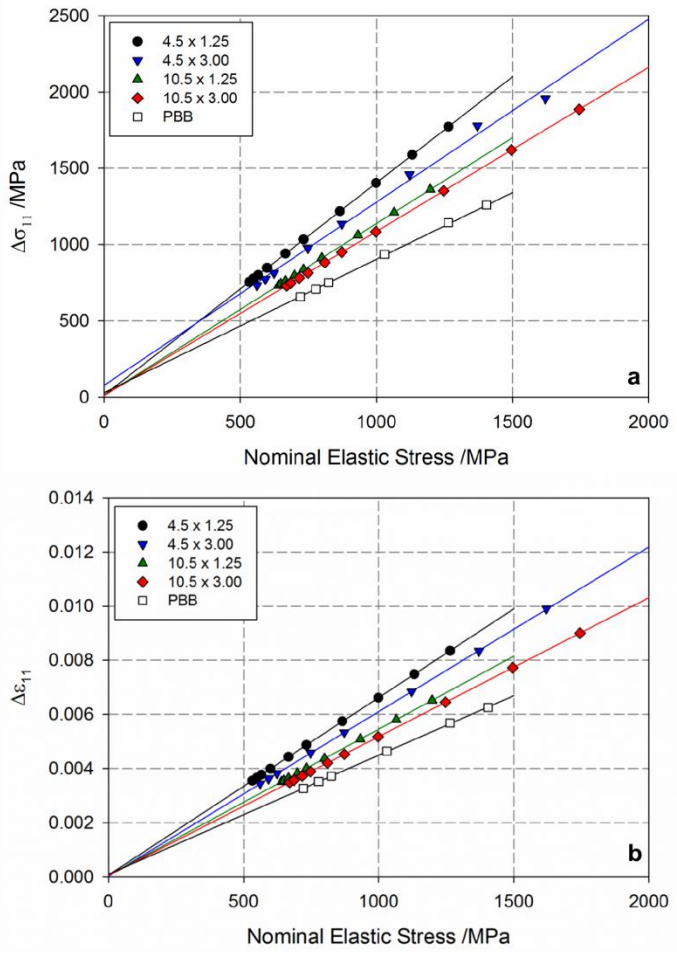

Figure 5- 9: (a) Stress and (b) strain ranges shown as a function of σ^{e}_{nom} in notched and PBB samples as determined by FE analysis.

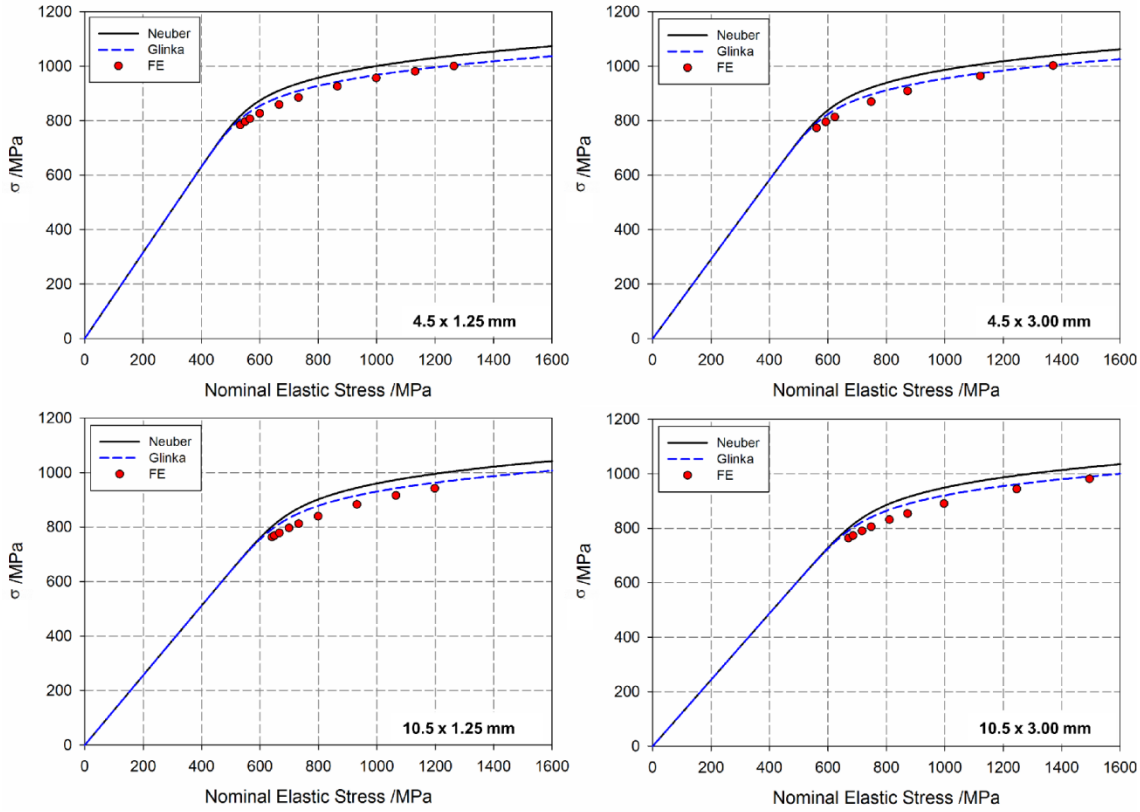

Figure 5- 10: Comparison of biaxial Neuber and ESED calculations of σ_{11}'' under maximum load with FE results for σ_{11} for each notch geometry.

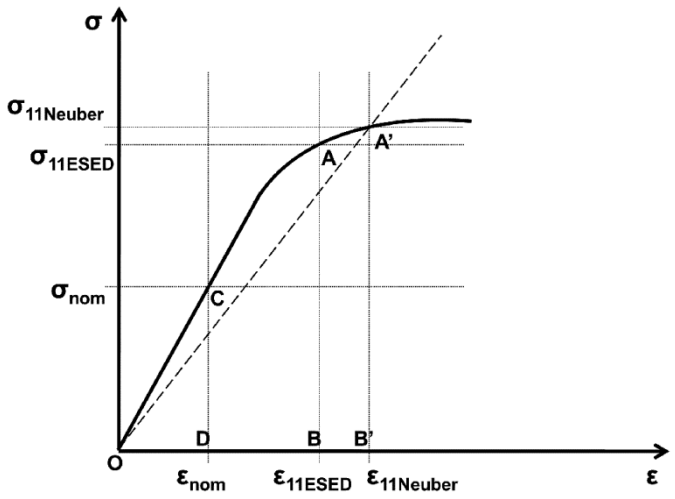

Figure 5- 11: Comparison of the physical meanings of the Neuber and ESED approaches. After Glinka [6].

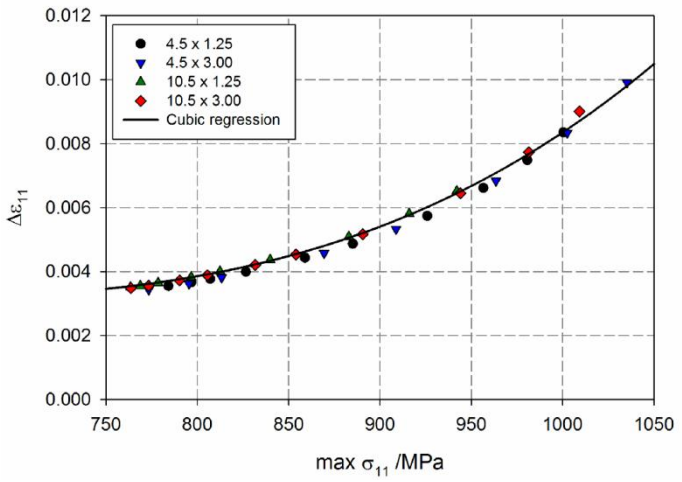

Figure 5- 12: Correlation between surface $\Delta\varepsilon_{11}$ and σ_{11} under maximum load in notched samples as determined by FE analysis.

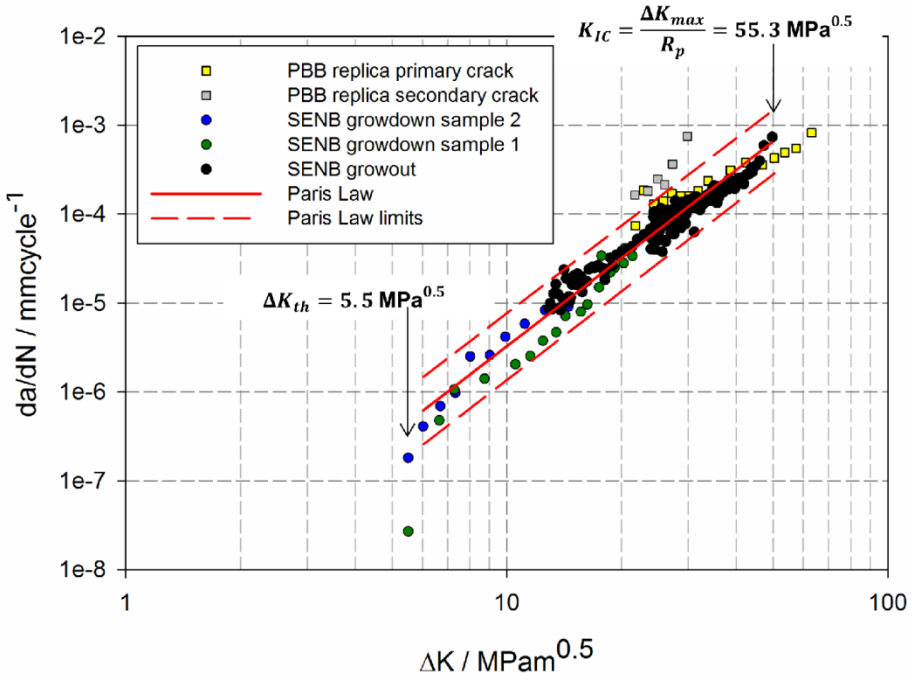

Figure 5- 13: Long crack propagation and Paris Law for FV448.

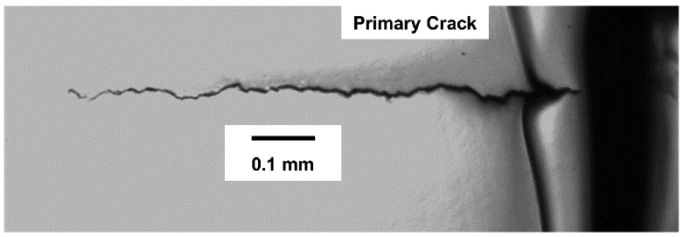

Figure 5- 14: First PBB replica obtained at 213373 cycles.

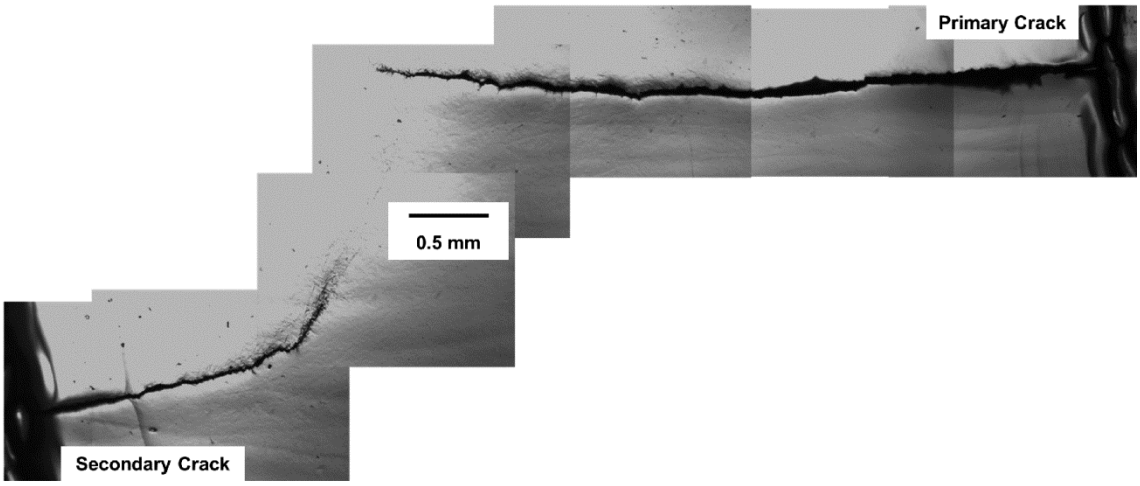

Figure 5- 15: Last PBB replica obtained at 228386 cycles.

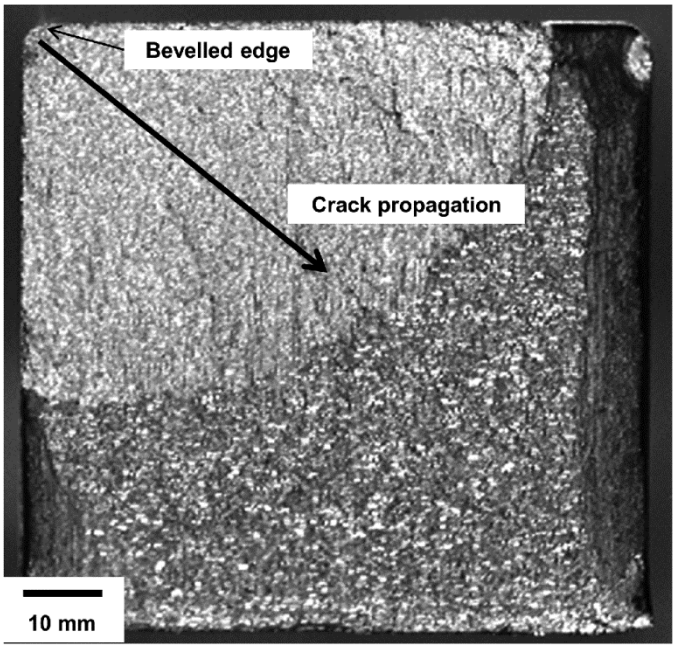

Figure 5- 16: Fracture surface of bevelled PBB sample tested at $\sigma_{11} = 0.9\ \sigma^0$.

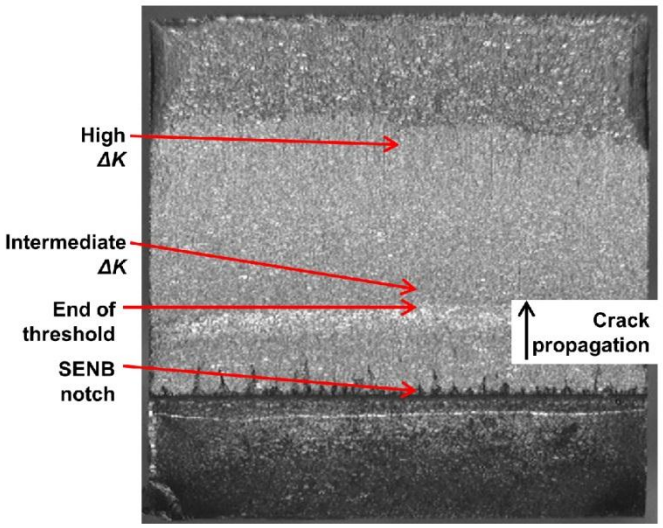

Figure 5- 17: Overview of SENB fracture surface.

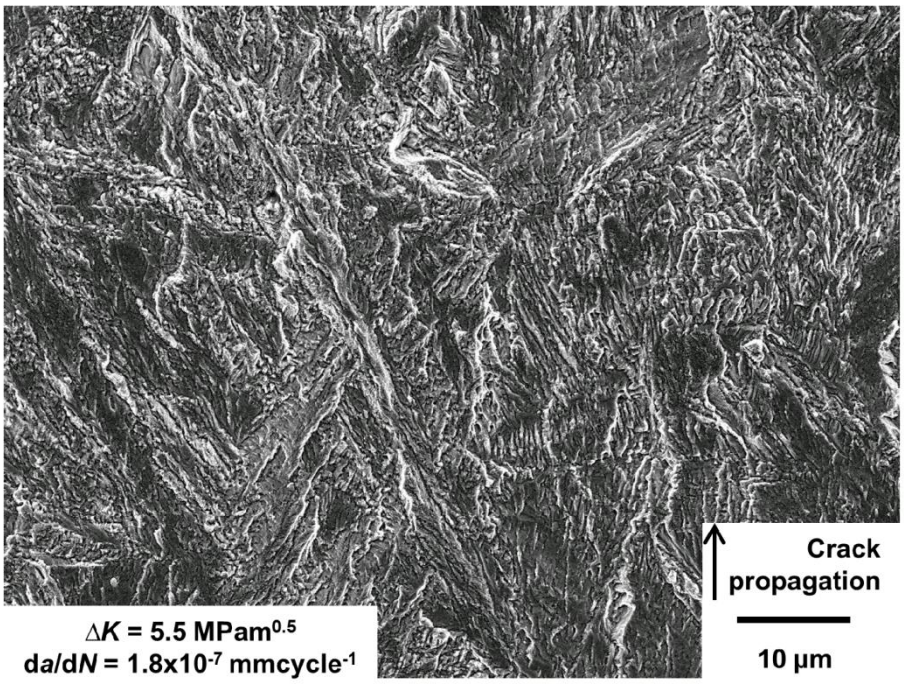

Figure 5- 18: SEI micrograph of SENB fracture surface near threshold.

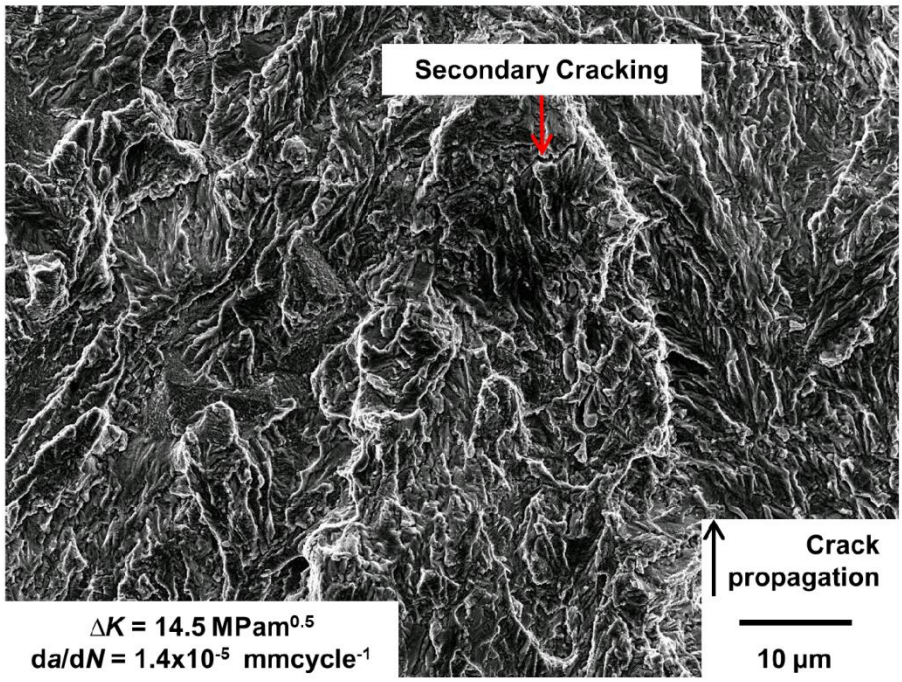

Figure 5- 19: SEI micrograph of SENB fracture surface at intermediate ΔK.

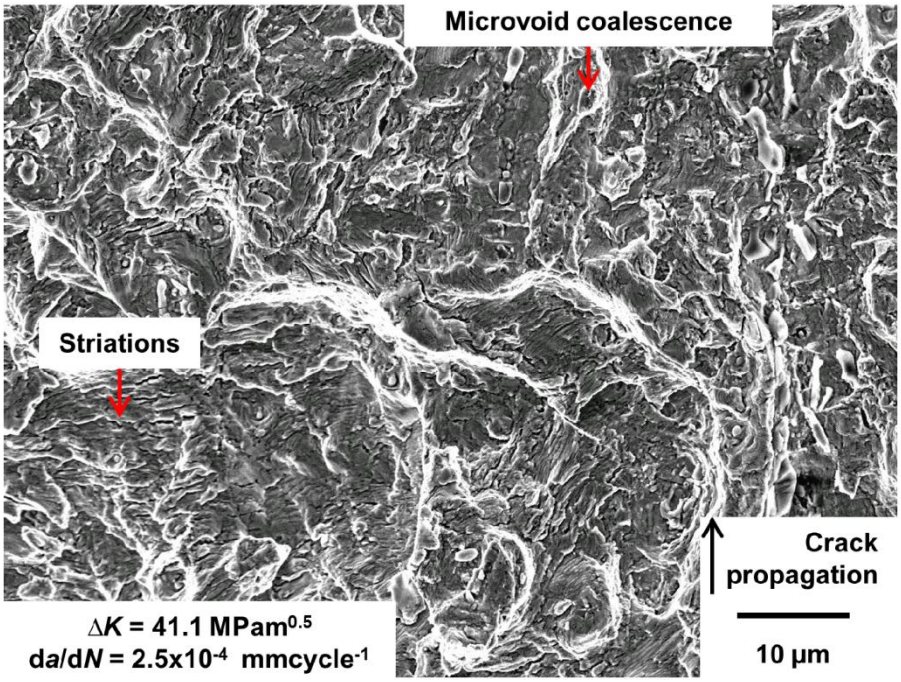

Figure 5- 20: SEI micrograph of SENB fracture surface at high ΔK.

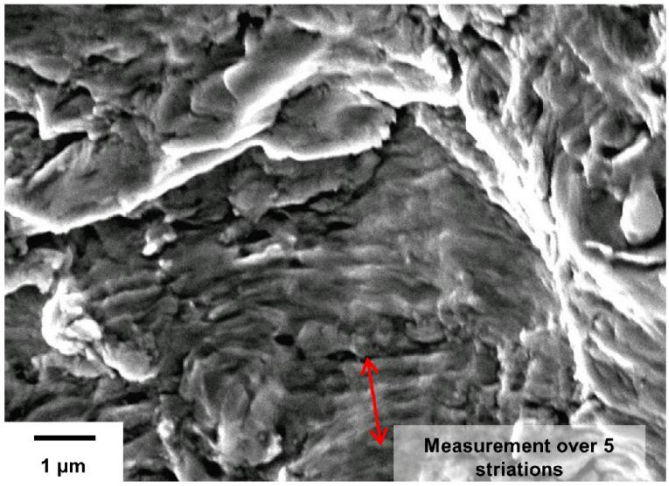

Figure 5- 21: SEI micrograph at ΔK = 41.1 MPam$^{0.5}$ illustrating striation measurement.

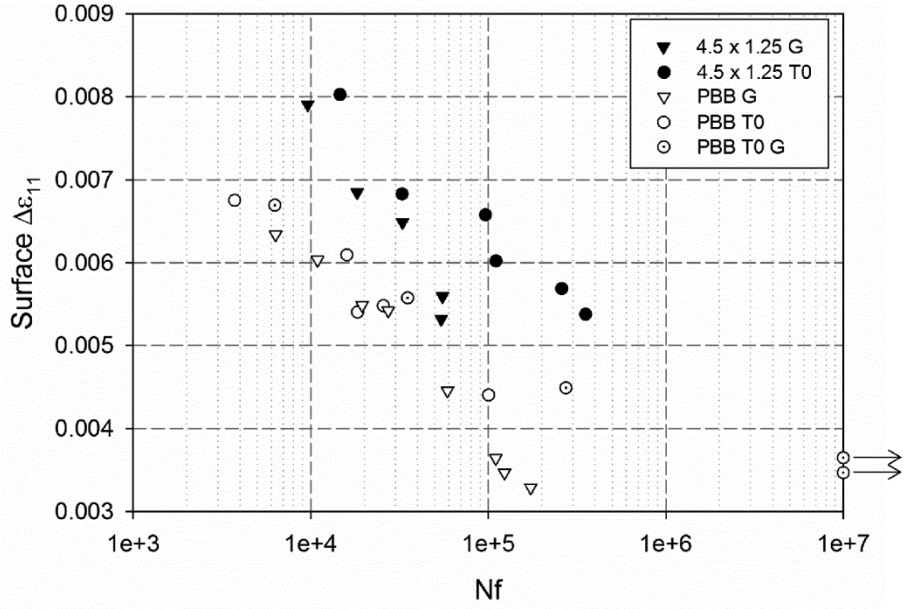

Figure 5- 22: Fatigue life comparison for shot peened (T0) notched and PBB samples.

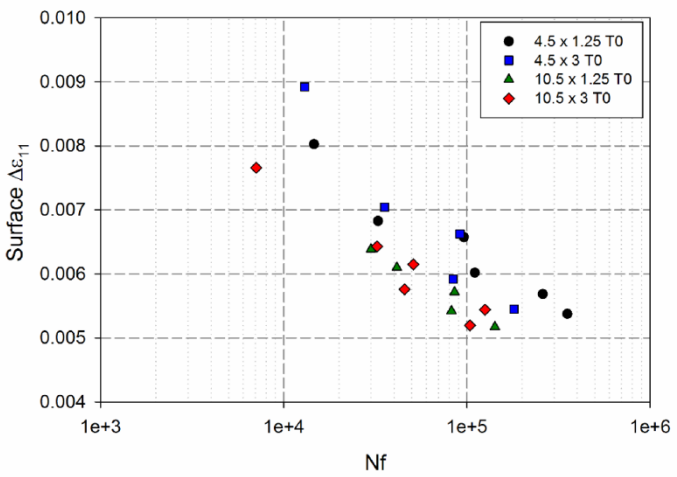

Figure 5- 23: Fatigue life comparison for shot peened (T0) notched samples of varying geometry.

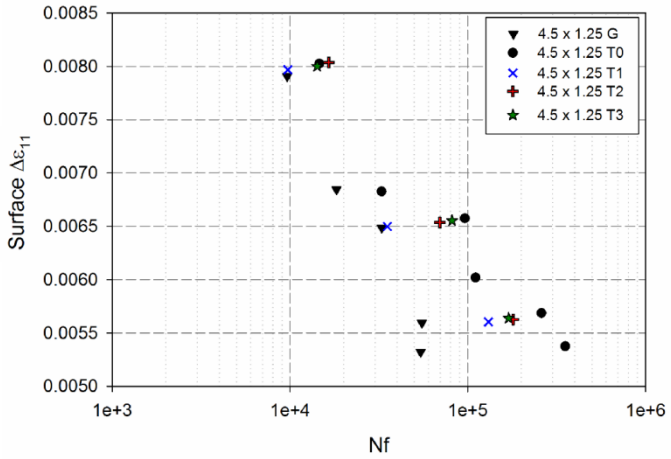

Figure 5- 24: Fatigue life comparison for notched samples (4.5 x 1.25 mm) shot peened using various peening processes with ground.

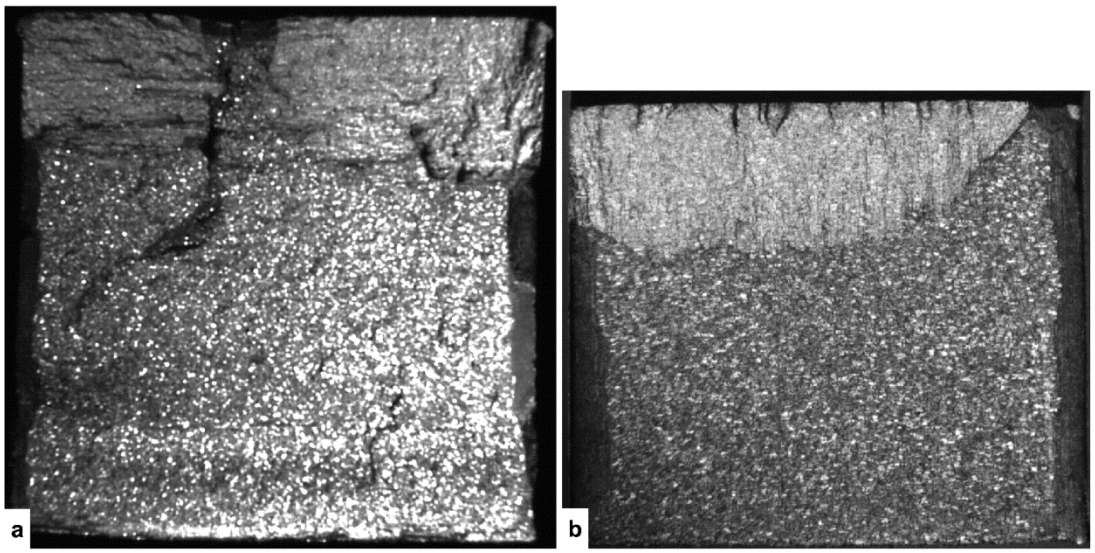

Figure 5- 25: Macro images of shot peened (T0) sample fracture surfaces after testing at $\Delta\varepsilon_{11}$ ~ 0.0068 in (a) PBB sample and (b) 4.5 x 1.25 mm notched sample.

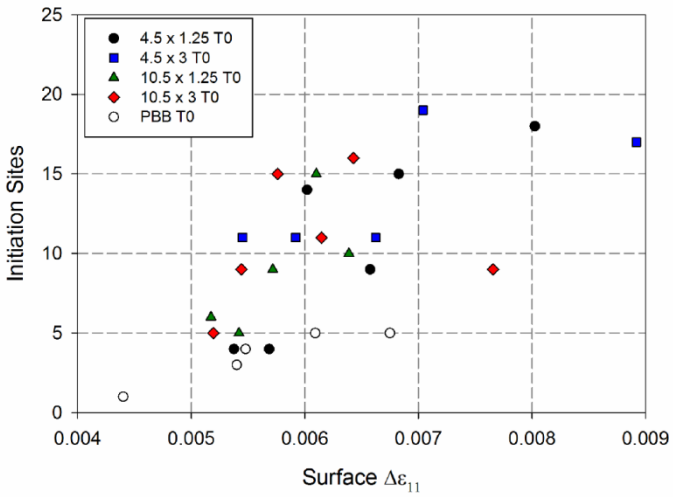

Figure 5- 26: Variation in number of fatigue crack initiation sites with notch geometry and strain range.

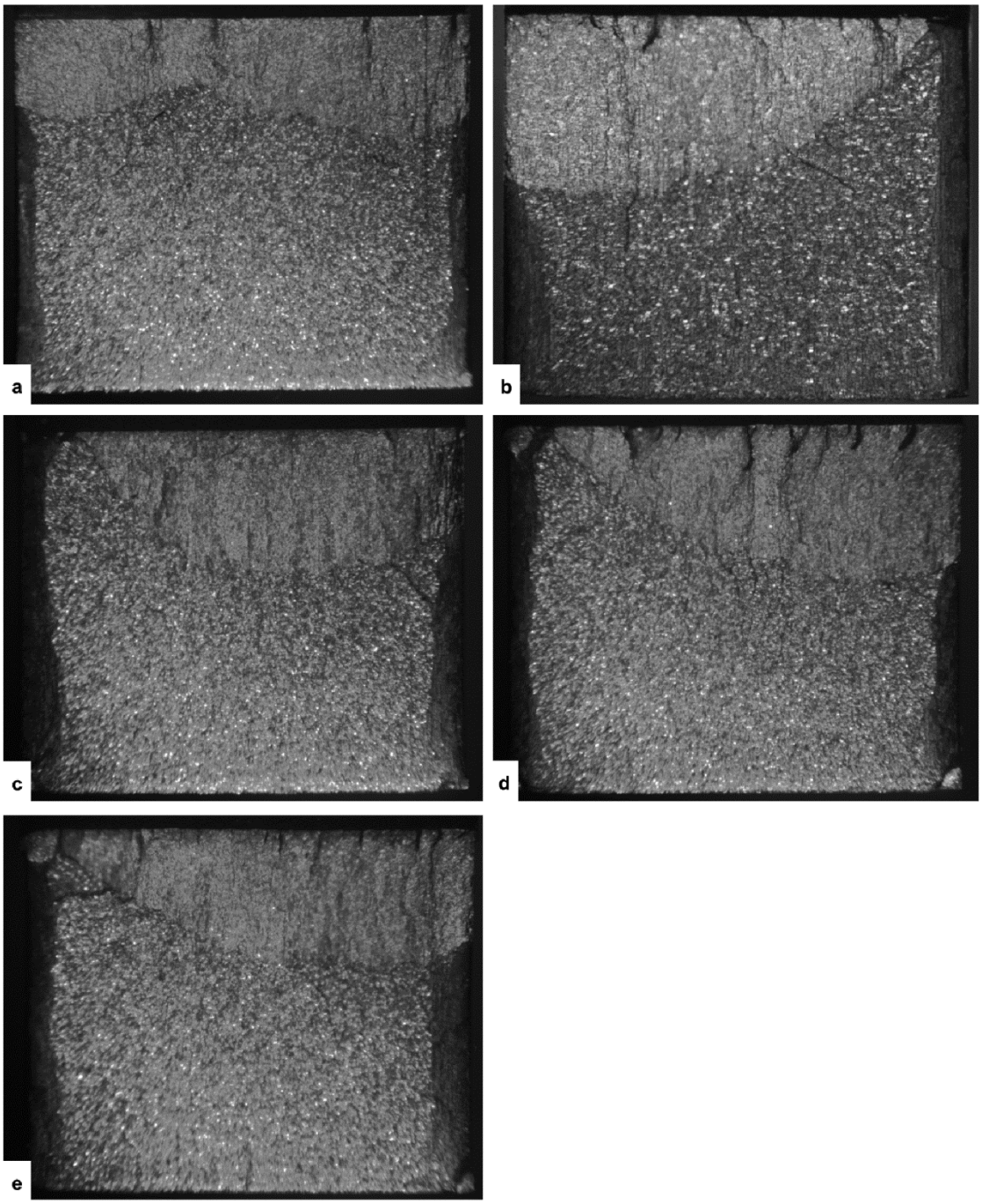

Figure 5- 27: Macro images of 4.5 x 1.25 mm notched sample fracture surfaces after testing at $\Delta\varepsilon_{11}$ ~ 0.0065 prepared using various surface preparations: (a) ground, (b) T0, (c) T1, (d) T2 and (e) T3.

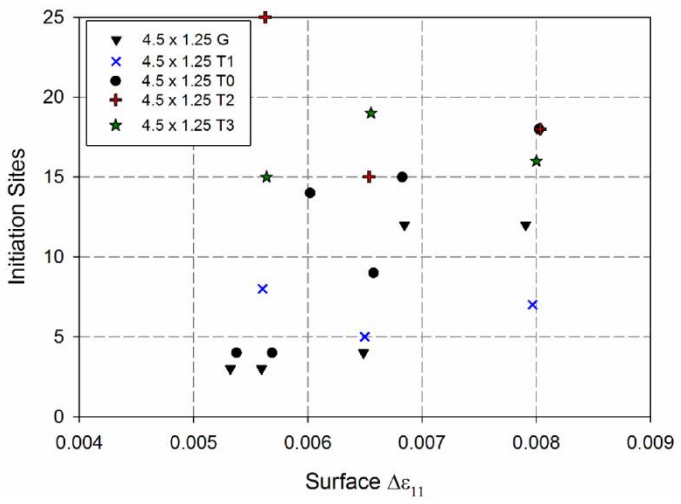

Figure 5- 28: Variation in number of fatigue crack initiation sites with surface preparation and strain range.

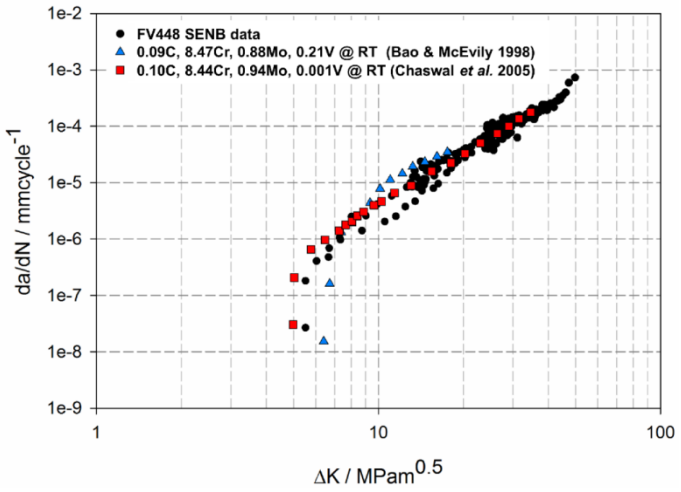

Figure 5- 29: Long crack propagation behaviour of FV448 compared with similar 9-12 %Cr steels. After Chaswal *et al.* and Bao and McEvily [16, 17].

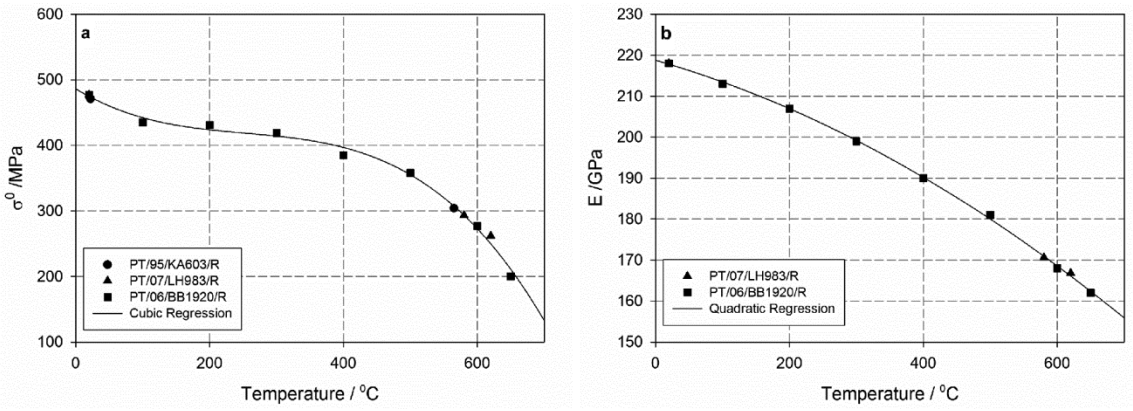

Figure 5- 30: Variations in (a) σ^0 and (b) *E* in P91 with temperature. After Mulvihill and Smith, Wignall and Wignall [21-23].

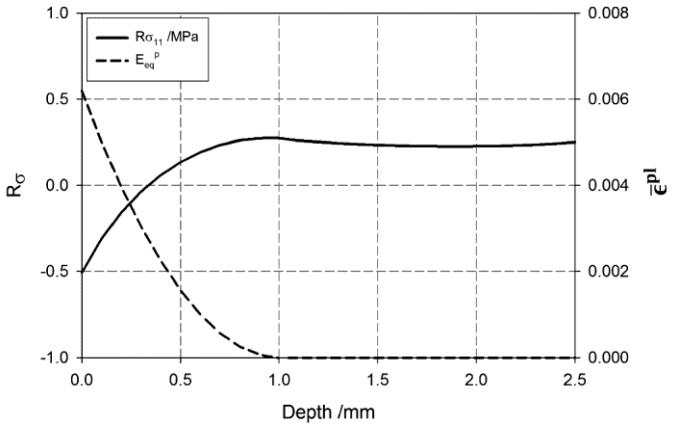

Figure 5- 31: Comparison of the depth variation of R_σ and $\bar{\epsilon}^{pl}$ for 4.5 x 1.25 mm notched sample at σ^e_{nom} = 1034 MPa.

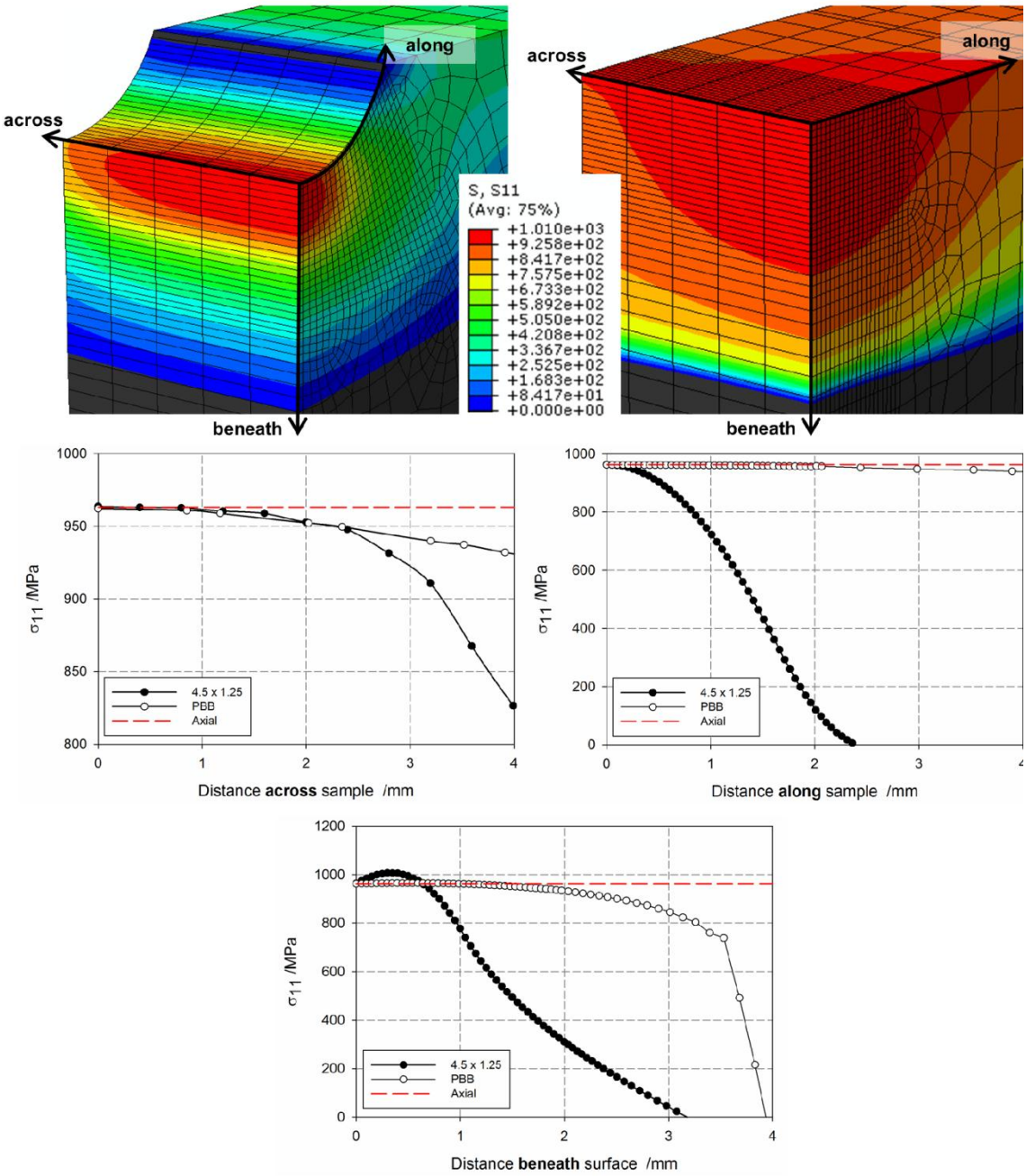

Figure 5- 32: Comparison of tensile stress distribution under maximum load in 4.5 x 1.25 mm notched sample tested at σ^{e}_{nom} = 1034 MPa with that in the PBB sample and an ideal axial sample tested at the same maximum σ_{11}.

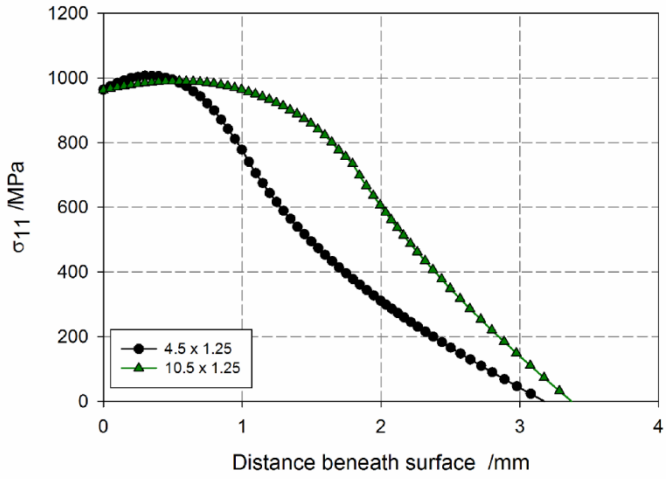

Figure 5- 33: Comparison of tensile stress distribution under maximum load in 4.5 x 1.25 mm notched sample tested at σ^{e}_{nom} = 1034 MPa with that in the 10.5 x 1.25 mm sample tested at the same maximum σ_{11}.

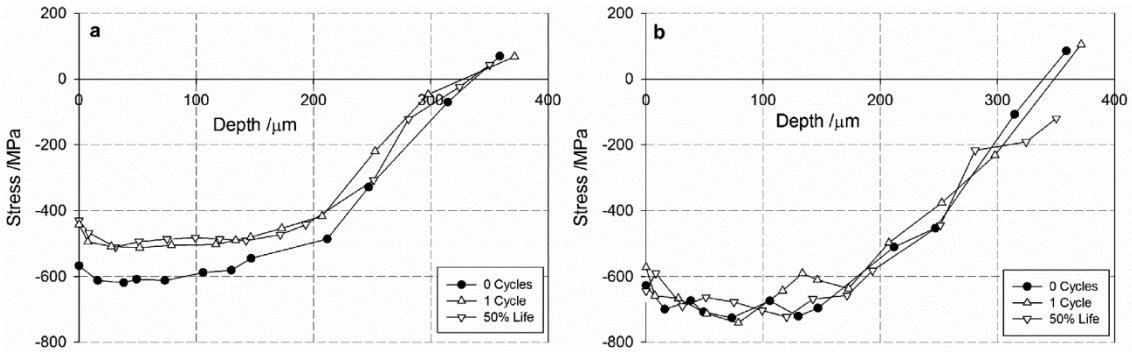

Figure 5- 34: Shot peening and post fatigue ($\Delta\varepsilon_{11}$ = 0.0068) residual stresses in 4.5 x 1.25 mm notched samples in (a) the transverse direction and (b) the longitudinal direction.

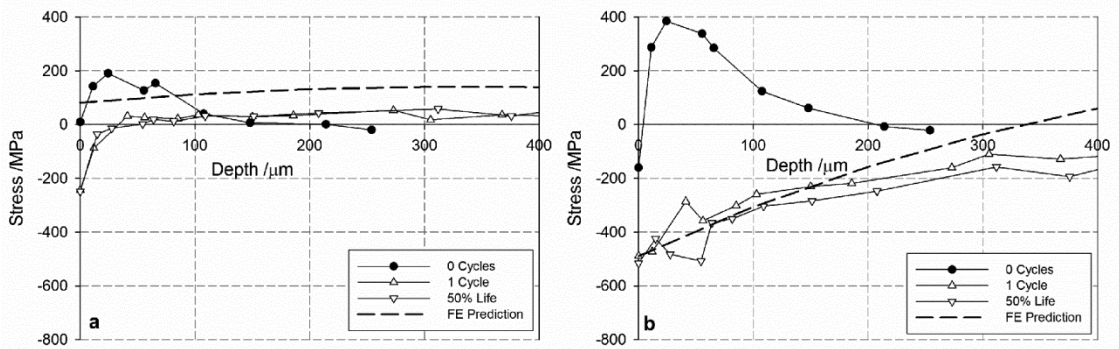

Figure 5- 35: Grinding and post fatigue ($\Delta\varepsilon_{11}$ = 0.0068) residual stresses in 4.5 x 1.25 mm notched samples in (a) the transverse direction and (b) the longitudinal direction.

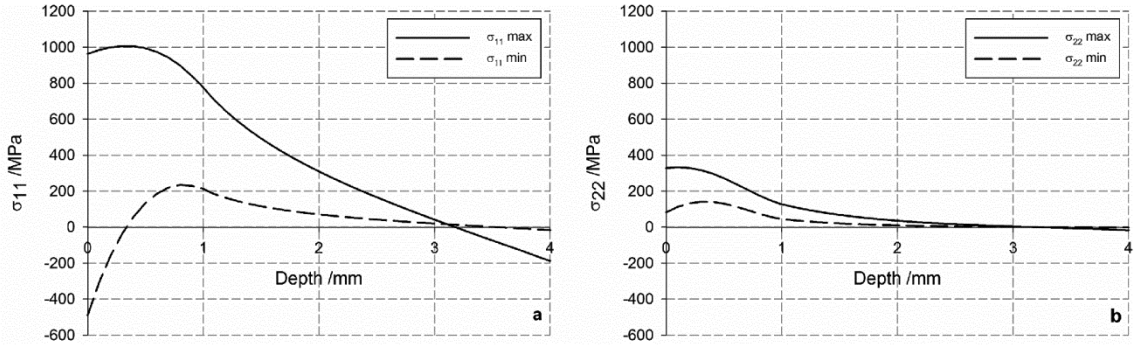

Figure 5- 36: Applied stresses in the (a) longitudinal and (b) transverse directions in notched 4.5 x 1.25 mm sample tested at σ^{e}_{nom} = 1034 MPa under maximum load and after release of load to minimum under R_p = 0.1 loading.

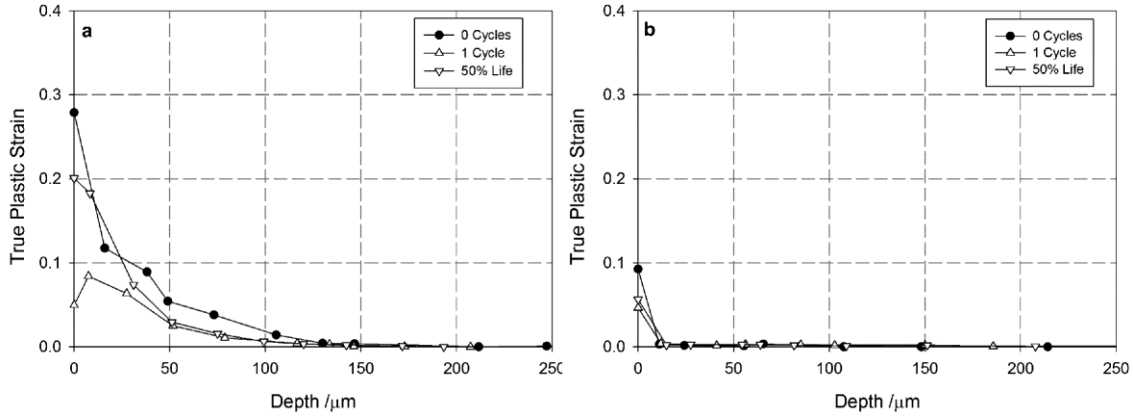

Figure 5- 37: Development in plastic strain profiles with fatigue ($\Delta\varepsilon_{11}$ = 0.0068) in 4.5 x 1.25 mm notched samples after (a) shot peening and (b) grinding.

5.7. References

1. British Standard, *BS ISO 12108:2002: Metallic materials - Fatigue testing - Fatigue crack growth method*, 2002.

2. ASTM, *ASTM E647: Standard test method for measurement of fatigue crack growth rates*, 1995.

3. Zhai, T., Xu, Y.G., Martin, J.W., Wilkinson, A.J. and Briggs, G.A.D., *A self-aligning four-point bend testing rig and sample geometry effect in four-point bend fatigue.* International Journal of Fatigue, 1999. **21**(9): p. 889 - 894.

4. Neuber, H., *Theory of stress concentration for shear-strained prismatical bodies with arbitrary non-linear stress-strain law.* Journal of Applied Mechanics, 1961. **28**(4): p. 544 - 550.

5. Molski, K. and Glinka, G., *A method of elastic-plastic stress and strain calculation at a notch root.* Materials Science and Engineering, 1981. **50**(1): p. 93 - 100.

6. Glinka, G., *Energy density Approach to calculation of inelastic stress-strain near notches and cracks.* Engineering Fracture Mechanics, 1985. **22**(3): p. 485 - 508.

7. Dowling, N.E., Brose, W.R. and Wilson, W.K., *Notched member fatigue life predictions by the local strain approach*, in *Fatigue Under Complex Loading: Analyses and Experiments*, Wetzel, R.M., Editor. 1977. Warrendale, PA: Society of Automotive Engineers: p. 55 – 84.

8. Sharpe Jr., W.N., Yang, C.H. and Tregoning, R.L., *An evaluation of the Neuber and Glinka relations for monotonic loading.* Journal of Applied Mechanics, 1992. **59**(2S): p. 50 - 56.

9. Zeng, Z. and Fatemi, A., *Elasto-plastic stress and strain behaviour at notch roots under monotonic and cyclic loadings.* Journal of Strain Analysis for Engineering Design, 2001. **36**(3): p. 287 - 300.

10. Knop, M., Jones, R., Molent, L. and Wang, C., *On the Glinka and Neuber methods for calculating notch tip strains under cyclic load spectra.* International Journal of Fatigue, 2000. **22**(9): p. 743-755.

11. Ye, D., Matsuoka, S., Suzuki, N. and Maeda, Y., *Further investigation of Neuber's rule and the equivalent strain energy density (ESED) method.* International Journal of Fatigue, 2004. **26**(5): p. 447 - 455.

12. Glinka, G., *Calculation of inelastic notch-tip strain-stress histories under cyclic loading.* Engineering Fracture Mechanics, 1985. **22**(5): p. 839 - 854.

13. Pickard, A.C., S*tress intensity solutions for planar cracks in three-dimensional bodies*, in *The Application of Three-Dimensional Finite Element Methods to Fracture Mechanics and Fatigue Life Prediction.* 1986. London, UK: Chameleon Press Ltd. Engineering Materials Advisory Sservice: p. 81 – 116.

14. Reed, P.A.S., *Effects of warm prestressing on A533B weld metal*. 1990, PhD Thesis: University of Cambridge.

15. Koizumi, T. and Ozazaki, M., *Crack growth and prediction of endurance in thermal-mechanical fatigue of 12Cr-Mo-V-W steel.* Fatigue and Fracture of Engineering Materials and Structures, 1979. **1**(4): p. 509 - 520.

16. Chaswal, V., Sasikala, G., Ray, S.K., Mannan, S.L. and Raj, B., *Fatigue crack growth mechanism in aged 9Cr-1Mo Steel: Threshold and Paris regimes.* Materials Science and Engineering A, 2005. **395**(1-2): p. 251 - 264.

17. Bao, H. and McEvily, A.J., *On plane stress-plane strain interactions in fatigue crack growth.* International Journal of Fatigue, 1998. **20**(6): p. 441 - 448.

18. Chang, H.J., Tsai, C.H. and Kai, J.J., *Effects of temperature on the cyclic deformation behaviour and microstructural changes of a 12Cr-1MoVW martensitic stainless steel.* International Journal of Pressure Vessels and Piping, 1994. **59**(1-3): p. 31 - 40.

19. Choudhary, B.K., Bhanu Sankara Rao, K. and Mannan, S.L., *High temperature low cycle fatigue properties of a thick-section 9wt.%Cr-1wt.%Mo ferritic steel forging.* Materials Science and Engineering A, 1991. **148**(2): p. 267 - 278.

20. Reed, P.A.S., Tucker, P.H. and Joyce, M.R., *Effects of mixed mode loading on fatigue and creep-fatigue in SRR-99 single crystals.* Materials Science and Engineering A, 2005. **394**(1-2): p. 256 - 265.

21. Mulvihill, P. and Smith, P., 1995. Power Technology report PT/95/KA603/R.

22. Wignall, C.M., 2007. Power Technology report PT/06/BB1920/R.

23. Wignall, C.M, 2007. E.ON Engineering report PT/07/LH983/R.

24. Guagliano, M. and Vergani, L., *An approach for prediction of fatigue strength of shot peened components.* Engineering Fracture Mechanics, 2004. **71**(4-6): p. 501- 512.

25. Li, J.K., Mei, Y. and Duo, W., *An analysis of stress concentrations caused by shot peening and its application in predicting fatigue strength.* Fatigue and Fracture of Engineering Materials and Structures, 1992.**15**(12): p. 1271 – 1279.

26. Koster, W.B., *Effect of residual stress on fatigue of structural alloys*, in *Proceedings of the 3rd International Conference on Practical Application of Residual Stress Technology*, Rudd, C., Editor. 1991. Indianapolis, IN: ASM: p. 1-9.

27. Dalaei, K., Karlsson, B. and Svensson, L.-E. *Stability of shot peening induced residual stresses and their influence on fatigue lifetime.* Materials Science and Engineering A, 2011. **528**(3): p. 1008 - 1015.

28. Kim, S.-B., Shackleton, J., Preuss, M., Withers, P.J., Evans, A. and Bruno, G., *Stress relaxation of shot-peened UDIMET 720Li under solely elevated-*

temperature exposure and under isothermal fatigue. Metallurgical and Materials Transactions A, 2005. **36**(11): p. 3041 - 3053.

29. Taylor, D. and Clancy, O.M., The f*atigue performane of machined surfaces.* Fatigue and Fracture of Engineering Materials and Structures, 1991. **14**(2-3): p. 329 - 336.

30. Benedetti, M., Bortolamedi, T., Fontanari, V. amd Frendo, F., *Bending fatigue behaviour of differently shot peened Al6082 T5 alloy.* International Journal of Fatigue, 2004. **26**(8): p. 889 - 897.

31. Holzapfel, H., Schulze, V., Vöhringer, O. and Macherauch, E., *Residual stress relaxation in an AISI 4140 steel due to quasistatic and cyclic loading at higher temperatures.* Materials Science and Engineering A, 1998. **248**(1-2): p. 9 - 18.

32. Balart, M.J., Bouzina, A., Edwards, L. and Fitzpatrick, M.E., *The onset of tensile residual stresses in grinding of hardened steels.* Materials Science and Engineering A, 2004. **367**(1-2): p. 132 - 142.

33. Bathias, C., Bonnafe, J.P., Lebrun, J.L. and Maeder, G., *X-ray diffraction and acousitc emission study of fatigue damage in aluminium alloys*, in *STP 1004, Analytical and Experimental Methods for Residual Stress Effects in Fatigue,* Champoux, R.L., Underwood, J.H., and Kapp, J.A., Editors. 1988. Warrendale, PA: ASTM: p. 25 - 36.

34. Quesnel, D.J., Meshii, M. and Cohen, J.B., *Residual stresses in high strength low alloy steel during low cycle fatigue.* Materials Science and Engineering, 1978. **36**(2): p. 207 - 215.

5.8. Appendices

5.8.1. Appendix A: Consideration of stress and strain development in fatigue samples modelled using the combined hardening law

When the combined isotropic and kinematic hardening material model is implemented in the three point bend notched (4.5 x 1.25 mm) fatigue samples, it is clear from Figure 5- 6 that a range of local stress and strain peaks and ranges are identified in the first 1000 cycles. This is a result of the cyclic softening occurring in the material. Since this is dependent on the accumulation of equivalent plastic strain, $\bar{\epsilon}^{pl}$, softening progresses at different rates through the sample thickness. Despite the relative insignificance of this behaviour in terms of strain range at the notch root (where the hot-spot strain range analysis throughout this chapter was focussed), in this Appendix, the softening behaviour is captured in more detail than was described in Section 5.3.1. This analysis is required because the development of softening in a notched sample loaded in bend is complicated by the high stress gradient near the surface and may have implications on stress and strain parameters should other approaches, such as the critical line method, be required in the future.

Since behaviour under bend load is dominated by behaviour along the tensile axis, occurrence of plasticity in the hysteresis loops are most clearly illustrated using σ_{11} and ε_{11}. However, it is important to note that the actual $\sigma - \varepsilon$ relationship and the occurrence of reverse plasticity is dependent on the equivalent von Mises stress and equivalent strain, parameters which was also extracted from the FE analysis but which are not shown in the present description due to the additional complication of no apparent negative stress and thus the inability to easily visualise reverse plasticity.

The hysteresis loops at the notch surface and the point of maximum σ_{11} are shown in Figure 5-A- 1 and Figure 5-A- 2 respectively. It is noted that due to different constraints (and hence triaxial stress fields) at the different points in the sample, the development of σ_{11} with ε_{11} does not appear equivalent when the two figures are compared. The development of equivalent von Mises stress and strain in the first tensile half cycle at the two locations is thus shown in Figure 5-A- 3 as reassurance of the equivalent material behaviour on the first cycle in the two locations.

At the notch surface there is clear forward and reverse plasticity in all cycles. This is further illustrated by the development of $\bar{\epsilon}^{pl}$ with cycle number in Figure 5-A- 4 which increases rapidly over the first 50 cycles and then increases at a more constant rate. In Figure 5-A- 1a, the σ_{11} vs. ε_{11} relationship up to 20 cycles is shown; there is evidence of ratchetting in the forward direction due to greater plasticity in the tensile direction than in the compressive direction. There is also evidence of mean stress relaxation. In

Figure 5-A- 1b, the σ_{11} vs. ε_{11} relationship beyond 20 cycles is shown. At this point, there is greater plasticity in the compressive direction than in the tensile direction, and the ratchet strain reverses. There is a concomitant slight increase in mean stress to around 200 MPa, where it appears to stabilise after around 200 cycles.

This behaviour can be compared with the behaviour at the point of maximum σ_{11}. It is clear from Figure 5-A- 2a and Figure 5-A- 3 that despite the higher σ_{11} at this location, the σ_{eq} and $\Delta\varepsilon_{11}$ are, as expected, lower than at the notch surface. Consequently, $\bar{\epsilon}^{pl}$ does not increase as rapidly as at the surface, as evidenced in Figure 5-A- 4 and as a result the material softens far less significantly at this location. There is also far less significant ratchetting illustrated in the first 20 cycles during which time there is only plasticity in the tensile direction. This plasticity shakes down and there is no increase in $\bar{\epsilon}^{pl}$ in the mid-range cycles with a slight reduction in mean stress being shown in this cycle range. After 500 cycles, the reduction in mean stress is sufficient for reverse plasticity in the compressive direction to begin and there is ratchetting in the compressive direction between cycles 500 and 1000 shown in Figure 5-A- 2b.

Additional analysis was also carried out at the surface of the PBB to assess the development of σ_{11} vs. ε_{11} (Figure 5-A- 5) in this simpler geometry where the location of maximum σ_{11} coincides with that of the maximum σ_{eq}. The development trend in hysteresis loops over the first 20 cycles shown in Figure 5-A- 5a closely resembles that at the notch surface shown in Figure 5-A- 1a. It is noted however that the magnitude of σ_{11} is lower and the magnitude of ε_{11} is higher in each cycle. This is because behaviour in the PBB is even more dominated by the '11' direction than in the notched sample. This domination is evidenced by the ratios presented in Table 5-A- 1 in terms of stress and strain ranges as calculated using the baseline isotropic material model based on tensile data in the direction perpendicular to rolling under the same loading conditions.

There is evidence of plasticity in both directions throughout life and of the mean stress reducing throughout life. As a result of the reductions in mean stress there is a reversal in ratchetting after 20 cycles (as for the notched sample) when the plasticity in compression is greater than that in tension. Unlike the notched sample there is no apparent stabilisation in the mean stress of the PBB; this is thought to be a result of the different constraint and development of softening throughout the two different geometries. Figure 5-A- 4 shows that the $\bar{\epsilon}^{pl}$ increases rapidly over the first 200 cycles before a reduction in the rate of increase compared to the notched sample after 500 cycles; this is reflected by the greater change in ε_{11} between cycle 500 and cycle 1000 in the notched sample compared to the PBB sample.

This different behaviour at the different locations in the notch and in the PBB is caused by the different rates of accumulation of $\bar{\epsilon}^{pl}$ at different locations combined with different triaxial stress states. Although not significant in the hot spot approach in the present work, the resulting changes in mean stress and implications on other stress analysis approaches such as when applying critical line methods must not be overlooked, and may be of increased importance when also considering materials properties gradients and residual stresses resulting from shot peening in future analyses.

	$\frac{\Delta\sigma_{eq}}{\Delta\sigma_{11}}$	$\frac{\Delta\varepsilon_{eq}}{\Delta\varepsilon_{11}}$
Notched	0.93	0.98
PBB	0.99	0.99

Table 5-A- 1: Dominance of the '11' direction in terms of stress and strain ranges in the notched and PBB geometries with fatigue cycling at σ^{e}_{nom} = 1034 MPa.

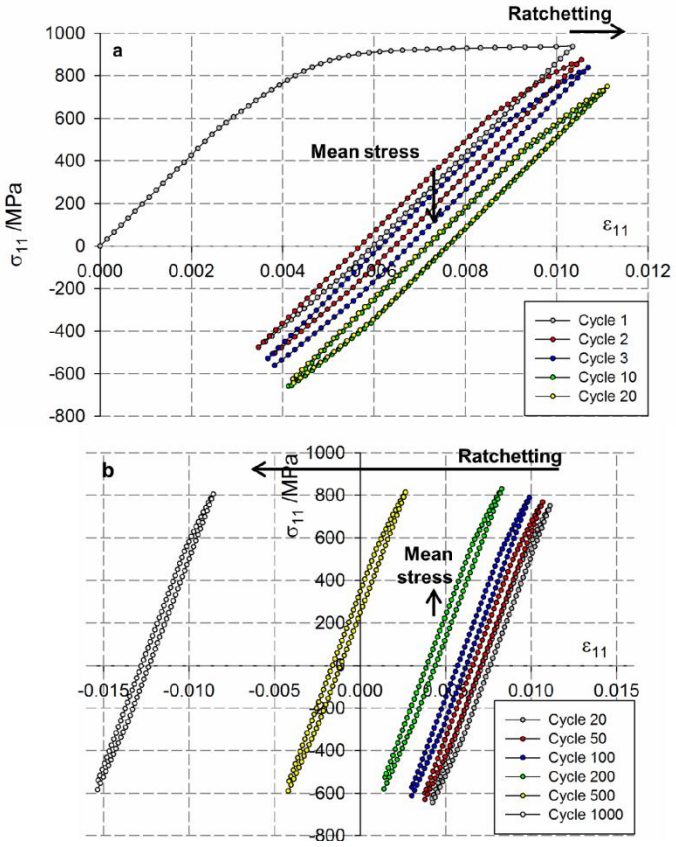

Figure 5-A- 1: Development of σ_{11} and ε_{11} at the notch (4.5 x 1.25 mm) surface with fatigue cycling at σ^{e}_{nom} = 1034 MPa on the first tensile half cycle.

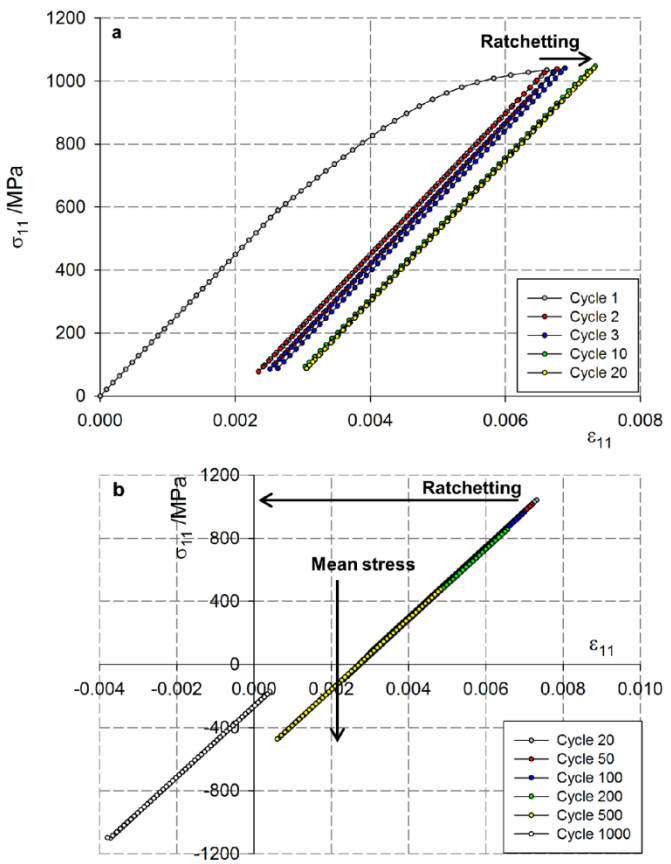

Figure 5-A- 2: Development of σ_{11} and ε_{11} at a depth beneath the notch (4.5 x 1.25 mm) of 0.4 mm (corresponding to the location of maximum σ_{11}) with fatigue cycling at σ^{e}_{nom} = 1034 MPa on the first tensile half cycle.

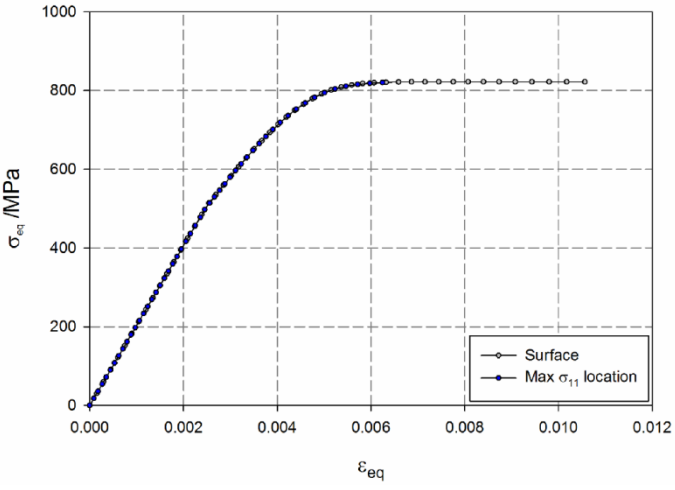

Figure 5-A- 3: Development of σ_{eq} and ε_{eq} at the notch surface and the location of maximum σ_{11} in the 4.5 x 1.25 mm notched samples in the first tensile half cycle to σ^{e}_{nom} = 1034 MPa.

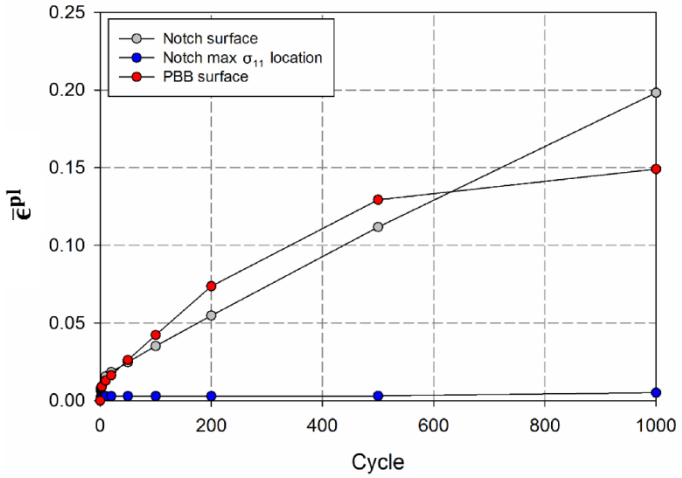

Figure 5-A- 4: Accumulation of $\bar{\epsilon}^{pl}$ with fatigue cycling at σ^{e}_{nom} = 1034 MPa on the first tensile half cycle at the notch surface and the location of maximum σ_{11} in the 4.5 x 1.25 mm notched samples and in the PBB.

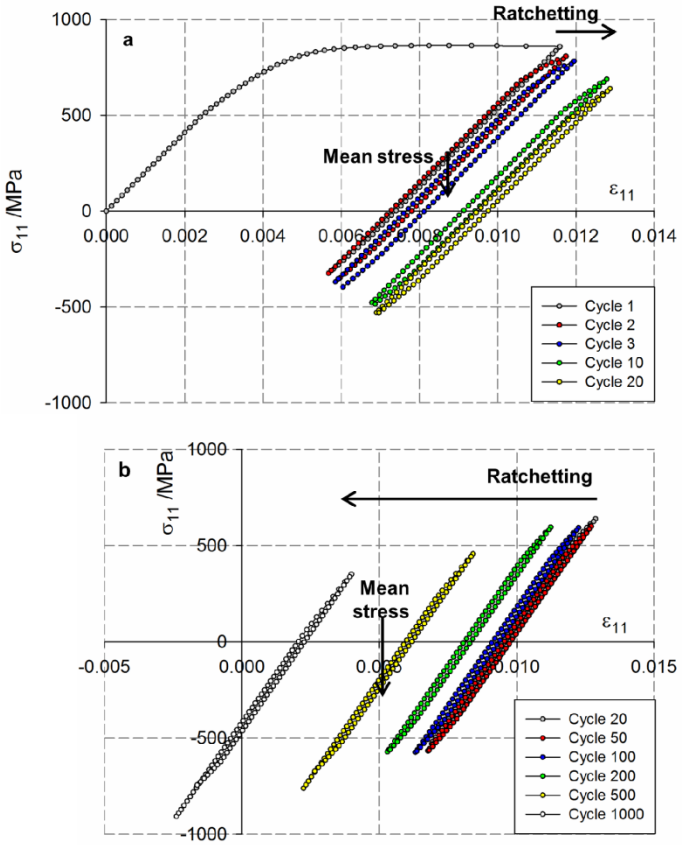

Figure 5-A- 5: Development of σ_{11} and ε_{11} at the PBB surface with fatigue cycling at σ^{e}_{nom} = 1034 MPa on the first tensile half cycle.

5.8.2. Appendix B: Noise reduction in SENB V/V_0 vs. N data

It was mentioned in Section 5.4.1 that during growout under constant load in the SENB samples there was too much noise in the V/V_0 vs. N data to apply the secant method directly to the data and that several approaches to reducing this noise were compared. The three noise reduction methods were:

i. Five overlapping polynomial fits were applied to the V/V_0 vs. N data.
ii. The Loess smoothing function was applied to the V/V_0 vs. N data; using a sampling proportion of 0.1 and a 2nd degree polynomial.
iii. 'Engauge' Digitizer software was used to extract data points from the V/V_0 vs. N curve 'by eye'.

The resulting da/dN vs ΔK data from each method is presented along with the data resulting from the secant method applied directly to the raw data at when $\Delta K > 25$ MPam$^{0.5}$ in Figure 5-B- 1:

Both the polynomial fit and the smoothed data show similar trends at low $\Delta K < 25$ MPam$^{0.5}$. However, there are several inherent problems with the overlapping polynomial fits; it can be seen that there are outlier points and step changes in the data (e.g. at $\Delta K \sim 30$ MPam$^{0.5}$). Whilst the outlier points could be removed from the dataset, the step change is much more difficult to overcome satisfactorily. Furthermore, the trend shown by the final polynomial fit at high $\Delta K > 40$ MPam$^{0.5}$ does not match the raw data well. The smoothed data begins to deviate from the raw data at around $\Delta K = 30$ MPam$^{0.5}$. This is a result of there being more significant increases in V/V_0 per cycle and thus a lower density of data points; hence the smoothing algorithm not performing as well in this regime.

The digitized data shows similar results to both the polynomial and smoothed data at low ΔK and continues to represent the raw data well to higher $\Delta K = 45$ MPam$^{0.5}$ than either of the other two methods. Additionally, there is some scatter shown at low $\Delta K <$ 20 MPam$^{0.5}$. For this reason the grow-out SENB data shown in Figure 5- 13 is a combination of the secant method applied to digitized data for the $14 < \Delta K < 25$ MPam$^{0.5}$ regime and the secant method applied directly to the raw data when $\Delta K > 25$ MPam$^{0.5}$ since this approach results in some representative scatter at all ΔK apart from $20 < \Delta K < 25$ MPam$^{0.5}$ and the best representation of the data at the highest ΔK.

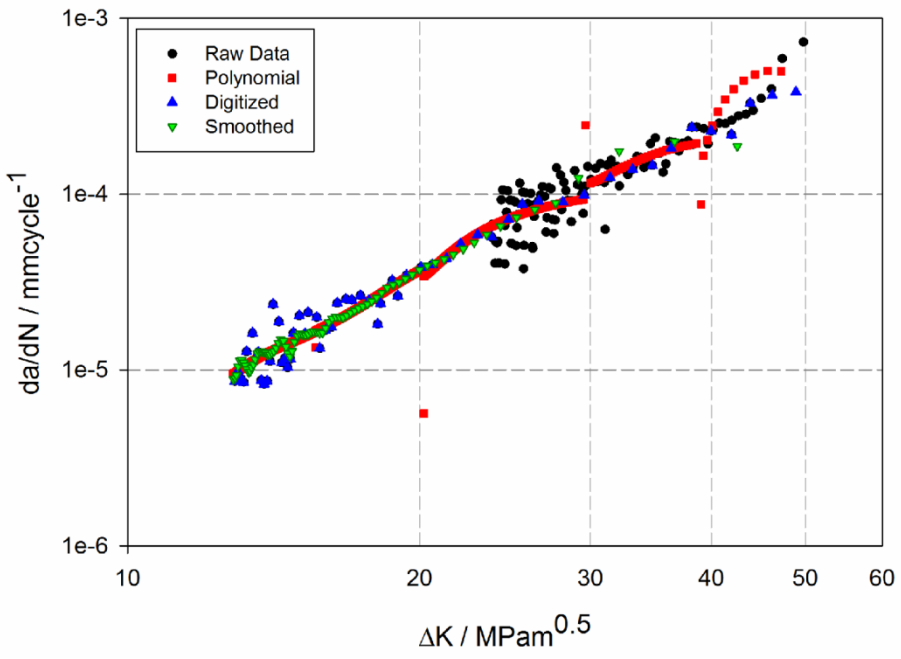

Figure 5-B- 1: Growout long crack propagation data for FV448 comparing the polynomial, digitizing and smoothing noise reduction methods with raw data at high ΔK.

Chapter 6

Conclusions

Shot peening is a well-known manufacturing process often applied to cyclically loaded components in regions of stress concentration to reduce their propensity to fatigue crack initiation and propagation. The life assessment procedures currently in use for shot peened components do not explicitly account for the benefits derived from shot peening, which are instead considered as additional conservatism in the models. However, the current drive towards reducing conservatism in remnant fatigue life estimates and optimising component repair and replacement scheduling to avoid unenforced outages has resulted in the need for an improved understanding of the margins to failure in shot peened components. Reducing the conservatism in current models could also allow for extended component life and reduced operating costs without compromising safety margins. Consideration of shot peening in the life assessment process requires inclusion of the effects of shot peening (surface roughness, strain hardening and compressive residual stresses) as well as the material response to cyclic load and any associated interactions.

Before surface roughness, strain hardening or residual stress effects can be considered in fatigue life estimates, the methods by which they are predicted or measured must be standardised. The approaches adopted must be not only accurate and repeatable but also applicable to a wide range of materials. The literature review confirmed that methods for measuring residual stresses are already well standardised and X-ray diffraction (XRD) was thus adopted for the measurement of compressive residual stresses after shot peening in the present investigation.

However, the measurement techniques for characterising surface roughness and near surface strain hardening resulting from shot peening required further investigation. Both tactile and optical measurement techniques were found to be sufficient to characterise the dimpled surface profile; however, despite the recent advances towards three dimensional characterisation of surface topography, it was found that the majority of surface roughness measurements are still presented in terms of line profile analysis rather than areal analysis. Comparison of two dimensional and three dimensional analyses showed that whilst the average surface profiles measured did not change significantly between the two approaches, a three dimensional analysis is more likely to capture the worst case peak to valley measurement than a two dimensional analysis. This may be significant when using surface topological measurements to estimate the elastic stress concentration factor resulting from shot peening. Thus a

three dimensional areal analysis is recommended as the optimum measurement technique to ensure that the most significant features in the area of interest are assessed and included in the remnant fatigue life estimate.

Strain hardening near the shot peened surface is the result of changes in the dislocation distribution in this region. Three methods for measuring these changes were compared: microhardness traverses, XRD line broadening as characterised by the profile full width at half maximum (FWHM) and electron backscatter diffraction (EBSD) local misorientation measurements. In conjunction with a series of calibration samples, the yield strength profile resulting from shot peening can thus be determined. In the present investigation, the profiles determined using XRD and EBSD were the most consistent whereas the use of microhardness traverses appeared to overestimate the extent of the strain hardened region. Hence either XRD or EBSD techniques could be applied in determining the variation in material properties with distance from the shot peened surface for inclusion in remnant fatigue life estimates. Other factors determine which technique is the most appropriate, as discussed below:

Where residual stress measurements are also required, XRD depth profile data are already likely to be available and thus re-analysis of the $\psi = 0^{\circ}$ data is sufficient to obtain a yield strength profile. Since the calibration R^2 value is higher than the corresponding EBSD value, analysis of the resulting discrete data points is sufficient to obtain a reliable estimate of the materials property gradient. Where residual stress analysis is not required, for example during a peening process optimisation procedure, EBSD local misorientation data may be used. Despite the lower R^2 value than XRD measurements, there are sufficient measurement points for the data to be well averaged and the materials property gradient may also be reliably estimated.

It was shown that increasing peening process intensity tended to increase both the indent diameter and the surface roughness, although at higher intensities, these effects did tend to saturate. A similar effect is also present in strain hardening data, however, rather than saturating the profile, increasing the intensity of the process may in fact reduce the magnitude of the surface plastic strain. Furthermore, increasing the intensity may not increase the depth of the plastic strain profile, but may result in the higher plastic strains being retained deeper in the profile. Additionally, the resulting plastic strain profile in a given target material was shown to be not just dependent on intensity but also on the specific combination of shot size and velocity.

Since the residual stresses resulting from shot peening are dependent on the plastic strain profile, it is likely that the residual stress profile will also be dependent on the specific combination of shot size and velocity for a given target material. It was shown using XRD that shot peening was sufficient to convert grinding tensile residual stresses

to compressive stresses of the form expected from shot peening which extended to around twice the depth of the strain hardening profile. However, the experimental analysis of the residual stress profile resulting from each peening process would be both time and resource consuming; thus various analytical and finite element (FE) procedures for estimating shot peening residual stresses were compared:

It was found that the best model for predicting the residual stresses was a simple physical model employing a bilinear material model based on monotonic tensile test data and a correction factor allowing for plasticity. This model was shown to be capable of predicting the industrial peening process residual stress profile to within 20 % of the experimentally measured profile. The main drawback of this approach is that the plasticity correction factor requires measurement of the dimple size resulting from the specific peening process applied to the specific target material. Hence the Metal Improvement Company in-house software Peenstress® and FE methods, both of which can be implemented with no experimental data regarding the peening process applied to the specific target material, were also used to predict the residual stress profile based on monotonic tensile data. The residual stress magnitudes predicted using these methods were quite similar, however they did not closely represent the experimental data. This is thought to be a result of the assumptions made about the material model: Cyclic behaviour and strain rate dependence would be expected to be significant features in these approaches, whereas the application of the plasticity correction factor in the simple physical model overcomes these material constitutive law modelling issues.

Application of the physical model and indent diameter measurements made using optical microscopy directly on a 200 % coverage surface showed that the maximum residual stress did not change with increasing intensity but that profile depth did increase. The difference between the two 13A processes investigated in this work was predicted to be relatively insignificant, which is in contrast to the experimental strain hardening results. Furthermore, comparisons of the experimental plastic strain profiles with the predicted residual stress profiles indicate that the measured strain hardening profiles cannot be used to directly scale the residual stress profile or vice versa. Hence the inclusion of strain hardening and residual stress in the component FE models used for fatigue life assessment requires both effects to be determined independently. This requirement was confirmed using S-N data for notched samples peened using different processes.

However, it is not just the post-shot peen start of life surface roughness, strain hardening and residual stresses that must be accounted for in remnant fatigue life estimates. It is also essential to consider their interaction with the applied cyclic stress fields and specific material behaviour under cyclic load since both residual stress and

strain hardening profiles can be relaxed by applied low cycle fatigue (LCF) stress distributions. It was found that component shape (the presence of a notch) did not affect the efficacy of the shot peening process as measured by the induced surface roughness, residual stress or plastic strain profiles. Indeed, in terms of total fatigue life, it was found that shot peening notched samples was beneficial even when operating at high LCF strain ranges (S-N data was represented in the present work based on a hot-spot approach) where shot peening was no longer beneficial to un-notched samples. This is a result of the applied through thickness bending stress distribution (which results in the same sample surface strain range) being different in un-notched samples compared to notched samples where the high stresses are more concentrated near the surface. This results in both intrinsic lifetime effects from increased sample volume effects in un-notched plain bend bar (PBB) samples and changes in the residual stress relaxation behaviour between the two sample geometries:

Residual stress relaxation is known to be significant in LCF where un-notched samples are loaded axially. However, this loading configuration is not as representative of service loading conditions as the notched three point bend load configuration investigated in the present work. In this configuration, near surface compressive residual stresses were retained in the direction of loading and only relatively small quasi-static relaxation in the orthogonal direction to approximately 80 % of the original value was observed. This retention of residual stress is a direct result of the high stress gradient in this loading configuration near the notch: The material near the surface is yielded in tension whereas the material beneath is not and upon release of the load, the elastically deformed material places the near-surface plastically deformed material into compression. Since the applied stress distribution in un-notched samples loaded in three point bend (PBBs) sits somewhat in-between that of the un-notched axially loaded samples and that of the notched samples in three point bend, more significant relaxation would be expected in the PBB configuration than was measured in the notched bend configuration. This results in the observed lack of benefit to fatigue life resulting from shot peening un-notched PBB samples.

Furthermore, there was only a slight reduction in the near surface plastic strain after one load cycle and no further appreciable changes through life in this shot peened system; this correlated well with the lack of continual through life changes in the residual stress distribution. This behaviour is strongly dependent on the cyclic stress-strain response of the tempered martensitic steel under investigation: At the strain range of interest, the material softened rapidly in the first few cycles as a result of the rearrangement of dislocations and then more slowly through life with a total reduction in yield strength in the combined isotropic and kinematic hardening material model (as

a percentage of the 0.2 % yield strength) of just 8.3 %. A sensitivity study showed that accounting for this cyclic softening as either a cyclically stabilised or combined isotropic and kinematic hardening material model did not result in a significant change in the hot spot strain range calculated at the sample surface. However, this is not to say that this is the case for all materials and the sensitivity of the stress distribution in a component of a given material to that material's cyclic stress-strain response must be considered before the material model for application in the FE model is finalised. This decision may be even more significant once shot peening residual stresses and strain hardening are incorporated in the model which is then required to also predict changes in the residual stress profile. It was shown using ground sample through life residual stress data and FE analysis of notched samples with no initial residual stresses or strain hardening that the residual stresses after fatigue cycling can be predicted using FE approaches. The prediction of changes to the shot peening residual stresses is thought to be essential to the success of the proposed life assessment approach:

Damage tolerant analysis dominates industrial component lifing practice for components operating in the LCF regime. This requires the input of crack propagation rate as a function of stress intensity factor range (typically using the Paris Law which has been determined in this investigation for the tempered martensitic steel in question) and the stress intensity factors resulting from loading a given component containing a defect. Most commonly, these stress intensity factors are calculated using the stress distributions in the uncracked component and appropriate weight functions, although FE based fracture mechanics analyses of cracked components may be required in the most complex cases.

The premise of the method under development is that these stress distributions or fracture mechanics parameters are calculated allowing for the changes induced by the shot peening strain hardening and residual stress profiles. Furthermore, providing the correct material model is implemented, the model is capable of predicting changes in near surface residual stress distribution under fatigue loading and, in materials where softening is significant, changes in the yield stress distribution near the surface. The most accurate representation would implement the combined hardening model and a complete representation of the service loading history experienced by the component. This would, however, be very computationally intensive and a first order approximation may be obtained by assuming cyclically stabilised materials properties in the component. Cyclic stabilisation appears to result in a reduction in the Ramberg Osgood parameter A of approximately 10.6 % and thus a reasonable prediction of the stabilised strain hardening profile might be obtained by a reduction of the initial yield strength profile by this ratio. The cyclically stabilised material model could then be applied in determining the expected redistribution of residual stresses; the most

accurate representation of the redistribution would be obtained in the case where the defect was included in the FE model.

In summary, a modelling approach has been developed which allows for the effect of shot peening to be explicitly accounted for in the damage tolerant life assessment process. The approach requires the input of experimentally determined residual stress, surface roughness and strain hardening profiles; the optimum means of determining both the surface roughness characteristics and the strain hardening profile has been established as a first step towards standardising these measurements. The retained benefit of the shot peening process in terms of total life even under very high strain range LCF conditions has been clarified in terms of the applied stress distribution, specific material cyclic characteristics and residual stress relaxation. This allows the shot peening process to be specified for notched components under high strain range cyclic bend load, such as low pressure turbine disc blade interfaces with an improved understanding of the resulting benefits.

Chapter 7

Current and future directions

7.1. Introduction

This chapter aims to introduce the work which is both on-going and planned in pursuit of a validated life assessment process accounting for the effects of shot peening. This work is being carried out as part of the continued collaboration between E.ON New Build and Technology and the Engineering Materials Research Group at the University of Southampton and involves several academics and researchers.

Significant progress has been made towards incorporating the effects of shot peening in the component life assessment process proposed in Figure 2-23. All the data required to generate the finite element (FE) model of the low pressure (LP) turbine blade-disc interface have been established: Constitutive models were developed in Chapter 3 and measured residual stress and strain hardening profiles were shown in Chapter 4. Furthermore, long crack growth rate data was presented in Chapter 5; this will allow the calculation of component remnant life following industrial standard processes (R5 [1], R6 [2] or BS7910 [3]). Data were also presented in Chapter 5 showing the changes in the residual stress and strain hardening profile resulting from the application of low cycle fatigue (LCF); this will be required to validate the prediction of residual stresses after fatigue in the model. Total life data were also presented in Chapter 5 and can be used as a first order validation dataset for the damage tolerant approach proposed on the assumption that a fatigue crack is initiated immediately in LCF The damage tolerant lifing process is under development and the progress that has been made in incorporating the residual stresses and strain hardening in FE models and in component modelling at an appropriate length scale is discussed in Section 7.2. This work is currently in progress as a collaboration between Dr. Mithila Achintha at the University of Southampton (who has significant experience in the use of the eigenstrain approach [4]) and myself (I will be working at E.ON New Build and Technology for the next 12 months as part of a Royal Commission for the Exhibition of 1851 Industrial Fellowship which was awarded in 2010 and as such will have the opportunity to remain involved in this project).

However, the assumption of immediate initiation in LCF may not necessarily be appropriate in shot peened materials and further work is under way to establish the number of cycles to, and micromechanisms of, crack initiation in this shot peened

system. Furthermore, the continuum approach described in this work is based on the assumption that it is the change in local stress and strain distributions in the components that affect the fatigue life, and that these changes can be appropriately considered using long crack growth rate data and linear elastic fracture mechanics (LEFM) approaches to component lifing. However, since the microstructural changes and the residual stresses are all present in the near surface region, where fatigue cracks tend to initiate, it is likely that the growth of short cracks is also affected by the peening process. These effects are currently under further investigation by Binyan He at the University of Southampton as part of her PhD work and will contribute to understanding the assumptions made in the lifing approach described here and the implications that these assumptions have on the margins in the resulting remnant life assessment. A brief discussion of this work is made in Section 7.3 and is largely based on the following paper which reported the initial findings of this investigation:

B. He, K. A. Soady, B. G. Mellor, A. Morris, P. A. S. Reed, *The effects of shot peening on short crack growth rate and resulting low cycle fatigue behaviour in a low pressure turbine blade material.* Materials Science and Technology, 2013. **29**(7): p. 788 – 796.

Finally, Section 7.4 contains the recommendations to operators which result from this work. This includes details on the selection of components whose fatigue behaviour could be improved by shot peening, the manner in which the shot peening process can be validated and the associated implications on supplier selection and quality assurance procedures, and consideration of other exemplar components to which the lessons learned from the present work may be applied.

7.2. Incorporating residual stresses and strain hardening in damage tolerant analyses

7.2.1. Objective

It has become apparent from the work presented in the main body of this thesis that any life assessment procedure which includes the effects of shot peening must be able to take into account both the resulting compressive residual stresses and strain hardening profile. Current work is focussed on incorporating these profiles in FE models with a view to considering the effects on the resulting local stress and strain distributions in the component.

In the literature review (Chapter 2, Section 2.2.3.2), two means of taking residual stresses into account were introduced: by directly specifying the residual stress profile or using the eigenstrain approach. Specifying the residual stresses directly as initial

conditions would require knowledge of all the components of stress through the thickness of the component; since these data are not available in the present study, the eigenstrain approach has been selected as the most appropriate. The eigenstrain mechanism characterises the 'misfit' strain between the plastically deformed region and the surrounding elastic bulk that results from the shot peening process. Hence in FE models, by specifying the misfit strain at the shot peened surface as a thermal strain such that the measured surface residual stresses are correctly represented, the complete residual stress field through the component can be incorporated. Once the eigenstrain is determined for a relatively simple geometry, the residual stress field in a more complex geometry can be calculated based on appropriate static FE models. This is a key advantage of the approach and also allows for modelling subsequent loading. The work to date on determining the eigenstrain profile is described further in Section 7.2.2.1. Furthermore, the effect of strain hardening must not be overlooked; consideration of these effects can be made by varying the material properties with distance from the shot peened surface as described in Section 7.2.2.2.

7.2.2. Incorporating residual stresses and strain hardening in FE models

7.2.2.1. Inverse eigenstrain approach for modelling residual stresses

The inverse eigenstrain analysis [4-6] was used[1] to determine the eigenstrain profile required to generate the experimentally measured residual stresses in FE models. The method was developed in shot peened (T0) plain bend bar (PBB) samples due to the additional complication of the circular geometry in the notched samples.

The basic premise of the method is that the unknown eigenstrain profile can be determined from the measured residual (elastic) stress profile (Figure 4-16). An initial eigenstrain distribution was assumed on the basis of the depth of the plastic strain profile (Figure 4-20a) and incorporated in a FE model (employing the isotropic hardening material model corresponding to the monotonic tensile data perpendicular to the rolling direction) of the PBB as a thermal strain. A quarter model of the PBB was used in conjunction with symmetry conditions; the element edge length in the surface region (to a depth of 0.8 mm) where the eigenstrains were imposed was ~5 μm. This thermal strain was modelled by varying the material's coefficient of thermal expansion (CTE) with distance from the peened surface and applying a uniform temperature field;

[1] The inverse eigenstrain analysis was performed by Dr. Mithila Achintha (Mithila.Achintha@soton.ac.uk) and is included here to show how the data obtained in Chapters 4 and 5 can be applied in the FE approaches commonly implemented in life assessments.

it was assumed that the eigenstrain was uniform in the in-plane directions and only varied with depth from the shot peened surface. After the static equilibration step in the FE model, the variation in in-plane residual stresses resulting from the imposed eigenstrain distribution was extracted; this approach ensured global stress equilibrium, strain compatibility and boundary condition criteria were satisfied. A least squares regression analysis was used to optimise the eigenstrain profile such that the difference between the experimentally measured residual stresses (which are known to a depth of 420 μm) and the elastic residual stresses from the FE model were minimised. Once optimised, the eigenstrain approach resulted in the inclusion of the full residual stress field across the component, the surface region of which was consistent with the measured surface in-plane residual stresses. The optimised eigenstrain profile is shown in Figure 7- 1 and the resulting contour plot of stress in the longitudinal direction (σ_{11}) is shown in Figure 7- 2a, the corresponding residual stress distributions in both the longitudinal and transverse (σ_{22}) directions are shown in Figure 7- 2b. It is clear that there is a compressive residual stress near the surface which becomes tensile in the sample bulk. The near-surface in-plane residual stresses are compared with the experimental results in Figure 7- 3. There is a slight difference in residual stress magnitudes with direction caused by the geometry of the sample; in notched samples, this directionality may be expected to be even more significant and further investigation in the notched sample is required. This result could go some way to explaining the more compressive residual stresses reported in the longitudinal direction of the notched sample shown in Figure 4-16.

Hence the inverse eigenstrain approach can model the residual stresses resulting from shot peening process T0 applied to a PBB. Current work is focussed on developing the method to allow for the more complex notch geometry and to scale the eigenstrain distribution optimised for the T0 process to predict the residual stresses resulting from the other shot peening processes applied in this investigation without the need for time consuming and expensive X-ray diffraction (XRD) analysis for each process. This scaling procedure is detailed further in Section 7.2.2.2. Future work will also focus on modelling the fatigue response in PBB and notched samples, this planned work is detailed further in Section 7.2.3.

7.2.2.2. Scaling the eigenstrain profile for other shot peening processes

XRD residual stress data are only available in the T0 condition, however cumulative plastic strain data from the full coverage peening process (from electron backscatter diffraction (EBSD) measurements shown in Figure 4-21) and analytical elastic-plastic strain data for one indent (from which plastic strain can be derived based on the material model; an example for the T0 process is shown in Figure 4-22) are available

for each peening process. By determining (for the T0 process) the ratio of these peak plastic strains to the peak eigenstrain, the ratio of the depths of the plastic strains to the depth of the eigenstrain and the point at which the relatively flat eigenstrain profile near the surface starts to reduce towards zero as a function of the overall eigenstrain depth, approximate eigenstrain profiles can be determined for each of the other peening processes.

The first step was to compare the T0 plastic strain profiles resulting from the EBSD measurement of cumulative plastic strain and the analytical determination of plastic strain after one impact with the previously derived eigenstrain profile (Section 7.2.2.1) in terms of the peak plastic strain and the depth of the plastic strain profile. This is shown graphically in Figure 7- 4 and in tabular form in Table 7- 1. Based on the ratios of peak plastic strain and plastic strain profile depth, the peak eigenstrain and depth of the eigenstrain profile resulting from the other peening processes could be determined as detailed in Table 7- 2.

The predicted peak eigenstrains resulting from scaling both the analytical plastic strain distribution and the EBSD cumulative plastic strain distribution are relatively consistent. However, in terms of eigenstrain depth, there is a significant variation between the two predictions. Since the EBSD measurements are subjected to error caused by experimental scatter as plastic strain approaches zero, and this error is critical when determining the profile depth, the scaling of the eigenstrain profile depth is to be performed using the analytical plastic strain profile.

Further work is still required to define a way of scaling the eigenstrain curve based on the form of the curve shown in Figure 7- 1 and the peak eigenstrains and eigenstrain profile depths detailed in Table 7- 2. It is anticipated that two low order polynomial curves will be sufficient to describe the form of the T0 eigenstrain profile, one in the near surface (depth < 200 μm) region and one in the region 200 < depth < 0.375 μm. The magnitude and depth parameters in Table 7- 2 will then be sufficient to predict the eigenstrain profiles resulting from each of the other peening processes. These eigenstrain profiles could then be incorporated in FE models to predict the corresponding residual stress profiles. The intention is to validate (or otherwise) this approach by obtaining residual stress measurements using XRD in the T1 condition. Should this approach be demonstrated to be sufficient for approximating the full residual stress profile resulting from shot peening, the possibilities for predicting residual stresses resulting from shot peening complex components are very powerful indeed:

Based on the residual stress measurements for just one peening process of a simple geometry in a given material system, the form of the eigenstrain profile can be

determined by inverse analysis. The eigenstrain profile can then be scaled to other intensity peening processes on that target material based on the analytical plastic strain profile (it is noted that this approach does require data for the indent size resulting from the specific process in question and thus requires a test peening run to be performed for the specific peening process / target material system). The eigenstrain profile can then be incorporated in FE models of components of complex geometry to determine the equilibrium residual stresses without the requirement of XRD. Furthermore, since a test sample for the specific peening process is required, EBSD measurements can be made of the cumulative plastic strain profile and the resulting material properties gradients can be incorporated in the FE model as described in Section 7.2.2.3.

7.2.2.3. Applying material properties gradients

The FE model must also be able to cope with the variation in material properties near the shot peened surface. In the simplest case, any cyclic softening that occurs as a result of the peening process is ignored (in the present case, the degree of softening is sufficiently insignificant that this assumption should not lead to significant errors) and the variation in material properties at the surface can be modelled as the variation in yield strength shown in Figure 4-20b. Inclusion of these variations in a FE model would be achieved using a similar approach to that implemented by Benedetti *et al.* [7, 8] in which the cyclic stress strain curve was scaled at each depth such that the elastic regime extended to the calibrated yield stress and the hardening curve was shifted to account for the offset due to residual deformation. To achieve the required variation, the hardening coefficients in the material model are forced to vary with distance from the shot peened surface if the eigenstrain is modelled by varying CTE with distance from the shot peened surface. Alternatively, the CTE could be held constant and a non-uniform temperature profile imposed across the sample in order to generate the eigenstrain profile required in Section 7.2.2.1. Depending on the material model in question, the relationship employed by Song *et al.* [9] in which the backstress in the kinematic hardening model was linearly proportional to plastic strain may be more appropriate.

7.2.3. Applying the finite element models

The overall objective going forwards is to use the FE models containing residual stresses and strain hardening in fatigue life assessments. This could be achieved using a hot spot FE approach (i.e. using local stresses and strains at the surface) similar to that which was applied without considering the effect of shot peening in Chapter 5 Section 5.3. The aim is to apply the method first to PBB samples and then to notched

samples once the inverse eigenstrain approach has been modified to account for the notch geometry and initially to reconsider the fatigue lives of the PBB and notched samples in terms of S-N curves.

The effects of the residual stresses and the strain hardening on the local stresses and strains under fatigue loading will first be determined independently before both effects are combined in the same model. This will firstly allow the relative importance of strain hardening effects and residual stresses on the total life based on S-N curves to be established: By re-plotting the S-N data originally shown in Figure 5-21, it is hoped that by considering the local stresses and strains the results for the shot peened samples will correspond with the un-shot peened samples. Any differences will facilitate making a judgement on the severity of the surface roughness effect and the significance of any changes in fatigue micromechanisms resulting from the shot peening process (this work is on-going and is reported further in Section 7.3). Furthermore, the FE model will be able to predict changes to the residual stresses after loading and unloading in a similar manner to that shown for samples containing no initial residual stresses in Figure 5-34.

The approach will initially be developed using the isotropic hardening material model based on monotonic tensile data in the direction perpendicular to rolling. However, an additional material model sensitivity study similar to that described in Section 5.3.1 is required because the addition of residual stresses and strain hardening to the model may result in more significant differences in local stress and strain predictions depending on the material model in use and other material models, e.g. the combined model may thus be more appropriate.

However, the overall objective of the work remains the development of a damage tolerant fatigue life assessment protocol which can account for the effects of the shot peening process. Hence consideration of the effect of the residual stresses and strain hardening on S-N data is not sufficient and further work is also required to incorporate the modified FE methods in the standard industrial R6 lifing process [2]. The current status of the methods for combined applied primary loads and residual secondary stresses in the low temperature fracture assessment procedure R6 are well described by Budden *et al.* [10] and Ainsworth and Hooton [11] and can be summarised as follows:

Essentially a failure assessment diagram is used which defines a ‘safe region’ by considering failure by both plastic collapse and fracture; an example is illustrated in Figure 7- 5. This approach requires the calculation of L_r, a normalised parameter which represents the plastic collapse criterion (and is a function of crack length (a) and yield strength (σ^0)) and K_r, a normalised parameter which represents the fracture criterion

(and is a function of the material fracture toughness (K_{Ic})). Whilst the calculation of L_r is dependent only on the primary stresses, the calculation of K_r (Equation 7-1) requires consideration of both primary (K^p) and secondary (K^s) components and any interactions between the two using ρ_k (which can also account for plastic redistribution of secondary stress if it assumes a negative value). The most desirable procedure from an accuracy perspective for calculating the contribution of secondary stresses is an inelastic analysis of the cracked body and use of the *J* integral; however, the less computationally expensive simplified weight function methods are often implemented where K^s is estimated based on an inelastic analysis of the uncracked body.

$$K_r = \frac{K^p + K^s}{K_{Ic}} + \rho_k \qquad (7\text{-}1)$$

7.2.4. Scaling up to the component level

Once the model is validated for the simple geometries of the fatigue test samples it can be scaled up to the component level. This section briefly introduces a last stage low pressure turbine blade-rotor model previously developed at E.ON New Build and Technology (ENT) initially for vibration analysis (Section 7.2.4.1) and the subsequent sub-modelling approach which was used to analyse the stresses in the rotor (Section 7.2.4.2). The final part of this section (Section 7.2.4.3) discusses how the analysis can be extended to allow a detailed analysis of the stress distribution in the blade fir tree root under steady state load at a scale such that the stress distributions in the region that would be affected by the shot peening process can be assessed. It is only at this modelling level that the residual stress and strain hardening effects can be incorporated in the FE model.

7.2.4.1. Full blade-rotor model for vibrational analysis

The initial blade-rotor FE model for vibration analysis was developed by Zanjani at ENT [12]. The geometry was measured from a new blade using the GOM white light scanning technique. Briefly, this system is based on optical triangulation and stereo viewing; striped fringe patterns are projected onto the surface which are then captured simultaneously by two measurement cameras from different angles; digital image processing allows the generation of 3D co-ordinate data. The captured data was used to develop the solid model of a blade and a 1/74th segment of the rotor.

Cyclic symmetry was used to represent the full 360° arrangement. The analysis was carried out in the full speed no load condition (centrifugal load only) in two stages. Frictionless contact conditions were set on the rotor steeple and blade root with the rotor being the master and the blade the slave surface respectively. The first stage

represented loading between 0-2000 rpm at which point the blades untwist, the snubbers contact and further untwisting is prevented. The results from this analysis were exported and used to define initial conditions for subsequent loading between 2000-3000 rpm; in this load step an additional cyclic symmetry condition was imposed on the snubber in order to represent the fully locked wheel. The elastic materials model detailed in Table 7- 3 was applied.

Since the original analysis was intended only for a vibrational assessment, a coarse mesh was implemented using 70665 10 node quadratic tetrahedral C3D10 elements in the rotor and 144950 C3D10 elements in the blade. Whilst not appropriate for in-depth stress analysis owing to the coarse mesh implemented, the stress distributions within the assembly rotating at 3000 rpm were examined as an initial indicator of the distributions that may be expected to be found in the sub-models and are shown in Figure 7- 6. Figure 7- 6 shows the complete assembly and the maximum principal stress on the aerofoil section at the trailing edge of the blade; removing the rotor from the assembly in Figure 7- 7 shows the maximum principal stress at the interface is on the outer edge of the upper lobe. It is, however, clear that the mesh is not optimised for stress analysis and the sub-model described in Section 7.2.4.2 was developed to overcome this.

7.2.4.2. Submodel for stress analysis in the rotor

A submodel based on the initial model developed in Section 7.2.4.1 was also developed at ENT by Zhang [13] in order to analyse the stresses in the rotor. The submodelling technique can be used to study a local part of a model with a refined mesh based on the interpolation of the solutions from an initial, relatively coarse, global model. The submodelling reported in this thesis is all based on the displacement nodal technique in which nodal displacement results from the global model are used to drive a local part of the submodel by forcing global displacements for each node on a bounding surface.

The submodel geometry used by Zhang is illustrated in Figure 7- 8. The method used to generate the geometry is clear; a cut was made removing the aerofoil section of the blade and just below the blade-disc interface, removing the centre section of the rotor. The mesh consisted of a combination of C3D20 20 node quadratic brick with C3D15 15 node quadratic triangular prism elements used in regions of geometric necessity. The rotor section was meshed using 139909 elements and the blade section using 84320 elements – the total number of elements was 224229, similar to the 215615 element in the global model but with significantly more elements in this region of

interest. The initial conditions of cyclic symmetry and contact used in the global model were also applied to the submodel along with the rotational speed of 3000 rpm.

Although the blade fir tree regions were not analysed as part of the original rotor safety case, the mesh refinement in this region was sufficient to allow a better representation of stresses in this region than that afforded by the original global model and the model was reanalysed as part of the present work to assess the stress distribution in the near notch region.

The location of the maximum principal stress is illustrated in Figure 7- 9. As in the original model, it is located at a 'notched' geometry at the centre of the outer curvature of the attachment although with this refined mesh it now appears at the next lobe down. Whilst the von Mises equivalent stress corresponding with the maximum principal stress is within the elastic regime of the material, it should be noted that the variation in integration point results for the associated element is too high; as a result the interpolated nodal surface value may be erroneous. This is a driving force for the generation of a further submodel in this region of interest. The nodal results for maximum principal stress depth profile across two elements from the maximum are shown in Figure 7- 10. It is noted that the near surface region of very high stresses are contained within the region that would be likely affected by shot peening. This is the region of interest for the new submodel discussed further in Section 7.2.4.3.

7.2.4.3. Further submodelling to the shot peening affected region length scale

In order to consider the stress-depth profile emanating from the identified 'notch' profile within the fir-tree interface region a further submodel is under development as part of the present work; this section reports the progress to date and the further work required.

This further submodel was generated by cutting ±12.5 mm from the centre of the initial submodel reported in Section 7.2.4.2 and driving the model using the nodal displacements from this initial submodel. The geometry of the resulting model is illustrated in Figure 7- 11. The model was meshed using the swept mesh generation feature in Abaqus Standard; the global element size was set as 1mm and the mesh was refined in the region where high stresses are predicted such that there was a fine mesh in the region of contact in the rotor (0.6 mm edge length) and contact and high stresses in the blade root (0.3 mm edge length); the mesh refinement is also illustrated in Figure 7- 11. Since this further submodel is much smaller in size than the original submodel, it was possible to obtain this more refined mesh whilst reducing the total number of elements in the model. There were 15093 C3D20 elements in the rotor and 80138 C3D20 elements in the blade. The same initial conditions of cyclic symmetry,

contact and rotational velocity as were used in the previous global models were also applied.

The maximum principal stresses in one half of the blade interface section (the cut is made at the mid-point in the *x*-direction) are shown in Figure 7- 12a. The maximum principal stress at the centre section of the model (Figure 7- 12b) occurs in the same region as in the original submodel (Figure 7- 9) with a variation in magnitude of 3 %; the distribution is shown over the first two elements which were in an approximately normal direction to the curvature of the notch in Figure 7- 13. The results are consistent with those shown in Figure 7- 10 and add a degree of confidence to the modelling approach under development.

There are, however, a couple of issues with this submodel in its current state and further work is required to refine the model and obtain more conclusive results on the stress gradient perpendicular to the edge on a scale which is comparable with the depth of influence of the shot peening process. The first issue is associated with the mesh. A partition is required that would enable elements to be defined along the perpendicular direction such that a stress distribution deeper than that shown in (Figure 7- 13) can be obtained. However, given the curved geometry of the blade in the ~*x* direction, this mesh proved very difficult to generate using the Abaqus Standard package and both Hypermesh and Patran will be used in the future in an attempt to achieve this mesh geometry. Furthermore, whilst less than in the original submodel, the stress gradient across the elements in the region of interest is still too high for a detailed stress analysis. The elements at the interface also need to be much smaller if shot peening residual stresses are to eventually be incorporated in the model; given the current size of the model and the desired element limit of ~250,000 elements, this refinement is not thought to be possible at the scale of the current submodel.

The second issue is that there are apparent stress anomalies at the driven edges of the model (Figure 7- 12a). These are thought to be a result of the relatively high exterior tolerance that was required in order to ensure that the nodes in the submodel were associated with nodes in the global model and may be a result of the successive submodelling approach which has been adopted in this work. This does not, however, appear to have significantly affected the stress results at the central region of interest which show good consistency with the results obtained from the first submodel. Creating a further 3D submodel based on this model to refine the mesh further is undesirable as the issues associated with the exterior tolerance would only be expected to get worse and a decision has been taken to move to a 2D approach in order to reach the scale required to consider the application of the shot peening process. In this 2D approach, loads will be applied such that the stress distribution in the region of interest (the thin layer near the surface where shot peening would be

applied) matches that in the region of high maximum principal stress in the current submodel.

An additional development to the submodel described above would be modifying the model to simulate an overspeed test at 3300 rpm where it has previously been reported that stresses in excess of yield may occur [14]. Understanding the distribution of stresses in excess of yield even if it only happens once is essential to understanding any possible relaxation in the initial residual stresses resulting from the shot peening process applied to the interface region.

7.3. Micromechanisms of fatigue crack initiation and growth in the layers affected by shot peening

7.3.1. Objective

The simple consideration of the effect of shot peening on local stress and strain distributions in the component may not be sufficient to fully explain the effect of shot peening on the fatigue life. There is an implicit assumption in the approach described in this work that for a given set of local stress/strain conditions the initiation life and propagation behaviour will be the same in peened and unpeened components. However, this does not account for any changes in fatigue micromechanisms that may result from shot peening. In particular, there may be changes to the micromechanisms in the short crack regime; such changes may include changes to the crack aspect ratio and the length scale over which short crack effects dominate.

Short cracks can be defined in several different ways, the most important to the present work being if the crack length is comparable to the scale of local plasticity, e.g. a crack which is in the plastic zone of a notch, or indeed in the region of material affected by shot peening plasticity, or if the crack length is physically small (e.g. ≤ 0.5 – 1 mm) [15]. Typically, short cracks propagate more quickly than long cracks under the same stress intensity factor range, ΔK, and short cracks emanating from notches propagate faster still when the notch plastic zone engulfs the short crack region [16]. In such situations, LEFM is not sufficient to explain the propagation behaviour and there are attendant problems in lifing components containing such short cracks, for example turbine blades and discs [15]; these problems are made more complex by the addition of the shot peening process. There have been some reports in the literature of short crack behaviour in shot peened materials; given the typical total depths of the compressive residual stress profile are in the range 200-500 μm, the effect of shot peening on the short crack growth regime may be of great significance.

The work of Mutoh *et al*. [17] was previously introduced in Chapter 2 (Section 2.1.3.1). In their work, a combination of replication and potential drop techniques were used to investigate the crack propagation rate as a function of ΔK in shot peened notched aluminium samples which were tested under a stress ratio R_σ = 0.1 in the elastic regime. In order to correlate the surface crack length, 2*c,* measured using replication techniques with the crack depth through the sample, *a*, some tests were interrupted at varying stages of life to show that the aspect ratio *a*/*c* increased as *a* increased before stabilising at a level lower than in unpeened samples; this was thought to be dependent on surface geometrical features and compressive residual stresses. However, this change was not reported in the work of Gao and Wu [18]. Mutoh *et al.* [17] also showed that the crack growth rate reduced with increasing ΔK until the crack length corresponded to the depth of the maximum residual stress after which the growth rate rapidly increased to a level corresponding to that of the unpeened samples. This reduction in short crack growth rate was also shown to be significant in aluminium samples by Gao and Wu [18] and in steel samples by de los Rios *et al.* [19]. Indeed it has been shown that non-propagating cracks, the depth of which typically coincide with the depth of the compressive residual stress layer, may exist [20]. De los Rios *et al.* [19] also indicate that crack arrest can occur; indeed they report that small cracks initiate quickly at the edges of dimples resulting from shot peening a 0.4 %C steel but that they arrest for a period of time before propagating. It was suggested that this happened when the residual stresses had relaxed sufficiently as to allow crack propagation to begin, but no evidence was available to support this.

Hence the primary objective of this current work package is to assess fatigue crack initiation and propagation behaviour in ground and shot peened notched samples with a view to understanding the micromechanisms by which the crack first initiates in and then propagates through the affected layer. Furthermore, the initiation life data for a crack that can be detected by non-destructive testing (NDT) will be essential in fully validating the damage tolerant fatigue lifing approach under present investigation.[2]

7.3.2. Experimental methods

Interrupted fatigue testing at strain range $\Delta\varepsilon_{11}$ = 0.0068 (the same loading conditions as were used when investigating the residual stress relaxation during fatigue) was carried

[2] The experimental and analysis work towards this objective reported here have been carried out by Binyan He (bh2g11@soton.ac.uk) as part of her PhD project at the University of Southampton. I have been actively involved in defining the scope of the work and in understanding how the work relates to the wider project and the associated implications on the remnant life assessment of shot peened components.

out using the same procedure as was described in Section 5.2.3 for polished, ground and shot peened (T0) 4.5 x 1.25 mm notched samples. A similar replication technique to that described previously was used to monitor crack initiation and short crack growth; however, the shape of the notched sample meant that rather than use acetate replicas, RepliSet-F5 (Struers Ltd.) was used. Since the samples were loaded in LCF conditions, the number of cycles to failure was expected to be much lower than the plain bend bar sample described in Section 5.2.3 and as such a replica of the notched surface was taken every 1000 cycles until a crack was first clearly observed and then every 500 cycles until failure. Initiation points were identified, and crack growth rates of surface cracks were calculated from the replica record using an Olympus BX51 polarised light microscope in conjunction with image analysis protocols (FIJJI). The short crack surface lengths, $2c$ (initiation was observed at the centre of the sample) were established and the corresponding surface crack growth rates determined.

7.3.3. Initial results and discussion

The data reported in this section corresponds to the cracks that coalesced in the late stages of fatigue and led to final failure. The crack development as a function of the fatigue life fraction in the polished, ground and shot peened samples is shown in Figure 7- 14, Figure 7- 15 and Figure 7- 16 respectively. Comparing the number of cycles to failure in these samples with the data previously presented in Figure 5-21 shows good reproducibility in the experimentally measured fatigue life. The surface crack length (c) as a function of fatigue life fraction (N/N_f) is shown in Figure 7- 17 whilst the surface crack growth rates are shown in Figure 7- 18.

It is noted from Figure 7- 17 that there appear to be pre-existing cracks on the shot peened surface. Furthermore, it appears from Figure 7- 16 that one example of these cracks has initiated from a shot peened dimple on the notch surface, supporting the viewpoint that the stress concentration at the edges of the shot peening dimples is detrimental to fatigue initiation life. Figure 7- 17 shows that at $N/N_f \sim 0.1$-0.25, the pre-existing cracks started to grow, with rapid increases in length occurring after ~80 % of the fatigue life when crack coalescence occurred frequently and secondary cracks began to grow. In the ground samples, the cracks first appeared at $N/N_f \sim 0.5$ and appeared to grow at a relatively constant rate along the grinding marks, only accelerating towards the end of life when the main cracks coalesced.

The fatigue crack growth rates shown in Figure 7- 18 are highly scattered; a feature which is consistent with short crack growth behaviour. In the ground case the crack growth rates are fairly constant ($\mathrm{d}c/\mathrm{d}N$ levels of between 10^{-3} and 10^{-5} mmcycle^{-1}, indicating that the relatively constant strain range rather than any ΔK level may be

acting as the crack driving force. For the shot peened case, the crack growth rates are generally lower and show a wider range, increasing with crack length.

Given the extent of the residual stresses and strain hardening resulting from the T0 shot peening process (Figure 4-16 and Figure 4-20a respectively), once the aspect ratio of the crack is considered, it is likely that the pre-existing cracks on the surface layer are contained within the strain hardened region, further complicating the analysis of the short crack behaviour. This initial non-propagation may be a result of the reduced mean stress as a result of the superposition of applied and residual stresses and of the strain hardening present in the material which is typically considered to act mainly in increasing initiation life (Table 2-3).

The slower crack growth observed in the shot peened samples is thought to be primarily a result of the crack growing through the region containing compressive residual stresses (Table 2-3). Compared to the ground sample behaviour, it is clear that the early stages of crack growth have been slowed in the shot peened samples. The total surface crack length in the shot peened samples has to be of the order of 400 – 600 μm before the dc/dN levels in the shot peened samples are similar to those of the ground samples; after allowing an approximate crack aspect ratio of 0.7, this correlates to an expected crack depth of a ~ 280 – 420 μm. However, statistically significant data pertaining to the actual crack aspect ratio in the short cracks under present investigation is yet to be obtained; this will allow correlation of dc/dN with da/dN and consideration of behaviour in terms of ΔK.

7.3.4. Future directions

7.3.4.1. Experimental work

Before reliable conclusions can be drawn as to the through thickness crack growth rate da/dN, statistically significant data is required which indicates the variation in crack aspect ratio in the shot peened layer in the present system. This data can be obtained by interrupted fatigue testing after different life fractions, heat tinting and breaking open the fracture surface for examination using both optical and scanning electron microscopy. Additional work is also planned which will reveal the three dimensional crack morphology in each surface condition. By interrupting a fatigue test in a shot peened sample at N/N_f ~ 0.8 and polishing away the notch surface in increments of ~1.5 μm, images of the surface taken at each depth increment can be stitched together and aligned in three dimensions. The amount of material removed on each polishing increment can be accurately measured using a hardness indent as a fiducial mark.

Once the aspect ratio is well defined, da/dN can be calculated as a function of ΔK using the approach of Scott and Thorpe to calculate ΔK [21]. A method similar to the 'negative ΔK' approach of Knott *et al.* [22] could then be used to calculate the apparent residual stress which would lead to the same difference in ΔK as was observed between the shot peened and the polished replica tests. Comparison with the measured initial residual stress field will aid understanding of the relative contributions of residual stress and strain hardening to crack propagation rates and could allow an initial analysis of the effects of residual stress redistribution as a crack grows through a residual stress field:

Some evidence was presented in Section 7.3.3 to suggest that the residual stresses may be influencing the crack growth rate up to a depth of 420 μm (i.e. beyond the initial measured depth of compressive residual stresses of 340 μm). In Chapter 5, it was shown that local plasticity under fatigue loading did not result in a significant redistribution of residual stresses in the present case. However, it is possible that residual stress relaxation may occur as a fatigue crack propagates through the material when the plastic zone that accompanies the fatigue crack interacts with the misfit strains that caused the initial residual stress [23]. The evolution of longitudinal residual stresses resulting from metal inert gas welding an aluminium plate was investigated by Liljedahl *et al.* [24]. It was found that the peak tensile residual stresses increased with crack growth until a surface crack length of ~ 14 mm from the weld centre at which point they began to reduce.

Hence whilst using the residual stress field resulting from shot peening in an uncracked component in conjunction with the weight function method for establishing stress intensity factors might be expected to result in an improved prediction of fatigue crack growth rate and hence damage tolerant life estimate compared with ignoring the residual stresses, the method could be improved by considering the residual stress field at each stage of crack growth [23, 25]. It was shown using FE methods that considering the redistribution of the residual stress field as an elastic process was sufficient to predict the changes in residual stress with crack extension in a welded aluminium plate and hence that local crack tip plasticity had only a minor effect [24]. These approaches were combined with LEFM weight function calculations of the residual stress intensity factor to predict fatigue crack growth rates using a superposition approach (i.e. ΔK is constant and R_σ changes. The predictions which accounted for residual stresses were shown to be more accurate and more conservative (given the tensile residual stresses resulting from welding) than those which did not account for residual stresses [24].

One of the key issues highlighted in Chapter 1 (Section 1.3.2) was the definition of initiation; based on the results shown here, initiation could be defined as the point at

which the cracks already present after shot peening begin to propagate. However, the issue remains that unless NDT can detect these small flaws, it must be assumed that a flaw equivalent in length to the tolerance of the technique is present. Assuming (using the eddy current arrays described in Section 1.1.2) this length is a minimum of 0.1 mm, the highly scattered data shown in Figure 7- 18b indicates that short crack effects appear to extend beyond the depth of the NDT tolerance.

Another planned extension of this work is the investigation of the blend-polish-peen repair process (the method was described in Section 1.1.2 and the application of this repair process is described further in Section 7.4.2). A crack of approximately a = 1 mm (N_f ~ 0.75) will be grown (using the same fatigue test method as was described previously in this section) in both a PBB and a 4.5 x 1.25 mm notched sample and sent for repair at Power Engineering Services. The samples will be further fatigue tested with the aim of establishing how the micromechanisms of crack growth and remnant life are affected by the repair process. The repair process is likely to result in three effects, the significance of which is also of great importance to the damage tolerant lifing approach:

i. The geometry of the sample will be changed. FE approaches will be used to quantify the effect on local stress and strain distributions.
ii. The surface finish after repair is also important. Assuming the blend-polish-peen process is completed, the repair will be shot peened. However, for certain components, it is possible to repair without peening and the effect of the surface finish (ground, ground-polished or ground-polished-peened) should be considered.
iii. There will be some residual stress redistribution effects; a first order approximation might be obtained using the Moore and Evans [26] solutions.

In summary, an investigation into the effect of shot peening on short crack initiation and propagation is under way. This work will add to the life assessment approach under development by providing an understanding of the significance of the assumptions that are made and the margins in the model that are present as a result of initiation and early stage short crack propagation. Since the model must be damage tolerant in nature it will, however, be difficult to remove the requirement of the assumption of a flaw equivalent in length to the tolerance of the NDT technique in apparently defect free components and hence there will always be some margin in the model; this work will also help clarify what this margin is. However, since short crack behaviour appears to dominate beyond the depth of the NDT tolerance, it may be necessary to modify the model to account for short crack growth behaviour.
Section 7.3.4.2 contains a brief review of how a damage tolerant analysis which

accounts for both short and long crack behaviour in a notch could be developed; it is noted that in the present case, the model would be further complicated by the addition of the shot peening effects.

7.3.4.2. Damage tolerant life assessment in notches accounting for short crack behaviour

The behaviour of short cracks in both flat and notched geometries is compared with long crack (linear elastic fracture mechanics, LEFM, dominated) behaviour in Figure 7-19. It is clear that short cracks in notches propagate far quicker than their long crack counterparts at the same ΔK. Cracks emanating from notches tend to grow relatively quickly at first with the rate continuously decreasing as crack length increases to reach a minimum propagation rate [27-30]. At this stage, the crack may become non-propagating if the crack driving force drops below threshold (typically this occurs in sharper notches where the bulk stress level to initiate a crack is relatively low compared to that needed to maintain crack growth outside the notch region of influence) or propagate under LEFM conditions. Four regimes of crack growth may be identified within notches:

i. Initiation of a dominant fatigue crack at the notch root. This is typically not considered significant in a traditional damage tolerant approach where an initial crack of a pre-defined length corresponding to the NDT detection limit is assumed present in the component.
ii. Early growth of this crack within the notch plastic zone.
iii. Fatigue crack growth in the elastic stress-strain field of the notch.
iv. Fatigue crack growth in the elastic stress field of the bulk material.

The parameters which are used to define the geometry of the notch are illustrated in Figure 7- 20. This discussion is a brief review of some of the work that has been previously published with the aim of predicting short and long crack behaviour at notches.

Typically, short crack behaviour tends to dominate whilst the crack is engulfed by the notch plastic zone since the scale of the plasticity is not small in comparison to the crack length [16]. It is relatively common therefore to assume that short crack behaviour dominates in this region and long crack behaviour dominates outside this region. Dowling [16] presents two equations for calculating the local stress intensity factor at notches, one in the short crack regime (Equation 7-2) and one in the long crack regime (Equation 7-3). In the long crack regime, the effective crack length a includes the notch depth c_n and the crack length from the notch surface l ($a = c + l$)

and the crack is no longer typically small in comparison to the scale of plasticity (which is now mostly comprised of crack tip plasticity), allowing LEFM to be applied [16, 31].

$$K_s = 1.12K_t\sigma\sqrt{\pi l} \tag{7- 2}$$

$$K_l = f\left(\frac{a}{W}\right)\sigma\sqrt{\pi a} \tag{7- 3}$$

The key differences between the approaches for predicting fatigue crack growth from notches is in how the short crack behaviour is accounted for and in how the transition point from short to long crack behaviour is defined.

Dowling [16] defines the transition from short to long crack behaviour using Equation 7-4 which is a function only of notch geometry and is of the order of the elastic notch field size [32]; this approach was also used by Sehitoglu [33].

$$l' = \frac{c_n}{\left(\frac{1.12K_t}{f\left(\frac{a}{W}\right)}\right)^2 - 1} \tag{7- 4}$$

These works were primarily different in their approach to accounting for short crack behaviour; Dowling [16] used a strain life approach to calculate the time taken to grow a crack of transition length, whereas by using an elastic plastic fracture mechanics (EPFM) approach such as in the work of Sehitoglu [33], it would be possible to define a shorter initiation length over which the strain life approach is used and then use a Paris Law type model based on ΔJ to determine the number of cycles to transition. The application of ΔJ in fatigue life estimates for notched plates was shown to produce results closer to the experimental data than the use of ΔK [33].

El Haddad *et al.* [34] also used ΔJ approaches in the short crack region dominated by notch plasticity. The crack length l was modified in the analytical solution of ΔJ with the addition of the material constant L (Equation 2-13) to account for the non-continuum behaviour of short cracks; this approach had previously been shown to eliminate the discrepancy between short crack and long crack da/dN vs. ΔJ behaviour for smooth samples [35]. It was shown that by using this approach in notched samples, the da/dN vs. ΔJ data points resulting from the short cracks were contained within the LEFM long crack scatter. Whilst this empirical approach appears to result in good correlation with experimental data, Suresh [36] indicates that the major drawback to the approach is that the physical reasoning for its validity is unconvincing. Furthermore, analytical solutions for ΔJ are limited to specific geometries and as such would typically be calculated for complex geometries using FE methods [30] which would make modifications allowing for L more complex. Whilst in this more recent work [30] no attempt was made to predict the actual fatigue crack growth rate from a notch, it was shown (by using an incremental node release FE crack propagation method that

allowed for closure) that a parameter combining the extents of monotonic and cyclic crack tip plasticity and a length dependent crack resistance term was able to predict the minimum point in the crack growth rate as a function of crack length and thus predict the transition from short crack to long crack behaviour.

These approaches, however, suffer from the requirement of strain-life data for specific short crack sizes; this data can be difficult to obtain. Furthermore, the strain-life to transition approach of Dowling [16] is incapable of predicting the decrease in crack growth rate or non-propagating cracks [32]. The issues in predicting decreasing crack growth rates can be overcome by using the total plastic shear deformation approach of Hammouda *et al.* [31, 32]. The model is constructed so as to be able to allow for both initiation and propagation. Initiation occurs if the plastic shear deformation at the uncracked notch root (Φ_s) is greater than the material threshold value Φ_{th} (Φ_s is assumed to be along a plane of maximum shear radiating from the notch root at 45° and is a function of loading conditions and the extent of the cyclic plastic zone along the direction of maximum shear, Δs_n). By assuming that the initiation life for smooth surfaces and notched surfaces is equal when Φ_s is equal, smooth specimen initiation data can be extrapolated to notched specimens, although the requirement of strain-life to initiation data remains.

The total plastic shear deformation at the tip of a sharp crack (Φ_t) is the sum of the contribution from LEFM plastic shear deformation at the crack tip (Φ_e) calculated using fracture mechanics and the contribution from notch plasticity (Φ_p). By assuming that Φ_t can be calculated from considering a long crack propagating in an elastically stressed bulk material at the same speed as the short crack of length l in the plastic zone, knowing the length of the long crack allows the calculation of Φ_t (since for long cracks $\Phi_t = \Phi_e$) and hence Φ_p for the short crack [31]. Since Φ_p decreases as the crack grows deeper into the notch plastic zone at a different rate from the rate of increase in Φ_e, a non-propagating crack may occur when $\Phi_t < \Phi_{th.}$ When stress levels are raised, the contribution of Φ_p increases due to elevated notch plasticity effects. Once $l > \Delta n$, Φ_p is zero and the result from LEFM can be applied since the crack is no longer dominated by bulk plasticity conditions but by local crack tip plasticity conditions. This definition of transition is the extent of the notch cyclic plastic zone and can be calculated using either analytical or FE methods.

More recently, the notch fatigue failure map (NFFM) approach was described by Ahmad and Yates [37]. As in the work of Hammouda *et al.* [31], Δn was used to define the transition from short crack to long crack behaviour and was calculated using FE analysis. Short crack growth rate data was obtained using replica techniques and was described as a function of strain amplitude (ε_a), Paris Law type constants (which must be found for the specific material) and an additional term $\Delta n - a$ where a accounts for

the notch contribution to crack length according to the approach of Smith and Miller [38]). Once $a > \Delta n$, the short crack growth law predicts no crack growth and a Paris Law approach for the long crack regime was implemented. This was also expressed in terms of strain amplitude and modified to account for both threshold conditions and high strain fatigue crack advance due to shear decohesion according to the model originally proposed by Tomkins [39, 40]. A non-propagating crack occurs unless the long crack equation (accounting for threshold) is able to predict crack growth. For a given material, contours of long and short crack growth rates can be plotted on axes of strain amplitude and crack length in an NFFM as shown schematically in Figure 7- 21. It is possible to show regions where fatigue is controlled by LEFM or EPFM. Short crack behaviour and long crack behaviour at high strain amplitudes (defined as a function of the cyclic yield strain amplitude ε_a^0) are governed by EPFM whilst long crack behaviour at low strain amplitudes is governed by LEFM. Furthermore, by superimposing the contours of strain distribution ahead of a notch from elastic plastic FE analysis and integrating the crack growth rate along the path of the notch strain profile, a prediction of fatigue lifetime to a given crack length can be obtained. The predictions in Figure 7- 22 correspond to the NFFM shown in Figure 7- 21; the NFFM model can lead to relatively good predictions of fatigue crack propagation behaviour from notches.

7.4. Wider applications of the work

Section 7.2 presented a very clear application route for the data obtained in the present work in component remnant life assessments. However, the work also has other wider applications, for example in quality assurance, as introduced in Section 4.4.3. The lessons learned from this work should also be considered when establishing whether shot peening is an appropriate fatigue mitigation strategy for a given component and in selecting the specific peening process. The decisions required are shown as process flow diagrams in Section 7.4.1. Furthermore, whilst the lifing approach is under development for low pressure turbine blade to disc interfaces, it was the intention from the outset of the project to broaden the applications of the work to other shot peened components, some examples of other components which have already been identified are given in Section 7.4.2.

7.4.1. Application and selection of shot peening processes

The first decision that must be made when considering the application of shot peening to components which are susceptible to fatigue is whether shot peening is likely to be beneficial to the fatigue life of the component. The decision process that should be followed is illustrated in Figure 7- 23. Information on the component loading should be

taken from a FE analysis. Information on the specific cyclic softening behaviour of the material (such as that presented in Chapter 3) should be used where possible; if this data is not available for the specific material in question, an indication on the behaviour expected in that class of material should be sought from the literature (such as that presented in Figure 1-6).

Once it has been established that shot peening is an appropriate strategy for reducing the propensity of the component to fatigue, the specific peening parameters need to be optimised; guidelines on liaising with the supplier to achieve this are given in Figure 7- 24. Guidelines are also supplied for assessing the outcomes of the peening process for quality control purposes.

7.4.2. Other components

Several other components have been identified as candidates for the exploitation of the lessons learned during this work including steam turbine blade snubber regions, wind turbine brackets and weld toes and blend polish peen repairs in F-class gas turbine disc rims where cracking has been identified in the blade attachment dovetail region. The blend-polish-peen repair process has been proposed as an option to reduce the stress concentration resulting from sharp changes in the airfeed slot geometry and remove some of the accumulated strain damage from the region [41]. However, in this high stress and high temperature environment, further analysis would be required to establish whether the compressive stress from shot peening results in a long term benefit to the turbine fatigue life.

There are also other areas where although shot peening is not applied, similar considerations as to the effects of impacting components with small particles as those made in this investigation may improve understanding of component behaviour. Components where these considerations may be important include boiler steam pipes where solid particle erosion occurs and components which are coated using high velocity oxy-fuel coatings and grit-blasted prior to coating application, such as the leading edges of last stage low pressure steam turbine blades which may be coated to improve their corrosion fatigue resistance.

Process T0	Eigenstrain Magnitude	Analytical plastic strain		EBSD cumulative plastic strain	
		Mag.	Ratio	Mag.	Ratio
Peak strain	0.00256	0.0557	21.8	0.1981	77.4
Depth /μm	375	333	0.887	150	0.400

Table 7- 1: Ratio of the analytical and EBSD peak plastic strains to the peak eigenstrain and ratio of the depths of the analytical and EBSD plastic strain profiles to the depth of the eigenstrain profile.

Process	Analytical plastic strain peak		Analytical plastic strain depth /μm		EBSD cumulative plastic strain peak		EBSD cumulative plastic strain depth /μm	
	Mag.	Eigenstrain peak	Mag.	Eigenstrain depth	Mag.	Eigenstrain peak	Mag.	Eigenstrain depth
T1	0.0378	0.00174	100	113	0.1195	0.00154	37.0	92.5
T2	0.0362	0.00166	358	403	0.1289	0.00167	86	215
T3	0.0396	0.00182	465	524	0.1563	0.00202	154	385

Table 7- 2: Predictions of peak eigenstrain magnitude and eigenstrain profile depth for shot peening processes T1, T2 and T3 based on the ratios reported for process T0 in Table 7- 1.

E /GPa	ν	Density /kgm^{-3}
200	0.3	7830

Table 7- 3: Elastic material properties. After Zanjani [12].

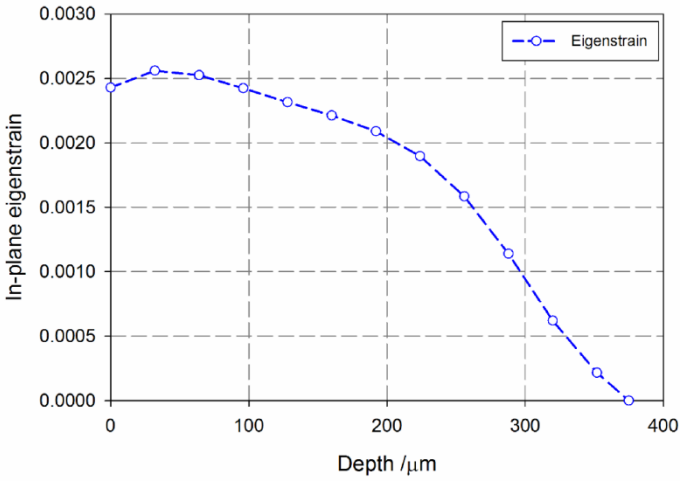

Figure 7- 1: Optimised eigenstrain profile corresponding to shot peening process T0.

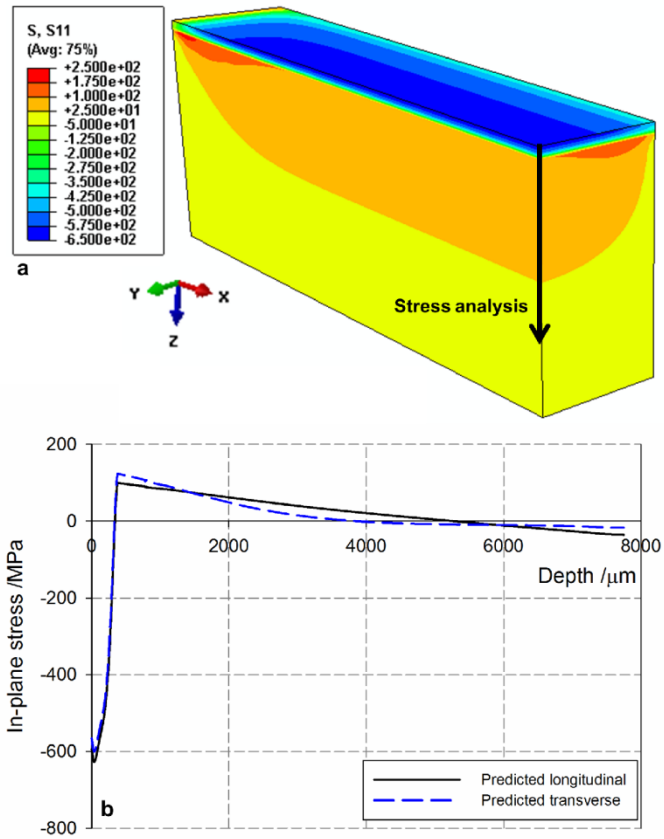

Figure 7- 2: (a) Contour plot showing residual σ_{11} in the PBB and (b) corresponding depth distributions of σ_{11} and σ_{22} resulting from the eigenstrain distribution shown in Figure 7- 1.

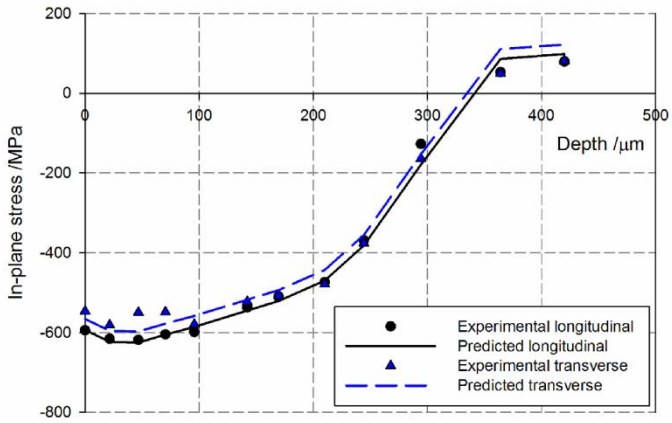

Figure 7- 3: Comparison of measured and predicted (using the inverse eigenstrain approach) residual stress distribution in a shot peened (T0) PBB.

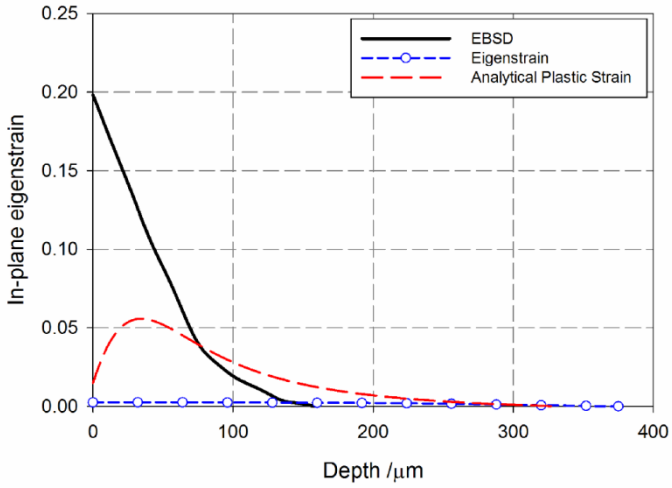

Figure 7- 4: Comparison of plastic strain measurements resulting from T0 shot peening process.

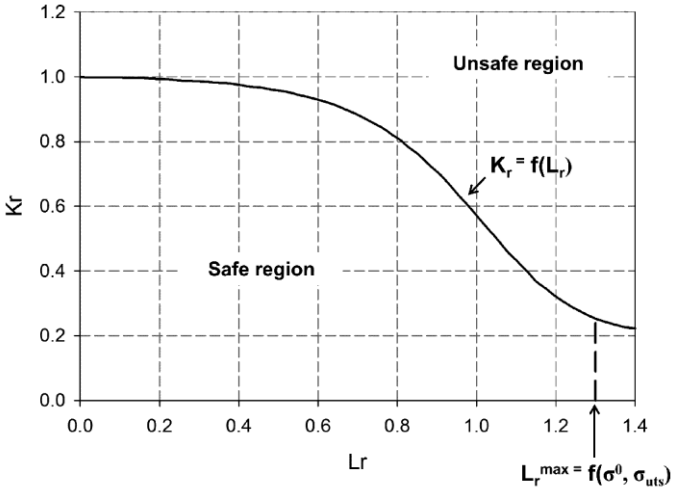

Figure 7- 5: Failure assessment diagram showing safe and unsafe regions. After Budden *et al.* and Ainsworth and Hooton [10, 11].

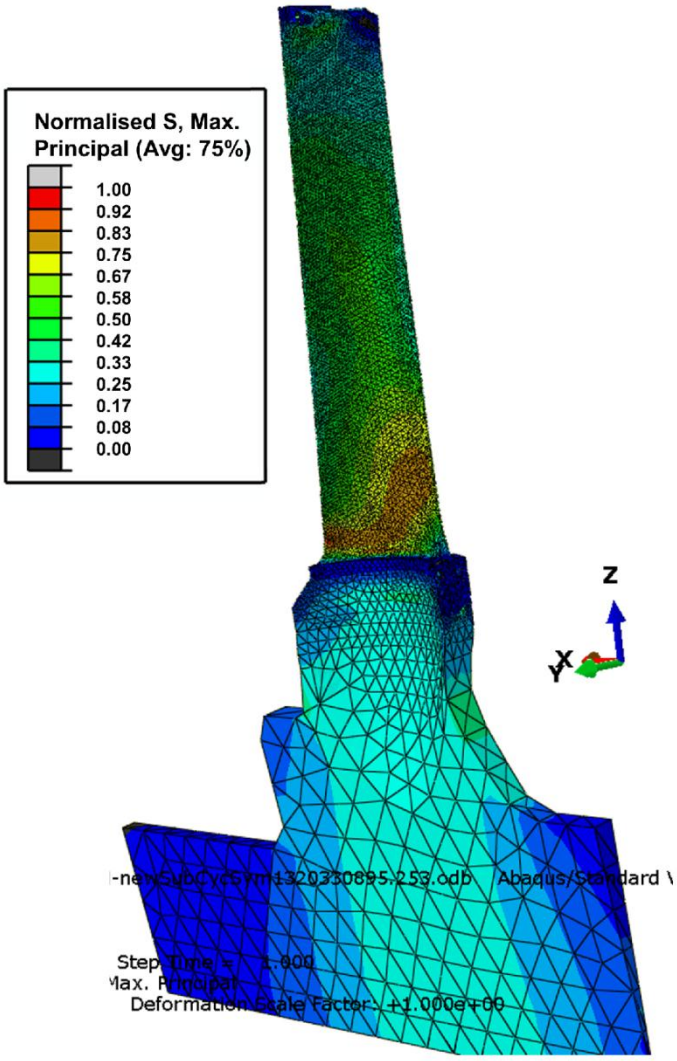

Figure 7- 6: Normalised maximum principal stress in the blade-rotor assembly.

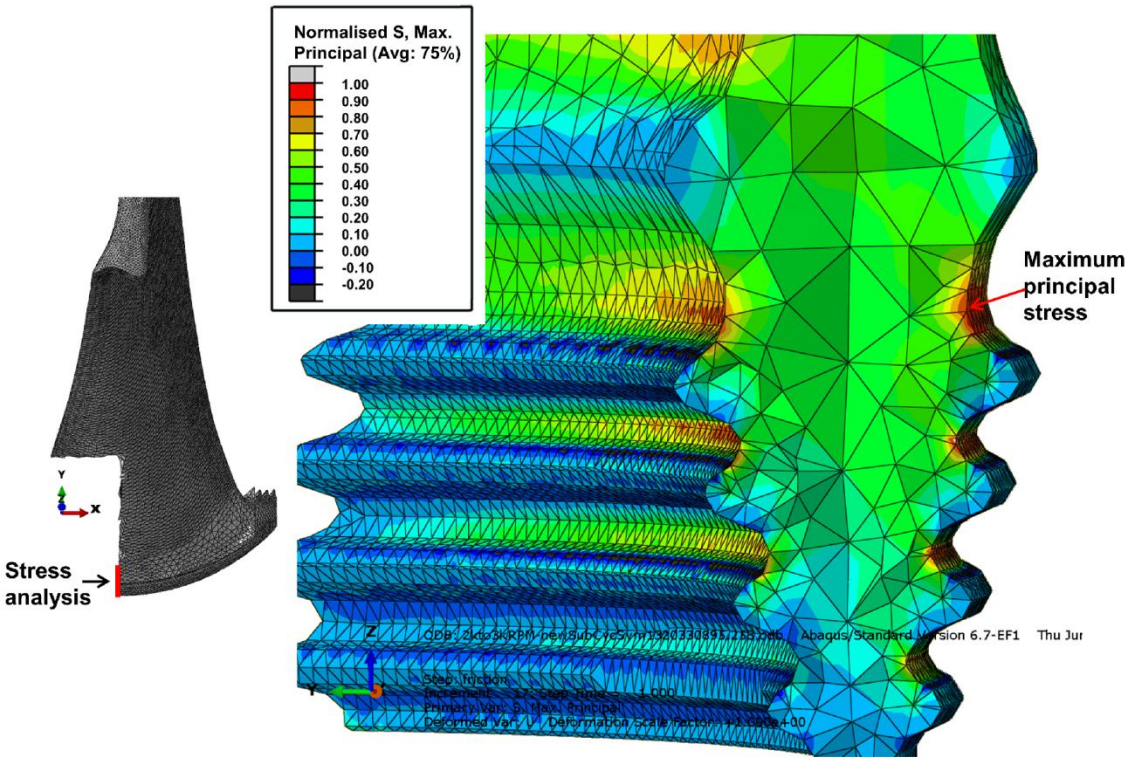

Figure 7- 7: Normalised maximum principal stress in the blade interface region taken at the centre of curvature.

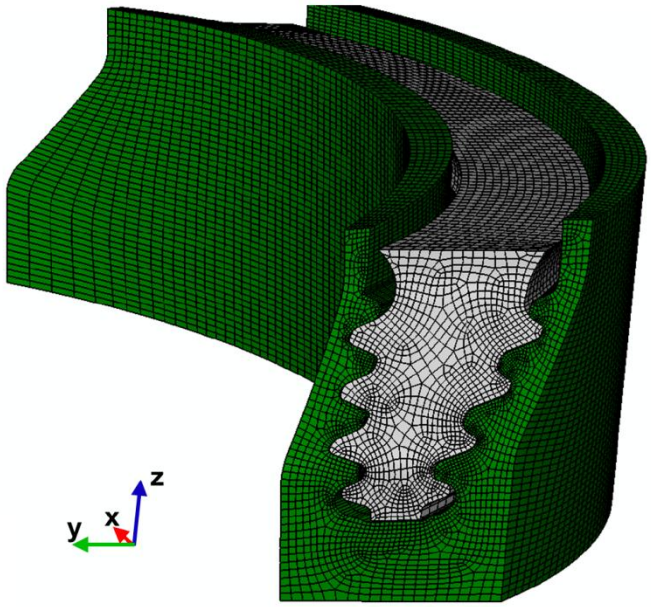

Figure 7- 8: Initial submodel geometry and mesh.

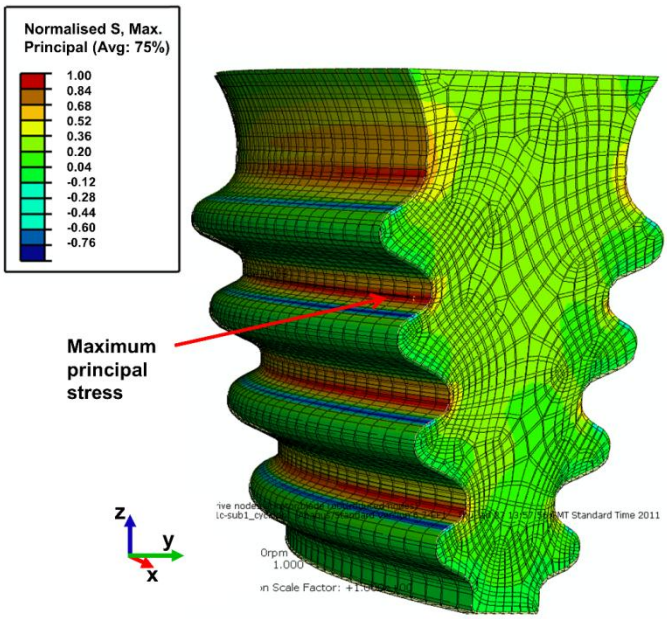

Figure 7- 9: Initial submodel normalised maximum principal stress distribution.

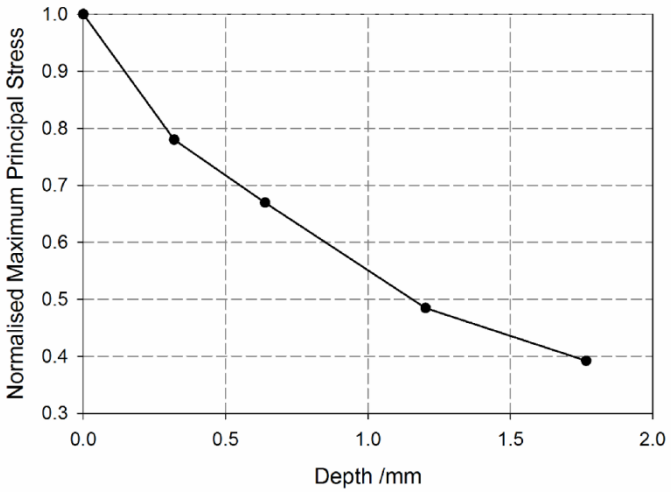

Figure 7- 10: Normalised maximum principal stress variation (normalised with respect to the same reference stress as Figure 7- 9) across two elements in the initial submodel moving away from the point of maximum in a direction approximately perpendicular to the curvature of the notch.

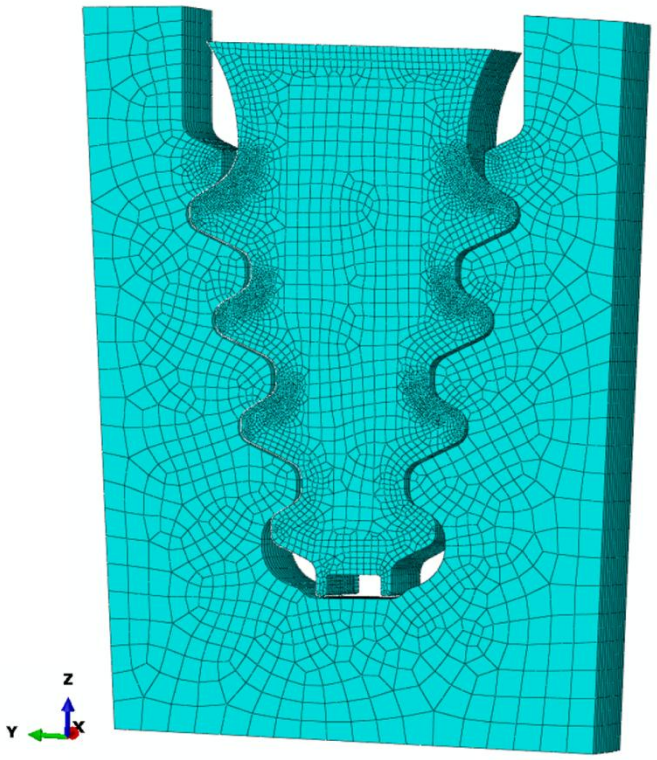

Figure 7- 11: Second submodel geometry and mesh.

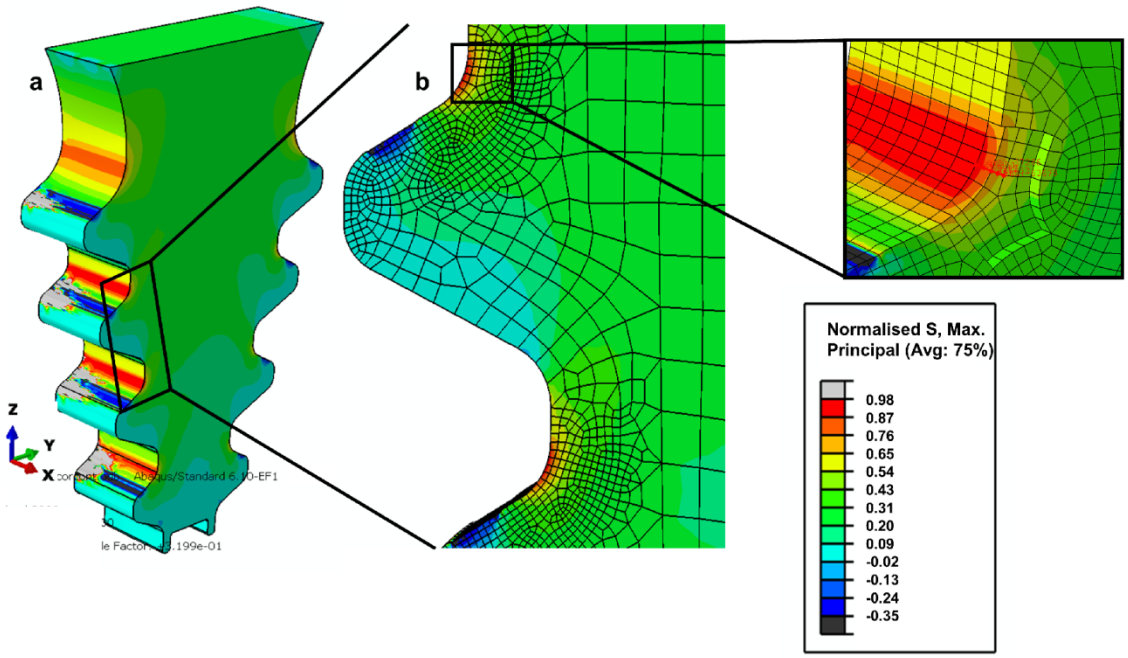

Figure 7- 12: Second submodel normalised maximum principal stress distribution (normalised with respect to the same reference stress as Figure 7- 9).

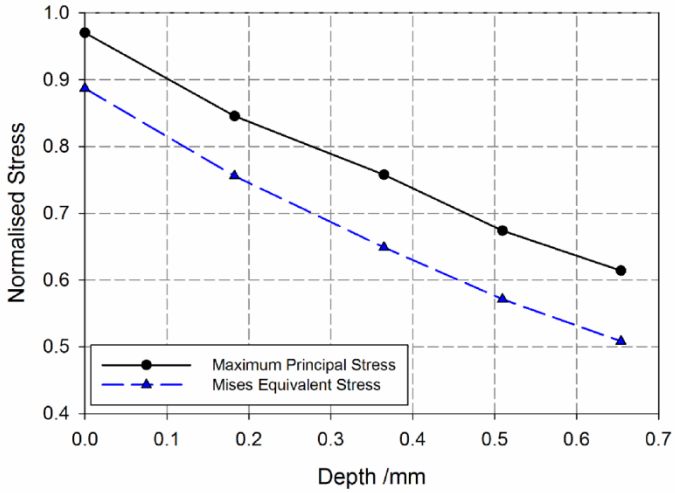

Figure 7- 13: Normalised maximum principal stress variation (normalised with respect to the same reference stress as Figure 7- 9) across two elements in the second submodel moving away from the point of maximum in a direction approximately perpendicular to the curvature of the notch.

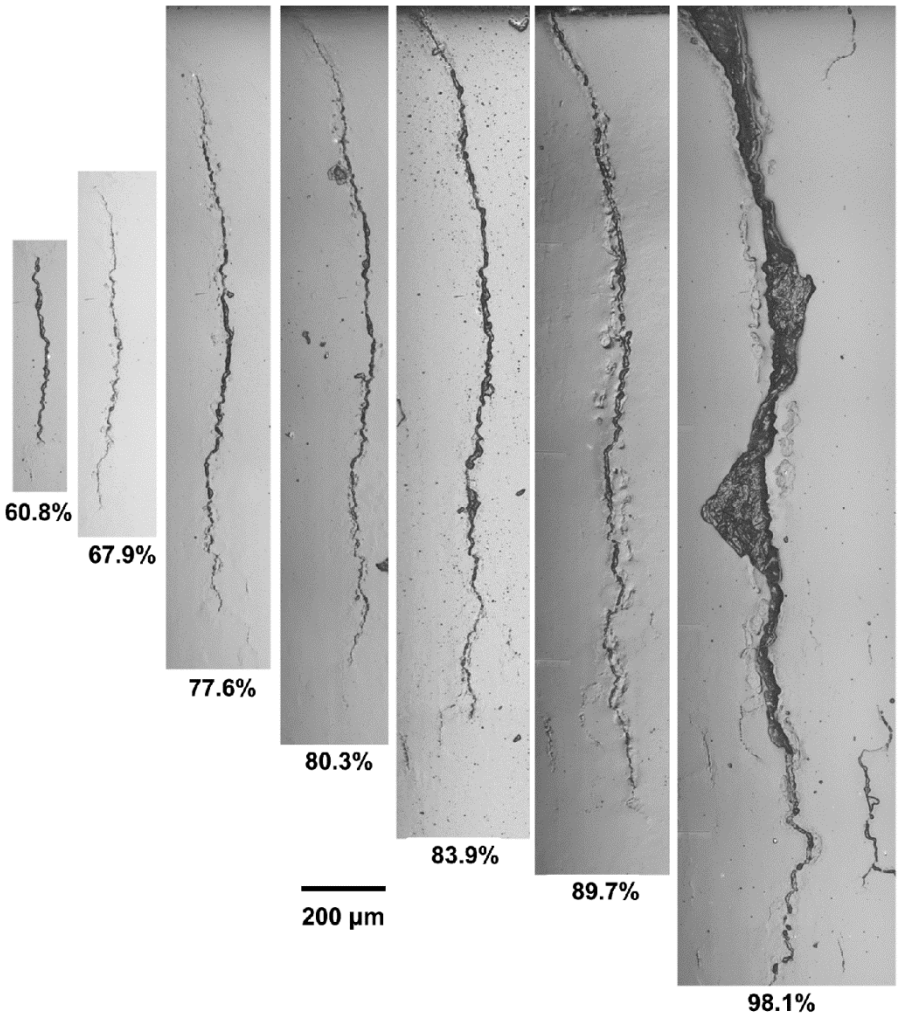

Figure 7- 14: Crack morphology on the polished surface as a function of fatigue life fraction (failure at 25353 cycles).

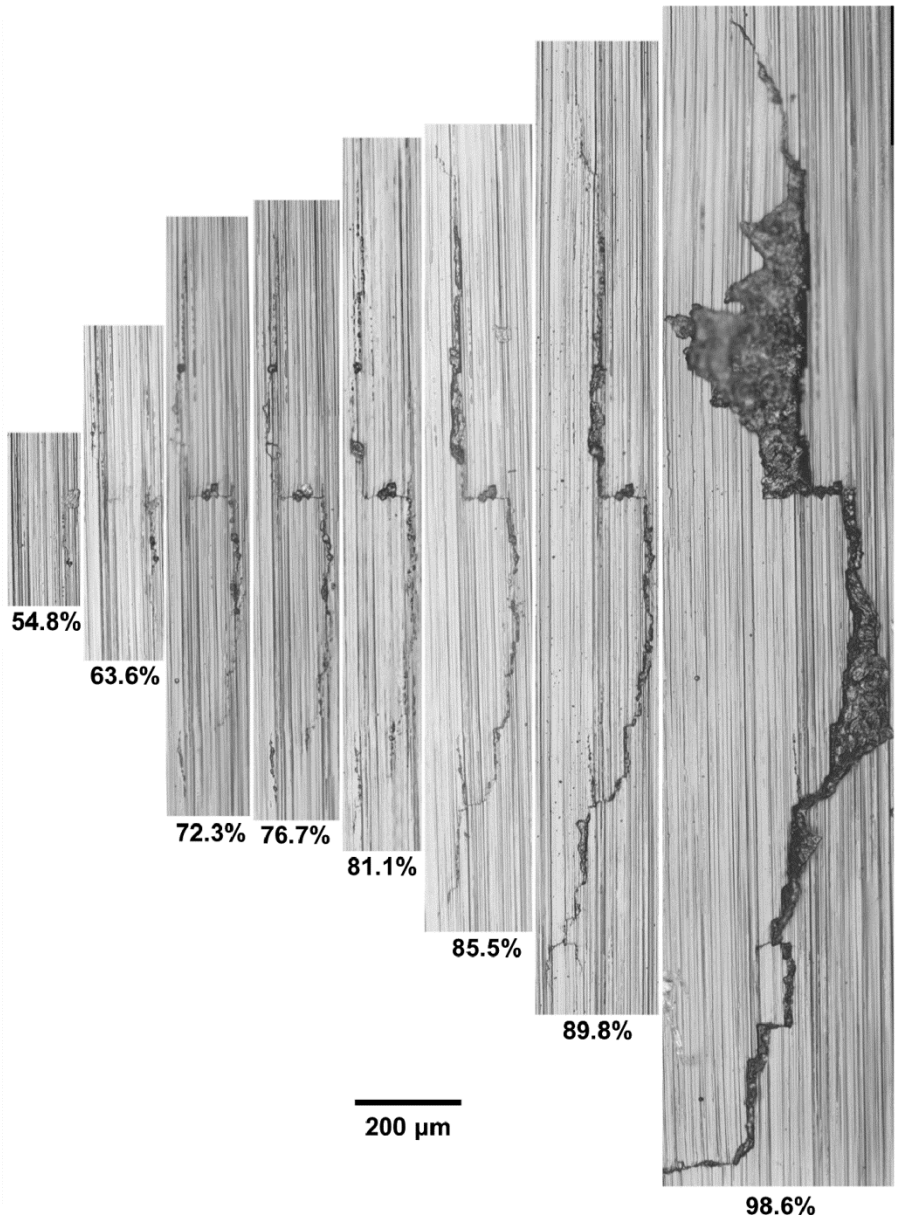

Figure 7- 15: Crack morphology on the ground surface as a function of fatigue life fraction (failure at 22816 cycles).

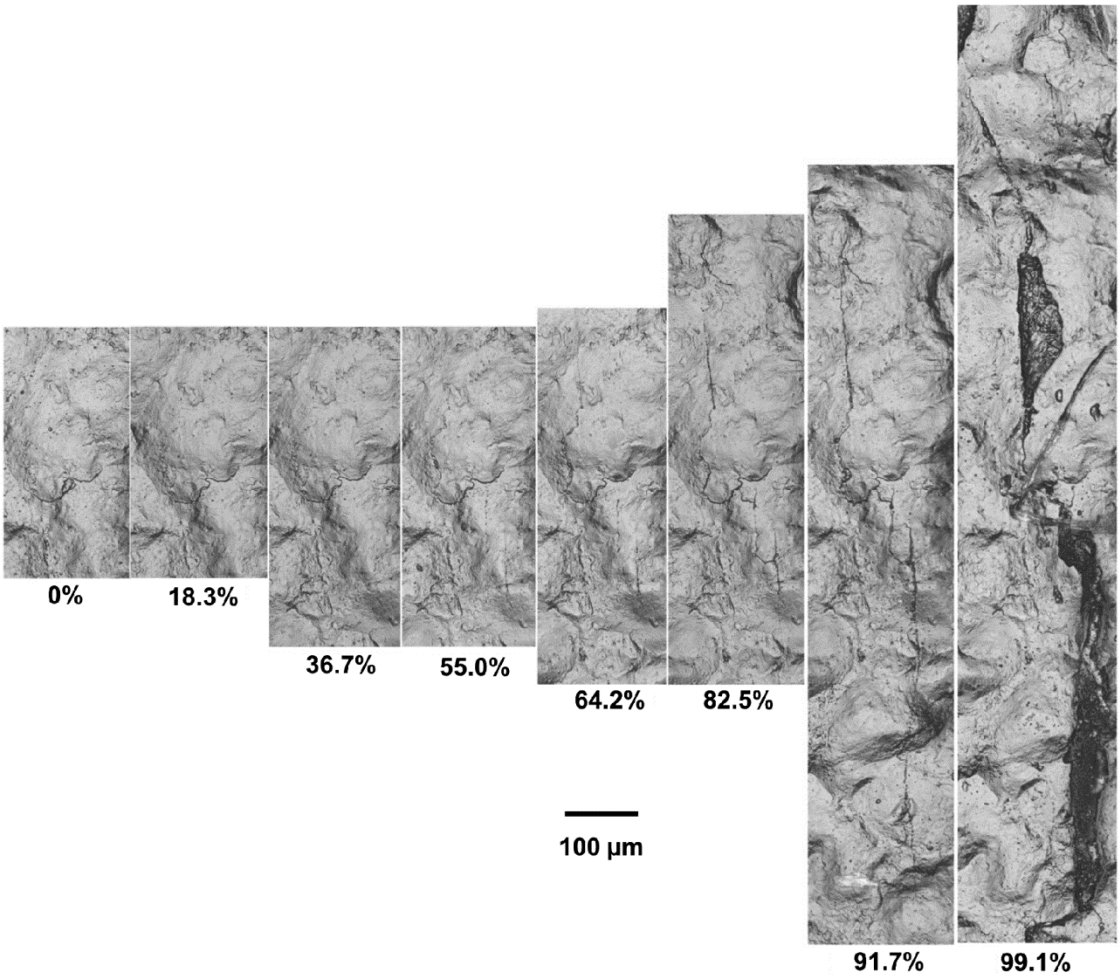

Figure 7- 16: Crack morphology on the shot peened surface as a function of fatigue life fraction (failure at 54504 cycles).

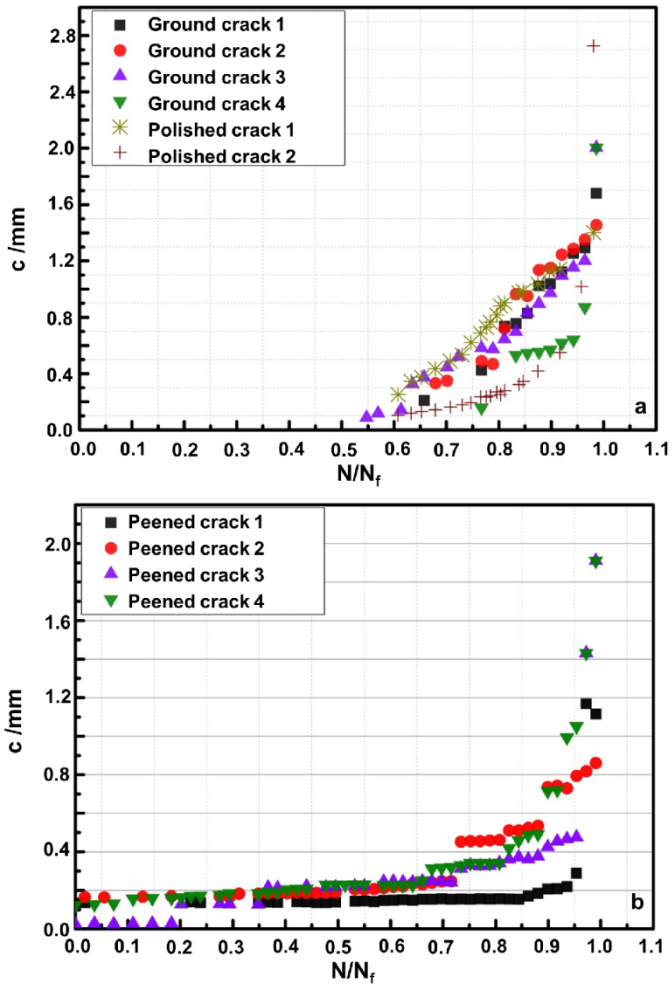

Figure 7- 17: Fatigue crack surface length as a function of fatigue life fraction for notched samples during fatigue at $\Delta\varepsilon_{11}$ = 0.0068 in (a) the polished and ground surface conditions and (b) the T0 shot peened surface condition.

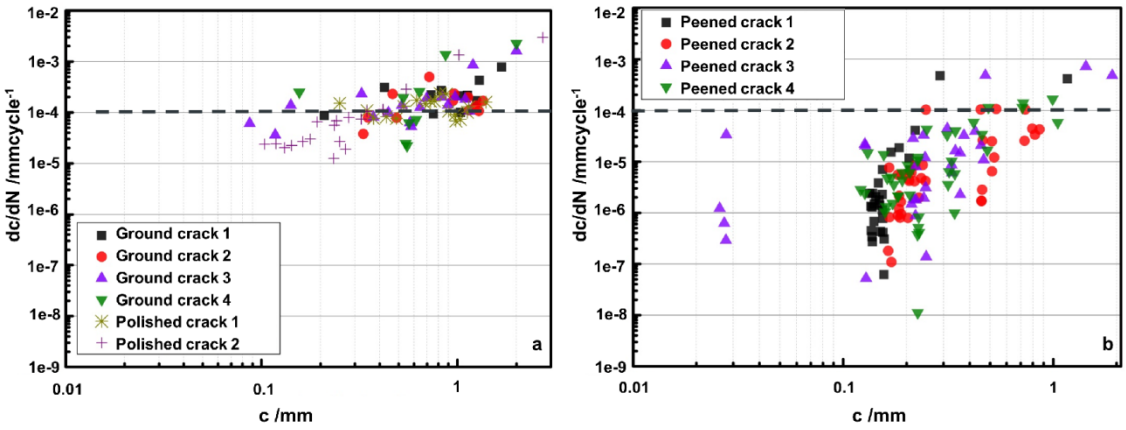

Figure 7- 18: Short crack surface growth rates as a function of crack surface length for notched samples during fatigue at $\Delta\varepsilon_{11}$ = 0.0068 in (a) the polished and ground surface conditions and (b) the shot peened surface condition.

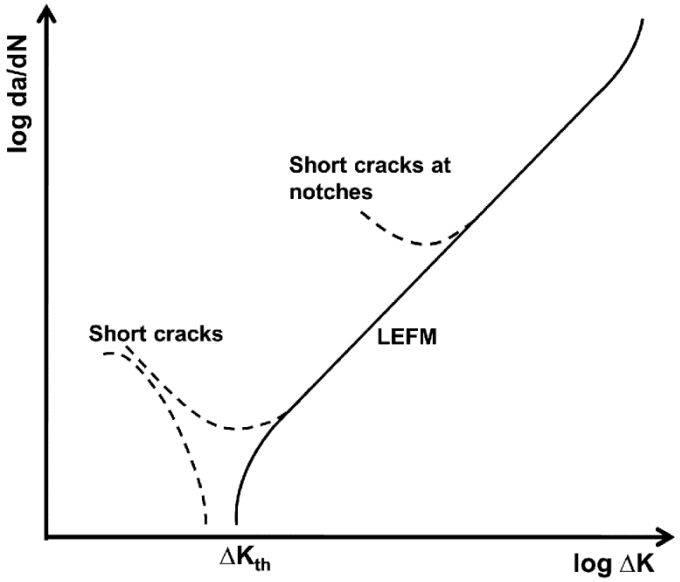

Figure 7- 19: Fatigue crack propagation behaviour for short cracks and short cracks at notches compared with long crack LEFM behaviour. After Suresh and Ritchie [15].

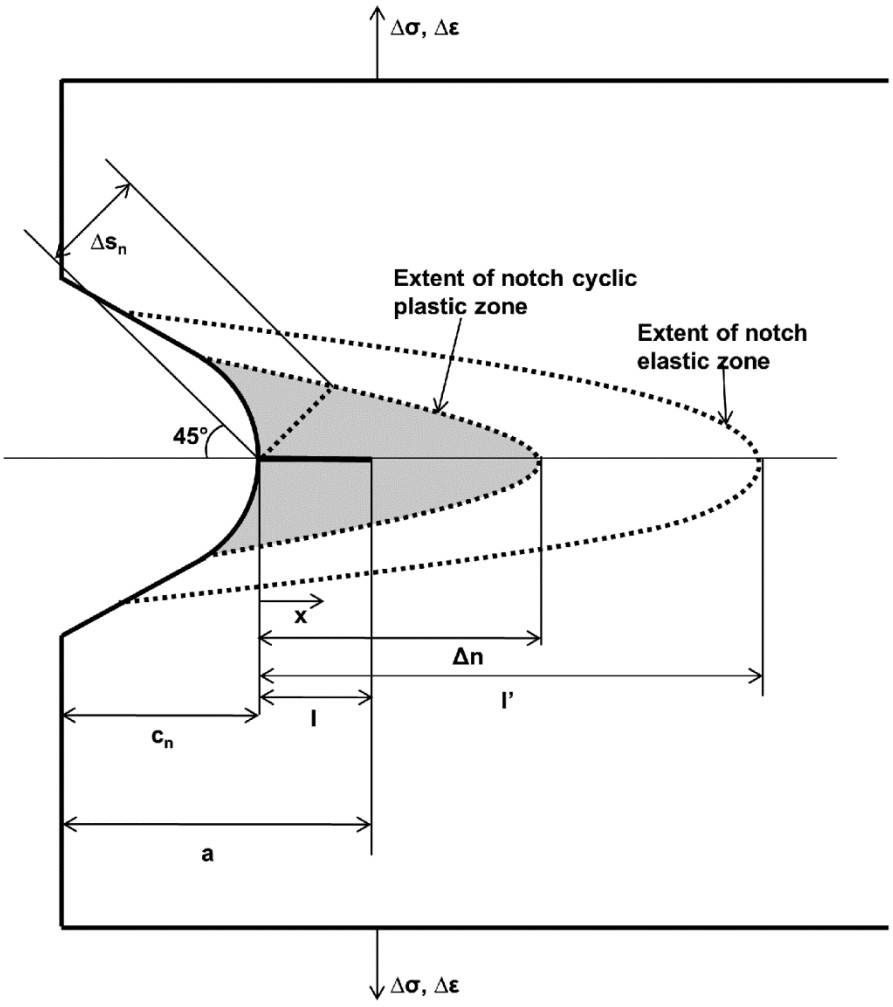

Figure 7- 20: Elastic and plastic zones in the notch region. After Dowling and Hammouda *et al.* [16, 31].

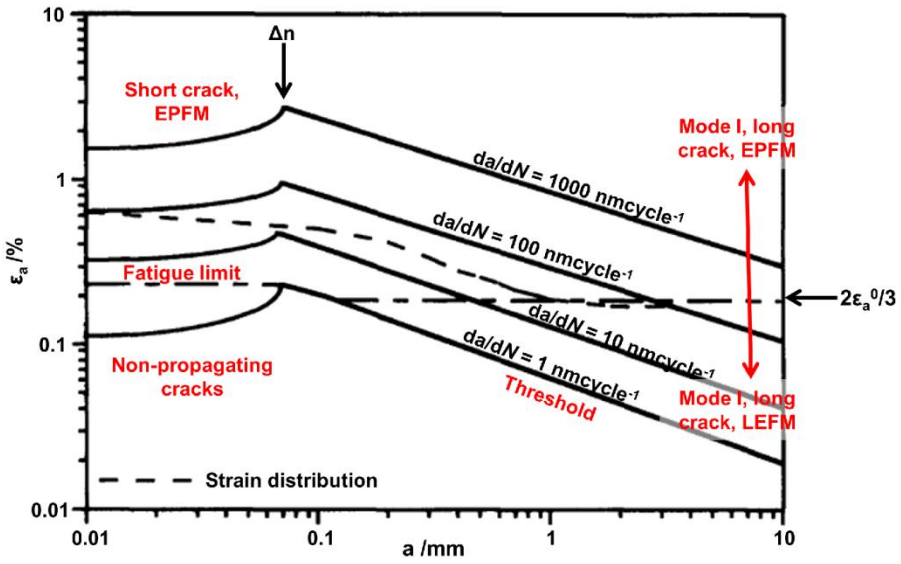

Figure 7- 21: NFFM illustrating fatigue zones, fatigue crack growth rates corresponding to Q1N medium strength quenched and tempered (bainitic microstructure) steel and the strain distribution corresponding to σ_a = 350 MPa notched round bars (K_t = 2.3). After Ahmad *et al.* [28].

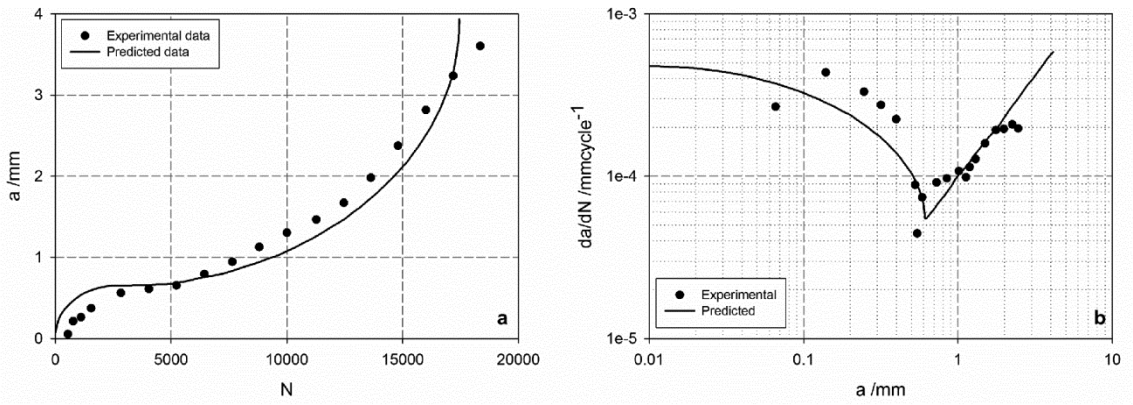

Figure 7- 22: Predicted crack growth rates based on the NFFM illustrated in Figure 7- 21 illustrating (a) crack length as a function of the number of fatigue cycles and (b) crack growth rate as a function of crack length. After Ahmad *et al.* [28].

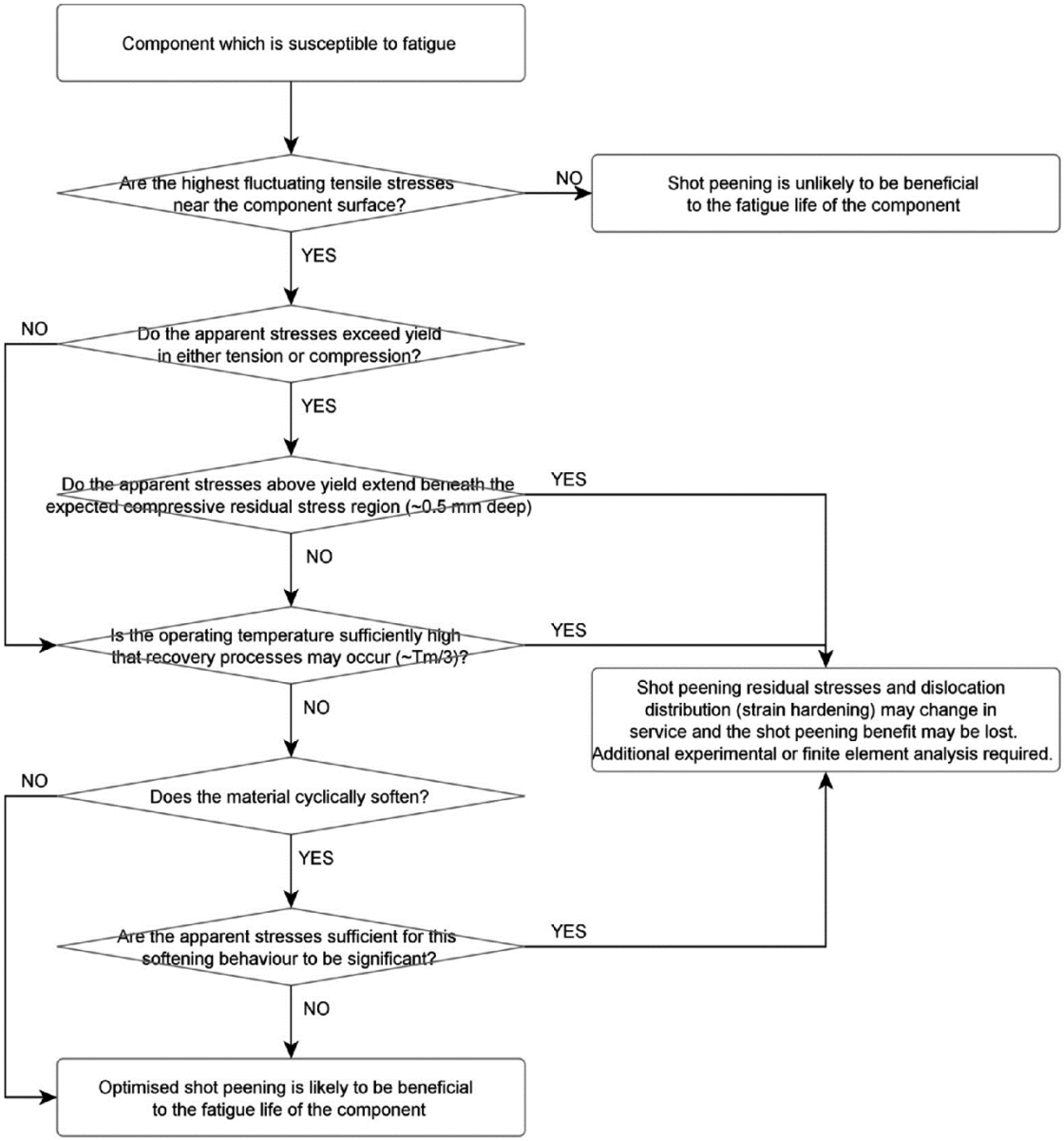

Figure 7- 23: Process flow diagram for establishing whether shot peening is an appropriate fatigue mitigation strategy for a particular component.

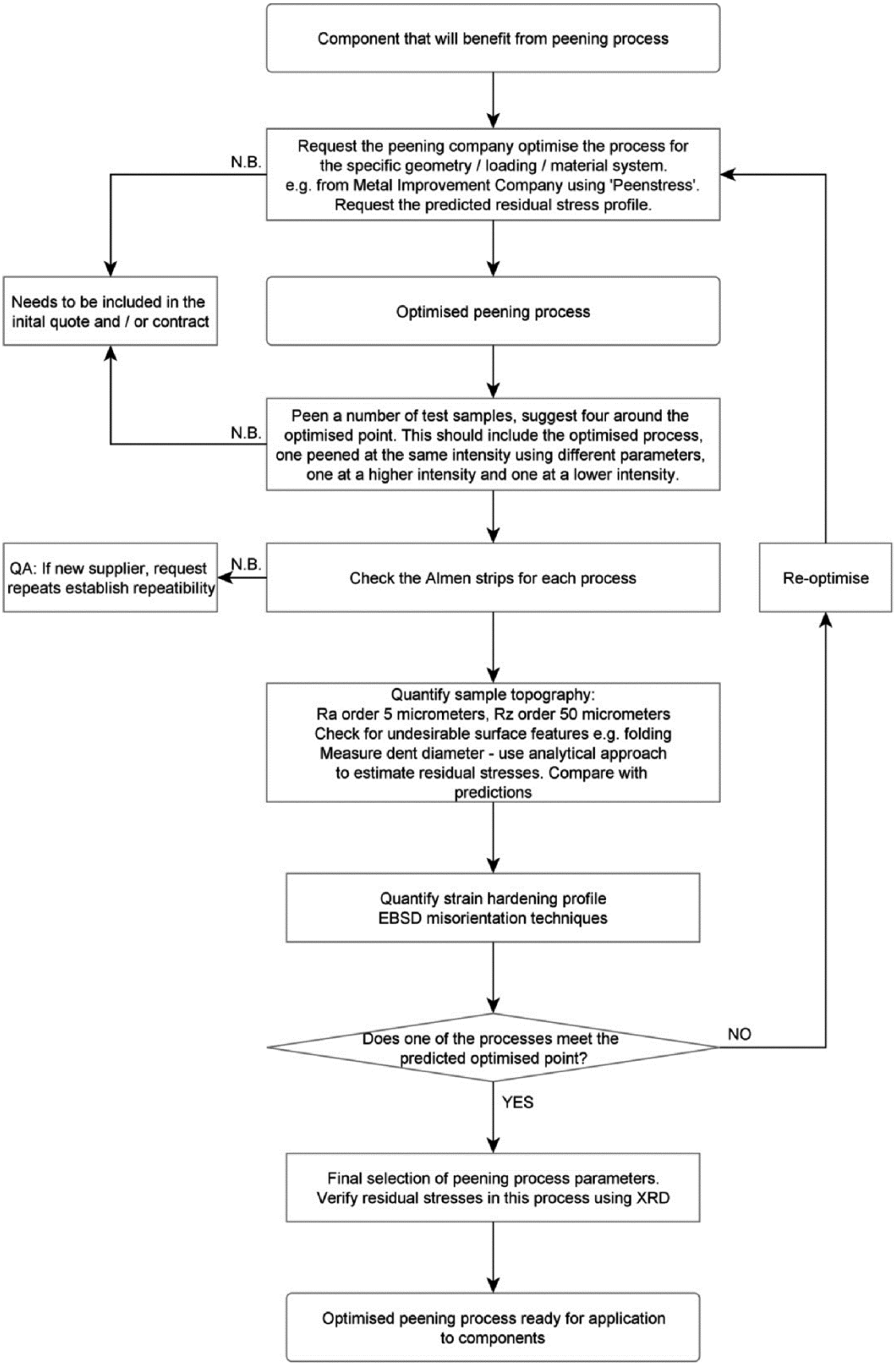

Figure 7- 24: Process flow diagram for shot peening process optimisation and quality assurance.

7.5. References

1. British Energy Generation Ltd., *R5 - Assessment procedure for the high temperature response of structures. Issue 3*, 2003.

2. British Energy Generation Ltd., *R6 - Assessment of the integrity of structures containing defects, Revision 4*, 2001.

3. British Standard, *BS 7910:2005: Guide to methods for assessing the acceptability of flaws in metallic structures*, 2005.

4. Achintha, M. and Nowell, D., *Eigenstrain modelling of residual stresses generated by laser shock peening.* Journal of Materials Processing Technology, 2011. **211**(6): p. 1091 - 1101.

5. Jun, T.-S. and Korsunsky, A.M., *Evaluation of residual stresses and strains using the eigenstrain reconstruction method.* International Journal of Solids and Structures, 2010. **47**(13): p. 1678 - 1686.

6. Jun, T.-S., Venter, A.M. and Korsunsky, A.M., *Inverse eigenstrain analysis of the effect of non-uniform sample shape on the residual stress due to shot peening.* Experimental Mechanics, 2011. **51**(2): p. 165 - 174.

7. Benedetti, M., Fontanari, V. and Monelli, B.D., *Numerical simulation of residual stress relaxation in shot peened high-strength aluminium alloys under reverse bending fatigue.* Journal of Engineering Materials and Technology, 2010. **132**.

8. Benedetti, M., Fontanari, V., Santus, C. and Bandini, M., *Notch fatigue behaviour of shot peened high-strength aluminium alloys: Experiments and predictions using a critical distance method.* International Journal of Fatigue, 2010. **32**(10): p. 1600 - 1611.

9. Song, X., Liu, W.C., Belnoue, J.P., Dong, J., Wu, G.H., Ding, W.J., Kimber, S.A.J., Buslaps, T., Lunt, A.J.G. and Korsunsky, A.M., *An eigenstrain-based finite element model and the evolution of shot peening residual stresses during fatigue of GW103 magnesium alloy.* International Journal of Fatigue, 2012. **42**: p. 284 - 295.

10. Budden, P.J., Sharples, J.K., and Dowling, A.R., *The R6 procedure: Recent developments and comparison with alternative approaches.* International Journal of Pressure Vessels and Piping, 2000. **77**(14-15): p. 895 - 903.

11. Ainsworth, R.A. and Hooton, D.G., *R6 and R5 procedures: The way forward.* International Journal of Pressure Vessels and Piping, 2008. **85**(3): p. 175 - 182.

12. Zanjani, M., 2009. E.ON Engineering Report EEN/09/OSP/SA/1330/R.

13. Zhang, X., 2011. E.ON New Build and Technology Report ENT/11/TSP/SA/981/R.

14. James, M.N., Newby, M., Hattingh, D.G. and Steuwer, A., *Shot-peening of steam turbine blades: Residual stresses and their modification by fatigue cycling.* Procedia Engineering, 2010. **2**(1): p. 441 - 451.

15. Suresh, S. and Ritchie, R.O., *Propagation of short fatigue cracks.* International Metals Reviews, 1984. **29**(6): p. 445 - 476.

16. Dowling, N.E., *Notched member fatigue life predictions combining crack initiation and propagation.* Fatigue and Fracture of Engineering Materials and Structures, 1979. **2**(2): p. 129 - 138.

17. Mutoh, Y., Fair, G.H., Noble, B. and Waterhouse, R.B., *The effect of residual stresses induced by shot peening on fatigue crack propagation in two high strength aluminium alloys.* Fatigue and Fracture of Engineering Materials and Structures, 1987. **10**(4): p. 261 - 272.

18. Gao, Y.K. and Wu, X.R., *Experimental investigation and fatigue life prediction for 7475-T7351 aluminium alloy with and without shot peening-induced residual stresses.* Acta Materialia, 2011. **59**(9): p. 3737 - 3747.

19. De los Rios, E.R., Walley, A., Milan, M.T. and Hammersley, G., *Fatigue crack initiation and propagation on shot-peened surfaces in A316 stainless steel.* International Journal of Fatigue, 1995. **17**(7): p. 493 - 499.

20. Guagliano, M. and Vergani, L., *An approach for prediction of fatigue strength of shot peened components.* Engineering Fracture Mechanics, 2004. **71**(4-6): p. 501- 512.

21. Scott, P.M. and Thorpe, T.W., *A critical review of crack tip stress intensity factors for semi-elliptic cracks.* Fatigue and Fracture of Engineering Materials and Structures, 1981. **4**(4): p. 291 - 309.

22. Knott, J.F., Bowen, P., Luo, J., Jiang, H. and Sun, H.L., *The structural integrity of cast aluminium automotive components subjected to fatigue loads.* Materials Science Forum, 2000. **331 - 337**: p. 1401 - 1412.

23. Fitzpatrick, M.E. and Edwards, L., *Fatigue crack/residual stress-field interactions and their implications for damage-tolerant design.* Journal of Materials Engineering and Performance, 1998. **7**(2): p. 190 - 198.

24. Liljedahl, C.D.M., Zanellato, O., Fitzpatrick, M.E., Lin, J. and Edwards, L., *The effect of weld residual stresses and their re-distribution with crack growth during fatigue under constant amplitude loading.* International Journal of Fatigue, 2010. **32**(4): p. 735 - 743.

25. Lam, Y.C. and Lian, K.S., *The effect of residual stress and its redistribution on fatigue crack growth.* Theoretical and Applied Fracture Mechanics, 1989. **12**(1): p. 59 - 66.

26. Moore, M.G. and Evans, W.P., *Mathematical correction for stress in removed layers in XRD residual stress analysis.* SAE Transactions, 1958. **66**: p. 340 - 345.

27. Ahmad, H.Y., de los Rios, E.R. and Yates, J.R., *The influence of notch plasticity on short fatigue crack behaviour.* Fatigue and Fracture of Engineering Materials and Structures, 1994. **17**(2): p. 235 - 242.

28. Ahmad, H.Y., Clode, M.P. and Yates, J.R., *Prediction of fatigue crack growth in notched members.* International Journal of Fatigue, 1997. **19**(10): p. 703 - 712.

29. Pasha, R.A. and Hammouda, M.M.I., *A model for notch fatigue life.* Materials Science and Engineering A, 2008. **483-484**: p. 319-321.

30. Hammouda, M.M.I., Sallam, H.E.M. and Osman, H.G., *Significance of crack tip plasticity to early notch fatigue crack growth.* International Journal of Fatigue, 2004. **26**(2): p. 173 - 182.

31. Hammouda, M.M.I., Smith, R.A. and Miller, K.J., *Elastic-plastic fracture mechanics for initiation and propagation of notch fatigue cracks.* Fatigue and Fracture of Engineering Materials and Structures, 1979. **2**(2): p. 139 - 154.

32. Hammouda, M.M.I. and Miller, K.J., *Prediction of fatigue lifetime of notched members.* Fatigue and Fracture of Engineering Materials and Structures, 1979. **2**(4): p. 377 - 386.

33. Sehitoglu, H., *Fatigue life prediction of notched members based on local strain and elastic-plastic fracture mechanics concepts.* Engineering Fracture Mechanics, 1983. **18**(3): p. 609 - 621.

34. El Haddad, M.H., Dowling, N.E., Topper, T.H. and Smith, K.N., *J-integral applications for short fatigue cracks at notches.* International Journal of Fracture, 1980. **16**(1): p. 15 - 30.

35. El Haddad, M.H., Smith, K.N. and Topper, T.H., *Fatigue crack propagation of short cracks.* Journal of Engineering Materials and Technology, 1979. **101**(1): p. 42 - 46.

36. Suresh, S., *Fatigue of materials*. 2nd edn.; 2004, Cambridge, UK: Cambridge University Press.

37. Ahmad, H.Y. and Yates, J.R., *An elastic-plastic model for fatigue crack growth at notches.* Fatigue and Fracture of Engineering Materials and Structures, 1994. **17**(6): p. 651 - 660.

38. Smith, R.A. and Miller, K.J., *Fatigue cracks at notches.* International Journal of Mechanical Sciences, 1977. **19**(1): p. 11 - 22.

39. Tomkins, B., *Fatigue crack propagation - an analysis.* Philosophical Magazine, 1968. **18**(155): p. 1041 - 1066.

40. Tomkins, B., *Fatigue failure in high strength metals.* Philosophical Magazine, 1971. **23**(183): p. 687 - 703.

41. Electric Power Research Institute, *F-class turbine disc cracking investigation interim report*, 2008. Palo Alto, CA: EPRI Report PID 063713.